WARWICK
THE UNIVERSITY OF WARWICK

Investigating the self-assembly behavior of diblock copolymers *via* copolymer blending and fluorescence labelling

Robert Keogh

Submitted for the degree of Doctor of Philosophy

University of Warwick

Department of Chemistry

December 2018

For Gemma

Table of Contents

List of Figures, Schemes and Tables

List of Figures

List of Schemes

List of Tables

Acknowledgements

Firstly, I would like to give my sincere thanks to my supervisor, Professor Rachel O'Reilly, for providing me the opportunity to work in her group on such an engaging and at times challenging project. I am truly grateful for all of your time, guidance, patience, advice, and mentorship over the past 4 years and suffice to say, I would not have managed to get to this point without your continued support and encouragement.

I would like to thank all of the members of the O'Reilly and Dove groups, both past and present, who have not only made my time within the group enjoyable but have helped me countless times during my PhD. Words cannot describe how much I am appreciative of the amount of time you have given to discuss my research and I don't think I would have achieved as much as I have if it wasn't for your combined expertise, numerous suggestions and constructive criticism that have helped me along the way.

I would especially like to thank my desk and lab buddy Dr. Rebecca Williams for all of her help, support and "humour" over the past four years. Credit must also go to Dr. Marianne Rolph and Dr. Alice Hill who have helped me to develop my lab and housekeeping skills from poor to somewhat respectable. Special mention goes to Dr. Daniel Wright for helping me in my first year and for introducing me to light scattering analysis and polymer self-assembly techniques. I would also like to thank Dr. Mathew Robin who always gave up his time to answer any chemistry-related question I had and for helping me to develop my understanding of RAFT polymerization and fluorescence. My sincere thanks to Dr. Maria Inam, Mr. Zachary Coe, Mr. Jon Husband, Miss. Lucy Arkinstall, Mr. Bo Li, Mr. Spyridon Varlas, Dr. Charlotte Zammit, and Mr. Matthieu Miclotte for making the lab a more entertaining place to work in and for raising my spirits

in times of hardship. I would like to thank Dr. Thomas Wilks and Dr. Jeffrey Foster for the many scientific discussions we have held over the past few years as without it, I don't think I would have been able to overcome the many research challenges I have faced throughout my PhD. A final thankyou goes to Dr. Lewis Blackman who apart from always making me laugh, provided his knowledge, expertise and at times seemingly unlimited number of suggestions on any chemistry-related problem I had.

I would like to thank all of the collaborators I have had the privilege to work with throughout my PhD. I would like to acknowledge EPRSC for funding and the University of Warwick for the use of their facilities. I am also thankful to all of the technical and admin staff in the Department of Chemistry for their assistance and time.

I would like to thank my parents, Patricia and Paul Keogh, for their support throughout my undergraduate and postgraduate studies at the University of Warwick. Whenever I needed to call, they have always been there to listen and for that I cannot thank them enough. Special mention goes to the members of the University of Warwick Squash and Pool Sports Clubs for providing an escape from the scientific bubble and reminding me that there's more to life than work.

Finally, I would like to thank Gemma Walton for all the love and patience you have shown me over the past three years. Whilst you may not understand the contents of this thesis, I will always be forever grateful for how you listened to my explanations and offered your thoughts. You turned bad days into good days and reminded me that it wasn't the end of the world when something had failed in the lab once again. Without your constant support and kindness, this thesis truly would not have been written.

Declaration of Authorship

This thesis is submitted to the University of Warwick in support of my application for the degree of Doctor of Philosophy. It has been composed by myself and has not been submitted in any previous application for any degree.

The work presented (including data generated and data analysis) was carried out by myself except in the following cases which are outlined below, and are clearly labelled in the corresponding text:

Chapter 2 – High resolution electrospray ionization time of flight mass spectrometry was performed by Dr. Lijiang Song at the University of Warwick.

Chapter 3 – Steady-state fluorescence spectroscopy measurements were conducted with assistance from Dr. Mathew Robin. High resolution electrospray ionization time of flight mass spectrometry was performed by Dr. Lijiang Song at the University of Warwick.

Chapter 4 – The synthesis, characterization, and self-assembly of amphiphilic diblock copolymers **4i-4iv** was performed by Dr. Lewis Blackman at the University of Warwick. Measurement of the cloud point temperatures for micellar solutions composed of amphiphilic diblock copolymers **4i-4iv** *via* variable temperature turbidimetry was also carried out by Dr. Lewis Blackman at the University of Warwick. Microcalorimetry analysis was conducted with the assistance of Mr. Zachary Coe. High resolution electrospray ionization time of flight mass spectrometry was performed by Dr. Lijiang Song at the University of Warwick.

Chapter 5 – Transmission electron microscopy imaging and analysis was performed with the assistance of Mr. Spyridon Varlas at the University of Warwick. High resolution electrospray ionization time of flight mass spectrometry was performed by Dr. Lijiang Song at the University of Warwick.

The experimental protocol and characterization data for the R group DBM-functionalized RAFT agent **2i**, and the R group ABM-functionalized RAFT agent **2ii** has been published in the following paper:

Reversibly Manipulating the Surface Chemistry of Polymeric Nanostructures via a "Grafting To" Approach Mediated by Nucleobase Interactions

Z. Hua, **R. Keogh**, Z. Li, T. R. Wilks, G. Chen, R. K. O'Reilly, *Macromolecules*, 2017, **50**, 3662–3670.

List of Publications

1. *Predicting Monomers for Use in Polymerization-Induced Self-Assembly*

   J. C. Foster, S. Varlas,§ B. Couturaud,§ J. R. Jones, **R. Keogh**, R. T. Mathers, R. K. O'Reilly, *Angew. Chem. Int. Ed.*, 2018, **57**, 15733-15737

2. *Structural Determinants of the Stability of Enzyme-Responsive Polyion Complex Nanoparticles Targeting Pseudomonas aeruginosa's Elastase*

   I. Insua, M. Petit, L. D. Blackman, **R. Keogh**, A. Pitto-Barry, R. K. O'Reilly, A. F. A. Peacock, A.-M. Krachler, F. Fernandez-Trillo, *ChemNanoMat.*, 2018, **4**, 807–814.

3. *Entrapment and Rigidification of Adenine by a Photo-Cross-Linked Thymine Network Leads to Fluorescent Polymer Nanoparticles*

   Z. Hua, T. R. Wilks, **R. Keogh**, G. Herwig, V. G. Stavros, R. K. O'Reilly, *Chem. Mater.*, 2018, **30**, 1408-1416.

4. *Precision Epitaxy for Aqueous 1D and 2D Poly(ε-caprolactone) Assemblies*

   M. C. Arno,§ M. Inam,§ Z. Coe, G. Cambridge, L. J. Macdougall, **R. Keogh**, A. P. Dove, R. K. O'Reilly, *J. Am. Chem. Soc.*, 2017, **139**, 16980–16985.

5. *Reversibly Manipulating the Surface Chemistry of Polymeric Nanostructures via a "Grafting To" Approach Mediated by Nucleobase Interactions*

   Z. Hua, **R. Keogh**, Z. Li, T. R. Wilks, G. Chen, R. K. O'Reilly, *Macromolecules*, 2017, **50**, 3662–3670.

§ These authors contributed equally.

List of Symbols and Abbreviations

[I]	Initiator concentration
$[I]_0$	Initial initiator concentration
[M]	Monomer concentration
$[M]_0$	Initial monomer concentration
$[M]_t$	Monomer concentration at time = t
4VP	4-Vinylpyridine
A	Absorbance
A	Amplitude
$A(\tau)$	Distribution of relaxation times
A_2	Second virial coefficient
AA	Acrylic acid
ABM	Aminobromomaleimide
ABMMA	Aminobromomaleimide-functionalized methacrylate monomer
ACP	4,4'-Azobis(4-cyano-1-pentanol)
ACVA	4,4′-Azobis(4-cyanovaleric acid)
AEAm	2-Aminoethylacrylamide hydrochloride
A_f	Relative amplitude of the fast mode in light scattering
AIBN	2,2'-Azobisisobutyronitrile
AIE	Aggregation-induced emission
AM	Aminomaleimide
AMPS	2-Acrylamido-2-methylpropane sulfonic acid
A_s	Relative amplitude of the slow mode in light scattering
ATRP	Atom transfer radical polymerization
BCP	Block copolymer

Boc	*Tert*-butyloxycarbonyl
br	Broad peak in ^{1}H NMR spectrum
BzMA	Benzyl methacrylate
c	Concentration
CAC	Critical aggregation concentration
CDSA	Crystallization-driven self-assembly
CL	*ε*-Caprolactone
CMC	Critical micelle concentration
Cryo	Cryogenic
CTA	Chain transfer agent
D	Diffusion coefficient
d	Doublet peak in ^{1}H NMR spectrum
DAAm	Diacetone acrylamide
D_{app}	Apparent diffusion coefficient
DBM	Dibromomaleimide
DBMMA	Dibromomaleimide-functionalized methacrylate monomer
DCM	Dichloromethane
DD	Direct dissolution
DEAEMA	2-(Diethylamino)ethyl methacrylate
DEAm	*N*,*N*-Diethylacrylamide
DEGMA	Diethylene glycol monomethyl ether methacrylate
D_h	Hydrodynamic diameter
DIAD	Diisopropyl azodicarboxylate
DIPAEMA	2-(Diisopropylamino)ethyl methacrylate
DLS	Dynamic light scattering
$Đ_M$	Molecular weight dispersity

DMAc	*N,N'*-Dimethylacrylamide
DMAEMA	2-(Dimethylamino)ethyl methacrylate
DMAP	4-Dimethylaminopyridine
DMAPS	3-Dimethyl(methacryloyloxyethyl) ammonium propane sulfonate
DMF	Dimethylformamide
DMIBMA	4-(3,4-Dimethylmaleimidio)butyl methacrylate
dn/*dc*	Refractive index increment
DNA	Deoxyribonucleic acid
DP	Degree of polymerization
DSC	Differential scanning calorimetry
DTM	Dithiomaleimide
DTMMA	Dithiomaleimide-functionalized methacrylate monomer
EDC·HCl	1-(3-Dimethylaminopropyl)-3-ethylcarbodiimide hydrochloride
EDPT	Electron driven proton transfer
EGAP	Ethylene glycol acrylate phosphate
EGDMA	Ethylene glycol dimethacrylate
em	Emission
eq	Equivalents
ESI-MS	Electrospray ionization mass spectrometry
ESI-ToF	Electrospray ionization time of flight
EtOx	2-Ethyl-2-oxazoline
ex	Excitation
f	Free radical initiator efficiency
FLIM	Fluorescence-lifetime imaging
FRET	Förster resonance energy transfer
FRP	Free radical polymerization

FT-IR	Fourier transform infra-red
$g_1(q, t)$	Electric field autocorrelation function
$g_2(q, t)$	Scattering intensity autocorrelation function
GalSMA	Galactose methacrylate
GMA	Glycerol methacrylate
GPC	Gel permeation chromatography
GTP	Group transfer polymerization
HBMA	2-Hydroxybutyl methacrylate
HDF	Human dermal fibroblast
HPLC	High-performance liquid chromatography
HPMA	2-Hydroxypropyl methacrylate
HPMAm	*N*-(2-hydroxypropyl) methacrylamide
HRMS	High resolution mass spectrometry
$I^{\bullet}$	Initiator derived radical
ICAR	Initiators for continuous activator regeneration
I_i	Intensity of light scattered from the species "i"
*i*PrOx	2-Isopropyl-2-oxazoline
I_{sample}	Intensity of light scattered from the sample
$I_{solvent}$	Intensity of light scattered from the solvent
$I_{standard}$	Intensity of light scattered from the standard
J	Coupling constant from ^{1}H NMR spectroscopy
K	Contrast factor in SLS analysis
$k_{add,\text{-}add,addP,\text{-}addP,\beta,\text{-}\beta}$	Rate constants in the RAFT equilibria
k_B	Boltzmann's constant
k_d	Rate constant for initiator decomposition
k_i	Rate constant for initiation

k_p	Rate constant for propagation
k_t	Rate constant for termination
LAM	Less activated monomer
l_c	Length of the hydrophobic block
LCST	Lower critical solution temperature
L_{max}	Maximum chain length
M	Monomer
m	Multiplet peak in ^{1}H NMR spectrum
m/z	Mass to charge ratio
MA	Methyl acrylate
macroCTA	Macro chain transfer agent
MADIX	Macromolecular design *via* the interchange of xanthates
MAM	More activated monomer
MB	Micelle blending
MBM	Monobromomaleimide
MEA	2-Methoxyethyl acrylate
M_i	Mass of polymer chain of length “i”
MMA	Methacrylic acid
MMA	Methyl methacrylate
M_n	Number average molecular weight
$M_{n,\ theo}$	Theoretical M_n calculated from monomer loading and conversion
MPC	2-Methacryloyloxyethyl phosphorylcholine
M_w	Weight average molecular weight
$M_{w,\ particle}$	Weight average molecular weight of the particle
$M_{w,\ polymer}$	Weight average molecular weight of the unimer
n	Refractive index

n_0	Refractive index of the solvent
N_A	Avogadro's constant
NAGA	*N*-Acryloylglycinamide
N_{agg}	Aggregation number
$N_{agg,\ app}$	Apparent aggregation number
*n*BA	*n*-Butyl acrylate
n-BuMA	*n*-Butyl methacrylate
N_i	Number of polymer chains of length "i"
NIPAM	*N*-Isopropylacrylamide
NMM	*N*-Methylmorpholine
NMP	Nitroxide-mediated radical polymerization
NMR	Nuclear magnetic resonance
NVC	*N*-Vinylcaprolactam
OEGMA	Oligoethylene glycol monomethyl ether methacrylate
p	Packing parameter
p	Poly
PAA	Propylacrylic acid
PBS	Phosphate-buffered saline
PD	Polydispersity
PEG	Polyethylene glycol
PEGMA	Poly(ethylene glycol) monomethyl ether methacrylate
Pet.	Petroleum
PISA	Polymerization-induced self-assembly
P_m	Polymer with DP = m
$P_m^{\bullet}$	Polymeric radical with DP = m
P_n	Polymer with DP = n

$P_n^{\bullet}$	Polymeric radical with DP = n
ppm	Parts per million
PRE	Persistent radical effect
q	Quartet peak in ^{1}H NMR spectrum
q	Scattering wave vector
$R^{\bullet}$	Chain transfer agent derived radical
RAFT	Reversible addition-fragmentation chain transfer
R_{core}	Core radius
RDRP	Reversible deactivation radical polymerization
ref	Reference
REPES	Regularized positive exponential sum
R_g	Radius of gyration
R_h	Hydrodynamic radius
$R_{h,\ app}$	Apparent hydrodynamic radius
RI	Refractive index
ROMP	Ring-opening metathesis polymerization
ROMPISA	Ring-opening metathesis polymerization-induced self-assembly
ROP	Ring-opening polymerization
R_p	Rate of polymerization
rt	Room temperature
R_θ	Rayleigh ratio
$R_{\theta,\ standard}$	Rayleigh ratio of the standard
s	Singlet peak in ^{1}H NMR spectrum
S	Spherical micelles
SAXS	Small angle X-ray scattering
SEC	Size exclusion chromatography

sept.	Septuplet peak in ^{1}H NMR spectrum
SLS	Static light scattering
SS	Solvent switch
St	Styrene
T	Temperature
t	Time
t	Triplet peak in ^{1}H NMR spectrum
^{t}BuA	*Tert*-butyl acrylate
T_{cp}	Cloud point temperature
TEGA	Triethylene glycol monomethyl ether acrylate
TEM	Transmission electron microscopy
TERP	Organotellurium-mediated radical polymerization
TF	Thin film rehydration
T_g	Glass transition temperature
THF	Tetrahydrofuran
TLC	Thin layer chromatography
TMS	Tetramethylsilane
T_p	Thermal transition temperature determined by DSC
TPE	1-Ethenyl-4-(1,2,2-triphenylethenyl)benzene
UA	Uranyl acetate
UB	Unimer blending
UCST	Upper critical solution temperature
UV	Ultraviolet
V	Vesicles
v	Volume
V-50	2,2'-Azobis(2-methylpropionamidine) dihydrochloride

VA-044	2,2'-Azobis(2-(2-imidazolin-2-yl)propane dihydrochloride
VBA	4-Vinylbenzoic acid
vis	Visible
VPip	*N*-Vinyl piperidone
W	Worms
wt%	Weight percentage
α	Ionization degree
α_o	Optimal area of the polar head group
Γ	Average relaxation rates
γ	Interfacial tension
δ	Chemical shift in NMR spectroscopy
η	Intrinsic viscosity
η_0	Specific viscosity
θ	Angle
λ	Wavelength
λ_0	Wavelength of the incident beam
ρ	Conversion
τ	Relaxation time
ϕ	Partition coefficient
Φ_f	Quantum yield
χ	Interaction parameter

Thesis Summary

This thesis explores the use of copolymer blending and fluorescence labelling for investigating, understanding and controlling the self-assembly and stimuli-responsive behavior of amphiphilic block copolymers in solution.

Chapter 1 provides an introduction to polymers and an overview of the various polymerization methodologies that exist, with a focus upon reversible addition-fragmentation chain transfer (RAFT) polymerization. The principles of block copolymer self-assembly in solution is discussed along with the numerous parameters and important factors that dictate solution state behavior.

In **Chapter 2** a range of novel RAFT agents are designed and synthesized for which the incorporation of an aminobromomaleimide (ABM) fluorophore into the chemical structure *via* both R and Z group functionalization is explored.

In **Chapter 3** the copolymer blending protocol is introduced as a method for predictably tuning the self-assembly and stimuli-responsive behavior of amphiphilic block copolymers. The limitations of this approach are examined through the blending of a series of pH-responsive micelles *via* two different mixing protocols. Core functionalized fluorescently-labelled polymer analogues are synthesized using an R group ABM-functionalized RAFT agent developed in Chapter 2, with their internal properties, self-assembly behavior and stimuli-responsiveness explored *via* fluorescence analysis.

In **Chapter 4** a series of thermoresponsive amphiphilic block copolymers are blended together in an attempt to modulate the cloud point transition in a controlled manner. A range of intermediate cloud points were measured for blended block copolymers with brush-like coronal chain architectures, in contrast to their homopolymeric analogues.

In **Chapter 5** fluorescently-labelled polymer nanostructures are prepared in solution *via* RAFT-mediated polymerization-induced self-assembly (PISA) using a Z group ABM-functionalized RAFT agent developed in Chapter 2. Pure phases of three different block copolymer morphologies are targeted and compared to literature predictions to determine the effect of ABM incorporation on the PISA mechanism.

1. Introduction

1.1. Introduction to polymers

Ubiquitous in nature, polymers represent a dynamic, industrially significant and continuously expanding field of chemical research. From naturally derived biological polymers such as DNA, proteins and nucleic acids to synthetic polymers produced on an industrial scale, such as nylon and polyethylene (Figure 1.1), polymers are a key component to our society that encompass a multitude of applications.

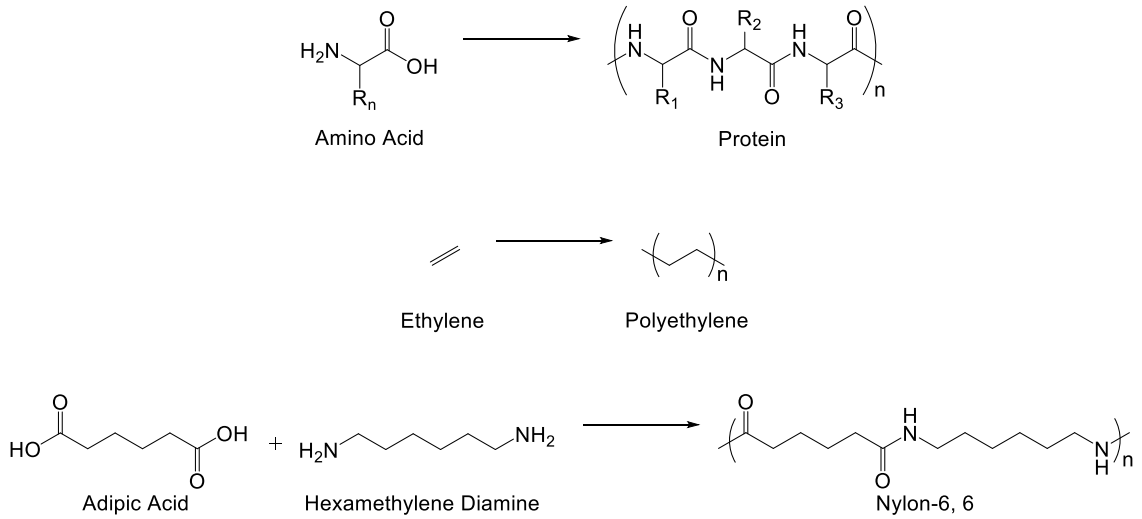

Figure 1.1: Chemical structures of a naturally derived polymer, in this case a protein, and synthetic polymers polyethylene and Nylon-6, 6 from their respective monomers.

Polymers can be defined as a compound that is comprised of a long sequence of one or more smaller units, termed as monomers, linked to one another either by covalent bonds or intermolecular interactions.[1] The chemical process by which polymers are synthesized is termed polymerization and the degree of polymerization (DP) is simply the total number of monomeric units within the polymer.[2] Due to their relatively higher molecular weight, polymers typically display significantly different macroscopic properties with respect to their constituent small molecules, for example: increased mechanical strength; wear; resistance; viscosity and the presence of a glass transition temperature (T_g).[3]

Therefore, polymers are often characterized by their DP and in turn their molecular weight as this provides an initial point of reference with regards to comparing their resultant properties.

Another key feature that is frequently used to characterize polymers is their molecular weight distribution or more commonly their dispersity ($Đ_M$). In this context, dispersity is simply a measure of the variation in length across all polymer chains. Two different molecular weight averages can be used to describe the molecular weight distribution – number average molecular weight (M_n) and weight average molecular weight (M_w), which are defined in equations (**1.1**) and (**1.2**) respectively where N_i is the number of chains with mass M_i.[4] The difference between M_w and M_n is that the former takes into consideration that polymer chains with a higher molecular weight account for a greater proportion of the total molecular weight of the polymer. A polymer's dispersity is simply the ratio of M_w to M_n as detailed in equation (**1.3**), thus if all polymer chains are of exactly the same molecular weight, $Đ_M = 1$. In practice, a polymer's dispersity and associated molecular weight distribution is determined experimentally by size exclusion chromatography (SEC).[5]

$$M_n = \frac{\sum N_i M_i}{\sum N_i} \qquad \textbf{1.1}$$

$$M_w = \frac{\sum N_i M_i^2}{\sum N_i M_i} \qquad \textbf{1.2}$$

$$Đ_M = \frac{M_w}{M_n} \qquad \textbf{1.3}$$

A critical advantage of polymers is their outstanding versatility and broad scope with regards to their properties and ultimately their applications which can be controlled *via* judicious manipulation of a wide range of elements. From a synthetic viewpoint, there

are three main elements through which control can be imparted: composition; architecture and functionality.[6] Ultimately, the key to the development of functional polymers with predetermined, well-defined structures is the mechanism by which the product polymer is formed. Numerous polymerization methodologies exist within the literature and their associated advantages and disadvantages will be comprehensively discussed. In general, there are two main classes of polymerization mechanism – step-growth polymerization and chain-growth polymerization.

1.2. Polymerization techniques

1.2.1. Step-growth polymerization

Despite its conceptually simplistic approach, step-growth polymerization remains one of the most utilized polymerization mechanisms within industry today. Step-growth polymerization entails a series of stepwise reactions between two mutually reactive functional groups resulting in the formation of linear high molecular weight polymers. Step-growth polymerizations proceed *via* individual reactions involving either one hetero-difunctional monomer or two different homo-difunctional monomers which react in a step-wise growth process.[7] Initially, a dimer is formed which can then either react with another monomer to produce a trimer or combine with another dimer to generate a tetramer. Step-growth polymerizations proceed in this fashion resulting in the formation of a large population of short chain polymers which continue to grow at the same rate until the limiting monomer is fully consumed. Therefore, throughout the polymerization the average molecular weight of each polymer chain remains relatively low until near-full conversion is reached; at which point the average molecular weight of each polymer chain significantly increases.

Step-growth polymerizations that involve the elimination of small molecules, typically water, are termed polycondensations whereas polyadditions are step-growth polymerizations that do not result in the co-generation of small molecules. A classic example of a polycondensation is the production of Nylon-6, 6 – a polyamide synthesized from a dicarboxylic acid and a diamine (Scheme 1.1). Alternatively, an important class of polymers formed from polyadditions are polyurethanes which are used as thermoplastic elastomers; the building blocks for which are a diisocyanate and a diol (Scheme 1.1).

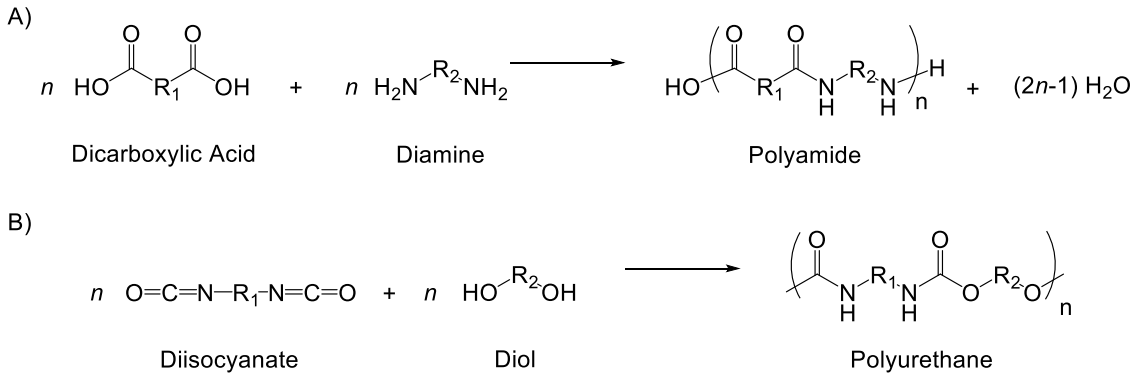

Scheme 1.1: Schematic representation of a) the polycondensation reaction between a dicarboxylic acid and a diamine to form a polyamide, and b) the polyaddition reaction between a diisocyanate and a diol to form a polyurethane.

A critical advantage of step-growth polymerizations is that only a single chemical reaction is utilized throughout the polymerization. Furthermore, step-growth polymerizations preclude the requirement of initiation, propagation and termination steps thereby preventing any chain transfer and termination events which commonly plague chain-growth polymerizations. However, to obtain high molecular weight polymers step-growth polymerizations necessitate a perfect stoichiometric ratio of the two mutually reactive moieties, a high degree of monomer purity coupled with high yielding chemical reactions.[7] Ultimately, step-growth polymerizations often suffer from side reactions and

contaminants; have a relatively limited scope regarding functionality and polymer architecture; lack control over the resultant polymer's dispersity and hence are often considered to be less versatile in comparison to chain-growth polymerization methodologies.

1.2.2. Chain-growth polymerization

Chain-growth polymerization primarily differs to step-growth polymerization through the introduction of initiation, propagation and termination reactions; all of which are absent in the latter.[8] Instead of one single chemical reaction being utilized throughout the polymerization and proceeding at a similar rate independent of molecular weight, chain-growth polymerizations involve multiple reactions with differing reaction rates and mechanisms. Typically, chain-growth polymerizations require an initiator to produce an activated species with a reactive moiety e.g. a free radical, cation or anion.[9] Subsequent reaction of the initiator species with a monomer results in the formation of a growing polymer chain, often referred to as the propagating species. Polymer chains continue to grow through a process known as propagation which comprises the addition of large amounts of monomer to the growing polymer chain *via* the active chain end. Chain-growth polymerizations continue in this manner until all monomer is consumed or the reactive chain end group is deactivated. However, unlike in step-growth polymerization, termination and chain transfer events are often prevalent in chain-growth polymerizations leading to the removal of the growing polymer chain's ability to propagate.

Pivotally, the utility of chain-growth polymerization resides in the control and flexibility in polymer design and synthesis with regards to composition, architecture and functionality. Variation in polymer composition can be easily achieved owing to the

greater range of monomers available as well as *via* block copolymer and copolymerization strategies. In certain cases, a high degree of sequence-control can be realized through optimization of the polymerization conditions whilst a wide variety of polymer architectures and functionalities can be attained through careful choice of monomer and/or nature of the initiator.

1.2.2.1. Free radical polymerization (FRP)

Conventional free radical polymerization (FRP) is a commonly applied polymerization method and is well-established in the industrial production of high molecular weight polymers, accounting for ~50% of all commercial polymers.[10] Several factors are responsible for FRP's preeminent position including: its compatibility with a wide range of monomers; its high tolerance towards unprotected functional groups and its robustness in relation to both solvent polarity and reaction conditions allowing polymerizations to be conducted in bulk, solution, emulsion or suspension.[11,12] Consequently, FRP is simple to implement and relatively inexpensive in comparison to alternative chain growth polymerization mechanisms.

As with all chain-growth polymerizations, the mechanism for a conventional free radical polymerization consists of three main stages: initiation; propagation and termination – the chemical equations for which are presented in Figure 1.2.[13]

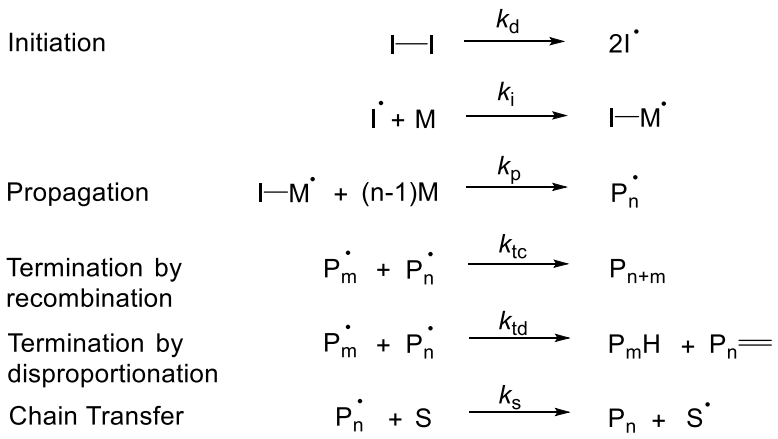

Figure 1.2: The key mechanistic steps with their associated rate constants involved in a FRP. I-I is a radical initiator, M is a vinyl monomer, P_n is a polymer chain with DP = n, and S is a chain transfer agent.

In the case of FRP, the activated species is unsurprisingly a free radical which is typically produced from the homolytic fission of a symmetrical radical source e.g. 2,2'-azobisisobutyronitrile (AIBN), either by heat or UV light. Initiation and propagation proceed in a similar manner as discussed previously for a chain-growth polymerization. Termination events can either occur *via* disproportionation which involves an abstraction of a hydrogen or by recombination whereby two propagating polymer species couple together to form one larger polymeric chain with no active chain end, see Scheme 1.2. Alternatively, radicals can be removed from the propagating species through chain transfer reactions with either the solvent, monomer or other propagating species leading to the formation of "dead" polymer chains.[14]

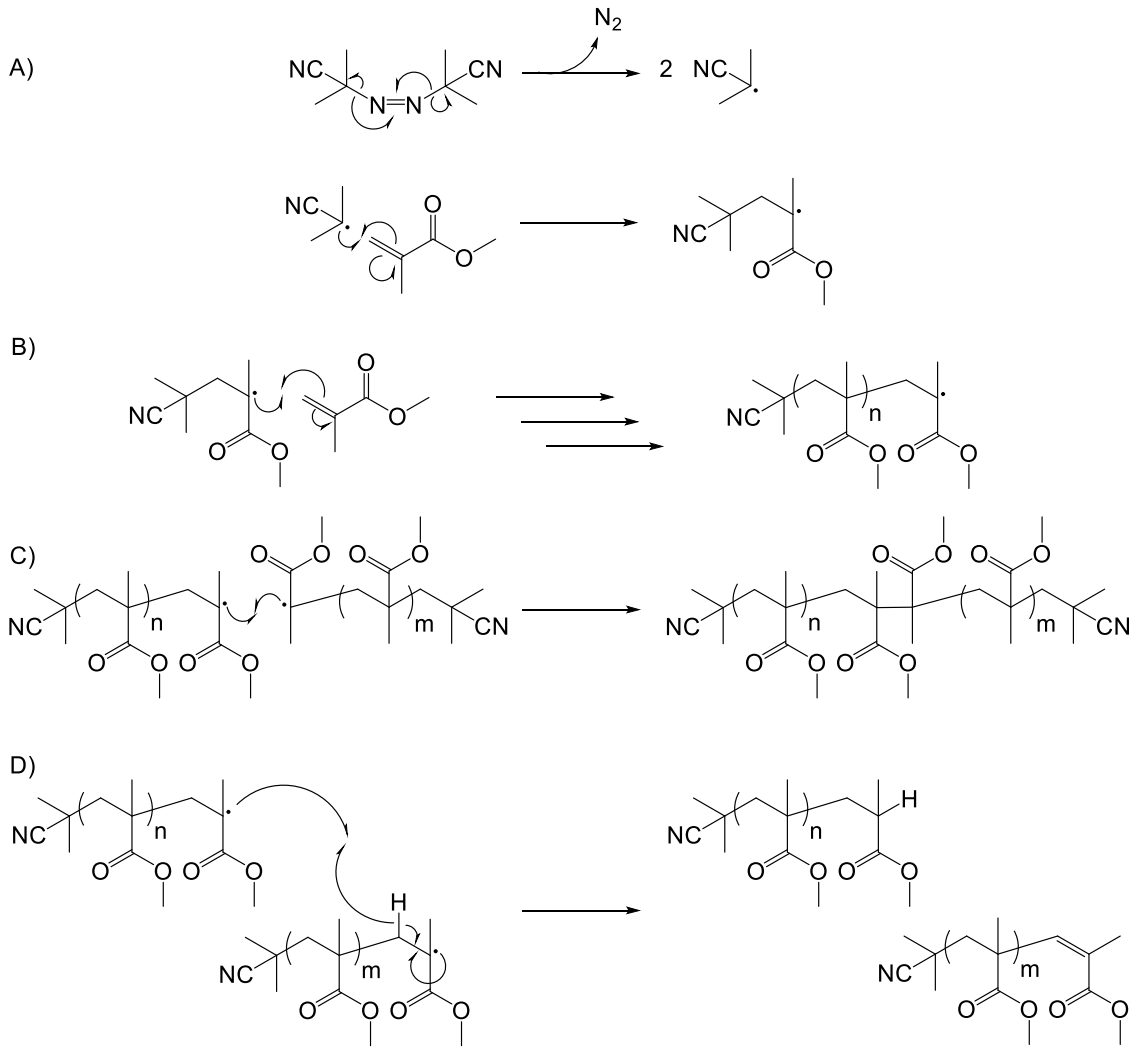

Scheme 1.2: Schematic representation of a conventional free radical polymerization of methyl methacrylate using AIBN as a thermally activated radical initiator with the mechanisms for a) initiation, b) propagation, c) termination by recombination, and d) termination by disproportionation outlined.

Kinetically, the rate of a free radical polymerization (R_p) can be expressed by equation (**1.4**) using a steady state approximation in which a constant free radical concentration is assumed. *f* is the initiator efficiency which refers to the fraction of unreacted radicals that leave the solvent cage upon decomposition of the radical initiator.[10]

$$R_p = k_p[M][I]^{0.5}\left(f\frac{k_d}{k_t}\right)^{0.5} \qquad \textbf{1.4}$$

Radical species are highly reactive in nature and thus conventional FRPs are incredibly fast and often only limited by the rate of diffusion. Consequently, termination and chain transfer events dominate in a FRP with the rate of bimolecular termination (k_t), either by recombination or disproportionation, typically five orders of magnitude greater than the rate of propagation (k_p).[14] Furthermore, due to the relatively slow initiation rate (k_i is often 1000 times smaller than k_p) a significant number of growing polymer chains will have reached their ultimate chain length and terminated whilst others are still initiating.

As a result, polymers produced *via* FRP are often ill-defined, highly disperse and have broad molecular weight distributions. This poor control over polymer synthesis is a major limitation of FRP which culminates in the production of non-uniform and irregular polymers with vastly different compositions, molecular weights and architectures. Ultimately, owing to its unpredictable nature and irreproducibility, FRP is not a viable polymerization mechanism for the synthesis of well-defined block copolymers.

1.2.2.2. "Living" Polymerization

In stark contrast to FRP, a "living" polymerization is a type of chain-growth polymerization whereby termination and/or irreversible chain transfer reactions are absent.[15] Therefore, growing polymer chains remain active even after full conversion has been reached allowing simple continuation of the polymerization upon further monomer addition and thus enables the synthesis of block copolymers. Select examples of living polymerizations from the literature include anionic, cationic, ring opening metathesis polymerization (ROMP) and group transfer polymerization (GTP).[16–19]

A key kinetic difference between a FRP and a living polymerization is that the rate of initiation is significantly greater than the rate of propagation in the case of the latter.[20] Consequently, all polymer chains are initiated before any growing polymer chains reach

their ultimate chain length, thereby ensuring that all polymer chains grow at the same time and at the same rate. Elimination of termination and/or chain transfer events is achieved using activated species which are non-reactive with respect to one another, such as in the case of living anionic polymerization. Therefore, polymers produced *via* living polymerization techniques are well-defined possessing narrow molecular weight distributions and controlled lengths.[16]

Experimentally, a living polymerization can be distinguished from other polymerization techniques by monitoring the molecular weight of the polymer with respect to monomer conversion. Polymer molecular weight is found to be directly proportional to monomer conversion in a living polymerization (Figure 1.3 a) with the resultant DP and dispersity of the product polymer calculated using equations (**1.5**) and (**1.6**) respectively. Whereas in a conventional free radical polymerization (Figure 1.3 b), individual polymer chains grow rapidly due to a high propagation rate leading to the formation of high molecular weight species at low conversion with residual monomer remaining at prolonged reaction times. In contrast, for step-growth polymerizations (Figure 1.3 c) polymer molecular weight remains low throughout until very high monomer conversion is attained resulting in an exponential increase in polymer molecular weight.

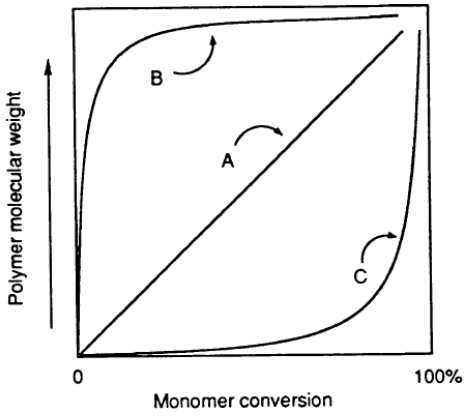

Figure 1.3: Evolution of polymer molecular weight *versus* monomer conversion for a) living polymerization, b) free radical polymerization, and c) step-growth polymerization. Figure adapted from ref 16.

$$Degree\ of\ Polymerization = [Monomer]/[Initiator] \quad \textbf{1.5}$$

$$Đ_M = 1 + \frac{1}{DP} \quad \textbf{1.6}$$

With regards to polymer design, composition in a living polymerization is determined by the order and ratio of monomers added to the growing polymer, whilst architecture and functionality can be controlled by selection of multifunctional initiators or monomers.[17,18] Moreover, end-functionalized polymers can be designed *via* selective termination of the active chain ends with appropriate reagents.[16] However, ensuring that no termination or chain transfer reactions are present necessitates stringent reaction conditions e.g. complete absence of oxygen or water as well as protection of certain functionalized monomers prior to polymerization, such as acidic and basic groups. Ultimately, living polymerization methodologies are somewhat hindered by strict synthetic protocols, a restricted range of monomer functionality and the requirement for extensive optimization of polymerization conditions.

1.2.2.3. Reversible deactivation radical polymerization (RDRP)

Reversible deactivation radical polymerization (RDRP) is a type of chain-growth polymerization that combines the versatility of a radical process with the benefits of achieving control similar to that obtained in a living polymerization.[21] The development of RDRP techniques in the last 20 years has revolutionized the field of radical polymerization enabling the synthesis of functional polymers with well-defined and predictable molecular weights; narrow molecular weight distributions; controlled molecular architecture in terms of chain topology and composition; high end-group fidelity; diverse functionality and capacity for continued chain growth.[10,12,22,23]

As discussed in Section 1.2.2.1, a critical drawback of FRP is the prevalence of chain transfer and termination events that significantly hinder control over the polymerization process. Due to the intrinsic nature of a free radical process, complete elimination of the aforementioned side reactions is conceptually impossible but can be reduced to a level that is undetectable *via* a RDRP mechanism. RDRP methodologies rely on establishing a dynamic equilibrium between a low concentration of active propagating radicals and a predominant concentration of dormant chains that are unable to propagate or terminate.[6] Dormant chains can be intermittently activated to form radicals that, after addition of a few monomer units, are converted back to their deactivated state. As a result, the relative concentration of propagating radicals at any one time and thus the rate of termination is decreased which is coupled with an increase in the average lifetime of the propagating species – similar to a living polymerization. Formation of the required dynamic equilibria in RDRP processes can be accomplished by two methods; the persistent radical effect or *via* a degenerative chain transfer process.[24]

1.2.2.3.1. Persistent Radical Effect (PRE)

Persistent radicals are species that cannot terminate with one another and are only able to cross couple with the propagating species i.e. a growing polymer chain. Atom transfer radical polymerization (ATRP)[25] and nitroxide-mediated radical polymerization (NMP)[26] are principal examples of RDRP methodologies that rely upon the persistent radical effect to promote a dynamic equilibrium between dormant chains and propagating radicals.[27]

In ATRP, the initiator usually employed is a secondary or tertiary alkyl halide (RX) which reacts with a transition-metal complex in a lower oxidation state (Mt^m/L) – often referred to as the activator.[28] As with all chain-growth polymerizations, the initiating species subsequently reacts with monomer to form a macromolecular propagating species (P_n^*).

Growing polymer chains can either continue to propagate or react with the oxidized metal species to regenerate the catalyst/activator and produce a stabilized halogenated end-capped polymer chain. Polymerization proceeds with dormant deactivated species (P_n-X) periodically reacting to form activated propagating radicals (P_n^*) and a deactivator (Mt^{m+1}) in a reversible manner.[24] ATRP is mediated by the transfer of the halide between the propagating macromolecular species and the transition metal complex *via* this activation/deactivation equilibrium (Figure 1.4) resulting in a high degree of polymerization control.

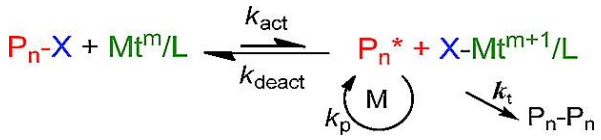

Figure 1.4: Main atom transfer radical polymerization (ATRP) equilibrium with associated rate constants. P_n is a growing polymer chain with DP = n, X is a halide atom and Mt^m/L is a transition metal complex in oxidation state = m and L is a ligand. Figure adapted from ref 24**.**

Overall, the rate of any given ATRP is governed by several factors including: chosen monomer; transition metal complex; nature of the ligand; reaction solvent; temperature and pressure.[28] Copper-mediated ATRP represents the most utilized transition metal catalyst system within the literature although other transition metals have been proven to be successful including molybdenum, iron, ruthenium and osmium.[29]

In nitroxide-mediated polymerization (Figure 1.5), the persistent radical or deactivated species is a stable nitroxide that reversibly end-caps the growing polymer chain in a similar fashion to the halide atom in ATRP.[26] In contrast to ATRP, neither a catalyst nor bimolecular exchange is required with NMP solely under thermal control. NMP initiators are typically alkoxyamines which undergo homolytic fission at elevated temperatures to generate a nitroxide radical and an initiating species.[30]

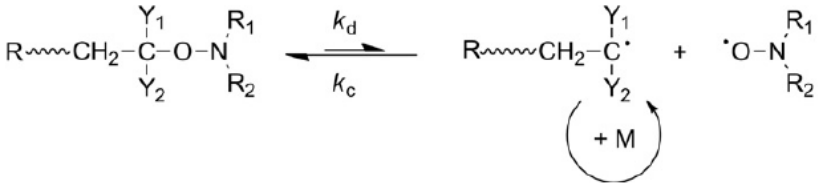

Figure 1.5: Activation-deactivation equilibrium in nitroxide-mediated radical polymerization (NMP) with associated rate constants. Figure adapted from ref 30.

ATRP and NMP are both reliant on a reversible termination mechanism whereby radical-radical bimolecular termination leads to an increase in the persistent radical concentration. Consequently, the activation-deactivation equilibrium is driven towards the deactivated species resulting in a reduction in the propagating radical concentration. Therefore, termination events are significantly retarded as persistent radicals are unable to self-terminate whilst propagating radicals remain predominantly dormant and thus living polymerization characteristics are observed. A fast activation-deactivation process is required to allow propagating radicals equal opportunity to react with monomer which ensures control over polymer molecular weight, dispersity and composition. Furthermore, if termination reactions are minimized then end group functionality is retained for the majority of polymer chains (i.e. alkoxyamine for NMP and alkyl halide for ATRP) allowing for subsequent chain extension for block copolymer synthesis and/or post-polymerization chain-end functionalization.

A significant drawback of ATRP and NMP is the difficulty in predicting the number of chains that undergo bimolecular termination. Calculating the latter is important in determining the degree of livingness of a polymerization which simply refers to the number fraction of chains that retain ω-end group functionality at a given monomer conversion.[31] Moreover, each radical-radical bimolecular termination event in a reversible termination mechanism leads to a loss of two living chain ends. Ultimately,

polymerizations reliant on the persistent radical effect are unsuitable for mulitblock synthesis if high conversions are desired. Upon reaching full monomer conversion, living chains will gradually die as activation continues to generate propagating radicals which have a certain probability to terminate.[32] Therefore, polymerizations are typically stopped at moderate monomer conversions (80%) to preserve a high proportion of living chains otherwise a loss of control is observed.

1.2.2.3.2. Reversible addition-fragmentation chain transfer (RAFT) polymerization

Discovered in 1998, reversible addition-fragmentation chain transfer (RAFT) polymerization is a RDRP technique in which the equilibrium between active and dormant chains is achieved *via* a degenerative transfer mechanism.[33] In a degenerative transfer system, radicals are neither created nor destroyed resulting in no change in the overall number of radicals during the activation-deactivation process.[23] Therefore, a radical source is required to initiate the polymerization, typically from the homolysis of a radical initiator. Other key examples of RDRP techniques that rely on a degenerative transfer approach include macromolecular design *via* the interchange of xanthates (MADIX),[34,35] organotellurium-mediated radical polymerization (TERP)[36] and iodide-mediated radical polymerization.[37]

RAFT polymerization closely mimics the key mechanistic steps of a conventional free radical polymerization (Figure 1.2) with initiation, propagation and termination events present throughout. Importantly, simple introduction of a thiocarbonylthio chain transfer (or RAFT) agent results in the establishment of the key RAFT equilibria that ultimately impart control over the polymerization.[22] Whilst in free radical polymerizations chain transfer is irreversible and leads to the formation of dead chains; in RAFT polymerization

chain transfer reactions are not only reversible but dominate and mediate the polymerization through the following activation-deactivation equilibria (Figure 1.6).[23]

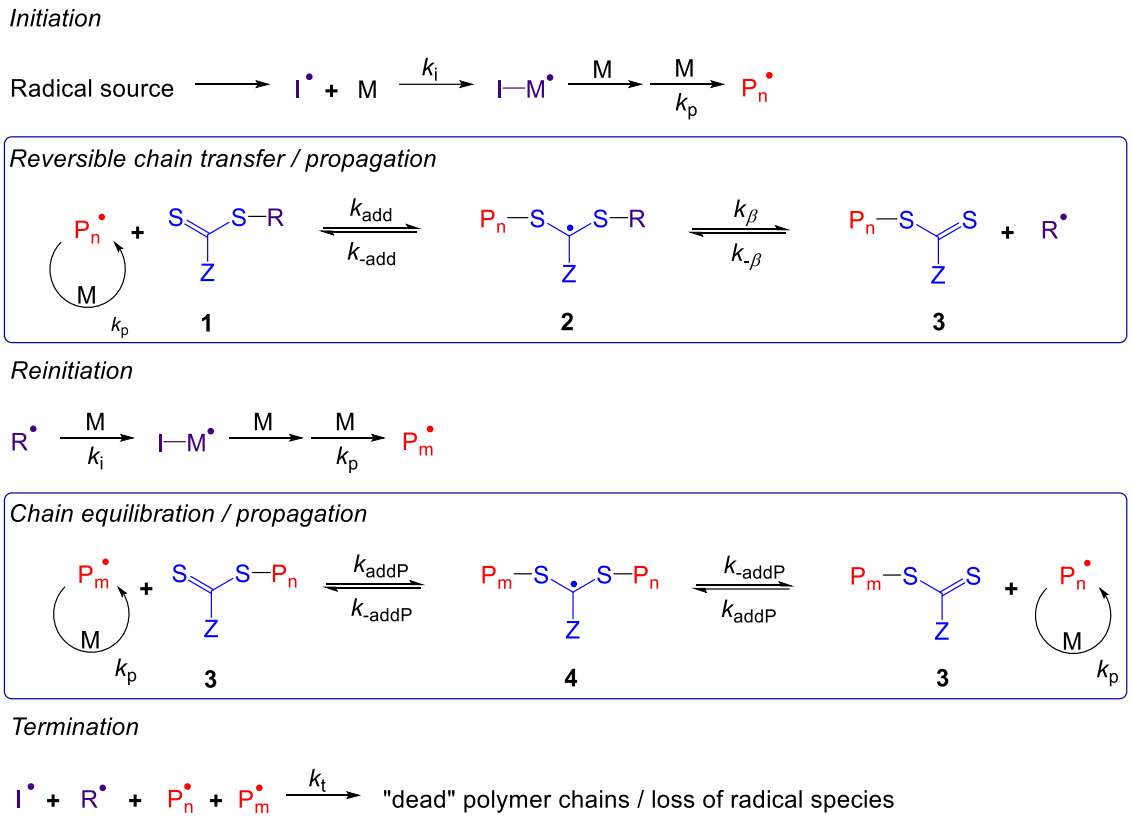

Figure 1.6: Reversible addition-fragmentation chain transfer (RAFT) polymerization mechanism with associated rate constants. Key reversible chain transfer equilibria are highlighted in blue.

After initiation, the growing polymer chain ($P_n^{\bullet}$) can either react with more monomer or with the C=S bond of the RAFT agent (**1**) in a reversible manner to form a radical intermediate species (**2**). This radical species can either fragment to regenerate the RAFT agent and initial propagating radical or fragment to expel a growing macro chain transfer agent (macroCTA) (**3**) and a CTA-derived radical ($R^{\bullet}$). This initial addition to the RAFT agent and associated fragmentation events comprises the pre-equilibrium stage. The CTA-derived radical subsequently reacts with monomer to form a new propagating species ($P_m^{\bullet}$) during the reinitiation step. Finally, the main activation-deactivation equilibrium is established whereby the CTA-derived radical intermediate (**4**) rapidly

fragments to allow propagation of one of the polymer chains before fast addition to reform the radical intermediate once again.[38] Overall, this series of reversible chain transfer reactions result in a statistical distribution of molecular weights as each propagating radical species has an equal chance of fragmenting due to the symmetrical nature of the CTA-derived radical intermediate (**4**).

In a well-controlled RAFT polymerization, $k_\beta > k_{\text{-add}}$ such that pre-equilibrium and reinitiation is completed rapidly allowing the system to progress to the main equilibrium for optimal equilibration. Furthermore, for an effective RAFT process $k_{\text{add}}/k_{\text{-add}} >>> k_p$ to ensure that less than one monomer unit is inserted per activation cycle and thus all chains will have a similar DP at any given time.[23]

The rate of a controlled RAFT polymerization (R_p) is defined in equation (**1.7**) and is principally limited to the initial radical concentration. Under ideal conditions the addition of a RAFT agent should have no effect upon the kinetics of a FRP.[23] However, this is often not the case with the rate of a RAFT polymerization with respect to an analogous FRP usually retarded; the magnitude of which is governed by several factors including choice of RAFT agent, monomer and reaction conditions used.[22]

$$R_p(t) = k_p[M]\sqrt{\frac{fk_d[I]_0 e^{-k_d t}}{k_t}} \qquad \textbf{1.7}$$

Although increasing the radical concentration will lead to faster polymerization rates, this is offset by the increase in the probability of termination reactions occurring resulting in larger dispersities.[35] Therefore, an optimal RAFT polymerization is a fine balance between a high polymerization rate and a low extent of termination which can be achieved by having a high rate of radical generation and/or solvent acceleration coupled with a low initiator concentration.[23]

Correct selection of the chain transfer or RAFT agent (Figure 1.7) is paramount in a RAFT polymerization with the choice of R and Z groups on the RAFT agent of prime importance.[39]

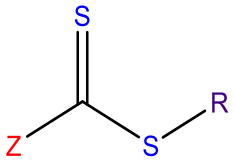

Figure 1.7: Generic structure of a thiocarbonylthio containing chain transfer (or RAFT) agent.

The Z group of a RAFT agent plays two important roles. Firstly, the Z group dictates the stability of the CTA-derived radical intermediates (**2** and **4**) and thus their susceptibility to fragmentation. Fragmentation events need to occur to some degree otherwise the polymerization rate is retarded but the radical intermediates need to be stable enough to favor successful radical addition i.e. $k_{add} > k_{-add}$. Moreover, the Z group governs how reactive the C=S bond is towards radical addition which is primarily affected by the electron density on the thiocarbonylthio group. Ideally, the C=S bond of a RAFT agent is at least 10 (preferably 100) times more reactive towards propagating radicals than the C=C bond of the monomer/s to ensure that rapid chain transfer reactions occur. Overall, the Z group of a RAFT agent directly influences two rate constants within a RAFT polymerization – k_{β} and k_{add}.[22] The extent to which Z group choice can affect the kinetics is exemplified by the fact that the value of k_{add} can be adjusted over a range of five orders of magnitude through simple manipulation of the Z group.[40] A final consideration of the Z group is that it should prevent side reactions from occurring either *via* hydrolysis, irreversible chain transfer or direct reaction with the monomer/s.

In comparison, the role of the R group is often understated as it contributes to the stabilization of the initial radical intermediate (**2**), as well as the reactivity of the C=S bond, to a lesser extent. Its key role is to reinitiate polymerization after initial

fragmentation therefore requiring it to be an effective reinitiating species towards the monomer/s used otherwise retardation is likely.[41] Furthermore, it needs to be a good homolytic leaving group with respect to the growing polymeric chain ($P_n^{\bullet}$) to promote rapid fragmentation of the CTA-derived radical intermediate (**2**) to favor formation of the desired products i.e. macroCTA (**3**) and CTA-derived radical ($R^{\bullet}$).

The partition coefficient (ϕ) corresponds to the relative rates of fragmentation of the initial CTA-derived radical intermediate (**2**) to either the starting materials ($P_n^{\bullet}$ and **1**) or the products ($R^{\bullet}$ and **3**), through equation (**1.8**), during the pre-equilibrium stage.[40]

$$\phi = \frac{k_{\beta}}{k_{-add} + k_{\beta}} \qquad \textbf{1.8}$$

The nature of the R group determines the value of the partition coefficient with the successful preparation of polymers with low dispersity when $\phi \geq 0.5$. Many factors affect the two fragmentation rates and in turn the partition coefficient including: radical stability (primary *vs* secondary *vs* tertiary); R group substituents capable of delocalizing the radical center, steric effects (polymeric R groups *vs* monomeric analogues) and electronic effects (electron withdrawing *vs* electron donating groups).[40] Overall, a fine balance between radical stability and reinitiation efficiency has to be found to achieve good polymerization control in the RAFT mechanism.[23]

Ultimately, the choice of R and Z group for a RAFT agent is largely governed by how "activated" the chosen monomer/s are. Radically polymerizable monomers are nominally divided into two classes with the classification reflecting the monomer's ability to react in a free radical process. More activated monomers (MAMs) react more readily with radicals than less activated monomers (LAMs) as the formation of a stable radical is favored with regards to the former. However, it is worth noting that the relative reactivity of the resultant propagating radical is the opposite and at odds with the former monomer

classifications with polymeric radicals formed from MAMs being much less reactive than polymeric radicals formed from LAMs.[22]

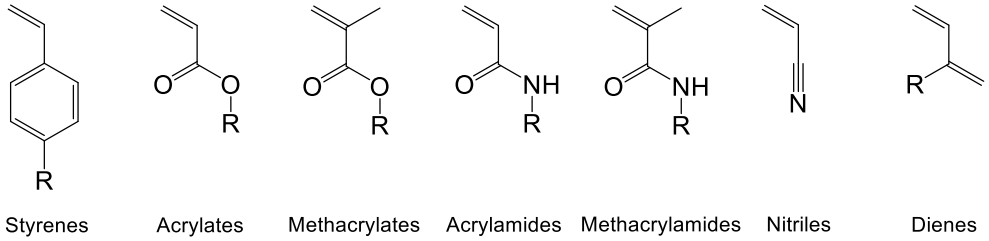

Figure 1.8: Chemical structures of select examples of more activated monomers (MAMs).

MAMs are typically conjugated to a neighboring functionality such as a double bond (e.g. butadiene); an aromatic ring (e.g. styrenes); a carbonyl group (e.g. (meth)acrylates and (meth)acrylamides) or a nitrile (e.g. acrylonitrile) (Figure 1.8).[23] Consequently, upon radical addition MAMs form propagating radicals ($P_n^{\bullet}$) which are not only stable, due to enhanced stabilization and often steric factors, but less reactive with regards to radical addition towards the RAFT agent. Furthermore, due to their more stabilized nature, polymeric radicals formed from MAMs provide excellent homolytic leaving groups from the CTA-derived radical intermediates (**2** and **4**). As such, a high rate of reversible chain transfer (k_{add}) with respect to the rate of propagation (k_p) is necessary to ensure rapid equilibration of growing chains.[22] Therefore, MAMs require more active RAFT agents such as dithioesters (**5**) or trithiocarbonates (**6**) (Figure 1.9) to promote radical addition and prevent a build-up of propagating radicals and dormant species (low ϕ).[40] Electron withdrawing or more weakly electron donating Z groups (such as C, Ph or S) make the C=S bond of the thiocarbonylthio moiety more electrophilic and thus ensure a sufficient rate of addition for the propagating radicals.

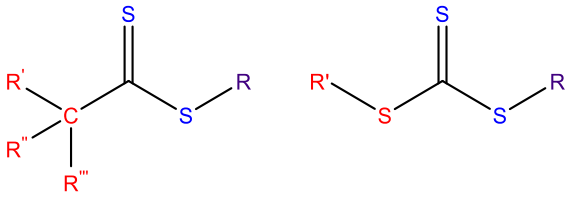

5 **6**

Figure 1.9: Chemical structures of dithioesters (**5**) and trithiocarbonates (**6**) which are examples of more active RAFT agents used for the controlled polymerization of more activated monomers (MAMs).

LAMs are monomers in which the vinylic group is located adjacent to an electron rich atom such as an oxygen or nitrogen lone pair (e.g. vinyl esters and *N*-vinyl amides); a halogen (e.g. vinyl chloride), a saturated carbon (e.g. diallyldimethyl ammonium chloride) or the heteroatom of a heteroaromatic ring (e.g. *N*-vinylcarbazole and *N*-vinyl pyrrolidone) (Figure 1.10).[40]

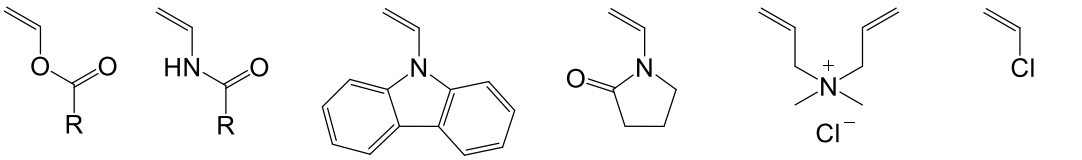

Vinyl esters | *N*-vinyl amides | *N*-vinyl carbazole | *N*-vinyl pyrrolidone | Diallyldimethyl ammonium chloride | Vinyl chloride

Figure 1.10: Chemical structures of select examples of less activated monomers (LAMs).

In contrast to MAMs, LAMs produce less stable polymeric radicals due to electron density being withdrawn from the radical center and thus are more reactive with regards to radical addition. Consequently, the rate of reversible chain transfer (k_{add}) needs to be tempered to counteract the slow fragmentation rate from the CTA-derived radical intermediates as polymeric radicals formed from LAMs make for poor homolytic leaving groups.[23] If left unchecked, propagation becomes encumbered due to the high rate of radical addition resulting in inhibition due to a predominant concentration of stabilized

CTA-derived radical intermediates which act as radical sinks.[22] Therefore, less active RAFT agents such as xanthates (**7**) and dithiocarbamates (**8**) are required for the controlled polymerization of LAMs. Electron rich Z groups (such as O and N) donate electrons into the thiocarbonylthio group as highlighted in the resonance forms depicted in Figure 1.11.[40]

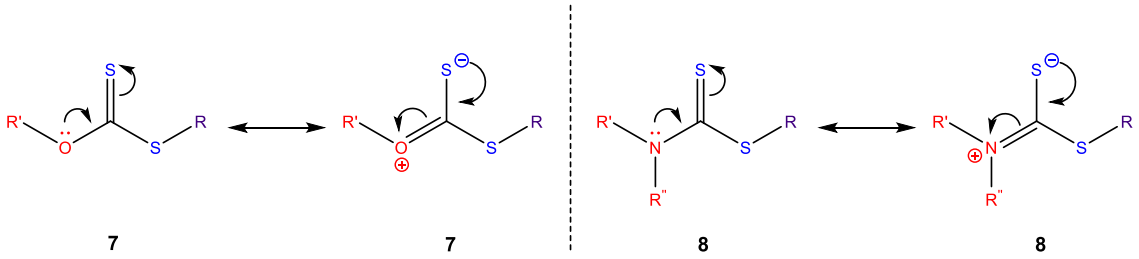

Figure 1.11: Resonance structures of xanthates (**7**) and dithiocarbamates (**8**) which are examples of less active RAFT agents used for the controlled polymerization of less activated monomers (LAMs).

As a result, the C=S bond of the thiocarbonylthio moiety becomes less electrophilic and deactivated towards radical addition. In turn, the CTA-derived radical intermediates become destabilized which combined with the former promotes monomer propagation and intermediate fragmentation rates. In conclusion, judicious selection of both R and Z group is vital to maintaining control in a RAFT polymerization and is highly dependent on the monomer/s chosen. General guidelines for R and Z group choice with respect to the nature of the monomer are shown in Figure 1.12.[38,40,42]

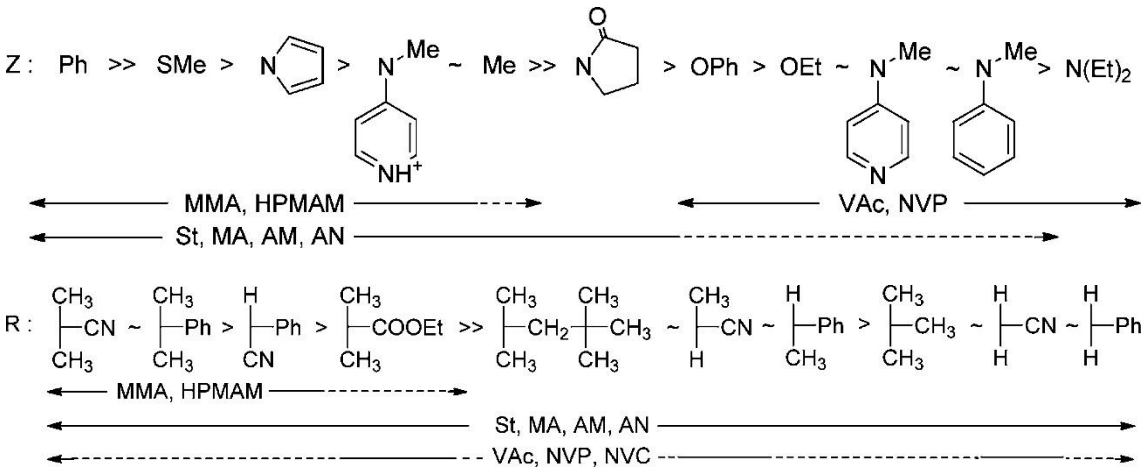

Figure 1.12: Empirical guide to RAFT agent selection. For Z, addition rates decrease and fragmentation rates increase from left to right. For R, fragmentation rates decrease from left to right. A bold line indicates good control. A dashed line indicates partial control. Figure and caption adapted from ref 40.

Ultimately, the RAFT process has been shown to facilitate the controlled polymerization of a plethora of radically polymerizable monomers regardless of their reactivity. Critically, one synthetic challenge still remains with regards to RAFT agent design which is a universal RAFT agent that can polymerize both LAMs and MAMs without retardation, inhibition or loss of control.[40] An elegant example of a universal RAFT agent is the pH-switchable *N*-(4-pyridinyl)-*N*-methyldithiocarbamate RAFT agent whereby the reactivity can be modulated *via* protonation of the pyridine ring (Scheme 1.3).[43] Using this RAFT agent, the authors successfully synthesized a range of p(MAM)-*b*-p(LAM) diblock copolymers with narrow molecular weight distributions ($Đ_M$ = 1.10 – 1.20).[43] However, whilst a number of viable solutions have been proposed within the literature, to date no single RAFT agent offers good control over both MAMs, specifically methacrylates, and LAMs.[23]

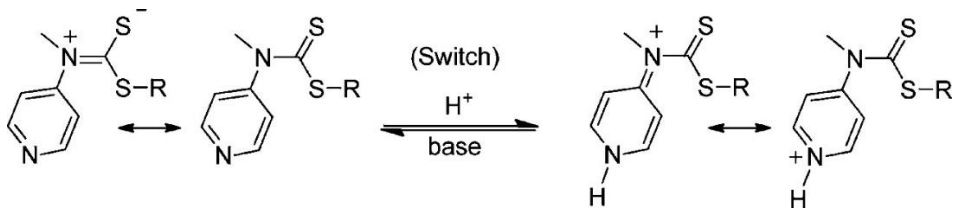

Scheme 1.3: pH-switchable *N*-(4-pyridinyl)-*N*-methyldithiocarbamate RAFT agent. In acidic conditions control over MAMs is favored and *vice versa* for LAMs. Figure adapted from ref 43.

Importantly, a key feature of the RAFT process is that in an ideal RAFT polymerization all the polymeric chains will retain α and ω end-group functionality i.e. thiocarbonylthio moiety (Z-C(=S)- group) and the R group. Therefore, polymer functionality and architecture can be manipulated simply by incorporating (multi)functional Z and R groups into RAFT agent design. For example, through the use of R- or Z-linked multi-functional RAFT agents, triblock copolymers and/or multi-arm stars have been successfully prepared.[44,45] Furthermore, more exotic polymer architectures have been synthesized *via* RAFT polymerization including branched; hyper-branched; graft; comb and dendritic with perhaps only the creativity of the polymer chemist being the limit in polymer architecture design.[46–48] Another significant advantage of RAFT polymerization is its cooperativity with other polymerization methodologies enabling orthogonal synthetic approaches to be realized thereby widening monomer range and access to unique topologies. For instance, bottlebrush copolymers have been successfully prepared by combining RAFT and ROMP techniques utilizing a RAFT agent bearing a norbornene functionality as the Z group (Scheme 1.4).[49]

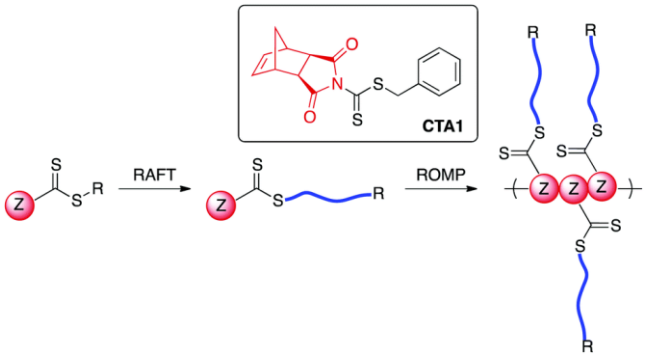

Scheme 1.4: Proposed preparation of bottlebrush copolymers using a dual ROMP/RAFT agent (**CTA1**) with a norbornene functionality as the Z group. Figure adapted from ref 49.

Overall, the RAFT process is tolerant to a wide range of unprotected functionalities on either the Z or the R group owing to the robust nature of the thiocarbonylthio moeity.[40] Moreover, the versatility of the thiocarbonylthio group can be exploited for polymer chain end functionalization in a similar fashion to other RDRP techniques. Polymers synthesized *via* RAFT polymerization can be transformed post-polymerization *via* an extensive range of processes (Scheme 1.5).[50–52] These transformations enable the polymer chemist to introduce a diverse range of functionalities easily and efficiently and include reactions such as: reductions; electrocyclic reactions; nucleophilic substitutions and 'click' processes to name but a few.[52] For some applications, complete removal of the thiocarbonylthio end-group is necessary with the most effective processes being either thermolysis or radical-induced transformations.[53]

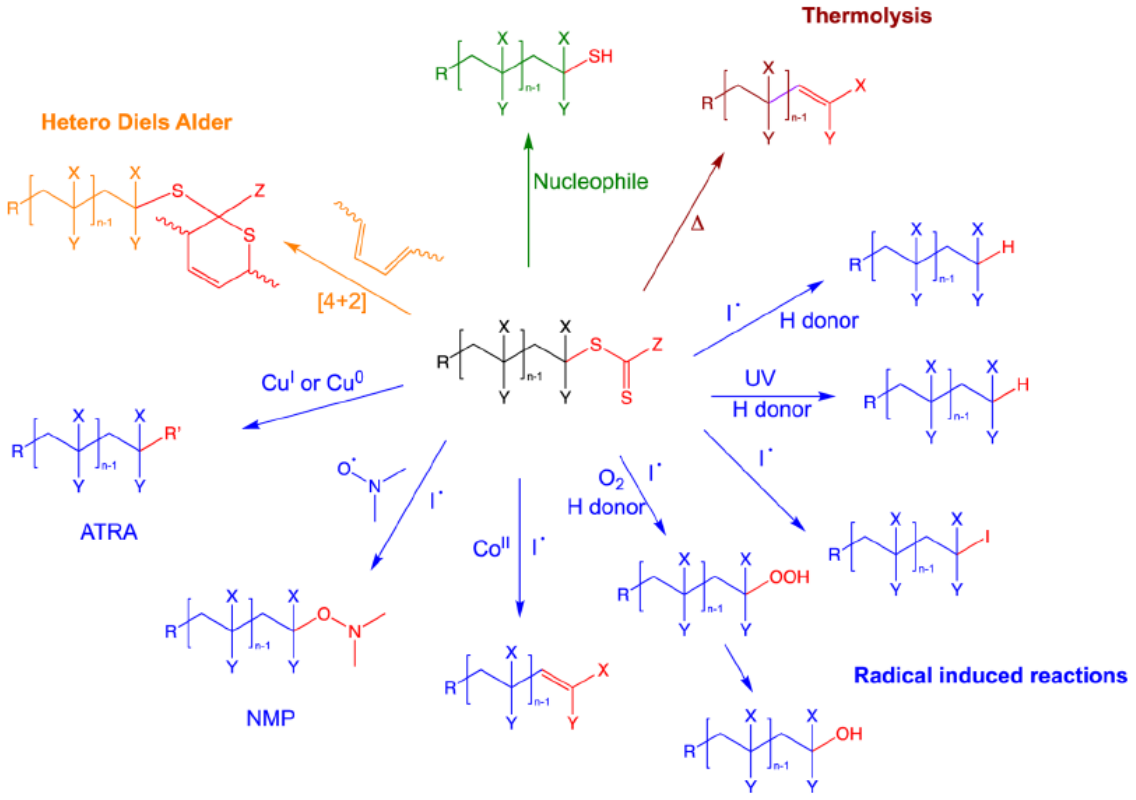

Scheme 1.5: Most commonly used synthetic pathways to thiocarbonylthio end-group modification grouped by types of reaction. Figure and caption adapted from ref 23, 52.

A critical advantage of RDRP techniques is retention of the transferable group if termination is kept to a minimum, i.e. alkyl halide for ATRP, alkoxyamine for NMP or thiocarbonylthio group for RAFT polymerization.[32] Consequently, RDRP techniques allow for subsequent chain extension using either the same, a different or a combination of more than one monomer to prepare block copolymers. Sequential block synthesis *via* RAFT polymerization is appealing for many reasons but there are several important factors to take into account including monomer order, α and ω end-group functionality, initiator concentration and unsurprisingly, RAFT agent selection.[22]

When designing block copolymers *via* RAFT polymerization, certain criteria has to be met regarding the order in which monomers are incorporated. During a block copolymer synthesis, the first monomer polymerized becomes the polymeric R group of the macroCTA utilized in the second polymerization. Subsequent chain extensions are highly

dependent on the monomer/s polymerized in the preceding block and careful consideration must be taken to prevent complete inhibition. Essentially, monomer order (Figure 1.13) is dictated by the leaving group ability of the resultant polymer chain; with the latter decreasing in the order of methacrylates and methacrylamides (stabilized tertiary radicals) >> acrylates, acrylamides and styrenes (stabilized secondary radicals) > vinyl esters and *N*-vinyl amides (more reactive secondary radicals).[22] Ultimately, the range of well-defined block copolymers that can be synthesized *via* RAFT polymerization, and competing RDRP techniques, is limited due to these strict conditions.

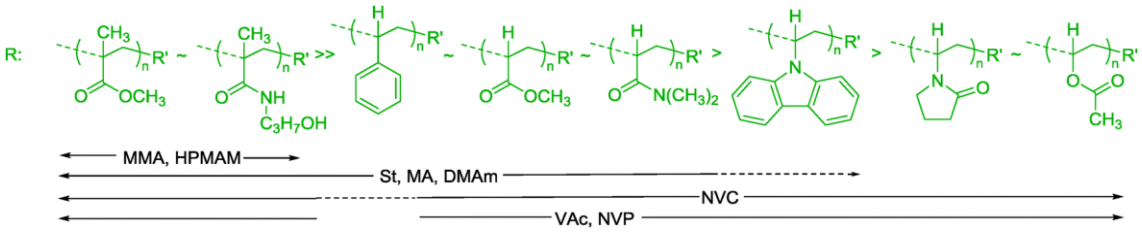

Figure 1.13: Guidelines for selection of macro-R group for the preparation of block copolymers. Bold line indicates good control. Dashed line indicates partial control/retardation. Figure adapted from ref 22.

In an ideal RAFT polymerization, all polymer chains would remain "living" and retain both α and ω end-group functionality but this is rarely the case. The requirement of an initiator in RAFT polymerization leads to two types of polymer defects which become more prevalent with each chain extension during block copolymer synthesis. Firstly, the formation of initiator-derived polymer chains instead of R-group derived polymer chains is unavoidable. Initiator addition is necessary for each chain extension during block copolymer synthesis which can also generate homopolymer impurities (Figure 1.14). The second type of defect is generally observed at very high monomer conversions and is simply the formation of dead polymer chains through irreversible bimolecular termination which is intrinsic to any radical polymerization.[22] Overall, the products of a RAFT polymerization can be nominally split into four categories: polymer chains with and

without the thiocarbonylthio moiety at the ω-end (living and dead chains respectively) and polymer chains with differing α-end group functionality (initiator-derived *vs* R-group derived).[23] Although the relative populations of the minor termination products and initiator-derived defects are typically very low, their existence should be noted when considering block copolymer composition.

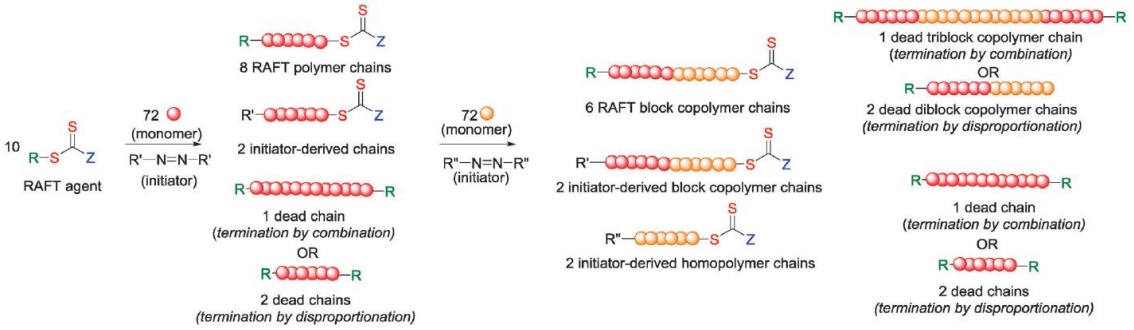

Figure 1.14: Outline of the possible various polymer species formed from a homopolymerization and a single chain extension *via* RAFT polymerization at full monomer conversion. Figure adapted from ref 22.

As discussed in Section 1.2.2.3.1, block copolymer synthesis using either NMP or ATRP typically requires the polymerization to be quenched at moderate conversions to maintain a high degree of livingness.[23] Given the number of possible side products and initiator-derived contaminants, RAFT polymerization may appear to be an unsuitable and inefficient methodology for large scale multiblock synthesis in which very high conversion rates are desired. However, unlike other RDRP techniques based on a reversible termination mechanism, the requirement of a radical initiator in RAFT polymerization allows the polymerization rate to be tuned as well as the extent of bimolecular termination.[32] Since the number of dead chains is directly proportional to the initial radical concentration, use of very low initiator concentrations would allow a high degree of livingness to be maintained. Consequently, the contribution of initiator-derived chains would be minimized but optimized polymerization conditions would be required

to counteract the reduction in polymerization rate. Perrier and co-workers have recently developed a one pot process utilizing this approach, in which low disperse block copolymers were successfully synthesized at 100% conversion with the number of blocks as high as 20.[31] To overcome the use of very low initiator concentrations, monomers with high propagation rates, in this case acrylamides, were polymerized at high concentrations in aqueous media to promote a high rate of polymerization (equation (**1.7**)).[31,32]

In conclusion, RAFT polymerization is arguably the most versatile RDRP process. For instance, it can control the polymerization of a broader range of functional monomers than competing technologies e.g. vinyl acetate and *N*-vinyl pyrrolidone unlike ATRP/NMP as well as ethylene and dienes unlike conventional FRP.[23] Moreover, RAFT polymerization is compatible with a wide range of reaction media (organic, aqueous, dispersion, emulsion); omits the use of metals which are often found in ATRP; does not require elevated temperatures unlike NMP and displays a greater tolerance to functional groups in comparison to living anionic and cationic polymerizations. Importantly, minimal process development is required with simply the addition of a RAFT agent to a conventional FRP protocol. As a result, RAFT polymerization has become increasingly popular in industry for the large scale batch production of well-defined polymers.[54] RAFT polymerization has the potential to become the gold standard of controlled polymerization techniques for applications including polymer-based therapeutics, microelectronics, green and sustainable materials, cosmetics, biosensors, paints and many others.[22,23,55,56] Herein, RAFT polymerization was chosen as the preferred polymerization methodology for the synthesis of diblock copolymers throughout this thesis.

1.3. Polymer self-assembly in aqueous solution

Controlled polymerization techniques have facilitated the design and preparation of functional polymers with an extensive range of architectures; some of which were described in Section 1.2.[47,48] Furthermore, each type of polymer topology can self-organize into aggregates of diverse morphologies under certain conditions.[57] In comparison to their small molecule analogues, polymer aggregates typically exhibit greater kinetic stability and robustness due to their enhanced mechanical and physical properties. As a result, polymer self-assembly has attracted significant research interest with a view to applications including drug delivery, enzyme mimics, enhanced oil recovery and diagnostic point-of-care devices to name but a few.[58]

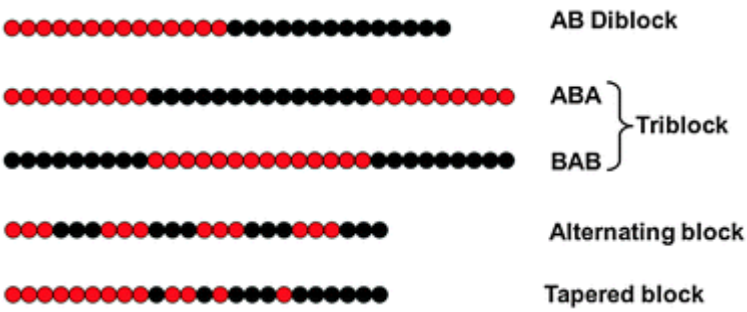

Figure 1.15: Typical structures of block copolymers (BCPs) containing two types of blocks, A and B. Figure and caption adapted from ref 59.

Block copolymers (BCPs) (Figure 1.15) typically consist of two or more chemically distinct and often immiscible blocks that are covalently bound together.[59] Due to this incompatibility, BCPs undergo microphase separation in order to minimize the interfacial surface area between the incompatible components in a process termed self-assembly.[60] Amphiphilic block copolymer self-assembly represents the simplest and most extensively studied system and is akin to the aqueous self-assembly of small molecule surfactants composed of a hydrophilic head group and one or more hydrophobic tail groups. Overall,

the self-assembly of amphiphilic block copolymers in solution is driven by the reduction in the total free energy of the system and is dependent upon both polymer-water interactions and polymer-polymer interactions.[59] Whilst there is an entropic penalty from amphiphilic block copolymer chains and water molecules becoming highly ordered in solution, a larger enthalpic penalty is prevented by decreasing the number of energetically unfavorable interactions between the hydrophobic block and the aqueous environment; this phenomenon is often referred to as the hydrophobic effect.[57]

When placed in a selective solvent above the critical aggregation concentration (CAC), amphiphilic block copolymers spontaneously self-assemble to generate a vast array of nanostructures including: spherical micelles; cylindrical micelles; vesicles; bicontinuous structures and lamellae amongst others (Figure 1.16).[59–61]

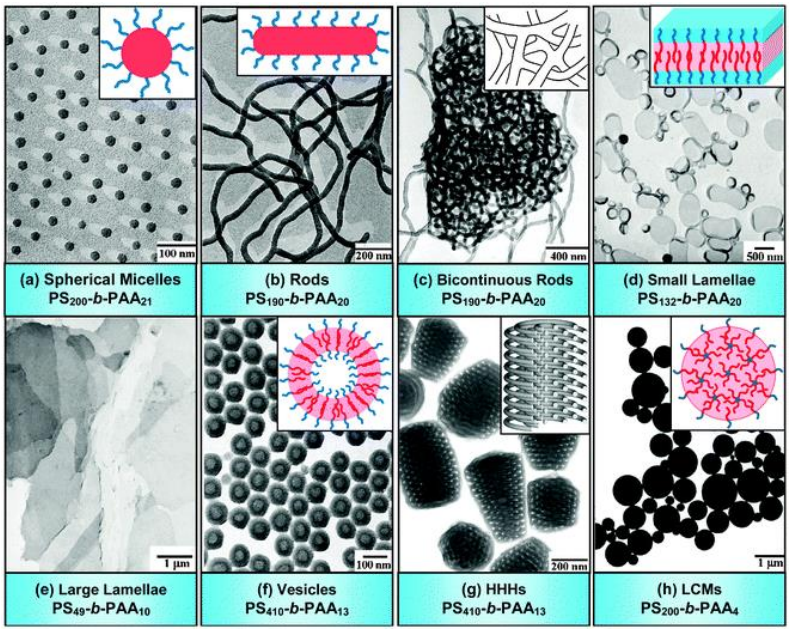

Figure 1.16: Transmission electron microscopy (TEM) images (with schematic diagrams) for various morphologies formed from amphiphilic poly(styrene)-*b*-poly(acrylic acid) block copolymers in water. Figure adapted from ref 59, 60.

The diverse range of morphologies that can be accessed *via* BCP self-assembly is dictated by the inherent molecular curvature and how the latter influences the packing of the BCP

chains.[62] As an initial reference point, the final equilibrium morphology can be predicted from the packing parameter (p) which can only be applied to dynamic aggregates – self-assembled systems under thermodynamic control.[62] The packing parameter relates the volume of the hydrophobic chains (v), the optimal area of the head group (a_o) and the length of the hydrophobic block (l_c) through equation (**1.9**).[63]

$$p = \frac{v}{a_o l_c} \qquad \textbf{1.9}$$

In general, the predicted formation of the three main types of morphology with regards to the value of the packing parameter is as follows: spherical micelles are favored when $p \leq ⅓$; cylindrical micelles are favored when $⅓ < p < ½$; and vesicles (or polymersomes) are favored when $½ < p < 1$ (Figure 1.17).[62] However, the absolute values of v, a_o and l_c for any given BCP are difficult to calculate. Therefore, the molecular curvature obtainable by the self-assembled polymer chains is often approximated using the relative weight fractions of solvophobic and solvophilic blocks within the constituent block copolymer.[64] Moreover, several other factors impact the final morphology observed and include: BCP composition and concentration; polymer solvent interactions; hydrophilic and hydrophobic block length; interaction between the incompatible blocks (known as the Flory-Huggins parameter, χ); selective solvent content with respect to good solvent content (a solvent that solubilizes all blocks); nature of the selective solvent and presence of additives.[59]

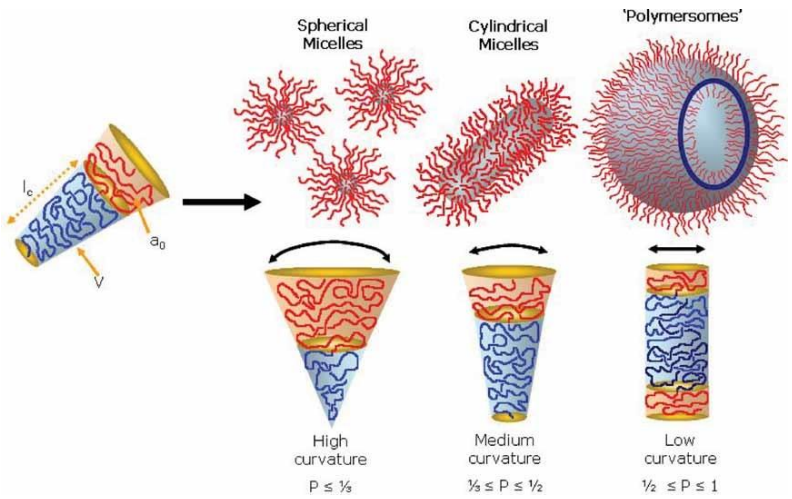

Figure 1.17: Illustration of the effect of the dimensionless packing parameter, *p*, upon the equilibrium morphology based on geometric arguments for amphiphilic block copolymers in a selective solvent. Figure adapted from ref 62.

Out of all the morphologies reported in the literature, the formation of "star-like" spherical micelles represent one of the most commonly studied. Aggregation of the hydrophobic blocks results in the formation of a dense core surrounded by hydrophilic blocks arranged in a diffuse hydrated corona upon dissolution in a non-solvent for the solvophobic block, commonly water (Figure 1.18).[65] Alternatively, reverse or inverse micelles are typically formed in apolar solvents, such as hexane, whereby the two incompatible blocks switch roles to form a hydrophilic core with a hydrophobic corona.[60]

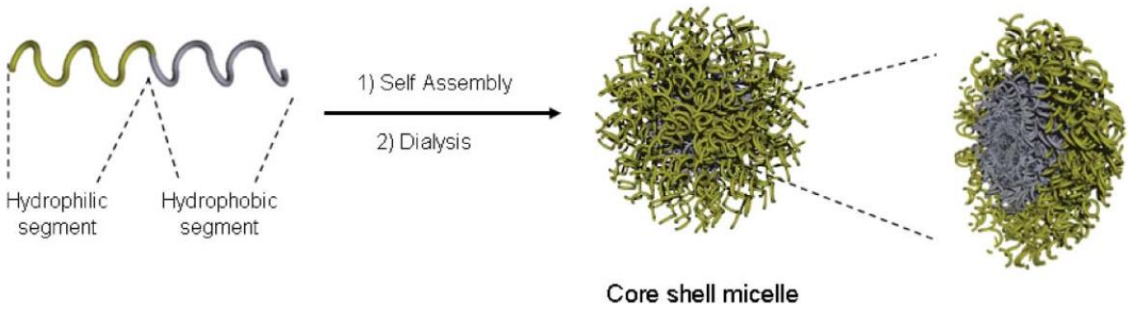

Figure 1.18: Solution-state self-assembly of amphiphilic block copolymers into core shell micelles. Figure and caption adapted from ref 65.

Micelles have provoked significant interest as polymeric materials suitable for a range of applications due to their properties at the nanoscale. Properties such as size,[66] molecular weight,[67] shape,[68,69] and equilibrium behavior,[70] can all be tuned by changing the physical and chemical nature of the BCPs from which micelles self-assemble. For example, manipulation of either the hydrophobic or hydrophilic block length has been shown to have a direct impact upon the aggregation number observed in the resultant micelles.[64,69-71] Moreover, it has been demonstrated that changing the hydrophobic nature of the core-forming block can also affect self-assembly, with an increase in hydrophobicity resulting in higher aggregation numbers.[74] The aggregation number (N_{agg}) simply refers to the average number of polymer chains that comprise the resultant self-assembled nanostructure and is defined in equation (**1.10**).

$$N_{agg} = \frac{M_{w,particle}}{M_{w,polymer}} \qquad \textbf{1.10}$$

Alternatively, "crew-cut" aggregates refer to BCPs in which the hydrophobic blocks are much longer than the hydrophilic segments generating nanostructures for which the coronas are much smaller than the hydrophobic regions. More than twenty "crew-cut" morphologies have been identified; some of which are thermodynamically induced whilst others can only be accessed *via* kinetic requirements.[59]

Overall, the self-assembly of BCPs in aqueous solution provides several advantages as a method of synthesizing polymeric materials with a view to biomedical applications. For instance, the use of stimuli-responsive monomers to form one or more of the constituent blocks allows the fabrication of nanoparticles whose assembly can be controlled by such stimuli. By using a core-forming or associative block that can transition between hydrophobic and hydrophilic states depending on the temperature, degree of

protonation/pH, wavelength of light irradiation amongst others, leads to self-assembled nanostructures whose self-assembly depends on these stimuli.[75,76]

1.3.1. Kinetic *vs* thermodynamic control

It is well established that amphiphilic block copolymers often form out-of-equilibrium or 'frozen' structures,[77,78] especially in aqueous media where unimer exchange is often energetically unfavorable. As a result, the final morphology of the nanostructures formed by BCPs is not only controlled by thermodynamic concepts such as entropic packing parameter (*p*), entropy of water or enthalpic interactions, but is also strongly influenced by kinetics.[79] This is highlighted by the fact that multiple morphologies can be prepared by the self-assembly of BCPs with identical or very similar block compositions and lengths (Figure 1.16).[60]

It is generally accepted that the mechanism for initial micelle formation involves rapid unimer association *via* nucleation and growth until micelles reach a limit at which the free energy of the system increases upon further growth.[78] For some systems, it was observed that thermodynamic equilibrium was reached after initial micelle formation which allowed rapid unimer exchange between micelles to occur. As a result, dynamic micelles formed which were independent of the preparation pathway. Conversely, out-of-equilibrium kinetically trapped 'frozen' structures often formed which showed little response to an external stimulus.[77,80] Ultimately, the self-assembly behavior of amphiphilic block copolymers can be difficult to predict; with many examples in the literature for which the characteristics of the formed nanostructures were primarily dictated by the chosen self-assembly methodology.

Direct dissolution (DD) is conceptually the simplest self-assembly methodology and involves the direct addition of the selective solvent to the purified BCP at a suitable

concentration to initiate self-assembly. Typically, self-assembled nanostructures prepared *via* this preparation pathway resemble the BCP's bulk phase separated morphologies which are often kinetically controlled but under certain conditions can equilibrate. An alternative self-assembly methodology is thin film rehydration (TF) which initially involves the dissolution of the BCP in a good solvent for all blocks to form a dispersed solution of unimers. Subsequent removal of the good solvent at elevated temperatures under vacuum leaves a thin film of BCP; to which the selective solvent is added driving the formation of self-assembled nanostructures. Again, kinetically controlled phase separated morphologies are anticipated to form which may reach thermodynamic equilibrium, again under certain conditions. Finally, the solvent switch method (SS) is largely considered the principal choice for BCP self-assembly as it often drives the formation of thermodynamically favored nanostructures. Initially, the BCP is dispersed in a good solvent for all blocks resulting in a solution of unimers. Subsequent slow addition of the selective solvent is followed by removal of the original good solvent with self-assembly occurring at a critical percentage content of the selective solvent. Formation of equilibrium-derived nanostructures is largely dependent upon how long the system remains under equilibration before the solvent quality for the associative block is greatly reduced upon further addition of the selective solvent (Figure 1.19).[81]

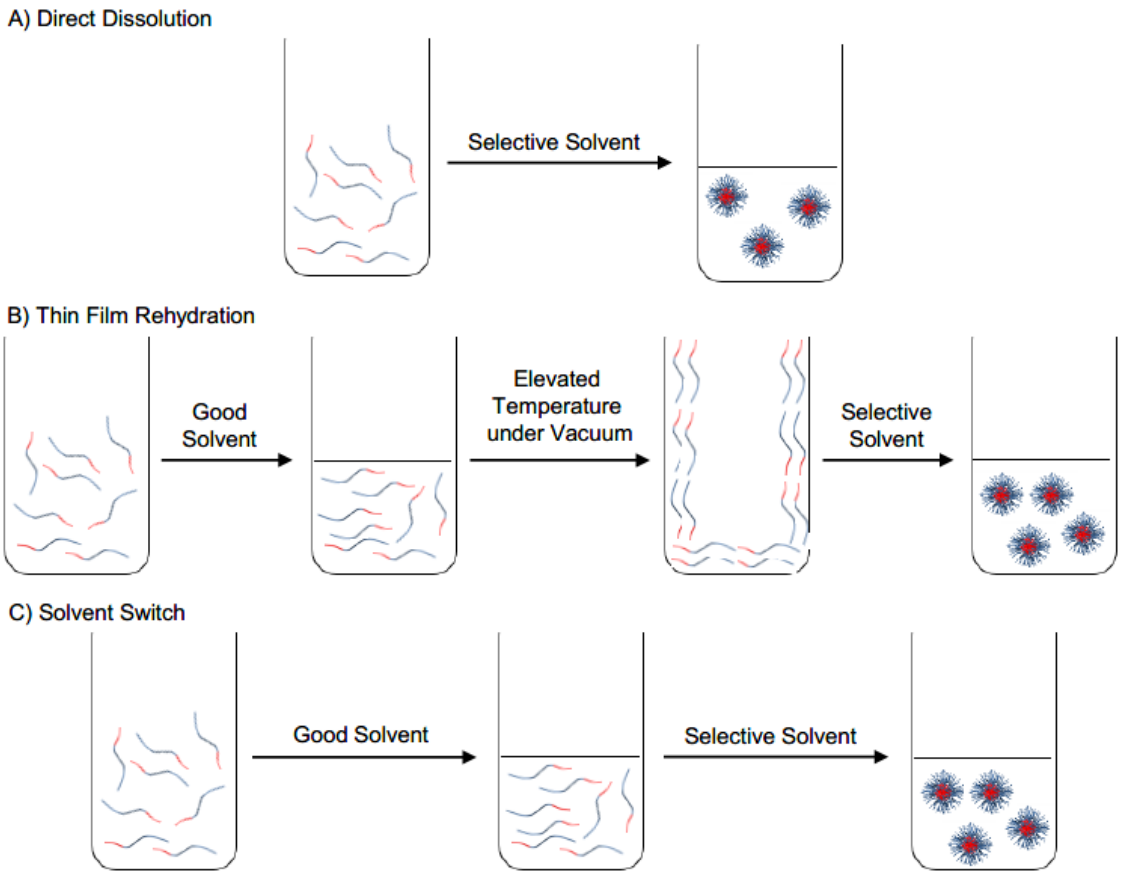

Figure 1.19: Diagram representing three common self-assembly methodologies for amphiphilic block copolymers with a) direct dissolution, b) thin film rehydration, and c) solvent switch.

Unlike small molecule surfactants, self-assembled amphiphilic block copolymers rarely reach the true Gibbs free energy minima of the system and in turn thermodynamic equilibrium.[78,82] Thermodynamic equilibrium is achieved with respect to the former through a constant exchange of surfactant molecules (free unimer chains) between nanostructures; with some portion of the chains ever present in both populations.[73,83] Therefore, upon a change in system conditions, the nanostructures can undergo morphological transitions to adapt and reach the new equilibrium-derived nanostructures as a result of this dynamic exchange of small surfactant molecules. Alternatively, thermodynamic equilibrium can be reached *via* particle-particle fusion events instead of unimer exchange but the energy barrier for this mechanism is extremely high and thus very unfavorable to occur.[84]

In contrast to small molecule surfactants, the dynamic exchange of polymer chains between nanostructures is predominantly kinetically hindered because the energy barrier for unimer exchange is too great and the concentration of polymer chains free in solution is typically negligible.[79,85] Furthermore, it is difficult to deduce how far from equilibrium a system truly is or if thermodynamic equilibrium is indeed reached.[78] Apart from careful selection of the self-assembly methodology, thermodynamic equilibrium for any given BCP self-assembled system can be reached by facilitating unimer exchange.

Unimer exchange between self-assembled nanostructures can occur but only if the associative block is sufficiently mobile and is of a relatively low hydrophobic nature thereby resulting in a low interfacial tension with respect to the selective solvent.[80,86] Other critical factors that can dictate whether unimer exchange is promoted include sterics; hydrophobic block length and the experimental temperature. Ultimately, the capability of self-assembled nanostructures to reach a global equilibrium is largely governed by two factors. Firstly, the BCP must have a core-forming block which has a glass transition temperature that is below the experimental temperature. Furthermore, the respective BCP self-assembled system must have an energy barrier low enough for unimer exchange to occur, to allow the lowest free energy of the system to be reached.[81]

1.4. Summary

Within this Chapter, several key concepts and topics central to the themes found throughout this thesis have been reviewed. An introduction to polymers and the individual elements that control can be imparted using the tools of modern synthetic chemistry was outlined. A detailed summary of the numerous polymerization methodologies available to the polymer chemist and their associated advantages and disadvantages was given. This section was followed by a comprehensive discussion of RAFT polymerization which was employed throughout this thesis for the synthesis of block copolymers. The importance of RAFT agent design with regards to controlled block copolymer synthesis and introducing functionality to polymers was highlighted, a concept which will be further explored in subsequent chapters. The next section focused upon the principles of block copolymer self-assembly and the extensive range of morphologies that can be accessed *via* judicious manipulation of the polymer composition. Finally, key thermodynamic and kinetic factors that dictate the self-assembly behavior of amphiphilic diblock copolymers in solution were discussed, for which diblock copolymer composition and chosen self-assembly methodology play a significant role.

1.5. References

1 R. J. Young and P. A. Lovell, *Introduction to Polymers, Third Edition*, Taylor & Francis, 2011.
2 J. Brandrup, E. H. Immergut and E. A. Grulke, *Polymer Handbook*, John Wiley & Sons, 4th edn., 1999.
3 P. C. Hiemenz and T. P. Lodge, *Polymer Chemistry*, CRC Press, New York, 2nd edn., 2007.
4 A. Rudin and P. Choi, *The Elements of Polymer Science & Engineering*, Academic Press, 3rd edn., 2013.
5 S. Mori and H. G. Barth, *Size Exclusion Chromatography*, Springer, 1999.
6 K. Matyjaszewski and J. Spanswick, *Mater. Today*, 2005, **8**, 26–33.
7 J. K. Stille, *J. Chem. Educ.*, 1981, **58**, 862.
8 G. Odian, *Principles of Polymerization*, John Wiley & Sons, 4th ed., 2007.
9 G. Odian, *Chain-Reaction Polymerization*, John Wiley & Sons, 2011.
10 W. A. Braunecker and K. Matyjaszewski, *Prog. Polym. Sci*, 2007, **32**, 93–146.
11 G. Moad and D. H. Solomon, *The Chemistry of Radical Polymerization*, Elsevier, 2006.
12 G. Moad, E. Rizzardo and S. H. Thang, *Acc. Chem. Res.*, 2008, **41**, 1133–1142.
13 K. Matyjaszewski and T. P. Davis, *Handbook of Radical Polymerization*, John Wiley & Sons, 2002.
14 D. Colombani, *Prog. Polym. Sci.*, 1997, **22**, 1649–1720.
15 M. Szwarc, *Nature*, 1956, **178**, 1168–1169.
16 O. Webster, *Science*, 1991, **251**, 887–893.
17 N. Hadjichristidis, M. Pitsikalis, S. Pispas and H. Iatrou, *Chem. Rev.*, 2001, **101**, 3747–3792.
18 A. Hirao, R. Goseki and T. Ishizone, *Macromolecules*, 2014, **47**, 1883–1905.
19 R. B. Grubbs and R. H. Grubbs, *Macromolecules*, 2017, **50**, 6979–6997.
20 M. Szwarc, *Living Polymers and Mechanisms of Anionic Polymerization*, Springer, 1983.
21 A. D. Jenkins, R. G. Jones and G. Moad, *Pure Appl. Chem.*, 2010, **82**, 483–491.
22 D. J. Keddie, *Chem. Soc. Rev.*, 2014, **43**, 496–505.
23 S. Perrier, *Macromolecules*, 2017, **50**, 7433–7447.
24 K. Matyjaszewski, *Macromolecules*, 2012, **45**, 4015–4039.
25 K. Matyjaszewski and J. Xia, *Chem. Rev.*, 2001, **101**, 2921–2990.
26 C. J. Hawker, A. W. Bosman and E. Harth, *Chem. Rev.*, 2001, **101**, 3661–3688.
27 H. Fischer, *Chem. Rev.*, 2001, **101**, 3581–3610.
28 K. Matyjaszewski, *Isr. J. Chem.*, 2012, **52**, 206–220.
29 F. di Lena and K. Matyjaszewski, *Prog. Polym. Sci.*, 2010, **35**, 959–1021.
30 J. Nicolas, Y. Guillaneuf, C. Lefay, D. Bertin, D. Gigmes and B. Charleux, *Prog. Polym. Sci.*, 2013, **38**, 63–235.
31 G. Gody, T. Maschmeyer, P. B. Zetterlund and S. Perrier, *Nat. Commun.*, 2013, **4**, 2505.
32 G. Gody, T. Maschmeyer, P. B. Zetterlund and S. Perrier, *Macromolecules*, 2014, **47**, 639–649.
33 J. Chiefari, Y. K. Chong, F. Ercole, J. Krstina, J. Jeffery, T. P. T. Le, R. T. A. Mayadunne, G. F. Meijs, C. L. Moad, G. Moad, E. Rizzardo and S. H. Thang, *Macromolecules*, 1998, **31**, 5559–5562.
34 M. Destarac, C. Brochon, J. Catala, A. Wilczewska and Z. Zard Samir, *Macromol. Chem. Phys.*, 2002, **203**, 2281–2289.
35 S. Perrier and P. Takolpuckdee, *J. Polym. Sci. Part A: Polym. Chem.*, 2005, **43**, 5347–5393.

36 S. Yamago, *Chem. Rev.*, 2009, **109**, 5051–5068.
37 G. David, C. Boyer, J. Tonnar, B. Ameduri, P. Lacroix-Desmazes and B. Boutevin, *Chem. Rev.*, 2006, **106**, 3936–3962.
38 G. Moad, E. Rizzardo and S. H. Thang, *Aust. J. Chem.*, 2012, **65**, 985–1076.
39 M. Destarac, *Polym. Rev.*, 2011, **51**, 163–187.
40 D. J. Keddie, G. Moad, E. Rizzardo and S. H. Thang, *Macromolecules*, 2012, **45**, 5321–5342.
41 M. Benaglia, M. Chen, Y. K. Chong, G. Moad, E. Rizzardo and S. H. Thang, *Macromolecules*, 2009, **42**, 9384–9386.
42 G. Moad, E. Rizzardo and S. H. Thang, *Polymer*, 2008, **49**, 1079–1131.
43 M. Benaglia, J. Chiefari, Y. K. Chong, G. Moad, E. Rizzardo and S. H. Thang, *J. Am. Chem. Soc.*, 2009, **131**, 6914–6915.
44 R. T. A. Mayadunne, E. Rizzardo, J. Chiefari, J. Krstina, G. Moad, A. Postma and S. H. Thang, *Macromolecules*, 2000, **33**, 243–245.
45 R. T. A. Mayadunne, J. Jeffery, G. Moad and E. Rizzardo, *Macromolecules*, 2003, **36**, 1505–1513.
46 J. Bernard, A. Favier, L. Zhang, A. Nilasaroya, T. P. Davis, C. Barner-Kowollik and M. H. Stenzel, *Macromolecules*, 2005, **38**, 5475–5484.
47 A. Gregory and M. H. Stenzel, *Prog. Polym. Sci.*, 2012, **37**, 38–105.
48 G. Moad, *Polym. Int.*, 2015, **64**, 15–24.
49 S. C. Radzinski, J. C. Foster and J. B. Matson, *Polym. Chem.*, 2015, **6**, 5643–5652.
50 H. Willcock and R. K. O'Reilly, *Polym. Chem.*, 2010, **1**, 149–157.
51 G. Moad, Y. K. Chong, A. Postma, E. Rizzardo and S. H. Thang, *Polymer*, 2005, **46**, 8458–8468.
52 G. Moad, E. Rizzardo and S. H. Thang, *Polym. Int.*, 2011, **60**, 9–25.
53 S. Perrier, P. Takolpuckdee and C. A. Mars, *Macromolecules*, 2005, **38**, 2033–2036.
54 C. Barner-Kowollik and S. Perrier, *J. Polym. Sci. Part A: Polym. Chem.*, 2008, **46**, 5715–5723.
55 M. Semsarilar and S. Perrier, *Nat. Chem.*, 2010, **2**, 811.
56 C. Boyer, V. Bulmus, T. P. Davis, V. Ladmiral, J. Liu and S. Perrier, *Chem. Rev.*, 2009, **109**, 5402–5436.
57 G. Riess, *Prog. Polym. Sci.*, 2003, **28**, 1107–1170.
58 P. Alexandridis and B. Lindman, *Amphiphilic Block Copolymers: Self-Assembly and Applications*, Elsevier, 2000.
59 Y. Mai and A. Eisenberg, *Chem. Soc. Rev.*, 2012, **41**, 5969–5985.
60 N. S. Cameron, M. K. Corbierre and A. Eisenberg, *Can. J. Chem.*, 1999, **77**, 1311–1326.
61 I. Hamley, *The Physics of Block Copolymers*, OUP Oxford, 1998.
62 A. Blanazs, S. P. Armes, A. J. Ryan, *Macromol. Rapid Commun.*, 2009, **30**, 267–277.
63 J. N. Israelachvili, D. J. Mitchell and B. W. Ninham, *J. Chem. Soc. Faraday Trans. 2 Mol. Chem. Phys.*, 1976, **72**, 1525–1568.
64 D. E. Discher and F. Ahmed, *Annu. Rev. Biomed. Eng.*, 2006, **8**, 323–341.
65 R. K. O'Reilly, C. J. Hawker and K. L. Wooley, *Chem. Soc. Rev.*, 2006, **35**, 1068–1083.
66 S.-H. Choi, F. S. Bates and T. P. Lodge, *J. Phys. Chem. B*, 2009, **113**, 13840–13848.
67 S. Fusco, A. Borzacchiello and P. A. Netti, *J. Bioact. Compat. Polym.*, 2006, **21**, 149–164.
68 Y.-Y. Won, H. T. Davis and F. S. Bates, *Science*, 1999, **283**, 960 LP-963.
69 N. Petzetakis, D. Walker, A. P. Dove and R. K. O'Reilly, *Soft Matter*, 2012, **8**,

7408–7414.
70 L. Meli and T. P. Lodge, *Macromolecules*, 2009, **42**, 580–583.
71 O. Colombani, M. Ruppel, M. Burkhardt, M. Drechsler, M. Schumacher, M. Gradzielski, R. Schweins and A. H. E. Müller, *Macromolecules*, 2007, **40**, 4351–4362.
72 J. P. Patterson, E. G. Kelley, R. P. Murphy, A. O. Moughton, M. Robin, A. Lu, O. Colombani, C. Chassenieux, D. Cheung, M. O. Sullivan, T. H. Epps III and R. K. O'Reilly, *Macromolecules*, 2013, **46**, 6319–6325.
73 R. Hadgiivanova, H. Diamant and D. Andelman, *J. Phys. Chem. B*, 2011, **115**, 7268–7280.
74 T. Rager, W. H. Meyer, G. Wegner and M. A. Winnik, *Macromolecules*, 1997, **30**, 4911–4919.
75 G. Moad, *Polym. Chem.*, 2017, **8**, 177–219.
76 E. G. Kelley, J. N. L. Albert, M. O. Sullivan and T. H. Epps III, *Chem. Soc. Rev.*, 2013, **42**, 7057–7071.
77 R. C. Hayward and D. J. Pochan, *Macromolecules*, 2010, **43**, 3577–3584.
78 T. Nicolai, O. Colombani and C. Chassenieux, *Soft Matter*, 2010, **6**, 3111–3118.
79 J. P. Patterson, M. P. Robin, C. Chassenieux, O. Colombani and R. K. O'Reilly, *Chem. Soc. Rev.*, 2014, **43**, 2412–2425.
80 R. Lund, L. Willner, D. Richter and E. E. Dormidontova, *Macromolecules*, 2006, **39**, 4566–4575.
81 D. B. Wright, J. P. Patterson, N. C. Gianneschi, C. Chassenieux, O. Colombani and R. K. O'Reilly, *Polym. Chem.*, 2016, **7**, 1577–1583.
82 J. Stejskal, D. Hlavatá, A. Sikora, Č. Konňák, J. Pleštil and P. Kratochvíl, *Polymer*, 1992, **33**, 3675–3685.
83 D. D. Bendejacq and V. Ponsinet, *J. Phys. Chem. B*, 2008, **112**, 7996–8009.
84 I. A. Nyrkova and A. N. Semenov, *Macromol. Theory Simul.*, 2005, **14**, 569–585.
85 S. Jain and F. S. Bates, *Macromolecules*, 2004, **37**, 1511–1523.
86 A. Halperin, *Macromolecules*, 2011, **44**, 5072–5074.

2. Design and synthesis of novel aminobromomaleimide (ABM) functionalized RAFT agents

2.1. Abstract

Aminobromomaleimides (ABMs) are small molecule fluorophores that are structurally similar to dithiomaleimides (DTMs) and offer a new class of highly emissive compounds which exhibit similar properties such as large Stokes shifts, high fluorescence quantum yields, and solvent dependent emission. Coupled with their enhanced stability and reactivity, ABMs are ideal candidates for the functionalization of block copolymers in order to probe and understand the internal properties and self-assembly dynamics of polymer nanostructures in solution. In this Chapter, the feasibility of using ABM-functionalized RAFT agents to synthesize fluorescent block copolymers in a reproducible and controlled manner was investigated. To this end, the incorporation of an ABM fluorophore into the chemical structure of a range of RAFT agents *via* both R and Z group functionalization was explored (Figure 2.1). Following this, kinetic studies were conducted with a variety of suitable monomers to determine the effect of fluorophore incorporation upon the polymerization rate and degree of control.

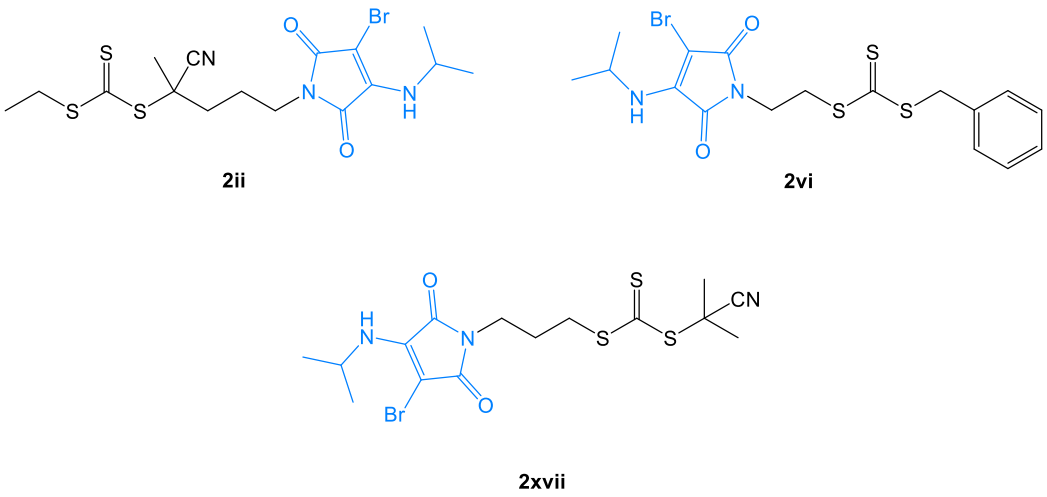

Figure 2.1: Chemical structures of novel aminobromomaleimide-functionalized RAFT agents **2ii**, **2vi** and **2xvii** developed in this Chapter.

2.2. Introduction

2.2.1. Small molecule fluorophores: dithiomaleimides (DTMs)

Dithiomaleimides (DTMs) represent a class of small molecule fluorophores formed by the addition-elimination reaction between 2,3-dibromomaleimide (DBM) and thiols, resulting in conjugation-induced fluorescence (Figure 2.2).[1] DTMs are highly emissive compounds that exhibit a broad excitation spectrum between 250-400 nm with a corresponding emission spectrum between 500-550 nm.[2–4] Due to their small size and intermediate polarity, DTMs have been shown to be versatile fluorophores for use in a myriad of applications, such as polymer/protein conjugation,[2,5–13] polymer labelling,[3,14–17] polymer synthesis,[18–21] and as contrast and imaging agents.[4,22,23]

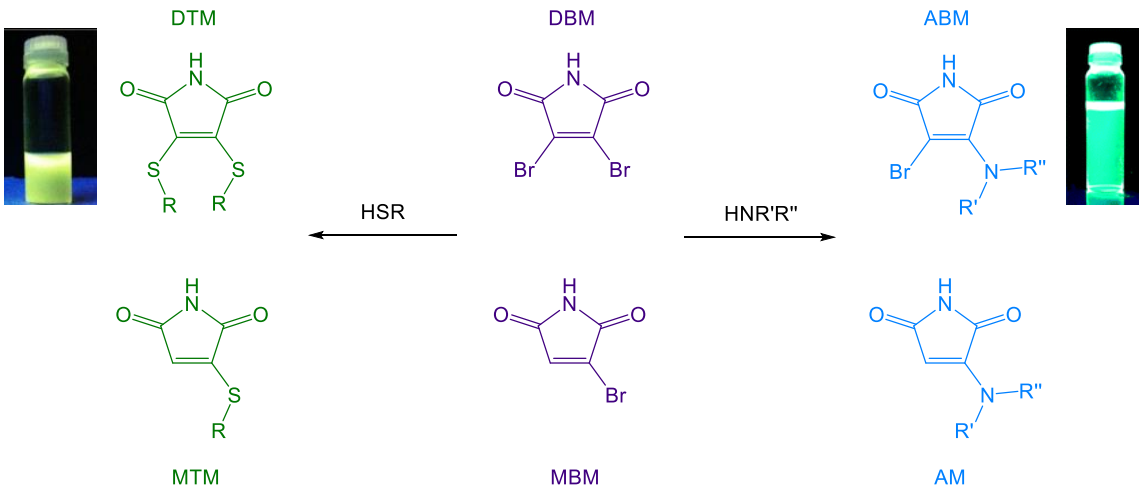

Figure 2.2: Conversion of mono- or dibromomaleimide (MBM/DBM) to monothio- or dithiomaleimides (MTMs/DTMs) and amino- or aminobromomaleimides (AMs/ABMs) by reaction with thiols and amines respectively. Figure and caption adapted from ref 1.

Fluorophore incorporation into the final polymer structure can be achieved by a pre-polymerization route *via* a fluorescent monomer/initiator/RAFT agent; or by a

post-polymerization approach either *via* end group modification or by conversion of pendant pro-fluorescent groups along the polymer backbone.[24] In the case of DTM-functionalized polymers, all four approaches have been explored within the literature.[2–4,14,16,22,23]

For instance, O'Reilly and co-workers synthesized a series of fluorescent and chemico-fluorescent responsive copolymers using DTM- and pro-fluorescent DBM-functionalized monomers respectively.[3] Subsequent copolymerizations with a range of acrylate and methacrylate monomers proceeded to high monomer conversions with excellent control over molecular weight achieved ($Đ_M$ < 1.3). Importantly, the C=C double bond of the DTM fluorophore was found to be unreactive under RAFT polymerization conditions and thus did not require protection. Furthermore, DTM incorporation appeared to not significantly alter the properties of the resultant copolymers, whilst no adverse effects were observed regarding the DTMs' fluorescence emission profiles. For example, triethylene glycol monomethyl ether acrylate (TEGA) and oligoethylene glycol monomethyl ether methacrylate (OEGMA) copolymers, with a 10 mol% loading of the DTM monomer in each case, were able to retain their water solubility and thermoresponsive behavior. Moreover, the respective copolymers displayed similar excitation and emission spectra in comparison to small molecule DTMs. The versatility of this approach was further demonstrated in this paper *via* the copolymerization of a pro-fluorescent DBM methacrylate monomer (DBMMA) with OEGMA. Upon thiol functionalization, the cloud point of the resultant fluorescent thermoresponsive copolymer could be progressively tuned over a range of 11 °C by simple manipulation of the thiol polarity (Figure 2.3).[3]

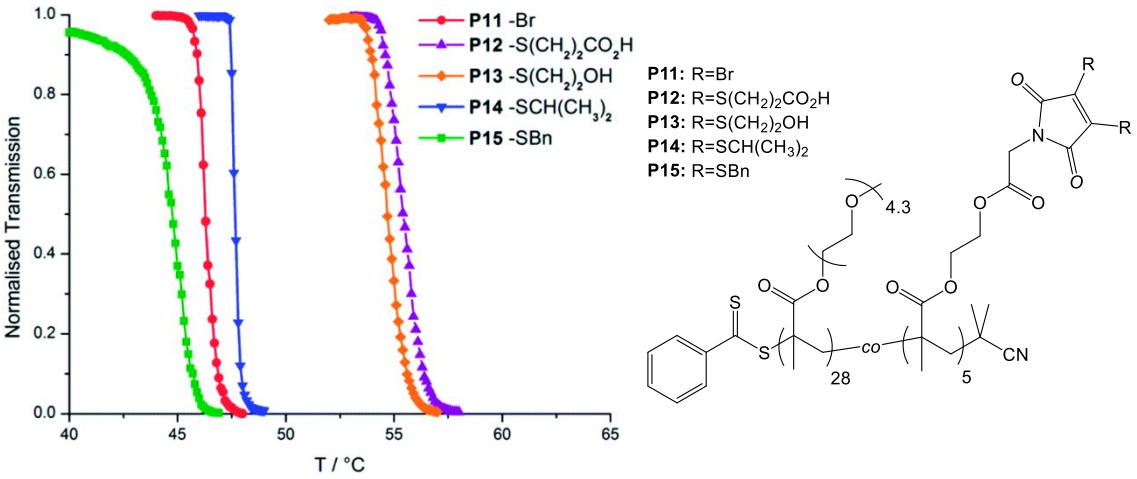

Figure 2.3: Cloud point measurements for solutions of **P11–15** at 10 g L^{-1} in water whereby **P12-P15** are DTM-functionalized copolymers formed from post-polymerization modification of a p(OEGMA$_{28}$-*co*-DBMMA$_5$) copolymer (**P11**) with the corresponding thiol. Figure and caption adapted from ref 3.

In another study conducted by O'Reilly and co-workers, a DTM-functionalized acrylate monomer was copolymerized either into the core-forming or corona-forming blocks of poly(triethylene glycol monomethyl ether acrylate)-*b*-poly(*tert*-butyl acrylate) block copolymer micelles *via* RAFT polymerization (Figure 2.4).[15] The sensitivity of the DTM fluorophore to its environment was highlighted in this study with a greater emission (Φ_f = 17% *c.f.* <1%) and a longer fluorescence lifetime (19 ns *c.f.* 7 ns) observed for the DTM fluorophore in core-labelled micelles when compared to corona-labelled micelles, as a result of better protection from collisional quenching.[15] Moreover, the simple use of a DTM label produced fluorescent block copolymer micelles capable of self-reporting on their supramolecular state. Furthermore, the presence or absence of an encapsulated molecule, such as Nile Red, could be confirmed *via* Förster resonance energy transfer (FRET) measurements with the DTM fluorophore.[15] Consequently, Cheng and co-workers successfully exploited the capability of DTMs to form successful FRET pairs as an non-invasive tool to monitor the drug release of camptothecin from DTM-based camptothecin-containing nanoparticles upon the addition of glutathione.[25]

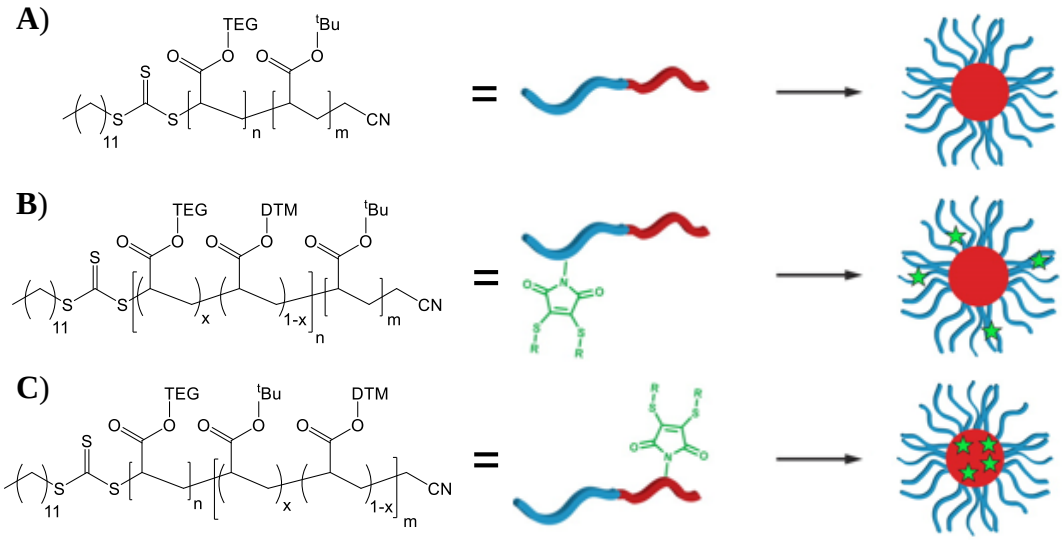

Figure 2.4: Schematic representation of the synthetic route to non-labelled micelles (a), corona-labelled micelles (b) and core-labelled micelles (c) containing the DTM fluorophore. Chemical structures of the respective diblock copolymers are shown as a guide. Figure and caption adapted from ref 15.

In addition to the copolymerization strategies highlighted above, a DTM-functionalized dual initiator/RAFT agent has also been used to successfully synthesize fluorescent amphiphilic block copolymers *via* sequential ring opening polymerization (ROP) and RAFT polymerization techniques (Figure 2.5).[16,22,23] Self-assembly of the corresponding poly(*rac*-lactide)-*b*-p(TEGA) amphiphilic star block copolymer resulted in the formation of block copolymer micelles, in which the DTM fluorophore was located at the core-shell interface. Critically, the authors found that DTM incorporation had no detrimental effect upon block copolymer self-assembly and was thus explored as a potential non-invasive method for the generation of self-reporting materials for nanomedicine applications. Significantly, the DTM fluorophore did not self-quench in the micellar state leading to a substantial increase in fluorescence emission, with a similar behavior observed in analogous DTM-functionalized block copolymer assemblies.[4,15,16,23] In addition, O'Reilly and co-workers showed that it was possible to locate and differentiate between various supramolecular states *in vitro* such as assembled micelles, disassembled micelles (unimers), and degraded polymer by measuring their respective fluorescence lifetimes

using time-domain fluorescence-lifetime imaging (FLIM).[22] The viability of using DTMs as effective sensors for tracking the cell internalization and uptake behavior of fluorescently-labelled polymeric nanostructures was further realized in a subsequent study investigating the development of drug delivery vehicles for neural stem cells.[23]

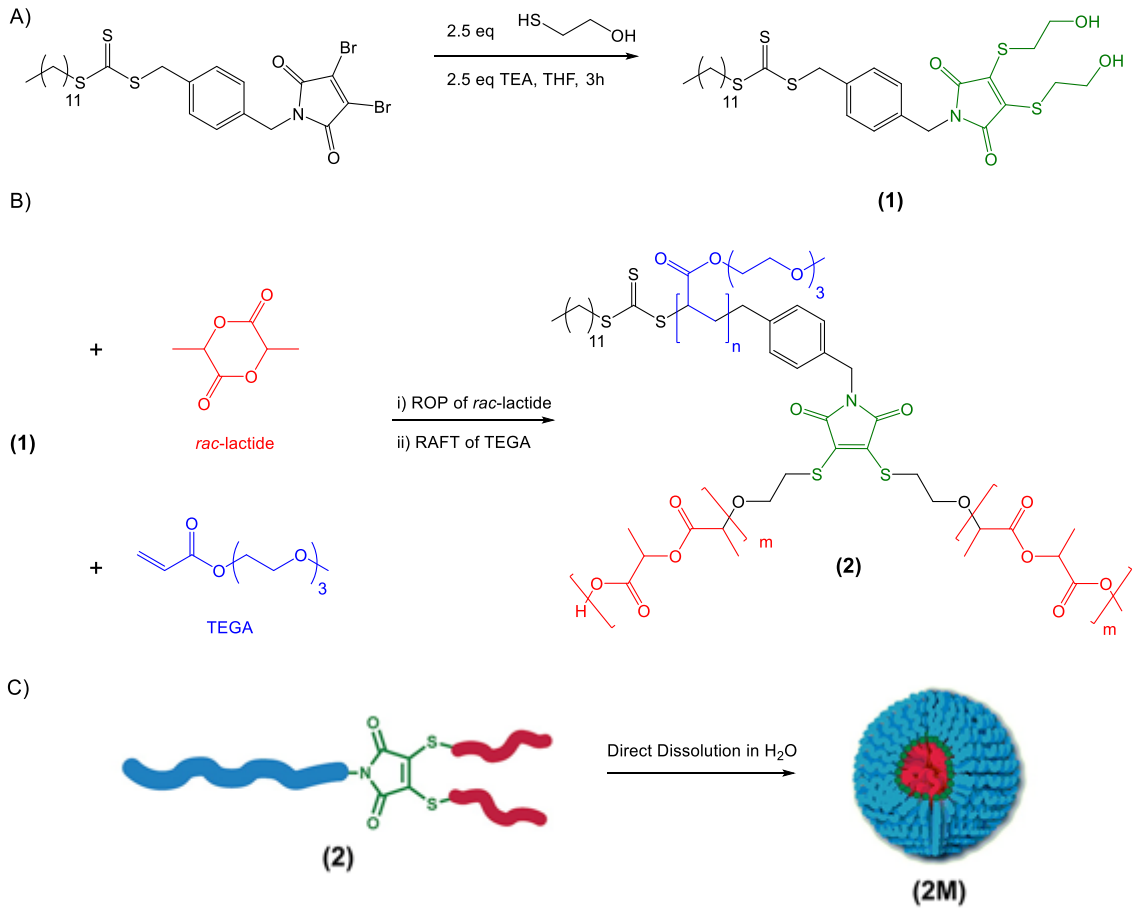

Figure 2.5: (a) Synthesis of a DTM-functionalized dual ROP initiator/RAFT agent (**1**); (b) synthesis of a poly(*rac*-lactide)$_{2m}$-b-p(TEGA)$_n$ amphiphilic star block copolymer (**2**) *via* sequential ROP and RAFT polymerization; (c) self-assembly of **2** *via* direct dissolution in water to produce spherical micelles (**2M**) with DTM fluorophore located at the core-shell interface. Figure and caption adapted from ref 22.

A critical drawback of organic dyes is that they typically display concentration-dependent molar emission. At low or high concentration, a significant change in molar emission is observed due to fluorophore aggregation and/or self-quenching. Conversely, DTMs have been shown to exhibit concentration independent molar emission with relatively flat

anisotropy profiles over a concentration range of three orders of magnitude upon incorporation into block copolymers.[15,22] The limitations of this concentration independent molar emissive behavior were further probed by O'Reilly and co-workers through the synthesis of a series of fluorescently-labelled nanogels with various degrees of DTM functionalization and crosslinking density (Figure 2.6).[4] Remarkably, neither self-quenching of the DTM fluorophore nor concentration-dependent molar emission were observed for very high localized DTM concentrations (16 mM) with respect to the nanoparticle cores. The authors therefore concluded that DTM-functionalized nanoparticles could be utilized as effective quantitative imaging agents, whereby fluorophore emission directly corresponds to local nanoparticle concentration.

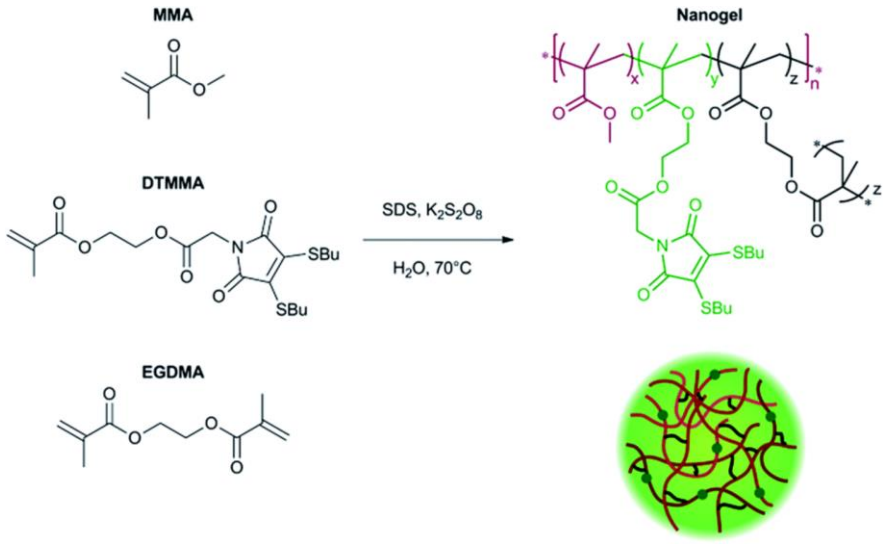

Figure 2.6: Synthesis of DTM-labelled nanogels by radical cross-linking emulsion polymerization in water at 70 °C using fluorescent DTM-functionalized methacrylate monomer (DTMMA), methyl methacrylate (MMA) and ethylene glycol dimethacrylate (EGDMA). Figure adapted from ref 4.

One potential disadvantage of DTMs is that they can undergo further substitution in the presence of excess thiol; and if the thiol is aromatic, the resultant DTM is non-emissive. Interestingly, O'Reilly and co-workers exploited this reversibility of thiol addition to DTM to induce a morphology transition from spherical micelles to vesicles coupled with

a simultaneous quenching of fluorescence emission.[16] Addition of thiophenol to previously reported poly(*rac*-lactide)-*b*-p(TEGA) block copolymer micelles (Figure 2.5 c) resulted in the elimination of the hydrophobic poly(*rac*-lactide) blocks, prompting a structural reorganization to compensate for the significant change in the volume fraction of the solvophobic block.

2.2.2. Small molecule fluorophores: aminobromomaleimides (ABMs) and aminomaleimides (AMs)

Aminobromomaleimides (ABMs) and aminomaleimides (AMs) (Figure 2.2) are structurally similar to DTMs and offer a new class of highly emissive compounds that exhibit comparable fluorescence properties to DTMs. These include large Stokes shifts (> 100 nm), high fluorescence quantum yields (up to 60%) and solvent-dependent wavelength and emission.[1] Formed by simple amino-substitution of either dibromomaleimide or monobromomaleimide, ABMs and AMs exhibit greater fluorescence emission than their respective DTM counterparts, particularly when functionalized with alkyl primary amines.[1] Notably, ABMs and AMs are quenched upon direct conjugation to aromatic rings or when functionalized with secondary amines; with a similar fluorescence behavior with respect to aromatic thiols observed for DTMs.[2] Two important advantages of ABMs and AMs are that they do not undergo further substitution upon the addition of excess amine or thiol and unlike their DTM counterparts, they do not require di-substitution to generate intense emission.[1]

A key attribute of ABM and AM fluorophores is that they are highly sensitive to their environment. For instance, O'Reilly and co-workers discovered that ABMs and AMs displayed greater fluorescence emission and higher quantum yields in aprotic solvents such as 1,4-dioxane and cyclohexane.[1] Alternatively, a loss of fluorescence emission was

observed in protic polar solvents, like methanol, as a result of electron driven proton transfer (EDPT), as confirmed by a separate photodynamic study.[26] Interestingly, O'Reilly and co-workers successfully exploited the solvent-dependent emissive behavior of ABMs to generate a fluorescent read-out regarding the hydrophilicity and corresponding degree of core hydration of core-crosslinked CO_2-responsive nanoparticles under different stimuli.[27] In this case, an ABM-functionalized methacrylate monomer (ABMMA) was incorporated into the core of fluorescent nanoparticles composed of a CO_2-responsive 2-(diethylamino) ethyl methacrylate (DEAEMA) core covalently stabilized with OEGMA and crosslinked using ethylene glycol dimethacrylate (EGDMA) (Figure 2.7). Upon bubbling the solution of ABM-functionalized nanoparticles with CO_2, the authors observed an increase in particle size along with a significant decrease in fluorescence intensity, which was attributed to an increase in core hydrophilicity due to particle swelling. Moreover, it was found that fluorescence emission could be recovered by simply purging the solution of hydrated swollen nanoparticles with N_2.

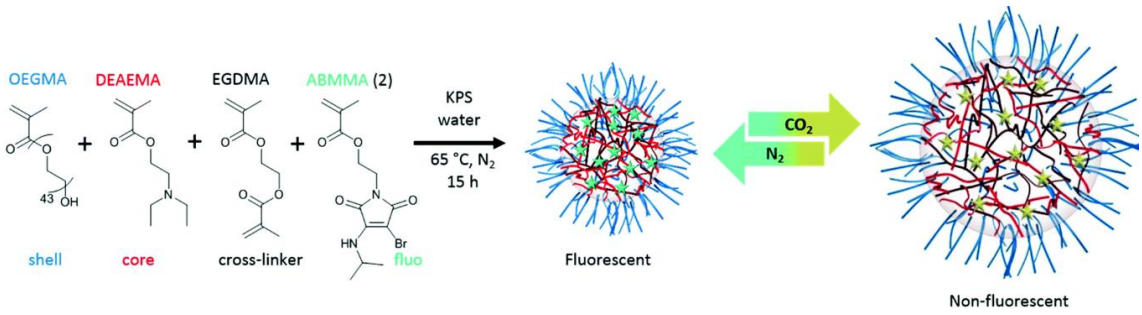

Figure 2.7: Synthesis of fluorescent CO_2-responsive ABM-functionalized nanoparticles *via* emulsion polymerization in water at 65 °C using a tertiary amine-functionalized monomer (DEAEMA), fluorescent ABM-functionalized methacrylate monomer (ABMMA), shell-forming monomer OEGMA and cross-linker (EGDMA). Non-fluorescent swollen nanoparticles form upon bubbling the solution with CO_2, with the reversible reaction achieved upon bubbling with N_2. Figure adapted from ref 27.

This study highlights the utility of ABM fluorophores as effective probes for the investigation and understanding of the self-assembly behavior of polymeric

nanostructures in response to an external stimulus. As highlighted above, DTMs have been employed in an extensive range of applications and offer several advantages for polymer nanoparticle labelling, including: ease of synthesis; high sensitivity; concentration independent molar emission; lack of self-quenching; stability under radical polymerization conditions; self-reporting nature; and small size to allow for facile incorporation into polymeric nanostructures without affecting or disrupting the assembly. Therefore, it was envisaged that ABMs could exhibit similar properties upon incorporation into a block copolymer structure given the numerous similarities between the two fluorophore classes. Moreover, ABMs could offer an attractive alternative to DTMs with regards to polymer functionalization considering the inherent advantages of ABMs with respect to substitution, stability and reactivity coupled with enhanced fluorescence behavior. In this Chapter, the design and synthesis of novel ABM-functionalized RAFT agents for the purpose of producing fluorescent block copolymers in a robust and controlled manner is explored.

2.3. Results and Discussion

As outlined in the introduction to this Chapter, incorporation of a fluorophore into the final polymer structure can be achieved *via* various methods, namely post-polymerization modification, copolymerization of a pro-fluorescent or fluorescent comonomer into the polymer backbone or using a pro-fluorescent or fluorescent RAFT agent for polymer synthesis. For the purposes of understanding self-assembly behavior and resultant exchange dynamics for any chosen block copolymer system, each polymer chain should ideally contain at least one fluorophore. Moreover, self-assembly behavior of fluorescently-tagged block copolymers should closely match their non-fluorescent counterparts to allow for direct comparison. Of the methods listed above, employment of a fluorescent RAFT agent to afford the target fluorescent block copolymers provided the most suitable option. By doing so, the requirement for high yielding post-polymerization modification reactions; the possible risk of synthesizing core-forming blocks that are gradient instead of statistical in nature; and the potential impact of changing the inherent nature of the block copolymer due to the introduction of a new fluorescent comonomer were all avoided.

Previously, a DTM-functionalized dual ROP initiator/RAFT agent (Figure 2.5) had been successfully utilized by O'Reilly and co-workers for the synthesis of fluorescently-tagged star copolymers *via* orthogonal polymerization techniques.[4,16,22,23] Most importantly, the studies demonstrated that the DTM fluorophore was highly tolerant to polymerization conditions with the fluorophore located at the core-shell interface of the resultant polymeric nanostructures upon self-assembly. Consequently, it was postulated that an analogous approach could be adopted for the successful design and synthesis of an ABM-functionalized RAFT agent capable of facilitating controlled RAFT polymerizations to generate fluorescently-labelled block copolymers.

As outlined in Chapter 1, polymers produced *via* RAFT polymerization are principally categorized by their respective α-end and ω-end group functionalities. In an ideal RAFT polymerization, all synthesized polymer chains would have 100% end group fidelity with terminal functionalities directly reflecting the chosen R and Z group of the employed RAFT agent. However, this is rarely the case with the potential for loss of both the R and Z group moieties from propagating polymer chains during the polymerization.[28] For instance, the requirement of an initiator in RAFT polymerization leads to unavoidable formation of initiator-derived polymer chains instead of R-group derived polymer chains. On the other hand, retention of the thiocarbonylthio moiety at the ω-end, and thus Z group functionality, is principally dictated by the rate of irreversible bimolecular termination during RAFT polymerization. Importantly, the relative populations of undesired initiator-derived and/or "dead" polymer chains can be significantly reduced to negligible amounts through careful manipulation of the polymerization conditions, as highlighted in the literature.[29–31] R group functionalization is often preferred over Z group functionalization due to the likelihood of hetero- or homolytic degradation of the reactive thiocarbonylthio moiety resulting in the loss of the ZCS_2 group.[32] Despite this, the incorporation of an ABM fluorophore into the chemical structure of various RAFT agents *via* both R and Z group functionalization will be explored in this Chapter. If successful, the range of fluorescent block copolymer compositions that can be targeted using an ABM-functionalized RAFT agent should be extensive.

2.3.1. Design and synthesis of an R group ABM-functionalized RAFT agent

With regards to RAFT agent design, judicious selection of both the R and Z group is paramount to ensure the controlled synthesis of well-defined, low disperse polymers *via*

RAFT polymerization. Furthermore, the choice of R and Z group is largely governed by the monomer classification of the chosen radically polymerizable monomers, i.e. more activated monomers (MAMs) *versus* less activated monomers (LAMs). Preferably, the range of monomers that can be polymerized in a controlled manner *via* RAFT polymerization utilizing an ABM-functionalized RAFT agent would be large. Therefore, an ideal scenario would be the design and synthesis of a ABM-functionalized universal RAFT agent capable of polymerizing both LAMs and MAMs without retardation, inhibition or loss of control.[33] However, to date no single RAFT agent that offers complete universal control currently exists and thus attempting to synthesize an ABM-functionalized analogue would be synthetically challenging. Consequently, this Chapter will primarily focus upon the synthesis of ABM-functionalized trithiocarbonates due to their relatively facile synthesis and robust nature with regards to functionalization. Furthermore, trithiocarbonates were selected as they exhibit improved hydrolytic stability in comparison to dithioesters and are capable of controlling the RAFT polymerization of more activated monomers such as (meth)acrylates, (meth)acrylamides and styrenes.[34]

For the synthesis of the DTM-functionalized dual RAFT agent/ROP initiator (Figure 2.5), the trithiocarbonate precursor was firstly prepared by O'Reilly and co-workers by the reaction of 1-dodecanethiol, carbon disulfide and 4-(chloromethyl)benzyl alcohol to afford a hydroxyl-functionalized RAFT agent.[35] In this case, a 1,4-substituted benzyl group was chosen as the R group to facilitate the controlled RAFT polymerization of acrylate, acrylamide and styrenic monomers.[36] Introduction of the pro-fluorescent DBM moiety *via* the pendant hydroxyl group was achieved using a modified version of the Mitsunobu reaction.[37] Thus, it was envisaged that a similar protocol could be adopted for the synthesis of an ABM-functionalized RAFT agent. Moreover, the range of polymerizable monomers could be expanded to include methacrylates and methacrylamides by changing the R group.

Previously, Ho and co-workers demonstrated a one-step synthesis of well-defined block copolymers *via* concurrent ROP and RAFT polymerization using 2-cyano-5-hydroxypentan-2-yl dodecyl carbonotrithioate (CHPDDT) as a dual initiator.[38] In this study, styrene, methacrylate, acrylate and acrylamide monomers were polymerized in a controlled manner producing diblock copolymers for which the second block was composed of cyclic monomers.[38] Subsequent reports showed that when the pendant hydroxyl group of CHPDDT was tosylated, the successful ROP of 2-methyl-2-oxazoline and 2-ethyl-2-oxazoline was facilitated, whilst control over the RAFT polymerization of various vinyl monomers was retained.[39–41] Recently, O'Reilly and co-workers utilized an ethyl analogue of CHPDDT, 2-cyano-5-hydroxypentan-2-yl ethyl carbonotrithioate (CHPET), to synthesize poly(*ε*-caprolactone)-*b*-poly(methyl methacrylate)-*b*-poly(*N,N'*-dimethylacrylamide), (p(CL)-*b*-p(MMA)-*b*-p(DMAc), triblock copolymers *via* consecutive ROP and RAFT polymerizations. Resultant crystallization-driven self-assembly (CDSA) successfully afforded crystalline polymer nanostructures for which exceptional control over both morphology and size dimensions was achieved by direct epitaxial crystallization in aqueous media.[42]

For each of the literature examples highlighted above, the respective hydroxyl-functionalized dual RAFT agent/ROP initiator was synthesized *via* the thermally-initiated radical reaction between azo initiator 4,4-azobis(4-cyano-1-pentanol) (ACP) and the corresponding bis-(alkylsulfanylthiocarbonyl) disulfide intermediate. However, ACP is relatively expensive and difficult to source so an alternative synthetic route to obtain CHPET was explored (Scheme 2.1). Initially, an acid functionalized precursor, 4-cyano-4-(((ethylthio)carbonothioyl)thio)pentanoic acid (CETPA), was synthesized in a 91% yield *via* a modified literature protocol in which the sodium salt of ethanethiol was used due to its relative ease of handling and less unpleasant odor.[43] Subsequent reduction of the acid group to the corresponding alcohol was achieved using

a borane-Lewis base complex, in this case borane-tetrahydrofuran (BH_3•THF), to afford CHPET in a 72% isolated yield.

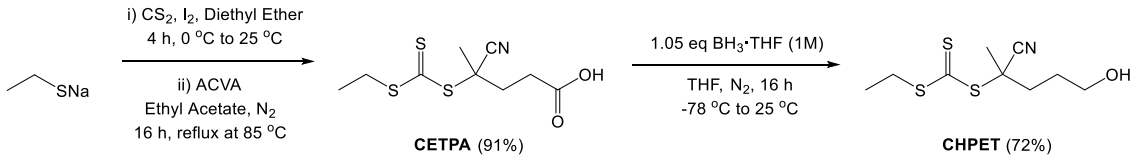

Scheme 2.1: Synthesis of 2-cyano-5-hydroxypentan-2-yl ethyl carbonotrithioate (CHPET) from the borane reduction of 4-cyano-4-(((ethylthio)carbonothioyl)thio)pentanoic acid (CETPA). ACVA = 4,4′-azobis(4-cyanovaleric acid).

Subsequent attachment of 2,3-dibromomaleimide with the hydroxyl-functionalized RAFT agent CHPET was achieved *via* a modified version of the Mitsunobu reaction.[37] In order to obtain the highest possible yield, it has been previously established that the order of addition for the reagents is critical to prevent the side reaction of DBM with triphenylphosphine (PPh_3) as well as potential inhibition from the Ph_3P-DIAD betaine intermediate.[37] Therefore, PPh_3 was added first followed by diisopropyl azodicarboxylate (DIAD), CHPET, neopentyl alcohol and finally DBM. Neopentyl alcohol was used as a "dummy ligand" to promote formation of the dioxaphosphorane intermediate to give the optimum yield relative to the desired alcohol, in this case CHPET. Consequently, a pro-fluorescent R group DBM-functionalized RAFT agent (**2i**) was obtained in an isolated yield of 68% (Scheme 2.2).

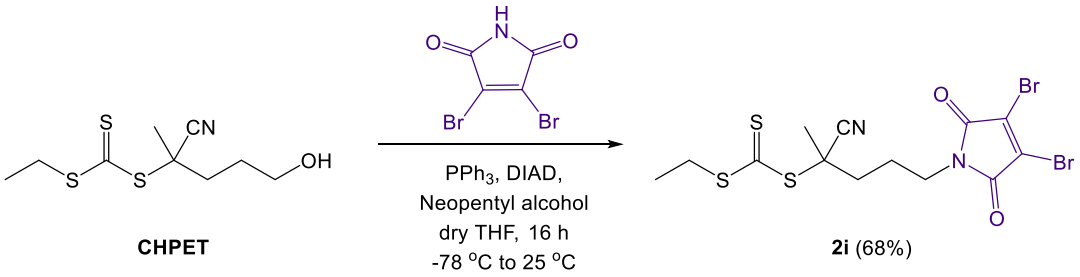

Scheme 2.2: Synthesis of the R group DBM-functionalized RAFT agent **2i** from CHPET *via* the Mitsunobu reaction.

Characterization *via* ^{1}H and ^{13}C NMR spectroscopy confirmed the desired structure (Figure 2.8), with the characteristic resonances of the dibromomaleimide group identified in the ^{13}C NMR spectrum at 163.8 and 129.5 ppm (C2 and C1 respectively) along with retention of the diagnostic resonance for the trithiocarbonate group (C9) at 217.0 ppm.

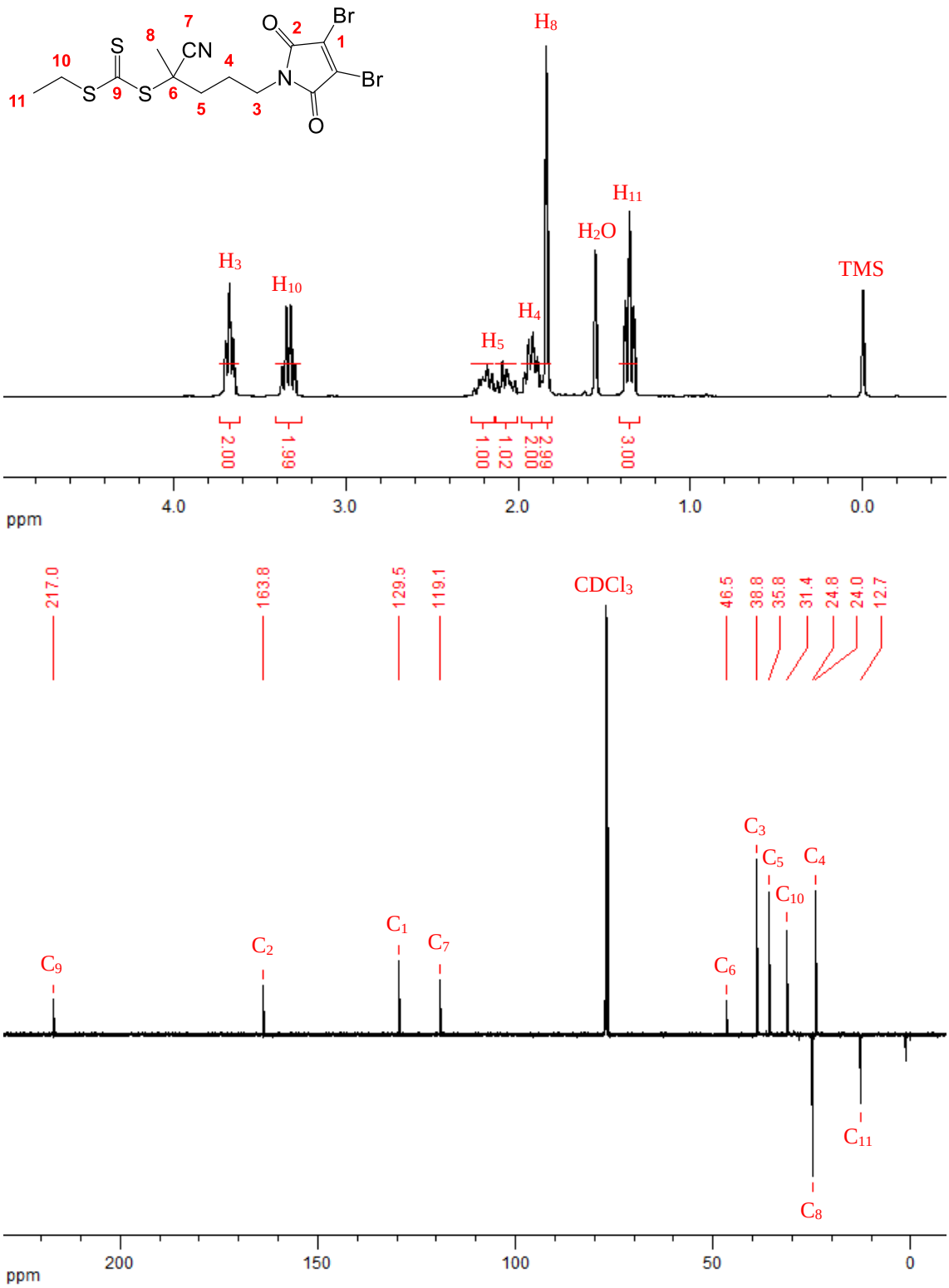

Figure 2.8: ^{1}H NMR (300 MHz, $CDCl_3$) and ^{13}C NMR (75 MHz, $CDCl_3$) spectra of the pro-fluorescent R group DBM-functionalized RAFT agent **2i**. TMS = Tetramethylsilane.

In Section 2.2.2, the facile synthesis of a library of highly emissive ABM fluorophores *via* substitution of one of the bromine atoms of DBM with a primary amine in the presence

of a base was highlighted.[1] Butylamine, isopropylamine and benzylamine produced ABMs with similar fluorescent quantum yields (Φ_f): 38%, 35% and 34% respectively.[1] In light of this, isopropylamine was selected to minimize the potential impact from the ABM-functionalized RAFT agent upon the self-assembly behavior of resultant fluorescent block copolymers due to steric and electronic interactions. Subsequently, reaction of **2i** with isopropylamine in the presence of sodium carbonate resulted in the formation of the desired R group ABM-functionalized RAFT agent **2ii** in a 60% yield (Scheme 2.3), and an overall yield of 27% *via* the four step synthetic route.

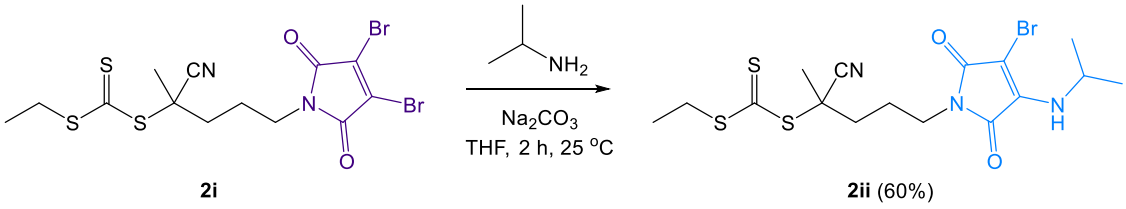

2i **2ii** (60%)

Scheme 2.3: Synthesis of the R group ABM-functionalized RAFT agent **2ii** from the addition-elimination reaction of isopropylamine with the R group DBM-functionalized RAFT agent **2i**.

Carbon resonances attributable to the ABM group were identified by ^{13}C NMR spectroscopy at 167.7, 166.0 and 142.2 ppm for C7, C6 and C4 respectively (Figure 2.9). Importantly, the carbon resonance corresponding to the trithiocarbonate group at 217.1 ppm (C14) was retained which showed that the addition of isopropylamine to **2i** under basic conditions did not result in degradation of the thiocarbonylthio moiety, providing the reaction was quenched within 2 hours.

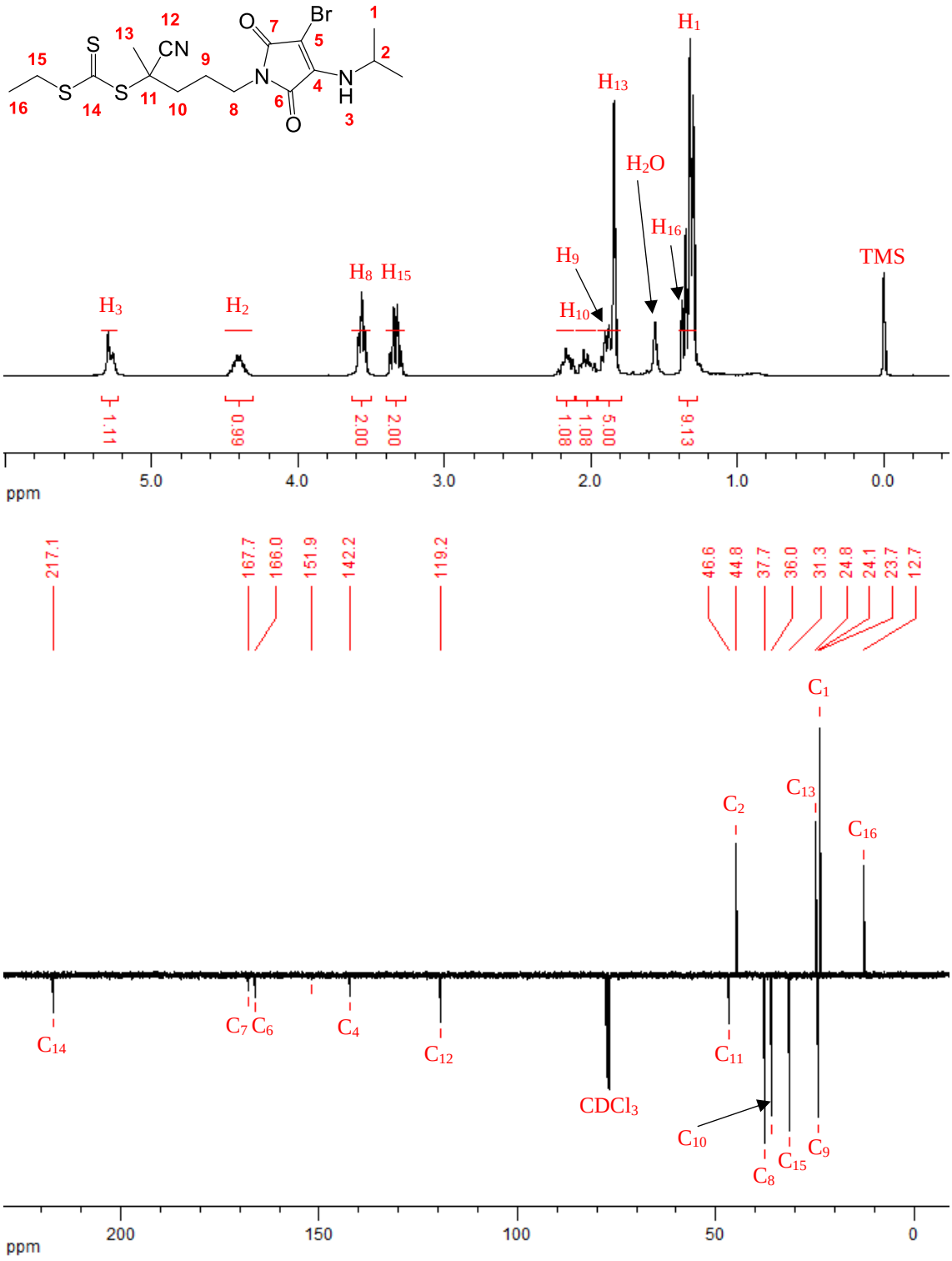

Figure 2.9: ^{1}H NMR (400 MHz, $CDCl_3$) and ^{13}C NMR (100 MHz, $CDCl_3$) spectra of the fluorescent R group ABM-functionalized RAFT agent **2ii**. TMS = tetramethylsilane.

2.3.2. RAFT polymerization utilizing an R group ABM-functionalized RAFT agent

Following the successful synthesis of **2ii**, it was important to confirm that the introduction of an ABM fluorophore into the chemical structure of a RAFT agent did not significantly hinder subsequent RAFT polymerizations. A previous study conducted by the O'Reilly group explored the effect that changing the substituents of the maleimide ring had upon RAFT polymerization.[44] The authors conducted a series of RAFT polymerizations in which a range of suitable monomers were chosen for which either a MBM-, a DBM- or a DTM-functionalized RAFT agent was used (Scheme 2.4).[44]

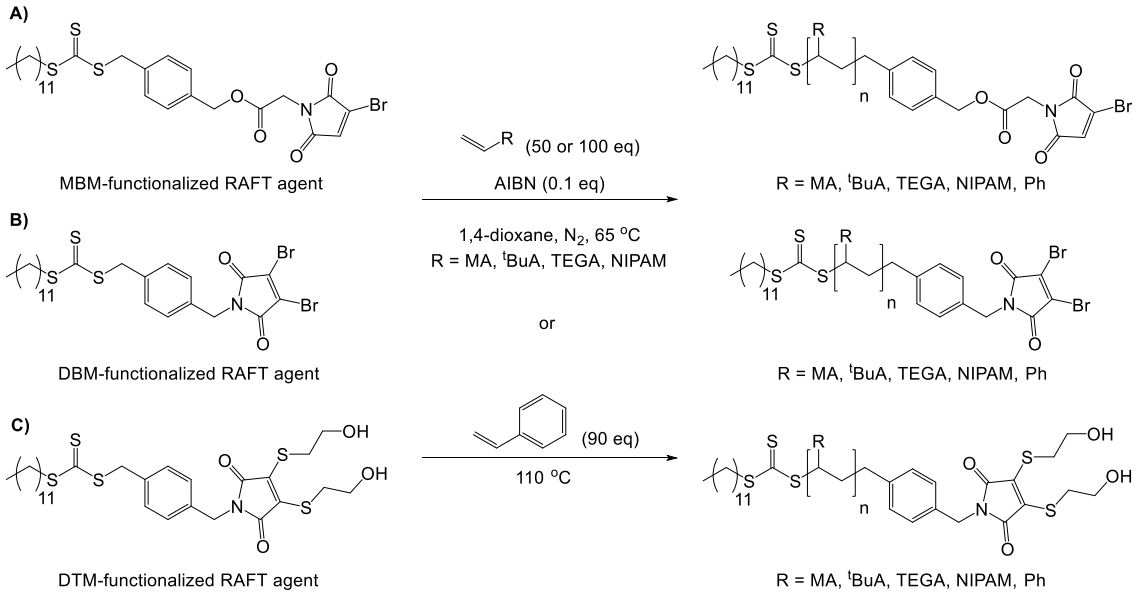

Scheme 2.4: A series of RAFT polymerizations previously conducted by O'Reilly and co-workers of methyl acrylate (MA), *tert*-butyl acrylate (^{t}BuA), triethylene glycol monomethyl ether acrylate (TEGA), *N*-isopropylacrylamide (NIPAM), and styrene in which with either: a) a MBM-functionalized RAFT agent; b) a DBM-functionalized RAFT agent; or c) a DTM-functionalized RAFT agent was used.[44]

Subsequent analysis of the obtained kinetic data (Table 2.1) highlighted that the electronic nature of the different maleimides, in terms of symmetry and electron density, coupled with steric crowding around the maleimides' C=C double bond played a significant role.[44]

RAFT agent functionality	Monomer	Time (h)	$M_{n,\,theo}$[a] (kDa)	$M_{n,\,SEC}$[b] (kDa)	$Đ_M$[b]	ρ[a] (%)
MBM	^{t}BuA	3	11.5	31.2	1.53	85
MBM	MA	3	7.4	25.6	1.46	79
MBM	TEGA	16	10.9	16.9	1.54	93
MBM	NIPAM	16	0.7	0.5	1.64	3
MBM	Styrene	16	2.4	7.2	2.42	19
DBM	^{t}BuA	6	6.0	5.7	1.15	84
DBM	MA	3	4.2	4.3	1.20	54
DBM	TEGA	16	5.9	5.5	1.27	48
DBM	NIPAM	16	0.7	0.8	1.12	1
DBM	Styrene	16	1.0	1.0	1.41	4
DTM	^{t}BuA	16	7.0	6.7	1.11	99
DTM	TEGA	4	5.7	3.9	1.20	46
DTM	NIPAM	16	2.7	3.3	1.16	36
DTM	Styrene	16	5.1	4.9	1.39	48

Table 2.1: Characterization data previously obtained by O'Reilly and co-workers for a series of RAFT polymerizations of methyl acrylate (MA), *tert*-butyl acrylate (^{t}BuA), triethylene glycol monomethyl ether acrylate (TEGA), *N*-isopropylacrylamide (NIPAM) and styrene with either a MBM-functionalized RAFT agent; a DBM-functionalized RAFT agent or a DTM-functionalized RAFT agent.[44] Key: [a] monomer conversion was calculated by ^{1}H NMR spectroscopy; [b] obtained by SEC analysis. $M_{n,\,theo}$ calculated from conversion.

For instance, the authors obtained low monomer conversions when a MBM-functionalized RAFT agent was selected for the RAFT polymerization of *N*-isopropylacrylamide (NIPAM) and styrene, whilst 100% conversion of the maleimide

C=C double bond was detected instead.[44] Moreover, branched polymers were formed in the presence of acrylate monomers due to RAFT copolymerization of both the vinyl and maleimide C=C double bonds (Table 2.1, entries 1-5).[44]

With respect to the DBM-functionalized RAFT agent, the authors observed complete polymerization retardation for both styrene and NIPAM, whilst acrylate polymerizations only suffered from retardation at high monomer conversions (Table 2.1, entries 6-10).[44] Significantly, the maleimide C=C double bond of the DBM-functionalized RAFT agent remained intact under polymerization conditions unlike the MBM-functionalized RAFT agent.[44]

Finally, RAFT polymerizations in which the DTM-functionalized RAFT was used were found to display linear characteristics with complete retention of DTM functionality (Table 2.1, entries 11-14).[44] However, the authors noted a small amount of polymerization retardation for NIPAM and styrene but this was to a lesser extent in comparison to the analogous RAFT polymerizations using the DBM-functionalized RAFT agent.[44]

In summary, the use of a MBM-functionalized RAFT agent led to a loss of polymerization control with significant deviations of number average molecular weight (M_n) from theoretical values, large dispersities and multimodal molecular weight distributions.[44] The authors attributed these results to the proposed attack of propagating radicals at the relatively unhindered position of the maleimide C=C double bond leading to the formation of a stabilized radical, which in turn continued to either self-propagate or cross-propagate with more monomer.[44] Importantly, out of the three investigated RAFT agents, the authors discovered that the DTM-functionalized RAFT agent offered the best control with RAFT polymerizations proceeding to high conversion in most cases.[44]

In another study conducted within the O'Reilly group, AMs were found to be significantly more emissive than their ABM counterparts.[1] For example, comparison of an ABM and an AM for which both fluorophores were functionalized with butylamine revealed an

increase in fluorescent quantum yield from 38% to 59% with respect to the latter.[1] Despite their enhanced fluorescence properties, it was proposed that an AM would be unsuitable for incorporation into the chemical structure of a RAFT agent due to the presence of a reactive maleimide proton and relatively unhindered maleimide C=C double bond. Therefore, ABM functionalization was selected herein as it was envisaged that similar polymerization control in relation to the DTM-functionalized dual ROP initiator/RAFT agent (Scheme 2.4) may be achieved whilst maintaining an appreciable amount of fluorescence emission for subsequent applications.

As highlighted above, it was essential that the introduction of an ABM fluorophore into the chemical structure of a RAFT agent did not significantly impact subsequent RAFT polymerizations. Consequently, it was envisaged that the utilization of a non-functionalized RAFT agent with a similar chemical structure to that of the R group ABM-functionalized RAFT agent **2ii** would provide a suitable control for comparison. In light of this, 2-cyanopropan-2-yl ethyl carbonotrithioate (CPET) was synthesized in an 81% yield (Scheme 2.5).

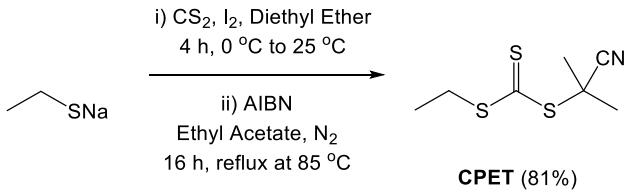

Scheme 2.5: Synthesis of 2-cyanopropan-2-yl ethyl carbonotrithioate (CPET) from sodium ethanethiolate. AIBN = 2,2'-azobisisobutyronitrile.

Importantly, the Z group remained unchanged (CH_3CH_2S) whilst the R group was switched from C(CN)(CH_3)((CH_2)$_3$ABM) to C(CN)(CH_3)$_2$, thereby ensuring that the sole difference between CPET and **2ii** was the addition of *N*-ethyl aminobromomaleimide into the R group structure of **2ii**.

To confirm that the choice of R and Z groups for **2ii** was indeed appropriate for the monomers of interest, an initial kinetic study was conducted for the RAFT copolymerization of a hydrophilic pH-responsive monomer, 2-(dimethyl amino) ethyl methacrylate (DMAEMA), and a permanently hydrophobic monomer, *n*-butyl methacrylate (*n*-BuMA), with CPET as the RAFT agent (Scheme 2.6).

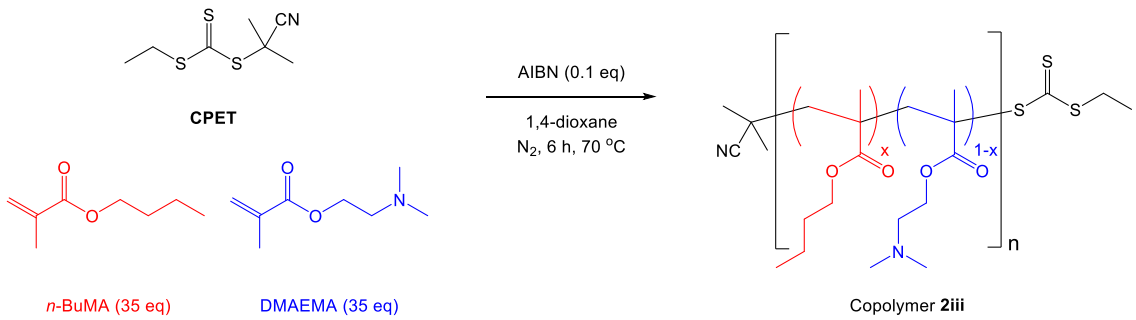

Scheme 2.6: RAFT copolymerization of *n*-BuMA and DMAEMA with 2-cyanopropan-2-yl ethyl carbonotrithioate (CPET) to produce a p(*n*-BuMA$_x$-*co*-DMAEMA$_{1-x}$)$_n$ copolymer (**2iii**).

The RAFT copolymerization was carried out at 70 °C with a total monomer/1,4-dioxane ratio of 1:1 (v/v) to ensure complete monomer dissolution, with 2,2'-azobisisobutyronitrile (AIBN) as the radical initiator and the following stoichiometric ratio of reagents employed: [CPET]/[AIBN]/[DMAEMA]/[*n*-BuMA] = 1:0.1:35:35. Aliquots of the polymerization mixture were taken every 30 min and analyzed *via* ^{1}H NMR spectroscopy and SEC analysis with the RAFT copolymerization quenched after 6 h.

Conversion of both DMAEMA and *n*-BuMA was monitored *via* ^{1}H NMR spectroscopy by comparing: the depleting peak integrals corresponding to the overlapping vinyl resonances for both DMAEMA and *n*-BuMA between 6.07-6.12 ppm and 5.51-5.58 ppm; the depleting peak integral corresponding to the monomer's OC*H*$_2$CH$_2$N resonance at 4.25 ppm; and the peak integral corresponding to the monomer and polymer's OCH$_2$C*H*$_2$N resonance at 2.57 ppm (H3) which was used as a reference (Figure 2.10).

The increasing peak integrals corresponding to the polymer's OCH_2CH_2N and $OCH_2(CH_2)_2CH_3$ resonances at 4.07 and 3.94 ppm (H2 and H1 respectively) overlapped with one another as well as the monomer's $OCH_2(CH_2)_2CH_3$ resonance at 4.14 ppm, and thus could not be used for determination of the monomer conversion. Moreover, an aliquot of the reaction mixture was taken prior to RAFT polymerization to ascertain the actual monomer feed ratio of the two respective comonomers. ^{1}H NMR spectroscopic analysis verified that the RAFT polymerization solution consisted of an equimolar ratio of *n*-BuMA with respect to DMAEMA as targeted.

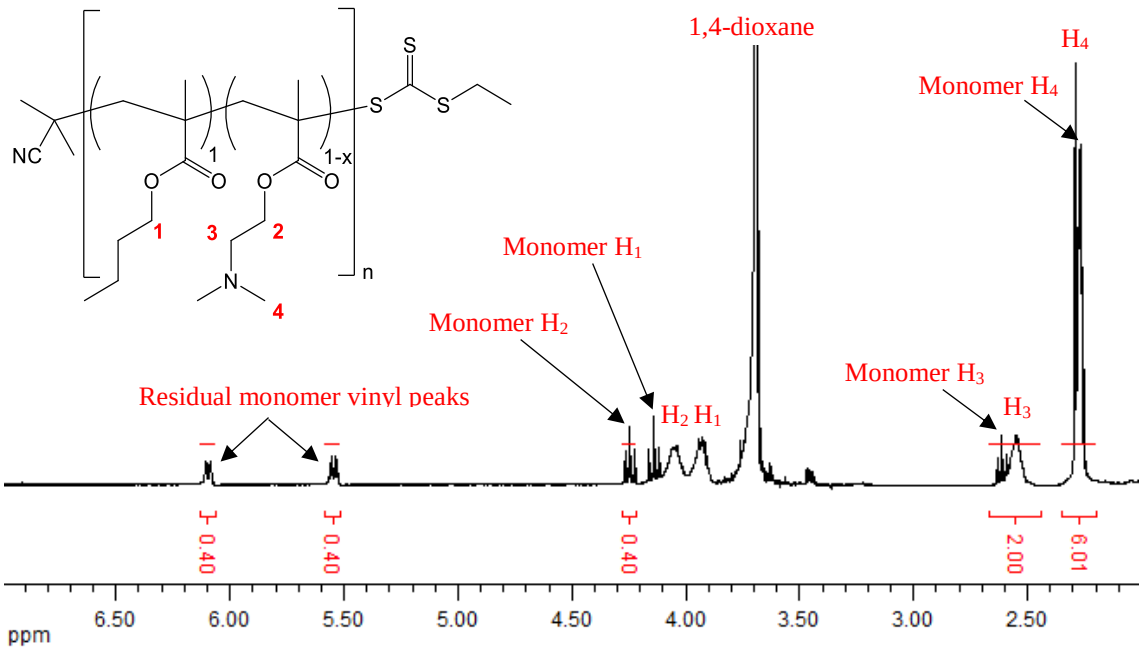

Figure 2.10: Example crude ^{1}H NMR spectrum (300 MHz, $CDCl_3$) of an aliquot taken from the RAFT copolymerization of *n*-BuMA and DMAEMA with CPET. Both DMAEMA and *n*-BuMA conversion was calculated to be 80% for an initial monomer feed ratio of *n*-BuMA:DMAEMA of 1:1.

Overall, the RAFT copolymerization of *n*-BuMA and DMAEMA using CPET proceeded within a reasonable experimental timeframe for a methacrylate copolymerization,[36] with 81% monomer conversion obtained after 6 h. Kinetic analysis confirmed an anticipated

linear increase of molecular weight with conversion coupled with a linear first-order rate plot for $\ln[M]_0/[M]_t$ *versus* time (Figure 2.11 a); thereby demonstrating that this combination of R and Z groups was indeed a suitable choice for the RAFT polymerization of the chosen monomers. An analogous RAFT copolymerization mediated by the R group ABM-functionalized agent **2ii** was also conducted under identical experimental conditions to those used with CPET (Scheme 2.7).

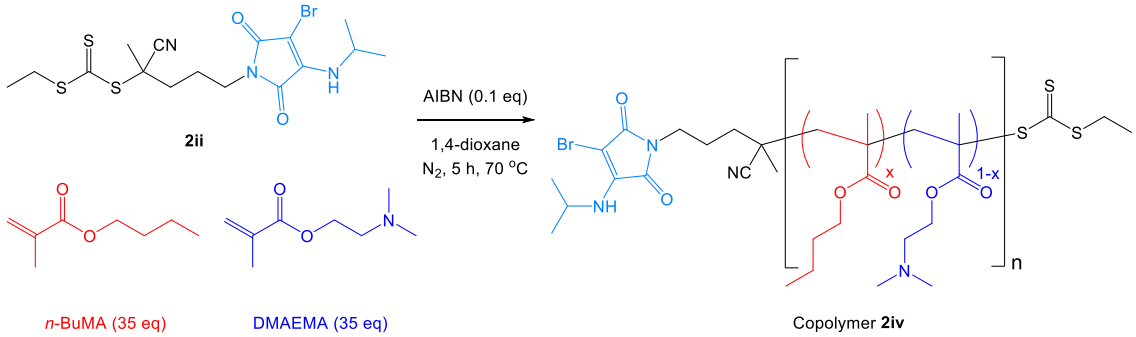

Scheme 2.7: RAFT copolymerization of *n*-BuMA and DMAEMA with the R group ABM-functionalized RAFT agent **2ii** to produce an ABM-functionalized p(*n*-BuMA$_x$-*co*-DMAEMA$_{1-x}$)$_n$ copolymer (**2iv**).

Importantly, RAFT copolymerization using **2ii** was indeed controlled with linear trends displayed for both $\ln[M]_o/[M]_t$ *versus* time and M_n *versus* conversion plots (Figure 2.11 b and c respectively). Both measured and theoretical values of M_n (based on conversion) were in good agreement whilst no significant induction period was observed upon switching the RAFT agent. Interestingly, a small increase in the polymerization kinetics was observed in comparison to those previously measured for CPET, with 82% conversion reached after 5 h for RAFT copolymerization using **2ii**. However, further kinetic repeats are required to confirm that any significant differences observed were due to the introduction of the ABM fluorophore and not from experimental deviations. Finally, no loss of control over the evolution of molecular weight was observed throughout the RAFT copolymerization, with $Đ_M \leq 1.25$ after 2 h (Figure 2.11 d).

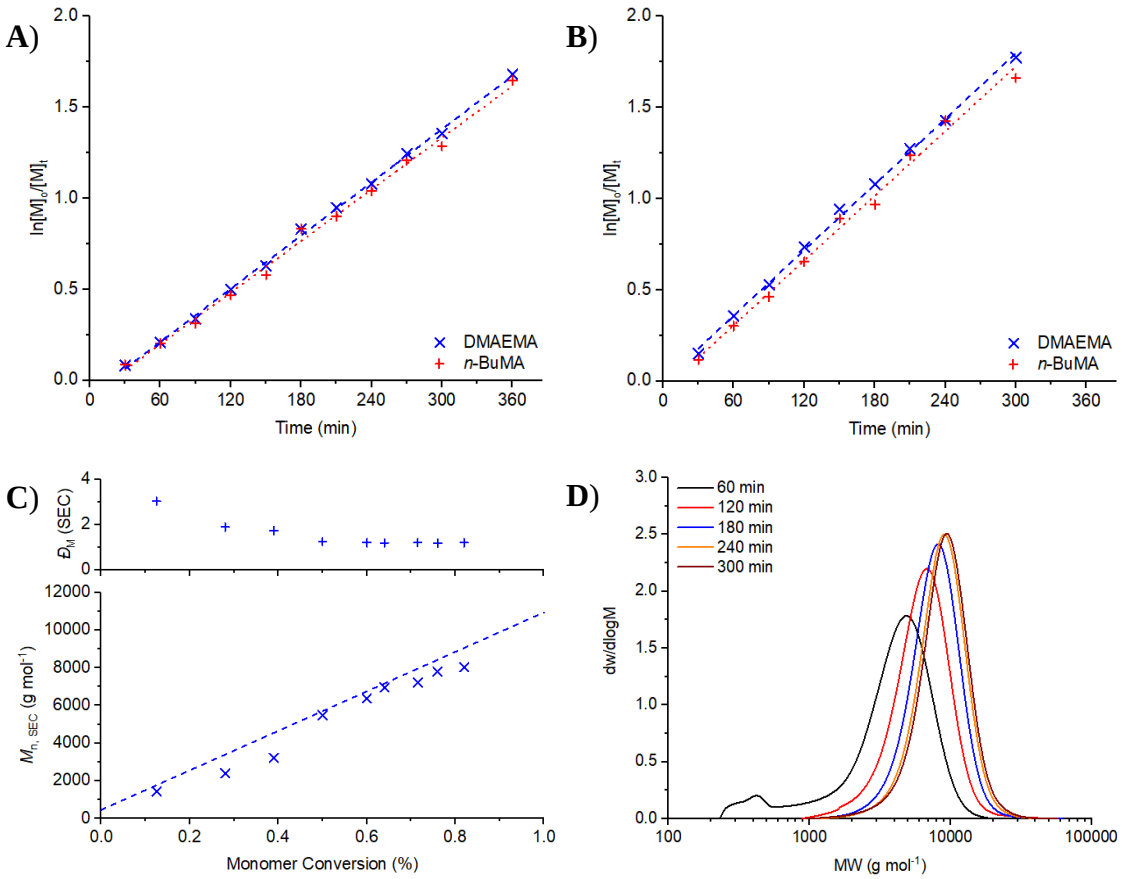

Figure 2.11: a) First order kinetics for the RAFT copolymerization of *n*-BuMA and DMAEMA with CPET as determined by ^{1}H NMR spectroscopy (300 MHz, $CDCl_3$) with linear fits; b) first order kinetics for the RAFT copolymerization of *n*-BuMA and DMAEMA with **2ii** as determined by ^{1}H NMR spectroscopy (300 MHz, $CDCl_3$) with linear fits; c) number average molecular weight (M_n) and $Đ_M$ as a function of monomer conversion with theoretical values (line) for the RAFT copolymerization of *n*-BuMA and DMAEMA with **2ii** (determined by SEC using $CHCl_3$ as the eluent and calibrated against poly(styrene) [p(St)] standards); d) evolution of molecular weight distribution as a function of time for the RAFT copolymerization of *n*-BuMA and DMAEMA with **2ii** (determined by SEC with $CHCl_3$ as the eluent and calibrated against p(St) standards).

Upon purification, two p(*n*-BuMA$_x$-*co*-DMAEMA$_{1-x}$)$_n$ copolymers (**2iii-2iv**) were isolated; characterization data for which is summarized in Table 2.2.

Copolymer	RAFT agent	ρ^a (%)	x^b	n^b	$M_{n,\,NMR}{}^b$ (kDa)	$M_{n,\,SEC}{}^c$ (kDa)	$Đ_M{}^c$
2iii	CPET	71	0.50	50	7.7	5.9	1.22
2iv	**2ii**	75	0.50	52	8.2	7.7	1.20

Table 2.2: Characterization data for p(*n*-BuMA$_x$-*co*-DMAEMA$_{1-x}$)$_n$ copolymers (**2iii**-**2iv**). Key: [a] monomer conversion was calculated by ^{1}H NMR spectroscopy of the crude polymerization mixture (300 MHz, $CDCl_3$); [b] determined by end group analysis using ^{1}H NMR spectroscopy (300 MHz, $CDCl_3$); [c] obtained by SEC analysis based on p(St) standards with $CHCl_3$ as the eluent.

^{1}H NMR spectroscopy (Figure 2.12) was utilized to determine the degree of polymerization (DP) through end group analysis with calculated DP (Table 2.2) in accordance with that expected from monomer conversion (DP = 50 for **2iii** and DP = 52 for **2iv**). Moreover, good agreement between the peak integrals for polymeric proton resonances with respect to the diagnostic trithiocarbonate end group C*H*$_2$S resonance at 3.25 ppm indicated that the ZCS_2 group was appreciably retained for both copolymers (**2iii** and **2iv**). Comparison of the ^{1}H NMR spectra obtained for copolymers **2iii** and **2iv** revealed no significant differences regarding overall copolymer structure, apart from the introduction of the characteristic proton resonances corresponding to the *N*-alkyl ABM group at 5.31, 4.40 and 3.52 ppm (H3, H2 and H4, respectively) for **2iv** (Figure 2.12, bottom).

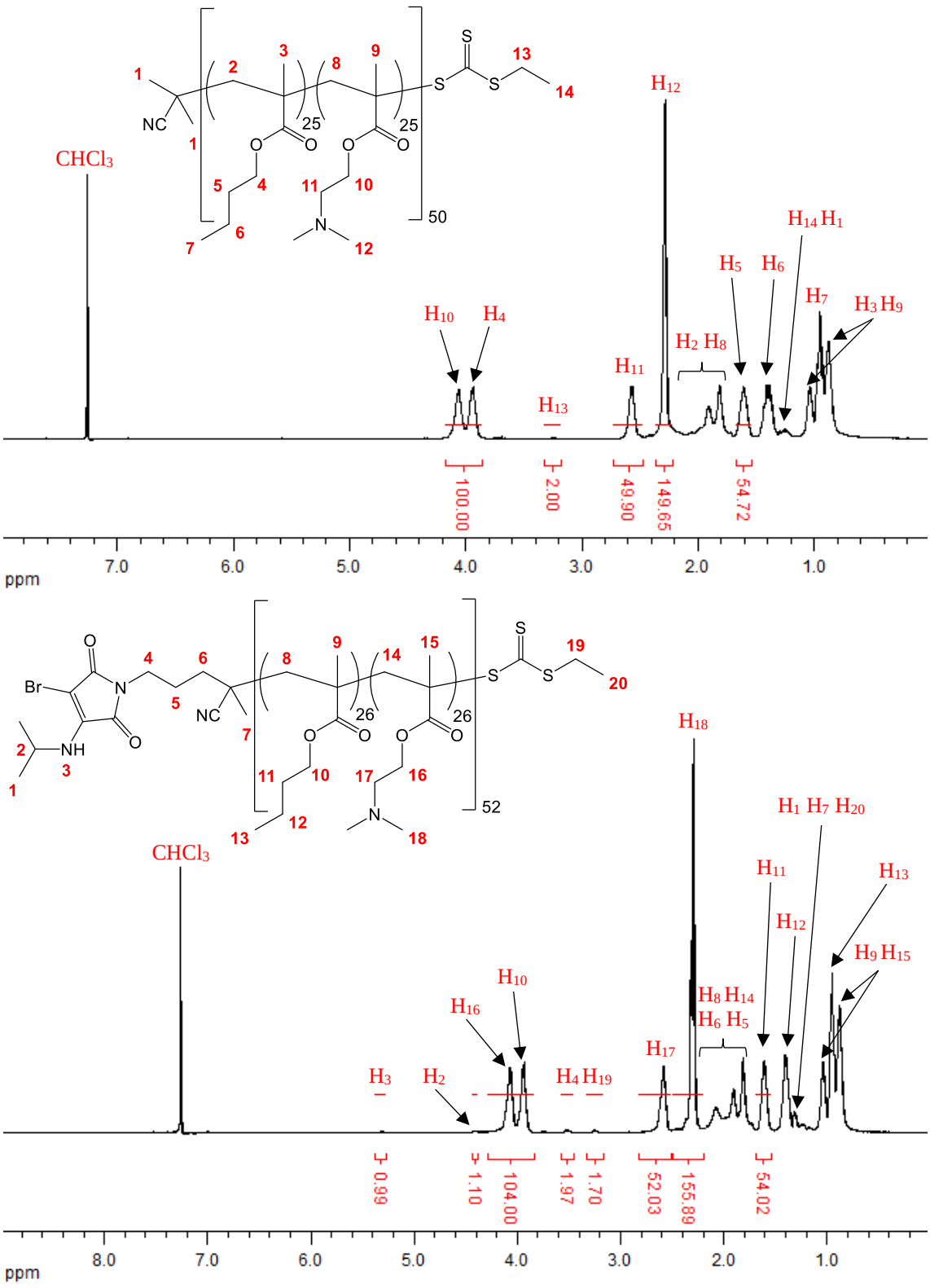

Figure 2.12: ^{1}H NMR spectra for the following p(*n*-BuMA$_{0.5}$-*co*-DMAEMA$_{0.5}$)$_n$ copolymers: **2iii** (top, 300 MHz, $CDCl_3$) and **2iv** (bottom, 400 MHz, $CDCl_3$).

High end group fidelity is essential for the successful synthesis of fluorescent block copolymers *via* RAFT polymerization with an ABM-functionalized RAFT agent. To this

end, the UV-vis absorbance spectrum for the R group ABM-functionalized RAFT agent **2ii** was recorded to determine the corresponding wavelengths at which the trithiocarbonate and ABM functional groups absorb (Figure 2.13).

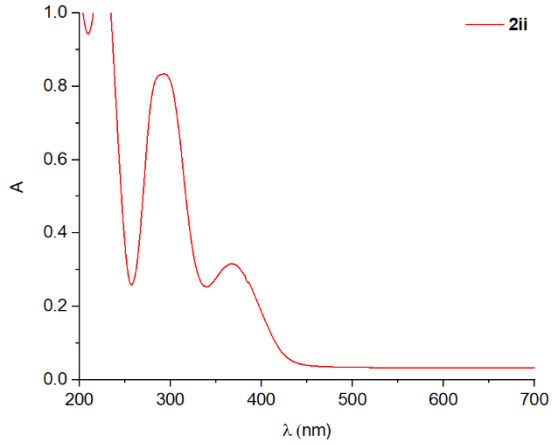

Figure 2.13: Baseline-corrected UV-vis spectrum of **2ii** in acetonitrile at 0.01 mM.

The UV-vis spectrum showed that the R group ABM-functionalized RAFT agent **2ii** had a characteristic $\lambda_{max,\ abs}$ at 294 nm corresponding to the trithiocarbonate group, with a secondary $\lambda_{max,\ abs}$ at 368 nm corresponding to the ABM group, as previously observed for small molecule ABMs.[1]

Retention of both the ABM and trithiocarbonate end groups was further confirmed by SEC analysis of the obtained copolymers using a refractive index (RI) and UV detector recording at 309 nm and 400 nm. As shown in Figure 2.14 b, the RI and UV molecular weight distributions overlay appreciably for copolymer **2iv**; thereby confirming that both α-end and ω-end group functionalities were effectively retained. For comparison, the RI and UV molecular weight distributions obtained for copolymer **2iii** displayed no UV trace at 400 nm as anticipated, whilst retention of the trithiocarbonate group was confirmed by the UV trace recorded at 309 nm (Figure 2.14 a). Importantly, both p(*n*-BuMA$_{0.5}$-*co*-DMAEMA$_{0.5}$)$_n$ copolymers (**2iii** and **2iv**) possessed symmetrical and narrow molecular weight distributions indicating excellent control over the RAFT copolymerization.

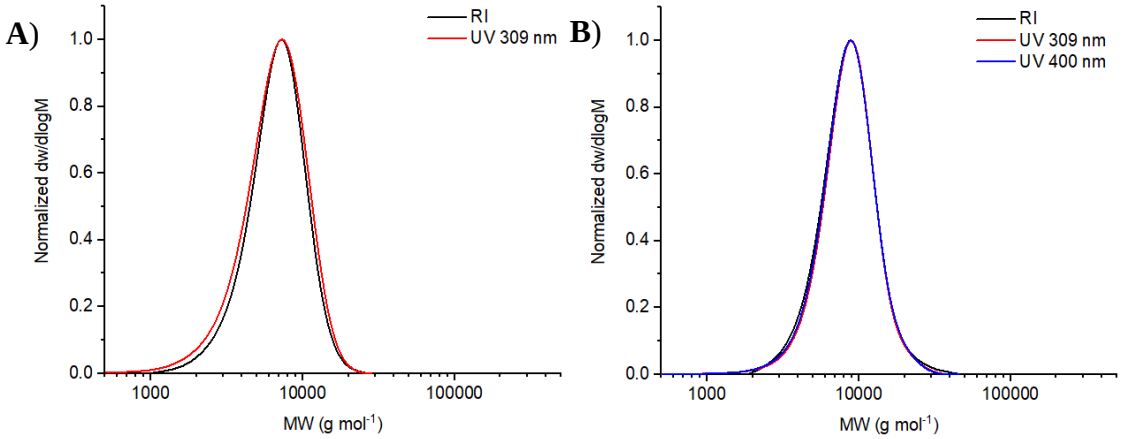

Figure 2.14: Molecular weight distributions determined by SEC ($CHCl_3$ as the eluent and calibrated against p(St) standards) using both an RI and UV (recorded at 309 and 400 nm) detector for the following p(*n*-$BuMA_{0.5}$-*co*-$DMAEMA_{0.5}$)$_n$ copolymers: a) **2iii**; b) **2iv**.

Steady-state fluorescence spectroscopy was next conducted to ascertain the effect the incorporation of an ABM fluorophore into the chemical structure of a RAFT agent had upon resultant fluorescence emission. To this end, the excitation and emission spectra of the R group ABM-functionalized RAFT agent **2ii** were recorded in 1,4-dioxane (Figure 2.15). Significantly, **2ii** was highly fluorescent and the absorption, excitation and emission spectra obtained were in good agreement with the fluorescence spectroscopy data previously recorded for small molecule ABMs.[1] For instance, **2ii** displayed excitation maxima at *ca.* 250 nm and *ca.* 375 nm with both excitation wavelengths resulting in the same emission maximum at *ca.* 482 nm.

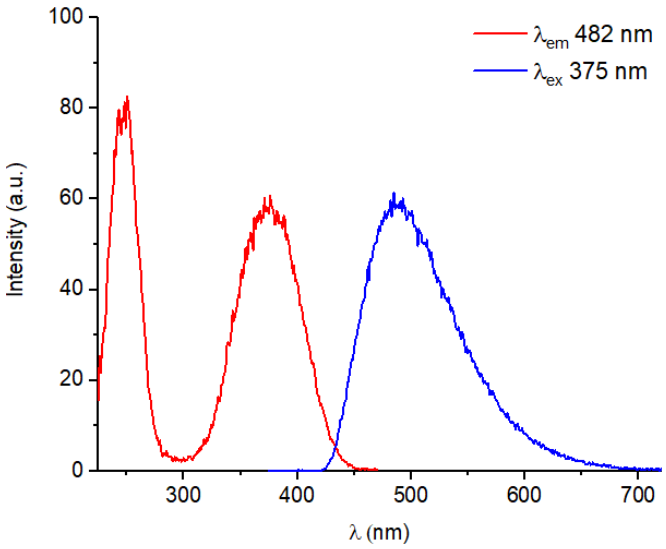

Figure 2.15: Excitation (red) and emission spectra (blue) of **2ii** in 1,4-dioxane at 0.01 mM**.** Excitation and emission were measured at λ_{em} = 482 nm and λ_{ex} = 375 nm respectively.

In conclusion, the successful design and synthesis of a fluorescent R group ABM-functionalized RAFT agent (**2ii**) was achieved. Furthermore, comparison of ^{1}H NMR spectroscopic and SEC data obtained for the RAFT copolymerization of *n*-BuMA and DMAEMA, using either CPET or **2ii**, verified that the choice of R and Z groups was indeed appropriate for the monomers of interest. Moreover, well-defined p(*n*-BuMA$_{0.5}$-*co*-DMAEMA$_{0.5}$)$_n$ copolymers with relatively low dispersities ($Đ_M$ ~ 1.20) were afforded independent of the RAFT agent used; with no inhibition period, polymerization retardation or loss of control observed. Therefore, the utilization of an R group ABM-functionalized RAFT agent to synthesize fluorescent block copolymers in a controlled manner *via* RAFT polymerization was shown to be viable.

2.3.3. Design and synthesis of Z group ABM-functionalized RAFT agents

As discussed in Chapter 1, block copolymer synthesis *via* sequential RAFT polymerization is highly appealing but requires careful consideration of a number of important factors including but not limited to: initiator concentration; α and ω end-group functionality; monomer order addition and RAFT agent selection.[32] Therefore, with regards to the design and synthesis of block copolymers whereby functionality is imparted through modification of the chosen RAFT agent, the precise location of the functional group post-polymerization is of primary concern, particularly for certain applications. As outlined in the introduction to this Chapter ABM fluorophores are highly sensitive to their environment, displaying intense fluorescence emission and high quantum yields in aprotic non-polar solvents, whilst the opposite behavior is observed in protic polar solvents.[1] As a result, it is important to consider the target block copolymer composition as well as the desired application before the optimum location of an ABM fluorophore within the final block copolymer structure can be determined.

In an ideal scenario, the production of a fluorescently-labelled analogue for any given well-defined non-fluorescent block copolymer, previously synthesized *via* RAFT polymerization, would be achieved through the use of an ABM-functionalized RAFT agent. However, the range of fluorescent block copolymers that can be targeted using the R group ABM-functionalized RAFT agent **2ii** is limited due to several constraints. Primarily, the choice of R and Z groups for **2ii** restricts the range of monomers that can be polymerized in a controlled manner to MAMs. Moreover, successful block copolymer synthesis *via* RAFT polymerization requires the correct order of monomer addition, with the latter dictated by the leaving group ability of the respective polymeric analogue of the monomer.[32] Consequently, the order in which the blocks are synthesized is predetermined

for many block copolymer compositions and cannot be changed. Notably, for fluorescent block copolymers synthesized *via* RAFT polymerization using **2ii**, the ABM fluorophore would be expected to be located adjacent to the first block synthesized i.e. α-functionalized polymers. Whilst this may be advantageous for certain block copolymer compositions, the ABM fluorophore may often be situated in a suboptimum position. In light of this, it was envisaged that the design and synthesis of an analogous Z group ABM-functionalized RAFT agent would expand the range of available fluorescent block copolymer compositions *via* ω-end group functionalization.

In Section 2.3.1, attachment of the pro-fluorescent DBM moiety to the R group of a RAFT agent was achieved *via* the Mitsunobu reaction upon reduction of an acid group to the corresponding alcohol. Therefore, an initial desired prerequisite for the Z group was a hydroxyl or acid group to allow for an analogous procedure to be conducted. O'Reilly and co-workers have previously reported a facile and high yielding one-pot synthetic route to produce an extensive range of functional RAFT agents under mild conditions (Scheme 2.8).[45]

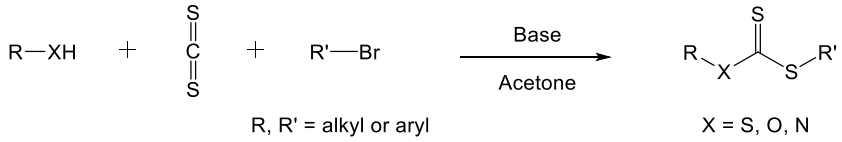

Scheme 2.8: General one-pot strategy for the synthesis of a range of RAFT agents. Figure recreated from ref 45.

Dithiocarbamates, trithiocarbonates and xanthates were successfully synthesized with a variety of functionalities attached to either the R or Z group including acid, hydroxyl, nitrile, phthalimide and benzyl groups. From the numerous RAFT agents produced, benzyl (2-hydroxyethyl) carbonotrithioate (BHET) provided a suitable starting point for the synthesis of a Z group ABM-functionalized RAFT agent owing to its facile synthesis

and more importantly its Z group functionality. Mercaptoethanol provided a Z group with an alkyl chain small enough to minimize the potential impact of the RAFT agent upon block copolymer self-assembly; as well as ensure a long enough spacer between the thiocarbonylthio and DBM groups to reduce any possible effect upon the reactivity of the RAFT agent.

In light of this, BHET was synthesized first following a literature protocol in a 33% yield (Scheme 2.9).[45] Importantly, the hydroxyl group of BHET allowed the successful attachment of the DBM moiety *via* the Mitsunobu reaction following identical experimental conditions to those previously utilized for the synthesis of R group DBM-functionalized RAFT agent **2i** (Scheme 2.2). Subsequent reaction between the pro-fluorescent Z group DBM-functionalized precursor (**2v**) and isopropylamine afforded the desired Z group ABM-functionalized RAFT agent **2vi** in an overall yield of 11% *via* the three step synthetic route (Scheme 2.9).

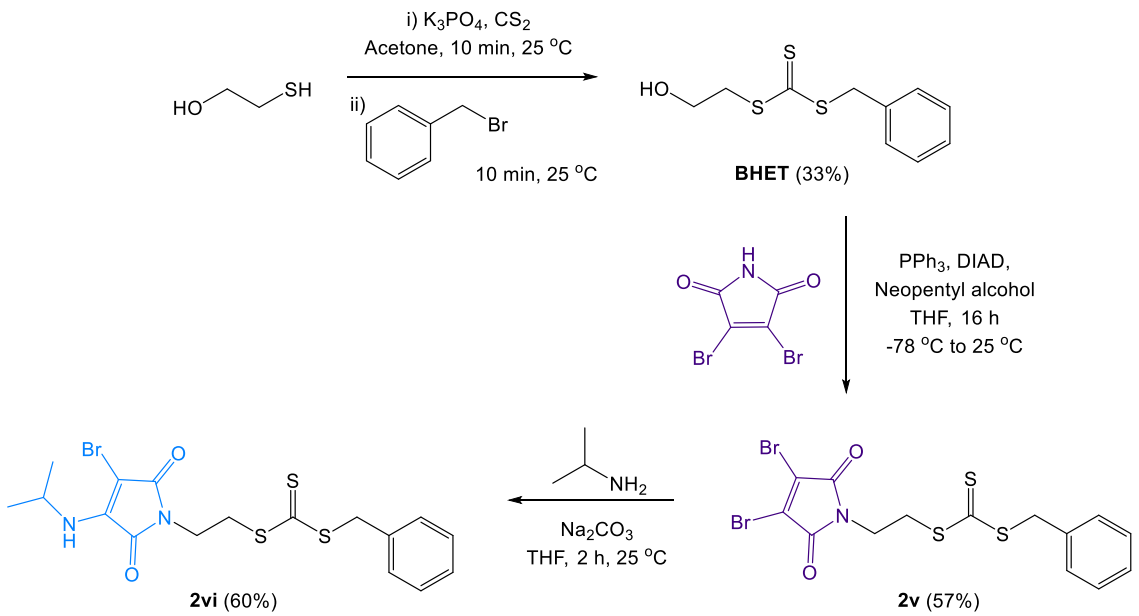

Scheme 2.9: Synthesis of the Z group ABM-functionalized RAFT agent **2vi** *via* the three step synthetic route.

^{13}C NMR spectroscopy of Z group DBM-functionalized RAFT agent **2v** (Figure 2.16, bottom) confirmed that DBM functionalization of BHET was successful with the expected carbon resonances of the DBM group observed at 164.8 and 130.3 ppm (C9 and C10 respectively). Moreover, upon functionalization with isopropylamine, the characteristic carbon resonances of the fluorescent ABM group were found at 168.8, 167.2 and 145.0 ppm (C9, C10 and C12 respectively) in the ^{13}C NMR spectrum of **2vi** (Figure 2.17, bottom).

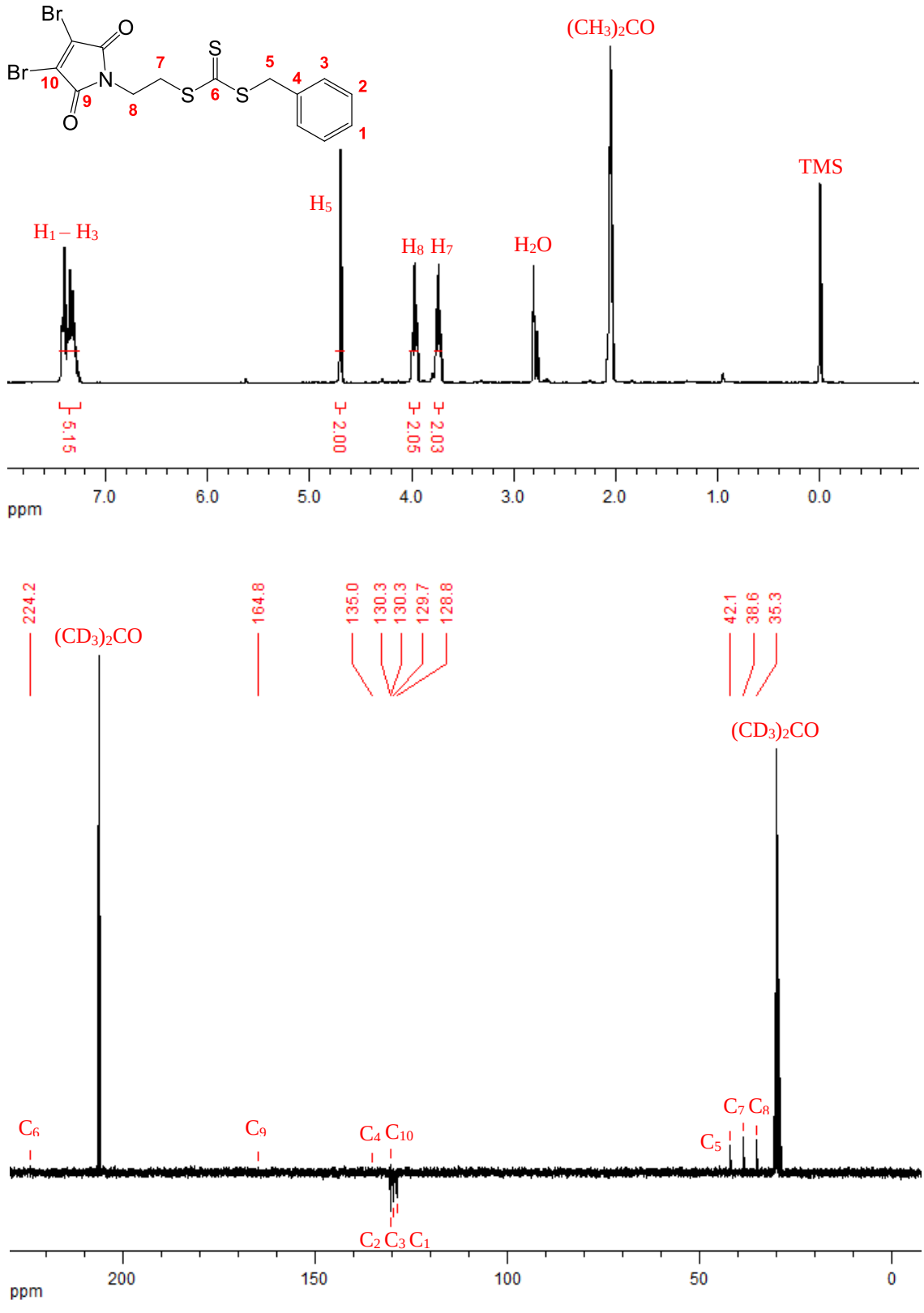

Figure 2.16: ^{1}H NMR (300 MHz, $(CD_3)_2CO$) and ^{13}C NMR (75 MHz, $(CD_3)_2CO$) spectra of the pro-fluorescent Z group DBM functionalized RAFT agent **2v**.

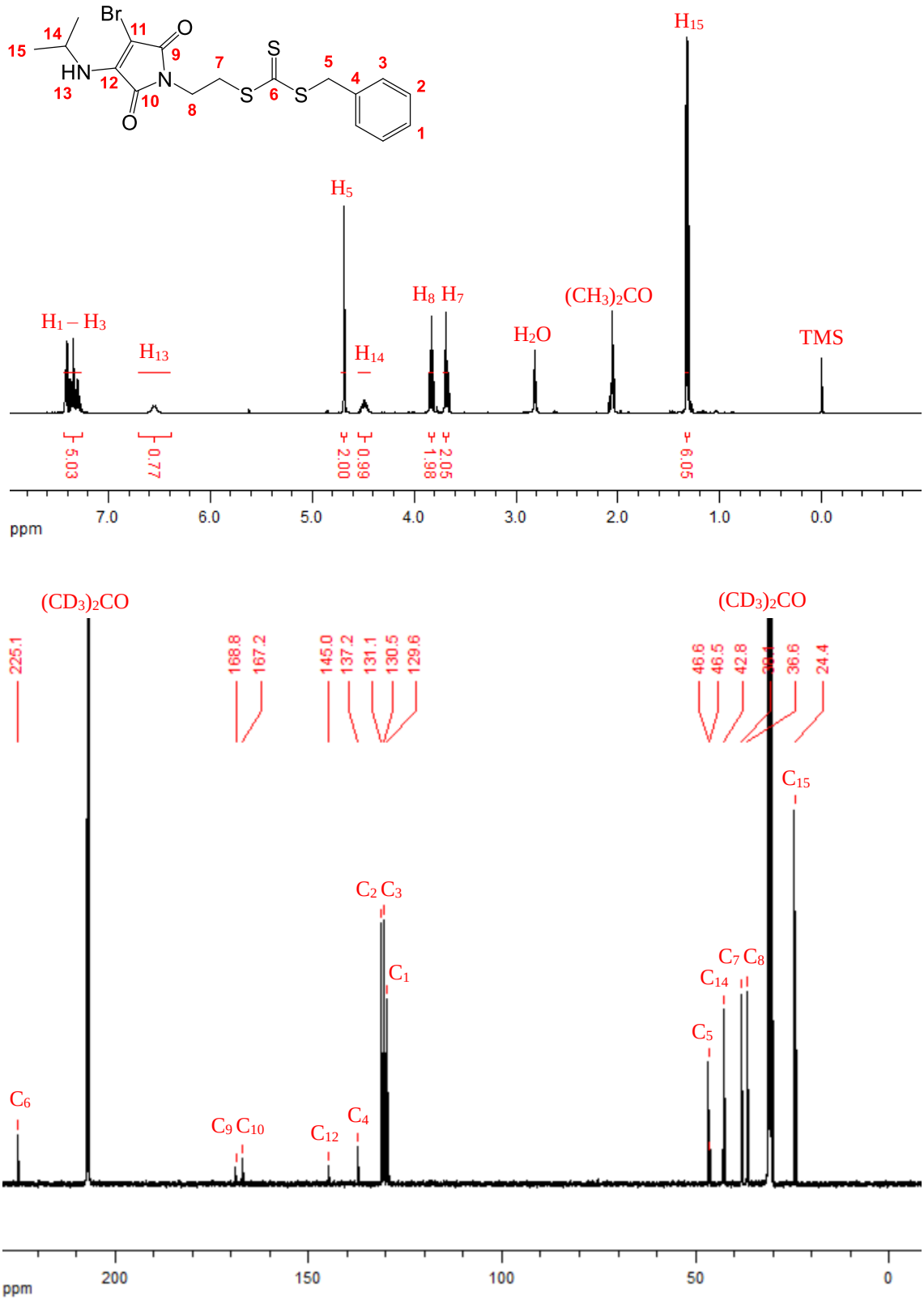

Figure 2.17: ^{1}H NMR (400 MHz, $(CD_3)_2CO$) and ^{13}C NMR (100 MHz, $(CD_3)_2CO$) spectra of the fluorescent Z group ABM-functionalized RAFT agent **2vi**.

Overall, Z group ABM-functionalized RAFT agent **2vi** should facilitate the controlled RAFT polymerization of acrylate, acrylamide and styrenic monomers to produce ω-functionalized fluorescent block copolymers. However, **2vi** is relatively limited in monomer scope in comparison to the R group ABM-functionalized RAFT agent **2ii** and thus a change in R group selection was considered to expand the range of polymerizable monomers to include methacrylates and methacrylamides. In Section 2.3.2, RAFT agents CPET and **2ii** successfully facilitated the controlled RAFT copolymerization of two methacrylate monomers to produce well-defined, low disperse copolymers. Therefore, switching the R group of the Z group ABM-functionalized RAFT agent **2vi** from benzyl to either isobutyronitrile or 4-cyanopentanoic acid should permit a similar extent of polymerization control to be achieved.

As detailed in Section 2.3.1, tertiary R groups such as $C(CN)(CH_3)_2$ and $C(CN)(CH_3)(CH_2CH_2COOH)$ are typically introduced into the RAFT agent structure *via* a thermally-initiated radical reaction between the corresponding azo initiator (in this case AIBN or ACVA) and a bis-(alkylsulfanylthiocarbonyl) disulfide intermediate. However, attempts to synthesize a di-functionalized bis-(alkylsulfanylthiocarbonyl) disulfide intermediate using either 2-mercaptoethanol or 3-mercaptopropionic acid, using the same experimental procedure utilized for the synthesis of both CPET and CETPA, proved to be unsuccessful, with no evidence of trithiocarbonate formation present in the crude ^{13}C NMR spectra (Scheme 2.10 a and b respectively). The desired product was not isolated in both cases which suggested the presence of an unwanted side reaction of the pendant hydroxyl or carboxylic acid functionality in the presence of iodine, thereby preventing the formation of the desired disulfide-bridged intermediate.

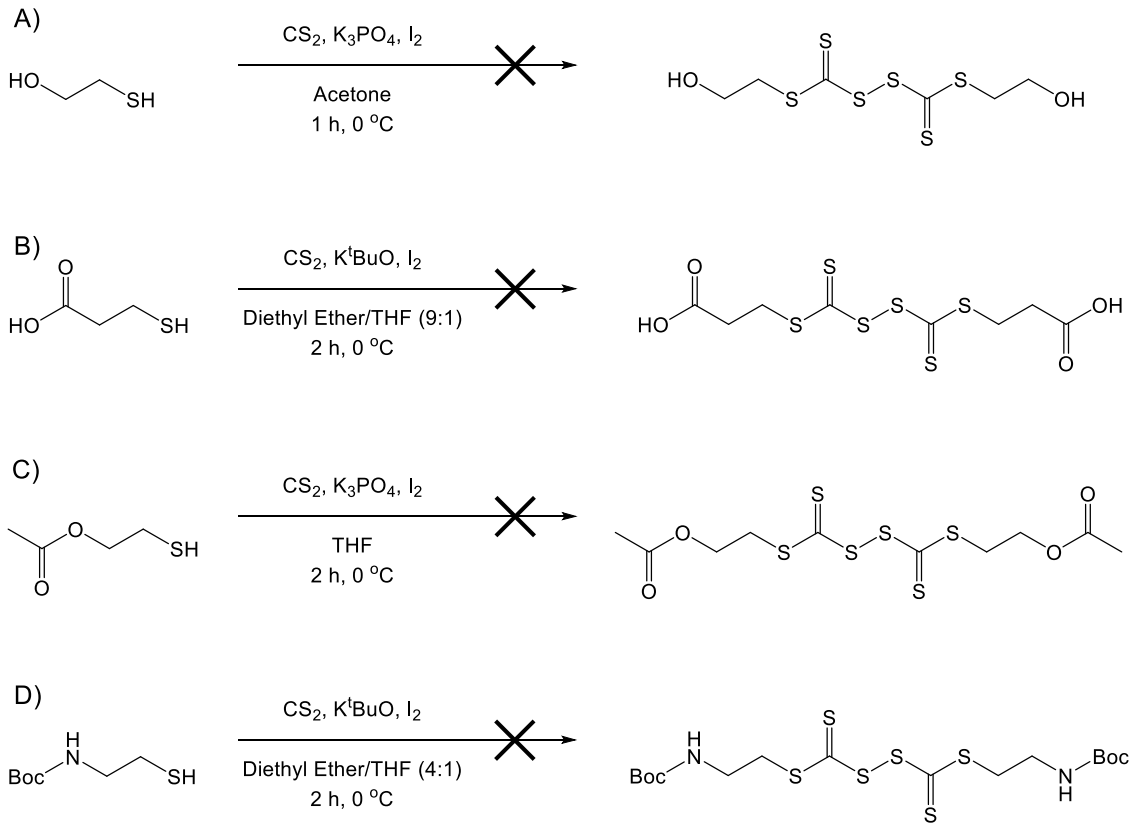

Scheme 2.10: Attempted syntheses of di-functionalized bis-(alkylsulfanylthiocarbonyl) disulfide intermediates using the following thiols: a) 2-mercaptoethanol; b) 3-mercaptopropionic acid; c) 2-mercaptoethyl acetate; and d) 2-(Boc-amino)ethanethiol.

Following this, the hydroxyl group of 2-mercaptoethanol was selectively acetylated to afford 2-mercaptoethyl acetate in a 47% yield following a literature procedure.[46] It was envisaged that selective protection of the reactive hydroxyl group of 2-mercaptoethanol may prevent any unwanted side reactions from occurring. However, the reaction of 2-mercaptoethyl acetate with carbon disulfide and iodine (Scheme 2.10 c) to form the corresponding disulfide-bridged intermediate was unsuccessful; with ^{13}C NMR spectroscopic analysis of the crude product confirming the absence of a trithiocarbonate group. Next, 2-(Boc-amino)ethane thiol was chosen as it was envisaged that subsequent deprotection of the Boc group would result in the corresponding primary amine that could then be reacted with DBM. Unfortunately, the isolation of the disulfide-bridged

intermediate using 2-(Boc-amino)ethane thiol was also unsuccessful (Scheme 2.10 d), and thus alternative synthetic routes were explored.

Previously, Haddleton and co-workers successfully synthesized *N*-propargyl DBM *via* the reaction of DBM and propargyl bromide in a 37% yield.[6] Considering this, a new synthetic approach was proposed whereby the introduction of the DBM moiety into the chemical structure of the RAFT agent would be achieved *via* a similar substitution reaction. First, the reaction of 3-chloro-1-propanethiol with carbon disulfide and iodine produced the Z group chloro-functionalized RAFT agent **2vii** in a 55% yield (Scheme 2.11). Similar experimental conditions were employed to those previously utilized for the synthesis of CETPA, with the addition of iodine after 10 min instead of 1 h to prevent anionic polymerization of the thiocarbonylthio salt intermediate *via* intramolecular nucleophilic attack.

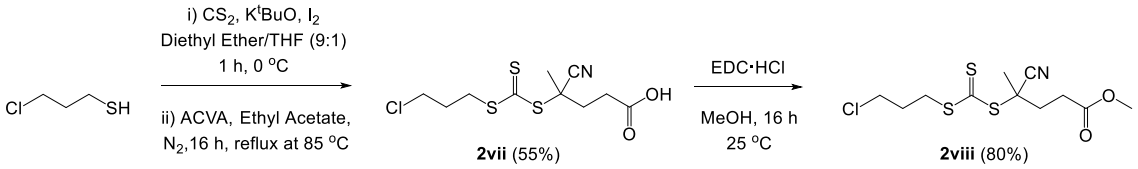

Scheme 2.11: Synthesis of the Z group chloro-functionalized RAFT agent **2vii** and the corresponding methylated ester analogue **2viii**.

To ensure that the substitution reaction of the terminal chloride group of **2vii** with DBM was preferred over deprotonation of the pendant carboxylic acid group, the methylated ester analogue (**2viii**) of **2vii** was synthesized in an 80% yield *via* an EDC·HCl/DMAP catalyzed coupling reaction (Scheme 2.11). Subsequently, a series of substitution reactions of **2viii** with DBM were attempted with a range of bases of varying strength, including K_2CO_3, Cs_2CO_3, 4-methylmorpholine (NMM), and sodium hydride (Scheme 2.12). Unfortunately, no substitution of the chloride group was observed *via* ^{1}H and ^{13}C NMR spectroscopic analysis of the crude reaction mixture, with starting material **2viii**

isolated in each case upon work-up. Thus, it was rationalized that one potential reason for the failed syntheses was that the relative leaving group ability of the chloride group was too poor for the substitution reaction to succeed.

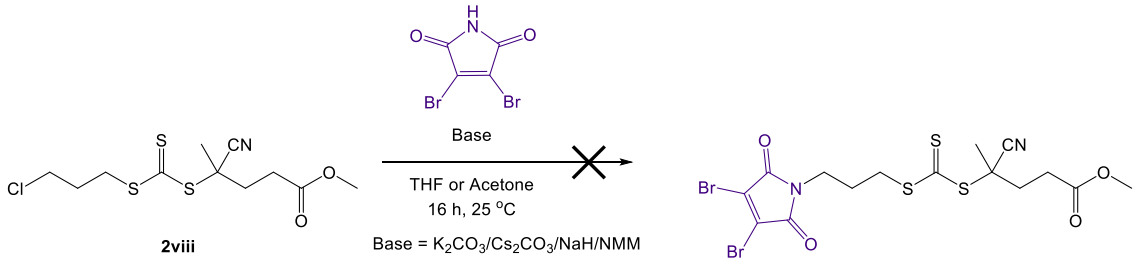

Scheme 2.12: Attempted synthesis of a Z group DBM-functionalized RAFT agent *via* the substitution reaction between Z group chloro-functionalized RAFT agent **2viii** and DBM.

Consequently, the introduction of alternative functionalities which would provide a better leaving group at the Z group terminus of **2viii** was explored. One such example involved the Finkelstein reaction which has been previously utilized in the literature for the successful halogen exchange of a chloride group with an iodide group.[47] Unfortunately, the corresponding synthetic attempt using the Z group chloro-functionalized RAFT agent **2viii** proved to be unsuccessful, with no formation of the desired product observed upon ^{1}H NMR spectroscopic analysis (Scheme 2.13 a). Finally, conversion of the chloride group into a more reactive functionality was also investigated, but these reactions either led to isolation of the starting materials or degradation of the trithiocarbonate group. For instance, the addition of sodium azide to **2viii** resulted in complete loss of the thiocarbonylthio moiety *via* nucleophilic attack within 1 h (Scheme 2.13 b).

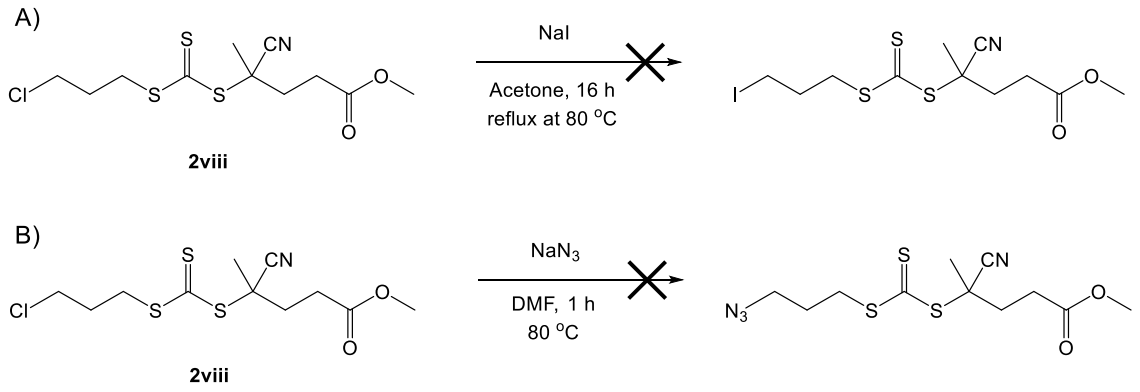

Scheme 2.13: a) Attempted Finkelstein reaction of the Z group chloro-functionalized RAFT agent **2viii** with NaI in acetone. b) Attempted synthesis of a Z group azido-functionalized RAFT agent by the reaction of the Z group chloro-functionalized RAFT agent **2viii** with NaN_3 in dimethylformamide (DMF).

Following these failed syntheses, it was proposed that the use of a stronger nucleophile in comparison to DBM may enable the successful substitution reaction of the terminal chloride group of **2viii** to produce the desired Z group ABM-functionalized RAFT agent. Consequently, *N*-hydroxyethyl ABM (**2xi**) was designed and afforded *via* the three step synthetic route in an overall yield of 20% (Scheme 2.14). Initially, ring closure of 2,3-dibromomaleic acid with ethanolamine produced acetylated *N*-hydroxyethyl DBM (**2ix**). Functionalization of **2ix** with isopropylamine afforded the corresponding fluorescent ABM analogue (**2x**). Subsequent deprotection of **2x** in methanol under basic conditions produced the target hydroxyl-functionalized ABM (**2xi**).

Next, the reaction of *N*-hydroxyethyl ABM (**2xi**) with the Z group chloro-functionalized RAFT agent **2viii** was tested under a variety of basic conditions with or without a KI catalyst (Scheme 2.15). However, upon purification no formation of the desired product was observed in each case, with the degradation of *N*-hydroxyethyl ABM (**2xi**) occurring over prolonged reaction times as indicated by ^{1}H NMR spectroscopic analysis.

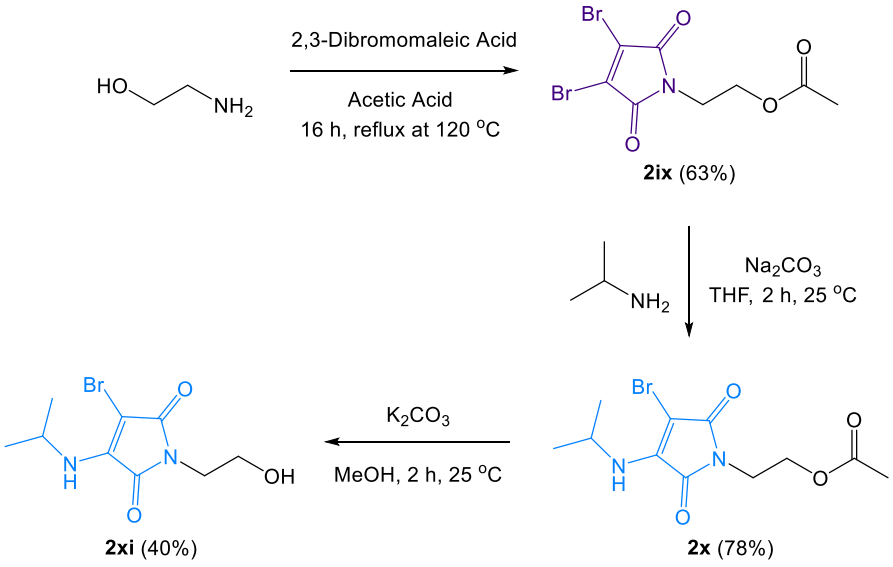

Scheme 2.14: Synthesis of *N*-hydroxyethyl ABM (**2xi**) from ethanolamine *via* the three step synthetic route.

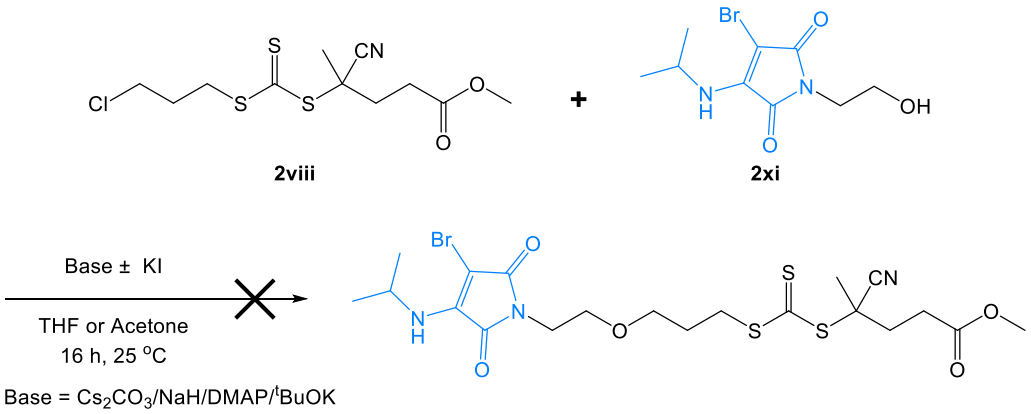

Scheme 2.15: Attempted synthesis of a Z group ABM-functionalized RAFT agent *via* a substitution reaction between the Z group chloro-functionalized RAFT agent **2viii** and *N*-hydroxyethyl ABM **2xi**.

At this point, the utilization of a protected functionalized thiol to synthesize a di-functionalized bis-(alkylsulfanylthiocarbonyl) disulfide intermediate was revisited. Carboxylic acid protecting group chemistry is extremely versatile with a wide array of protecting groups to select from, including methyl esters, benzyl esters, *tert*-butyl esters, silyl esters, orthoesters and oxazolines.[48] Mercaptopropionic acid was chosen owing to its dual functionality and relatively short alkyl chain between the carboxylic acid and thiol functionalities. With regards to carboxyl protection of the former, it was important to

select a protecting group and corresponding experimental conditions that facilitated the chemoselective protection of the carboxylic acid group whilst leaving the thiol moiety unprotected. Moreover, the chosen protecting group needed to be stable under oxidative conditions (iodine addition) as well as to undergo efficient deprotection without resulting in the degradation of the trithiocarbonate moiety.

Benzyl protection offered the most suitable option with respect to the formerly outlined prerequisites. Subsequent esterification of 3-mercaptopropionic acid was performed using an excess of benzyl alcohol and 0.2 equivalents of *p*-toluenesulfonic acid to afford benzyl 3-mercaptopropanoate (**2xii**) in a 58% yield (Scheme 2.16). Importantly, the synthesis of the corresponding disulfide-bridged intermediate of **2xii** was successful, which indicated that benzyl protection of the carboxylic acid functionality prevented any unwanted side reactions which had plagued previous synthetic attempts (Scheme 2.10). With regards to R group selection, isobutyronitrile was preferred over 4-cyanopentanoic acid to avoid the formation of a dual acid-functionalized RAFT agent upon carboxyl deprotection. Synthesis of the latter would become problematic with regards to subsequent functionalization with DBM as the resultant RAFT agent would consist of two pro-fluorescent groups instead of one. Therefore, AIBN was used as the azo initiator for the thermally-initiated radical reaction with the protected dicarboxyl bis-(alkylsulfanylthiocarbonyl) disulfide intermediate to produce the desired benzyl protected Z group acid-functionalized RAFT agent **2xiii** in a 24% yield (Scheme 2.16).

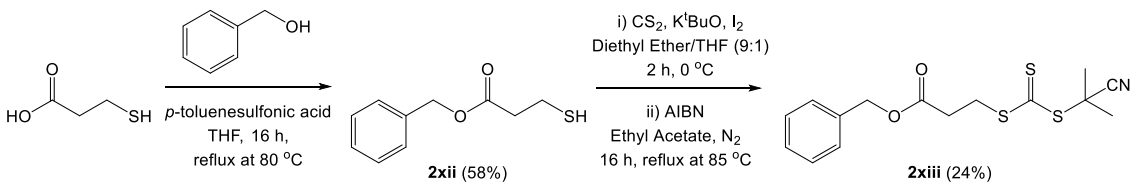

Scheme 2.16: Synthesis of the benzyl protected Z group acid-functionalized RAFT agent **2xiii**.

Next, a number of deprotection strategies were investigated to determine the optimum experimental conditions for the removal of the benzyl group (Table 2.3). Initially, hydrogenation of **2xiii** using a Pd/C catalyst was attempted in both methanol and THF. However, ^{1}H and ^{13}C NMR spectroscopic analysis of the crude reaction mixtures indicated the unsuccessful deprotection of the starting material **2xiii** (Table 2.3, entries 1-2). Following these failed syntheses, two catalytic transfer hydrogenation reactions were also tested using either formic acid,[49] or 1,4-cyclohexadiene,[50] as the hydrogen source but in both cases the starting material was isolated upon work-up (Table 2.3, entries 3 and 4 respectively). Palladium acetate has been previously utilized in the literature for the *in situ* generation of an active Pd/C catalyst with subsequent hydrogenolysis of benzyl esters achieved.[51] However, no conversion to the carboxylic acid was observed upon ^{1}H NMR spectroscopic analysis for an analogous reaction with **2xiii** (Table 2.3, entry 5). Consequently, it was proposed that the presence of the trithiocarbonate group in **2xiii** poisoned and deactivated the Pd/C catalyst and thus prevented successful benzyl deprotection *via* this method.

An alternative benzyl deprotection strategy is the use of a Lewis acid with several successful examples reported in the literature, including nickel boride,[52] aluminum chloride,[53,54] and tin chloride.[55] Unfortunately, the majority of subsequent deprotections using a Lewis acid resulted in complete degradation of the thiocarbonylthio moiety (Table 2.3, entries 6-8).

Entry	Reagents	Experimental Conditions	Yield (%)	Ref.
1	Pd/C (10 wt%)	H_2 atm in THF, r.t.	0	-
2	Pd/C (10 wt%)	H_2 atm in MeOH, r.t.	0	-
3	Pd/C (100 wt%) + 5% Formic acid	MeOH, r.t.	0	49
4	Pd/C (100 wt%) + 1,4-cyclohexadiene (10 eq.)	EtOH, r.t.	0	50
5	Pd/C + $Pd(OAc)_2$ (90:10 wt%)	H_2 atm in dry THF, r.t.	0	51
6	$NiCl_2.6H_2O$ (3 eq.) + $NaBH_4$ (9 eq.)	MeOH, r.t.	0	52
7	$AlCl_3$ (3 eq.) + Anisole (6 eq.)	CH_2Cl_2, r.t.	0	53
8	$SnCl_4$ (0.5 eq.)	Dry CH_2Cl_2, 40 °C	0	55
9	$AlCl_3$ (5 eq.) + *N*,*N*-Dimethylaniline (5 eq.)	CH_2Cl_2, r.t.	33	54

Table 2.3: Experimental conditions and isolated yields for a series of benzyl deprotection reactions to afford the Z group acid-functionalized RAFT agent **2xiv** from the benzyl protected precursor (**2xiii**).

Significantly, the use of aluminium trichloride in the presence of *N*,*N*-dimethylaniline facilitated the successful benzyl deprotection of **2xiii** with retention of the trithiocarbonate group (Table 2.3, entry 9). Upon purification, the desired Z group acid-functionalized RAFT agent **2xiv** was obtained in a 33% yield (Scheme 2.17).

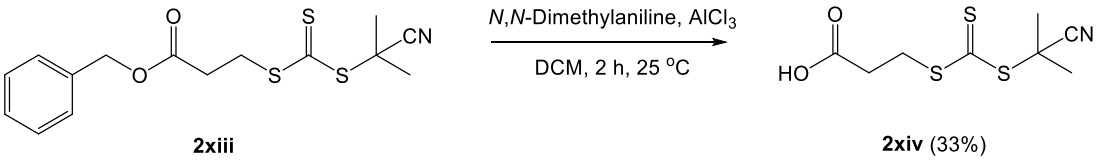

2xiii **2xiv** (33%)

Scheme 2.17: Successful benzyl deprotection of **2viii** to produce the Z group acid-functionalized RAFT agent **2xiv** using aluminium trichloride and *N*,*N*-dimethylaniline.

As detailed in Scheme 2.18, the final three reactions were conducted following identical experimental protocols to those previously utilized for the synthesis of the R group ABM-functionalized RAFT agent **2ii**. Reduction of the Z group acid-functionalized RAFT agent **2xiv** to the corresponding hydroxyl-functionalized counterpart (**2xv**) was

achieved using the borane-Lewis base complex BH_3·THF. Subsequent attachment of the pro-fluorescent DBM moiety *via* the Mitsunobu reaction produced the Z group DBM-functionalized RAFT agent **2xvi** in a 67% yield. Finally, the desired Z group ABM-functionalized RAFT agent **2xvii** was isolated in a 65% yield upon addition of isopropylamine to **2xvi**, with **2xvii** being obtained in an overall yield of 0.5% *via* a six step synthetic route.

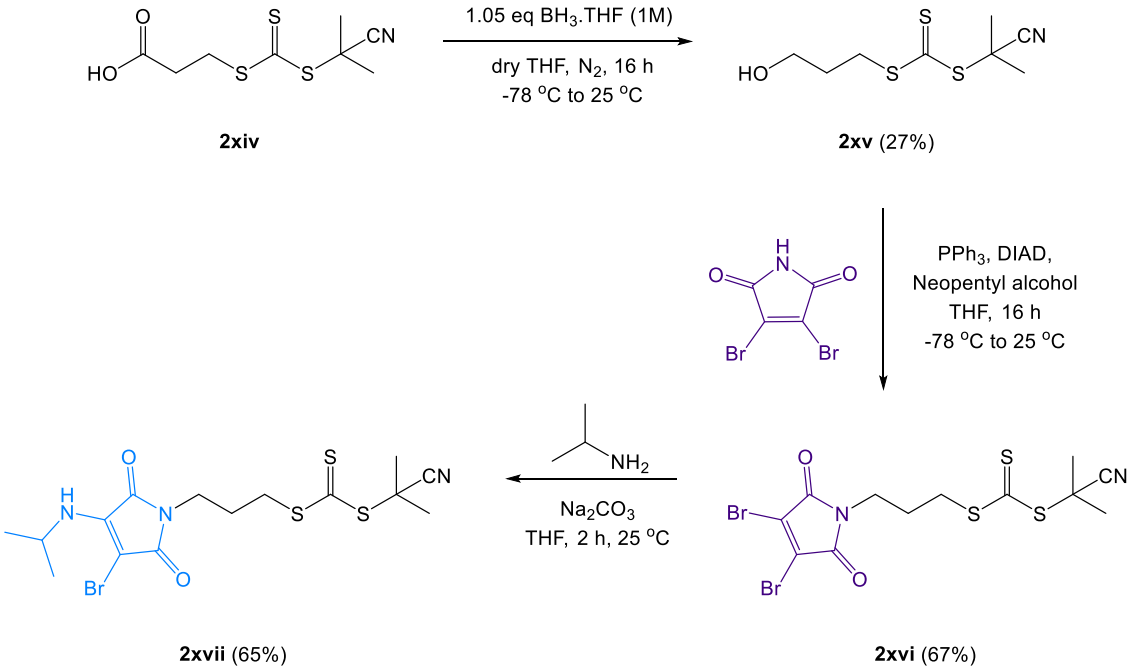

Scheme 2.18: Synthesis of the Z group ABM-functionalized RAFT agent **2xvii** whereby the R group is isobutyronitrile and the Z group is *N*-mercaptopropyl ABM.

To date, there are no literature reports for the successful synthesis of **2xiv** and **2xv** and thus the synthetic route discovered herein expands the range of functionalized RAFT agents available for the design and synthesis of ω-functionalized block copolymers composed of methacrylate and/or methacrylamide monomers. Ultimately, the Z group ABM-functionalized RAFT agent **2xvii** should facilitate the controlled RAFT polymerization of (meth)acrylate, (meth)acrylamide and styrenic monomers to produce

ω-functionalized fluorescent block copolymers, thereby matching its respective R group ABM-functionalized counterpart **2ii**.

2.3.4. RAFT polymerization utilizing a Z group ABM-functionalized RAFT agent

As discussed previously in Section 2.3.2, it was important that incorporation of the ABM fluorophore into the chemical structure of a RAFT agent did not result in a loss in polymerization control. Consequently, it was proposed that a similar kinetic study for the Z group ABM-functionalized RAFT agent **2vi** to the one conducted for the R group ABM-functionalized RAFT agent **2ii** (Section 2.3.2) would confirm whether Z group functionalization had a detrimental impact upon subsequent RAFT polymerizations. To this end, RAFT homopolymerization of *N*,*N*-dimethylacrylamide (DMAc) was conducted in 1,4-dioxane at 70 °C with either BHET or **2vi** as the chosen RAFT agent (Scheme 2.19).

Note, that the sole difference between RAFT agents BHET and **2vi** was the replacement of the hydroxyl group in the Z group structure of BHET with an ABM for **2vi**. Moreover, DMAc was selected to ascertain whether the choice of R and Z groups for **2vi** would enable the production of well-defined ω-functionalized fluorescent polymers *via* RAFT polymerization of acrylate, acrylamide and/or styrenic monomers. In this case, aliquots of the polymerization mixtures were taken every 10 minutes and analyzed *via* ^{1}H NMR spectroscopy and SEC analysis, with both RAFT homopolymerizations quenched within 2 hours. Upon purification, two p(DMAc)$_n$ homopolymers (**2xviii-2xix**) were isolated; characterization data for which is summarized in Table 2.4.

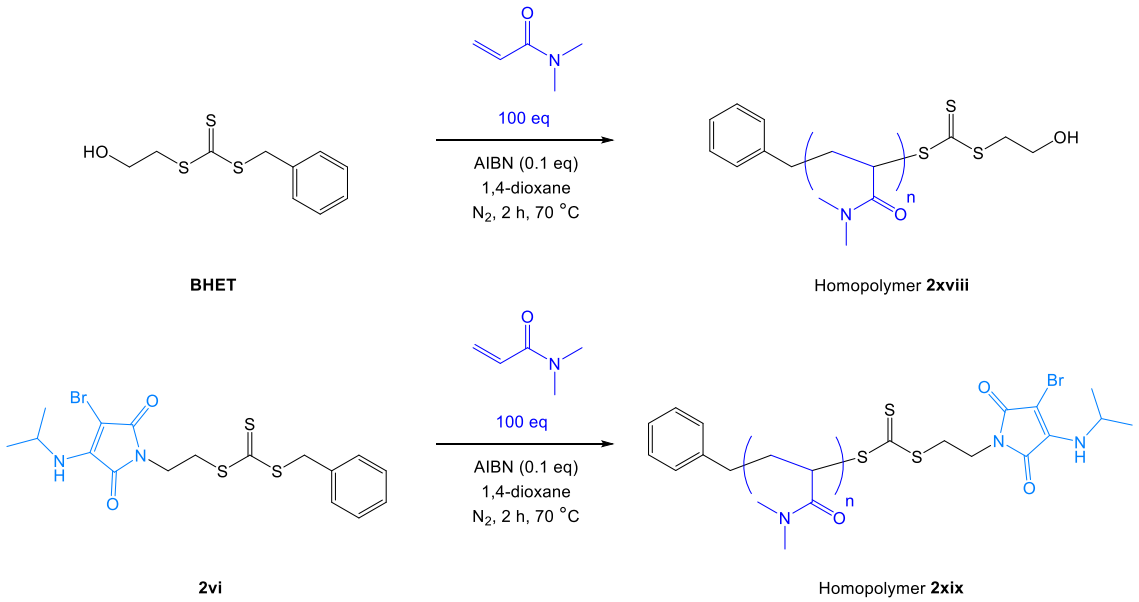

Scheme 2.19: RAFT homopolymerization of DMAc with either benzyl (2-hydroxyethyl) carbonotrithioate (BHET) or the Z group ABM-functionalized RAFT agent **2vi** to produce two p(DMAc)$_n$ homopolymers (**2xviii-2xix**).

Homopolymer	RAFT agent	Time (min)	ρ^a (%)	n^b	$M_{n,\,NMR}{}^b$ (kDa)	$M_{n,\,SEC}{}^c$ (kDa)	$Đ_M{}^c$
2xviii	BHET	70	89	89	9.1	8.5	1.11
2xix	**2vi**	100	69	69	7.3	6.7	1.15

Table 2.4: Characterization data for p(DMAc)$_n$ homopolymers (**2xviii-2xix**). Key: [a] monomer conversion was calculated by ^{1}H NMR spectroscopy of the crude polymerization mixture (300 MHz, $CDCl_3$); [b] determined by end group analysis using ^{1}H NMR spectroscopy (300 MHz, $CDCl_3$); [c] obtained by SEC analysis based on p(St) standards with $CHCl_3$ as the eluent.

Kinetic analysis of the DMAc homopolymerization using **2vi** revealed a linear increase of molecular weight with respect to monomer conversion, with good agreement between measured and theoretical values of M_n (Figure 2.18 b). However, whilst linear first-order rate plots were obtained for both RAFT homopolymerizations (Figure 2.18 a), a significant induction period of 45 min was observed for **2vi** whereas for BHET the induction period was only 15 min. Moreover, a pronounced reduction in polymerization

rate was measured for **2vi** in comparison to BHET, with only 69% conversion reached after 100 min when **2vi** was used whilst DMAc conversion reached 89% after 70 min when BHET was employed. As a result, a slight deviation from ideal RAFT polymerization kinetics was observed upon the introduction of the ABM fluorophore into the Z group structure of **2vi** which could be attributed to the C=S bond of the thiocarbonylthio moiety becoming less electrophilic and more deactivated towards radical addition due to induction effects from the electron rich N of the ABM fluorophore. However, as was the case with the R group ABM-functionalized agent **2ii**, further kinetic experiments are needed to confirm that the significant difference in polymerization rate was not from experimental deviations but primarily due to the introduction of the ABM fluorophore. Despite the decrease in polymerization kinetics, no loss in control over the evolution of molecular weight was observed throughout the RAFT homopolymerization of DMAc using **2vi**, with $Đ_M \leq 1.16$ after 60 minutes (Figure 2.18 c).

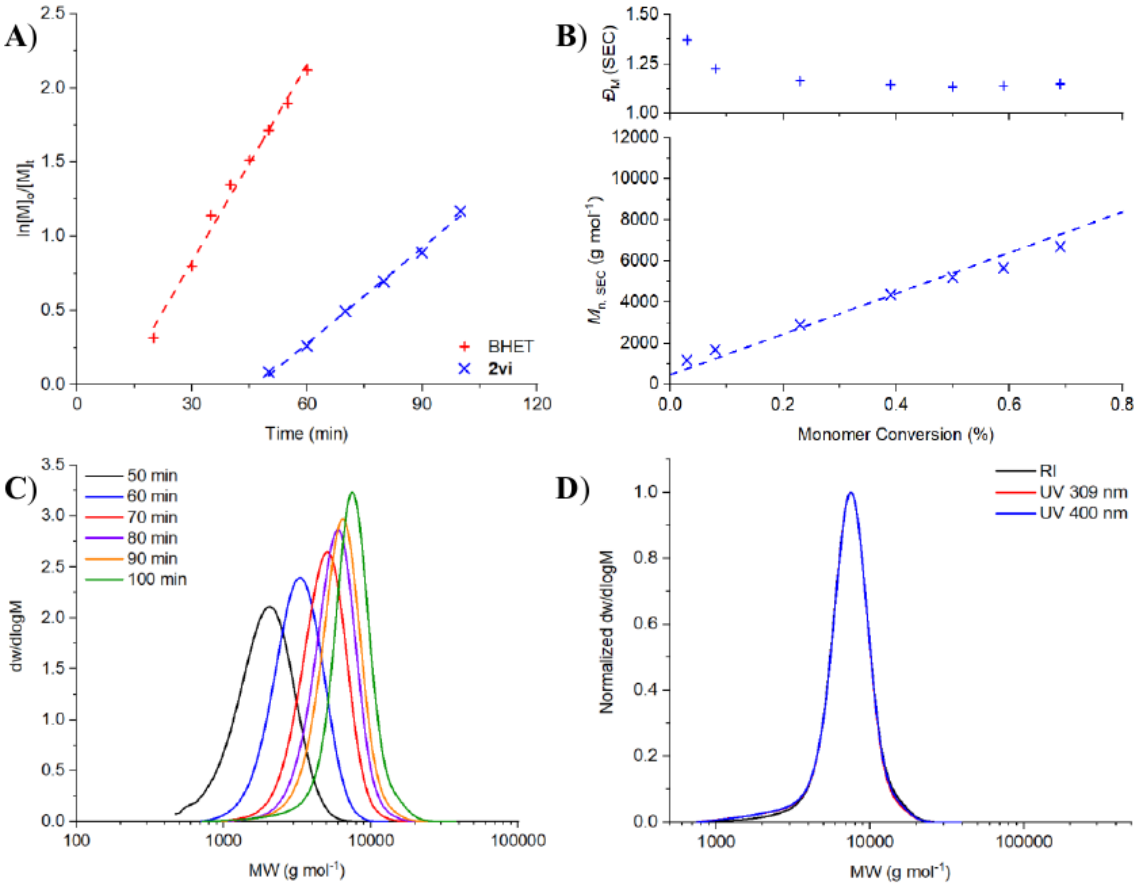

Figure 2.18: a) First order kinetics for the RAFT homopolymerization of DMAc with BHET or **2vi** as determined by ^{1}H NMR spectroscopy (300 MHz, $CDCl_3$) with linear fits; b) number average molecular weight (M_n) and $Đ_M$ as a function of monomer conversion with theoretical values (line) for the RAFT homopolymerization of DMAc with **2vi** (determined by SEC using $CHCl_3$ as the eluent and calibrated against p(St) standards); c) evolution of molecular weight distribution as a function of time for the RAFT homopolymerization of DMAc with **2vi** (determined by SEC with $CHCl_3$ as the eluent and calibrated against p(St) standards); d) Molecular weight distributions determined by SEC ($CHCl_3$ as the eluent and calibrated against p(St) standards) using both an RI and UV (recorded at 309 and 400 nm) detector for the ABM-functionalized $p(DMAc)_n$ homopolymer **2xix**.

Importantly, good agreement between the molecular weight distributions obtained using an RI and UV detector (recorded at 309 nm and 400 nm) for the purified fluorescent $p(DMAc)_{69}$ homopolymer **2xix** confirmed the retention of the ZCS_2 group (Figure 2.18 c). Overall, $p(DMAc)_n$ homopolymers **2xviii** and **2xix** possessed similarly low dispersities

($Đ_M$ = 1.11 *c.f.* 1.15) which indicated that control over the RAFT polymerization of DMAc was appreciably maintained upon switching the RAFT agent from BHET to **2vi**.

2.4. Conclusions

In this Chapter, a range of novel ABM-functionalized RAFT agents have been successfully designed and synthesized for which the ABM fluorophore was incorporated into either the R or Z group structure. Critically, the R group ABM-functionalized RAFT agent **2ii** facilitated the controlled RAFT copolymerization of two methacrylate monomers with no significant induction period or polymerization retardation observed. Furthermore, a high degree of end group fidelity was achieved with both the fluorophore and trithiocarbonate functionalities effectively retained as confirmed *via* SEC analysis. Moreover, the Z group ABM-functionalized RAFT agent **2vi** demonstrated a similar degree of polymerization control in comparison to its respective non-functionalized counterpart despite the presence of an extended induction period and reduced polymerization rate. Due to the limited monomer scope for **2vi**, the synthesis of a Z group ABM-functionalized RAFT agent capable of polymerizing (meth)acrylate, (meth)acrylamide and styrenic monomers to produce ω-functionalized fluorescent block copolymers was investigated. The importance of the chosen protecting group for functionalized thiols with respect to forming the required disulfide-bridged intermediate was highlighted. However, the overall yield for the successful isolation of a Z group ABM-functionalized RAFT agent (**2xvii**) with a tertiary R group was significantly low (0.5%), and thus optimization of the synthetic route reported herein is required for future studies. Overall, the viability of utilizing an ABM-functionalized RAFT agent to synthesize α- and ω-functionalized block copolymers with a highly emissive fluorophore attached has been established.

2.5. Experimental Section

2.5.1. Methods and materials

Materials. The following reagents were used as received: sodium ethanethiolate (Sigma-Aldrich, technical grade, 80%); triphenylphosphine (Sigma-Aldrich, 99%); diisopropyl azodicarboxylate (DIAD, Alfa Aesar, 94%); neopentyl alcohol (Acros Organics, 99%); 2,3-dibromomaleimide (Sigma-Aldrich, 97%); isopropylamine (Sigma-Aldrich, 99.5%); ethanolamine (Sigma-Aldrich, >99.5%); 3-chloro-1-propanethiol (Sigma-Aldrich, 98%); 2-mercaptoethanol (Sigma-Aldrich, 99%); carbon disulfide (Sigma-Aldrich, 99%); 1-(3-dimethylaminopropyl)-3-ethylcarbodiimide hydrochloride (EDC·HCl, Carbosynth, 98%); 2,6-diaminopyridine (Sigma-Aldrich, 98%); dibromomaleic acid (Sigma-Aldrich, 97%); benzyl bromide (Sigma-Aldrich, 98%); 3-mercaptopropionic acid (Acros Organics, 99%); *p*-toluenesulfonic acid (Alfa Aesar, 97%); benzyl alcohol (Acros Organics, 99%); potassium *tert*-butoxide (Acros Organics, 98%); potassium phosphate tribasic (Sigma-Aldrich, 98%); iodine (Fisher Scientific, 99%); *N*,*N*-dimethylaniline (Sigma-Aldrich, 99%); aluminium trichloride (Fluka, 99%); borane tetrahydrofuran complex solution (1 M in THF, Sigma-Aldrich); 4,4′-azobis(4-cyanovaleric acid) (ACVA, Sigma-Aldrich, 98%). 2,2'-azobisisobutyronitrile (AIBN) was received from Sigma-Aldrich (98%), recrystallized from methanol and stored in the dark at 4 °C. All solvents, including high-performance liquid chromatography (HPLC) grade solvents, were purchased from Fisher Scientific and used as received. Monomers and 1,4-dioxane were filtered through a plug of basic alumina prior to use and stored at 4 °C. Diethyl Ether and tetrahydrofuran (THF) were purchased from Fisher Scientific and dried using an Innovative Technology Inc. Pure Solv MD-4-EN solvent purification system. Deuterated solvents and silica gel (40-63 μm) were used as received from Apollo Scientific.

^{1}H and ^{13}C NMR spectroscopy. ^{1}H NMR spectroscopy was performed at 300 MHz on a Bruker Avance AV-300 spectrometer or a Bruker Avance III HD-300 spectrometer, or at 400 MHz on a Bruker Avance III HD-400 spectrometer. ^{13}C NMR spectroscopy was performed at 75 MHz on a Bruker Avance AV-300 spectrometer or a Bruker Avance III HD-300 spectrometer, or at 100 MHz on a Bruker Avance III HD-400 spectrometer. ^{1}H and ^{13}C NMR spectra were recorded in either deuterated chloroform or acetone. Chemical shifts are reported as δ in parts per million (ppm) and are reported relative to the residual solvent peaks at 7.26 ppm or 77.0 ppm for chloroform, and 2.05 ppm and 30.83 ppm for acetone. Coupling constants (J) correspond to $^{3}J_{\text{H-H}}$ unless otherwise stated. All spectra were obtained at 25 °C.

Size Exclusion Chromatography. SEC analysis was performed on a Varian PL-GPC 50 system with a set of two PLgel Mixed-C columns plus one guard column and fitted with an RI and UV detector measuring at 309 nm or 400 nm. SEC measurements were performed with HPLC-grade chloroform with 0.5% triethylamine at 40 °C at a flow rate of 1 mL min^{-1}. The molecular weights of the synthesized polymers were calculated relative to poly(styrene) (p(St)) standards and analyzed using Cirrus v3.3 software.

Mass Spectrometry. High resolution electrospray ionization time of flight mass spectrometry (HRMS (ESI-ToF)) was performed on a Bruker UHR-Q-TOF MaXis spectrometer by Dr. Lijang Song, University of Warwick.

Fluorescence Spectroscopy. Steady-state fluorescence spectra were recorded using an Agilent Cary Eclipse Fluorescence spectrophotometer. Quartz cells with screw caps and four polished sides (Starna) were used for fluorescence measurements.

2.5.2. Synthetic protocols

Benzyl (2-hydroxyethyl) carbonotrithioate (BHET) was synthesized as previously reported.[45]

Synthesis of 4-cyano-4-(((ethylthio)carbonothioyl)thio)pentanoic acid (CETPA).

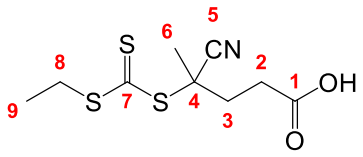

4-Cyano-4-(((ethylthio)carbonothioyl)thio) pentanoic acid was prepared according to a modified literature procedure.[43] To an oven-dried round bottom flask, sodium ethanethiolate (10.0 g, 119 mmol) was added followed by the addition of diethyl ether (500 mL) with the resulting solution cooled to 0 °C. Carbon disulfide (7.74 mL, 131 mmol) was subsequently added dropwise over 10 min producing a thick yellow precipitate of sodium S-ethyl trithiocarbonate. After 2 h of stirring at ambient temperature, solid iodine (15.1 g, 59.4 mmol) was added. After 2 h of stirring at ambient temperature, the reaction mixture was washed with sodium thiosulfate solution (1 M, 3 × 300 mL), deionized water (3 × 300 mL) and finally with brine (300 mL). The organic layer was dried over $MgSO_4$ and evaporated to leave a residue of bis-(ethyl-sulfanylthiocarbonyl) disulfide (16.2 g, quantitative).

A solution of 4,4'-azobis(4-cyanovaleric acid) (ACVA) (24.8 g, 88.5 mmol) and bis-(ethyl-sulfanylthiocarbonyl) disulfide (16.2 g, 59.0 mmol) in ethyl acetate (500 mL) was refluxed overnight under a nitrogen atmosphere. After removal of ethyl acetate *in vacuo*, purification was carried out using column chromatography (silica gel, 1:1

dichloromethane (DCM)/petroleum ether 40-60 °C (pet. ether)) to yield 4-cyano-4-(((ethylthio)carbonothioyl)thio) pentanoic acid (CETPA) as an orange red oil (27.4 g, 108 mmol, 91%). ^{1}H NMR (400 MHz, $CDCl_3$) δ_H/ppm: 3.35 (2H, q, J = 7.6 Hz, H8), 2.68 (2H, m, H2), 2.34-2.59 (2H, m, H3), 1.88 (3H, s, H6), 1.36 (3H, t, J = 7.6 Hz, H9); ^{13}C NMR (100 MHz, $CDCl_3$) δ_C/ppm: 216.6 (C7), 177.1 (C1), 118.8 (C5), 46.2 (C4), 33.4 (C3), 31.4 (C8), 29.5 (C2), 24.8 (C6), 12.7 (C9); HRMS (ESI-TOF) m/z: $[M + H]^+$ calculated for $C_9H_{14}NO_2S_3$: 264.0187; found: 264.0188.

Synthesis of 2-cyano-5-hydroxypentan-2-yl ethyl carbonotrithioate (CHPET).

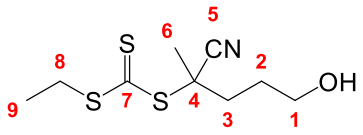

To a flame-dried round bottom flask, 4-cyano-4-(((ethylthio)carbonothioyl)thio) pentanoic acid (CETPA) (8.98 g, 34.1 mmol) was added followed by the addition of dry THF (200 mL) with the resulting solution cooled to -78 °C. 1 M Borane THF complex solution (35.8 mL, 35.8 mmol) was subsequently added dropwise over 30 min. The reaction mixture was left to stir for 1 h, after which the cooling bath was removed and the reaction was stirred overnight at ambient temperature under a nitrogen atmosphere. After 24 h of stirring, methanol (100 mL) was added in five portions and stirred for 10 min after each addition or until no further bubbling was observed. After removal of THF and methanol *in vacuo*, the organic residue was dissolved in diethyl ether (250 mL) and washed with saturated $NaHCO_3$ solution (3 × 250 mL) and then with brine (250 mL). Further extraction using diethyl ether (3 × 100 mL) from the collected aqueous layers was carried out. Combined organic layers were dried over $MgSO_4$, filtered and evaporated to dryness. Purification was carried out using column chromatography (silica gel, 1:1 ethyl

acetate/pet. ether) to yield 2-cyano-5-hydroxypentan-2-yl ethyl carbonotrithioate (CHPET) as an orange red oil (6.13 g, 24.6 mmol, 72%). ^{1}H NMR (300 MHz, $CDCl_3$) δ_H/ppm: 3.72 (2H, t, J = 6 Hz, H1), 3.34 (2H, q, J = 7.5 Hz, H8), 2.02-2.34 (2H, m, H3), 1.89 (3H, s, H6), 1.78-1.88 (2H, m, H2), 1.35 (3H, t, J = 7.5 Hz, H9); ^{13}C NMR (75 MHz, $CDCl_3$) δ_C/ppm: 217.4 (C7), 119.5 (C5), 61.7 (C1), 46.9 (C4), 35.7 (C3), 31.3 (C8), 27.9 (C2), 24.9 (C6), 12.8 (C9); HRMS (ESI-TOF) *m/z*: $[M + Na]^+$ calculated for $C_9H_{15}NNaOS_3$: 272.0208; found: 272.0216.

*Synthesis of 2-cyano-5-(3,4-dibromo-2,5-dioxo-2,5-dihydro-1H-pyrrol-1-yl)pentan-2-yl ethyl carbonotrithioate (**2i**).*

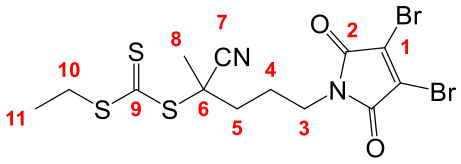

To a flame-dried round bottom flask, triphenylphosphine (6.45 g, 24.6 mmol) was added followed by the addition of dry THF (250 mL) and the resulting solution cooled to -78 °C. Diisopropyl azodicarboxylate (DIAD) (4.84 mL, 24.6 mmol) was added dropwise over 2-3 min. The reaction mixture was stirred for 5 min after which a solution of 2-cyano-5-hydroxypentan-2-yl ethyl carbonotrithioate (CHPET) (6.13 g, 24.6 mmol) dissolved in dry THF (25 mL) was added using air sensitive techniques and the resultant mixture was stirred for 5 min. Neopentyl alcohol (1.08 g, 12.3 mmol) was added and the reaction mixture was left to stir for 10 min. 2,3-Dibromomaleimide (6.26 g, 24.6 mmol) was then added to the reaction mixture. The resulting suspension was allowed to remain at -78 °C for 10 min before the cooling bath was removed and the reaction was stirred overnight at ambient temperature under a nitrogen atmosphere. After removal of THF *in vacuo*,

purification of the crude mixture was carried out using column chromatography (silica gel, 2:1 DCM/pet. ether) to yield 2-cyano-5-(3,4-dibromo-2,5-dioxo-2,5-dihydro-1*H*-pyrrol-1-yl) pentan-2-yl ethyl carbonotrithioate (**2i**) as an orange red oil (8.16 g, 16.8 mmol, 68%). ^{1}H NMR (300 MHz, $CDCl_3$) δ_H/ppm: 3.68 (2H, t, J = 6.9 Hz, H3), 3.33 (2H, q, J = 7.5 Hz, H10), 2.01-2.27 (2H, m, H5), 1.85-1.98 (2H, m, H4), 1.84 (3H, s, H8), 1.35 (3H, t, J = 7.5 Hz, H11); ^{13}C NMR (75 MHz, $CDCl_3$) δ_C/ppm: 217.0 (C9), 163.8 (C2), 129.5 (C1), 119.1 (C7), 46.5 (C6), 38.8 (C3), 35.8 (C5), 31.4 (C10), 24.8 (C8), 24.0 (C4), 12.7 (C11); HRMS (ESI-TOF) *m/z*: $[M + Na]^+$ calculated for $C_{13}H_{14}Br_2N_2NaO_2S_3$: 506.8476; found: 506.8476.

*Synthesis of 5-(3-bromo-4-(isopropylamino)-2,5-dioxo-2,5-dihydro-1H-pyrrol-1-yl)-2-cyanopentan-2-yl ethyl carbonotrithioate (**2ii**).*

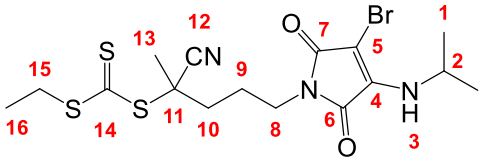

To a suspension of 2-cyano-5-(3,4-dibromo-2,5-dioxo-2,5-dihydro-1*H*-pyrrol-1-yl)pentan-2-yl ethyl carbonotrithioate (**2i**) (6.83 g, 14.0 mmol) and Na_2CO_3 (3.72 g, 35.1 mmol) in THF (HPLC-grade, 150 mL), isopropylamine (3.02 mL, 35.1 mmol) was added. The reaction mixture was stirred at ambient temperature with the conversion of **2i** monitored by thin layer chromatography (TLC). After 1 h, THF was removed *in vacuo* and the organic residue dissolved in DCM (250 mL) and washed with deionized water (3 × 250 mL). The organic layer was dried over $MgSO_4$, filtered and evaporated to dryness. Purification was carried out using column chromatography (silica gel, 9:1 DCM/pet. ether) to yield 5-(3-bromo-4-(isopropylamino)-2,5-dioxo-2,5-dihydro-1*H*-

pyrrol-1-yl)-2-cyanopentan-2-yl ethyl carbonotrithioate (**2ii**) as an orange red oil (3.92 g, 8.44 mmol, 60%). ^{1}H NMR (400 MHz, $CDCl_3$) δ_H/ppm: 5.28 (1H, br d, J = 8.5 Hz, H3), 4.41 (1H, d of sept., J = 6.5 and 8.5 Hz, H2), 3.57 (2H, t, J = 7.0 Hz, H8), 3.34 (2H, q, J = 7.5 Hz, H15), 1.98-2.21 (2H, m, H10), 1.85-1.92 (2H, m, H9), 1.84 (3H, s, H13), 1.35 (3H, t, J = 7.5 Hz, H16), 1.31 (6H, d, J = 6.5 Hz, H1); ^{13}C NMR (100 MHz, $CDCl_3$) δ_C/ppm: 217.1 (C14), 167.7 (C7), 166.0 (C6), 151.9 (C4), 119.2 (C12), 46.6 (C11), 44.8 (C2), 37.7 (C8), 36.0 (C10), 31.3 (C15), 24.8 (C13), 24.1 (C9), 23.7 (C1), 12.7 (C16); HRMS (ESI-TOF) m/z: $[M + Na]^+$ calculated for $C_{16}H_{22}BrN_3NaO_2S_3$: 485.995; found: 485.995.

Synthesis of 2-cyanopropan-2-yl ethyl carbonotrithioate (CPET).

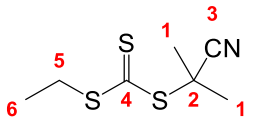

To an oven-dried round bottom flask, sodium ethanethiolate (10.0 g, 119 mmol) was added followed by diethyl ether (500 mL) with the resulting solution cooled to 0 °C. Carbon disulfide (7.74 mL, 131 mmol) was subsequently added dropwise over 10 min producing a thick yellow precipitate of sodium S-ethyl trithiocarbonate. After 2 h of stirring at ambient temperature, solid iodine (15.1 g, 59.4 mmol) was added. After another 2 h of stirring at ambient temperature, the reaction mixture was washed with sodium thiosulfate solution (1 M, 3 × 300 mL), deionized water (3 × 300 mL) and finally with brine (300 mL). The organic layer was dried over $MgSO_4$ and evaporated to leave a residue of bis-(ethyl-sulfanylthiocarbonyl) disulfide (15.7 g, quantitative).

A solution of 2,2'-azobisisobutyronitrile (AIBN) (14.1 g, 85.8 mmol) and bis-(ethyl-sulfanylthiocarbonyl) disulfide (15.7 g, 57.2 mmol) in ethyl acetate (500 mL) was

refluxed overnight under a nitrogen atmosphere. After removal of ethyl acetate *in vacuo*, purification was carried out using column chromatography (silica gel, 1:1 DCM/pet. ether) to yield 2-cyanopropan-2-yl ethyl carbonotrithioate (CPET) as an orange red oil (19.8 g, 96.6 mmol, 84%). ^{1}H NMR (300 MHz, $CDCl_3$) δ_H/ppm: 3.35 (2H, q, J = 7.5 Hz, H5), 1.87 (6H, s, H1), 1.35 (3H, t, J = 7.5 Hz, H6); ^{13}C NMR (75 MHz, $CDCl_3$) δ_C/ppm: 217.6 (C4), 120.4 (C3), 42.3 (C2), 31.2 (C5), 27.0 (C1), 12.7 (C6); HRMS (ESI-TOF) m/z: $[M + Na]^+$ calculated for $C_7H_{11}NNaS_3$: 227.9946; found: 227.9946.

*Synthesis of benzyl (2-(3,4-dibromo-2,5-dioxo-2,5-dihydro-1H-pyrrol-1-yl)ethyl) carbonotrithioate (**2v**).*

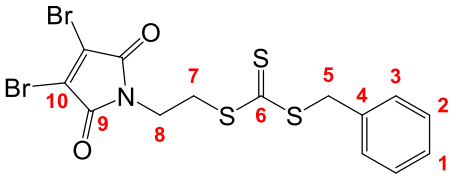

To a flame-dried round bottom flask, triphenylphosphine (1.30 g, 4.96 mmol) was added followed by the addition of dry THF (40 mL) and the resulting solution cooled to -78 °C. Diisopropyl azodicarboxylate (DIAD) (977 µL, 4.96 mmol) was added dropwise over 2-3 min. The reaction mixture was stirred for 5 min after which benzyl (2-hydroxyethyl) carbonotrithioate (1.21 g, 4.96 mmol) dissolved in dry THF (10 mL) was added using air sensitive techniques and the resultant mixture was stirred for 5 min. Neopentyl alcohol (219 mg, 2.48 mmol) was added and the reaction mixture was left to stir for 10 min. 2,3-Dibromomaleimide (1.26 g, 4.96 mmol) was then added to the reaction mixture. The resulting suspension was allowed to remain at -78 °C for 10 min before the cooling bath was removed and the reaction was stirred overnight at ambient temperature under a nitrogen atmosphere. After removal of THF *in vacuo*, purification of the crude mixture

was carried out using column chromatography (silica gel, 1:1 DCM/pet ether) followed by 100% ethyl acetate) to yield benzyl (2-(3,4-dibromo-2,5-dioxo-2,5-dihydro-1*H*-pyrrol-1-yl) ethyl) carbonotrithioate as a yellow solid (1.36 g, 2.82 mmol, 57%). ^{1}H NMR (300 MHz, $(CD_3)_2CO$) δ_H/ppm: 7.25-7.45 (5H, m, H1,2,3), 4.70 (2H, s, H5), 3.97 (2H, t, *J* = 6.4 Hz, H8), 3.74 (2H, t, *J* = 6.4 Hz, H7); ^{13}C NMR (75 MHz, $(CD_3)_2CO$) δ_C/ppm: 224.2 (C6), 164.8 (C9), 135.0 (C4), 130.4 (C10), 130.3 (C2), 129.7 (C3), 128.8 (C1), 42.1 (C5), 38.6 (C7), 35.3 (C8); HRMS (ESI-TOF) *m*/*z*: $[M + H]^+$ calculated for $C_{14}H_{13}Br_2NO_2S_3$: 479.8397; found: 479.8391.

*Synthesis of benzyl (2-(3-bromo-4-(isopropylamino)-2,5-dioxo-2,5-dihydro-1H-pyrrol-1-yl)ethyl) carbonotrithioate (**2vi**).*

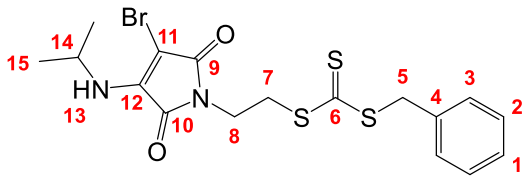

To a suspension of benzyl (2-(3,4-dibromo-2,5-dioxo-2,5-dihydro-1H-pyrrol-1-yl) ethyl) carbonotrithioate (**2v**) (1.36 g, 2.82 mmol) and Na_2CO_3 (749 mg, 7.07 mmol) in THF (HPLC-grade, 50 mL), isopropylamine (607 µL, 7.07 mmol) was added. The reaction mixture was stirred at ambient temperature with the conversion of **2v** monitored by TLC. After 1 h, THF was removed *in vacuo* and the organic residue dissolved in DCM (50 mL) and washed with deionized water (3 × 50 mL). Organic layer was dried over $MgSO_4$, filtered and evaporated to dryness. Purification was carried out using column chromatography (silica gel, 1:3 pet. ether/DCM followed by 100% ethyl acetate) to yield benzyl (2-(3-bromo-4-(isopropylamino)-2,5-dioxo-2,5-dihydro-1*H*-pyrrol-1-yl)ethyl) carbonotrithioate as an orange solid (777 mg, 1.69 mmol, 60%). ^{1}H NMR (400 MHz,

$(CD_3)_2CO$) δ_H/ppm: 7.26-7.44 (5H, m, H1,2,3), 6.55 (1H, br d, J = 8.0 Hz, H13), 4.69 (2H, s, H5), 4.49 (1H, d of sept., J = 6.4 Hz and 8.0 Hz, H14), 3.83 (2H, t, J = 6.4 Hz, H8), 3.68 (2H, t, J = 6.4 Hz, H7), 1.32 (6H, d, J = 6.4 Hz, H15); ^{13}C NMR (100 MHz, $(CD_3)_2CO$) δ_C/ppm: 224.3 (C6), 167.0 (C9), 166.3 (C10), 145.7 (C12), 136.3 (C4), 130.3 (C2), 129.7 (C3), 128.7 (C1), 45.8 (C14), 42.0 (C5), 37.3 (C7), 35.7 (C8), 23.6 (C15); HRMS (ESI-TOF) m/z: $[M + Na]^+$ calculated for $C_{17}H_{19}BrN_2NaO_2S_3$: 480.9690; found: 480.9688.

*Synthesis of 4-((((3-chloropropyl)thio)carbonothioyl)thio)-4-cyanopentanoic acid (**2vii**).*

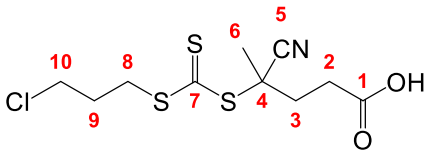

To a solution of potassium *tert*-butoxide (1 M in THF) (10.3 mL, 10.3 mmol) in diethyl ether (40 mL) at 0 °C, 3-chloro-1-propanethiol (1.00 mL, 10.3 mmol) was added with the reaction mixture stirred for 10 min. Carbon disulfide (619 µL, 10.3 mmol) was added dropwise over 5 min producing a yellow slurry and the reaction mixture was left to stir for 10 min. After allowing the reaction to warm up to ambient temperature, iodine (1.30 g, 5.12 mmol) was added with the reaction mixture left to stir for 1 h. The organic layer was then washed with sodium thiosulfate solution (1 M, 200 mL) before being dried over $MgSO_4$ and evaporated to dryness. Purification was carried out using column chromatography (silica gel, 9:1 pet. ether/ethyl acetate) to yield bis-(chloropropylsulfanylthiocarbonyl) disulfide as an orange oil (1.78 g, 4.80 mmol, 93%). A solution of 4,4'-azobis(4-cyanovaleric acid) (ACVA) (2.02 g, 7.19 mmol) and bis-(chloropropylsulfanylthiocarbonyl) disulfide (1.78 g, 4.80 mmol) in ethyl acetate (50 mL) was refluxed overnight under a nitrogen atmosphere. After removal of ethyl

acetate *in vacuo*, purification was carried out using column chromatography (silica gel, 1:1 pet. ether/ethyl acetate) to yield 4-((((3-chloropropyl)thio)carbonothioyl)thio)-4-cyanopentanoic acid as an orange red oil (0.82 g, 2.64 mmol, 55%). ^{1}H NMR (400 MHz, $CDCl_3$) δ_H/ppm: 3.61 (2H, t, J = 6.4 Hz, H10), 3.50 (2H, t, J = 6.8 Hz, H8), 2.68 (2H, d of d, J = 7.6 Hz, H2), 2.34-2.58 (2H, m, H3), 2.17 (2H, t of t, J = 6.4 Hz and 6.8 Hz, H9), 1.88 (3H, s, H6); ^{13}C NMR (100 MHz, $CDCl_3$) δ_C/ppm: 216.2 (C7), 176.9 (C1), 118.7 (C5), 46.4 (C4), 43.2 (C10), 33.6 (C9), 33.4 (C3), 30.5 (C8), 29.4 (C2), 24.8 (C6).

*Synthesis of methyl 4-((((3-chloropropyl)thio)carbonothioyl)thio)-4-cyanopentanoate (**2viii**).*

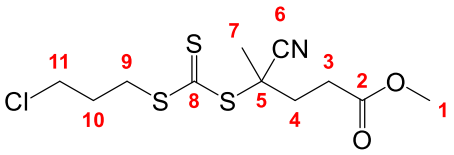

To a solution of 4-((((3-chloropropyl)thio)carbonothioyl)thio)-4-cyanopentanoic acid (**2vii**) (700 mg, 2.24 mmol) and 2,6-diaminopyridine (137 mg, 1.12 mmol) in methanol (50 mL), EDC·HCl (859 mg, 4.48 mmol) was added and the reaction mixture was left to stir at ambient temperature. After 16 h, methanol was removed *in vacuo* and the organic residue was dissolved in DCM (50 mL) and washed with deionized water (3 × 50 mL). The organic layer was dried over $MgSO_4$, filtered and evaporated to dryness. Purification was carried out using column chromatography (silica gel, 3:1 pet. ether/ethyl acetate) to yield methyl 4-((((3-chloropropyl)thio)carbonothioyl)thio)-4-cyanopentanoate as an orange-red oil (585 mg, 1.79 mmol, 80%). ^{1}H NMR (300 MHz, $CDCl_3$) δ_H/ppm: 3.71 (3H, s, H1), 3.61 (2H, t, J = 6.0 Hz, H11), 3.50 (2H, t, J = 6.9 Hz, H9), 2.62 (2H, d of d, J = 7.8 Hz, H3), 2.30-2.55 (2H, m, H4), 2.17 (2H, t of t, J = 6.0 Hz and 6.9 Hz, H10), 1.87 (3H, s, H7); ^{13}C NMR (75 MHz, $CDCl_3$) δ_C/ppm: 216.3 (C8), 171.8 (C2), 118.7

(C6), 52.1 (C1), 46.5 (C5), 43.2 (C11), 33.8 (C10), 33.6 (C4), 30.5 (C9), 29.5 (C3), 24.8 (C7); HRMS (ESI-TOF) *m*/*z*: $[M + H]^+$ calculated for $C_{11}H_{17}ClNO_2S_3$: 326.0110; found: 326.0112.

*Synthesis of 2-(3,4-dibromo-2,5-dioxo-2,5-dihydro-1H-pyrrol-1-yl)ethyl acetate (**2ix**).*

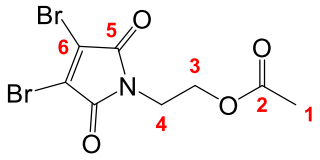

Dibromomaleic acid (2.00 g, 7.30 mmol) was dissolved in acetic acid (100 mL) at 4 °C and ethanolamine (485 µL, 8.03 mmol) was then added to the reaction mixture. The reaction mixture was then refluxed overnight under a nitrogen atmosphere. After the removal of acetic acid *in vacuo*, purification was carried out using column chromatography (silica gel, 1:1 pet. ether/ethyl acetate) to yield 2-(3,4-dibromo-2,5-dioxo-2,5-dihydro-1*H*-pyrrol-1-yl)ethyl acetate as an off-white solid (1.58 g, 4.63 mmol, 63%). ^{1}H NMR (300 MHz, $CDCl_3$) δ_H/ppm: 4.24 (2H, t, J = 6.4 Hz, H3), 3.88 (2H, t, J = 6.4 Hz, H4), 2.03 (3H, s, H1); ^{13}C NMR (75 MHz, $CDCl_3$) δ_C/ppm: 170.8 (C2), 163.7 (C5), 129.5 (C6), 61.2 (C3), 38.7 (C4), 20.7 (C1).

*Synthesis of 2-(3-bromo-4-(isopropylamino)-2,5-dioxo-2,5-dihydro-1H-pyrrol-1-yl)ethyl acetate (**2x**).*

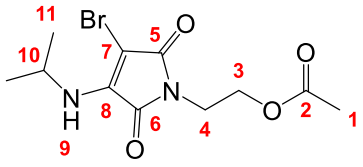

To a suspension of 2-(3,4-dibromo-2,5-dioxo-2,5-dihydro-1*H*-pyrrol-1-yl)ethyl acetate (**2ix**) (1.07 g, 3.12 mmol) and Na_2CO_3 (363 mg, 3.43 mmol) in THF (HPLC-grade, 50 mL), isopropylamine (295 µL, 3.43 mmol) was added. The reaction mixture was stirred at ambient temperature with the conversion of **2ix** monitored by TLC. After 1 h, THF was removed *in vacuo* and the organic residue was dissolved in DCM (50 mL) and washed with deionized water (3 × 50 mL). The organic layer was dried over $MgSO_4$, filtered and evaporated to dryness. Purification was carried out using column chromatography (silica gel, 3:1 DCM/pet. ether) to yield 2-(3-bromo-4-(isopropylamino)-2,5-dioxo-2,5-dihydro-1*H*-pyrrol-1-yl)ethyl acetate (**2x**) as a fluorescent yellow solid (778 mg, 2.43 mmol, 78%). ^{1}H NMR (300 MHz, $CDCl_3$) δ_H/ppm: 5.28 (1H, br d, *J* = 7.8 Hz, H9), 4.40 (1H, d of sept., *J* = 6.9 and 7.8 Hz, H10), 4.19 (2H, t, *J* = 6.8 Hz, H3), 3.76 (2H, t, *J* = 6.8 Hz, H4), 2.02 (3H, s, H1), 1.30 (6H, d, *J* = 6.9 Hz, H11); ^{13}C NMR (75 MHz, $CDCl_3$) δ_C/ppm: 170.8 (C2), 167.5 (C5), 166.0 (C6), 144.7 (C8), 61.5 (C3), 44.8 (C10), 37.5 (C4), 23.7 (C11), 20.8 (C1).

*Synthesis of 3-bromo-1-(2-hydroxyethyl)-4-(isopropylamino)-1H-pyrrole-2,5-dione (**2xi**).*

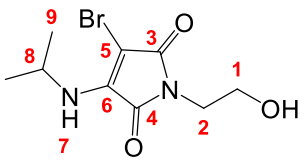

To a suspension of K_2CO_3 (336 mg, 2.43 mmol) in methanol (25 mL), 2-(3-bromo-4-(isopropylamino)-2,5-dioxo-2,5-dihydro-1*H*-pyrrol-1-yl) ethyl acetate (778 mg, 2.43 mmol) was added. The resulting suspension was stirred at ambient temperature for 30 min, at which point TLC of the crude reaction mixture confirmed full conversion of

the starting material. The reaction mixture was then diluted with deionized water (125 mL) and ethyl acetate (150 mL). The organic layer was washed with deionized water (2 × 125 mL) and brine (125 mL) before being evaporated to dryness. Purification was carried out using column chromatography (silica gel, 3:2 pet. ether/ethyl acetate) to yield 3-bromo-1-(2-hydroxyethyl)-4-(isopropylamino)-1*H*-pyrrole-2,5-dione as a fluorescent yellow solid (267 mg, 0.96 mmol, 40%). ^{1}H NMR (300 MHz, $CDCl_3$) δ_H/ppm: 5.32 (1H, br d, *J* = 7.8 Hz, H8), 4.41 (1H, d of sept., *J* = 6.9 Hz and 7.8 Hz, H9), 3.67-3.82 (2H, m, H3 and H2), 2.20 (1H, br s, H1), 1.30 (6H, d, *J* = 6.9 Hz, H10).

*Synthesis of benzyl 3-mercaptopropanoate (**2xii**).*

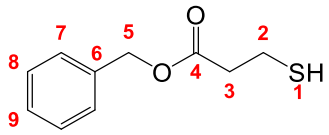

3-Mercaptopropionic acid (10.0 mL, 115 mmol) was added to a solution of *p*-toluenesulfonic acid (4.37 g, 23.0 mmol) in benzyl alcohol (13 mL) and THF (125 mL). The reaction mixture was refluxed overnight at 80 °C and then allowed to cool down to ambient temperature. After the volatiles were removed *in vacuo*, the organic residue was redissolved in ethyl acetate (250 mL) and washed with saturated $NaHCO_3$ solution (3 × 250 mL). The combined organic layers were dried over $MgSO_4$, filtered and evaporated to dryness. Purification was carried out using column chromatography (silica gel, 3:1 pet. ether/ethyl acetate) to yield benzyl 3-mercaptopropanoate as an off-white liquid (13.2 g, 67.0 mmol, 58%). ^{1}H NMR (300 MHz, $(CD_3)_2CO$) δ_H/ppm: 7.25-7.46 (5H, m, H7,8,9), 5.15 (2H, s, H5), 2.78 (2H, t, *J* = 7.8 Hz, H3), 2.71 (2H, d of t, *J* = 7.8 Hz and 8.4 Hz, H2), 1.93 (1H, t, *J* = 8.4 Hz, H1); ^{13}C NMR (75 MHz, $(CD_3)_2CO$) δ_C/ppm:

172.1 (C4), 137.5 (C6), 129.5 (C8), 129.1 (C7), 129.0 (C9), 66.8 (C5), 39.3 (C3), 20.4 (C2).

*Synthesis of benzyl 3-((((2-cyanopropan-2-yl)thio)carbonothioyl)thio)propanoate (**2xiii**).*

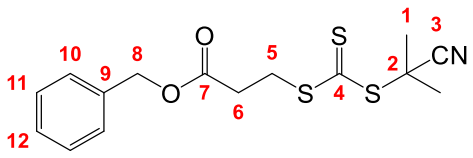

To a solution of potassium *tert*-butoxide (7.54 g, 67.2 mmol) in diethyl ether (240 mL) and THF (15 mL) at 0 °C, benzyl 3-mercaptopropanoate (**2xii**) (13.2 g, 67.2 mmol) was added to the reaction mixture and then stirred for 10 min. Carbon disulfide (4.04 mL, 67.2 mmol) was added dropwise over 5 min producing a yellow slurry and the reaction mixture was left to stir for 1 h. After allowing the reaction to warm up to ambient temperature, iodine (8.52 g, 33.6 mmol) was added with the reaction mixture left to stir for 1 h. The organic layer was then washed with sodium thiosulfate solution (1 M, 250 mL) before being dried over $MgSO_4$ and evaporated to leave a residue of dibenzyl 3,3'-((disulfanne-1,2-dicarbonothioyl)bis(sulfanediyl)) dipropionate (14.0 g, quantitative). A solution of 2,2′-azobis(2-methylpropionitrile) (AIBN) (6.36 g, 38.7 mmol) and dibenzyl 3,3'-((disulfanne-1,2-dicarbonothioyl)bis(sulfanediyl)) dipropionate (14.0 g, 25.8 mmol) in ethyl acetate (250 mL) was refluxed overnight under a nitrogen atmosphere. After removal of ethyl acetate *in vacuo*, purification was carried out using column chromatography (silica gel, 1:1 DCM/pet. ether) to yield benzyl 3-((((2-cyanopropan-2-yl)thio)carbonothioyl)thio)propanoate as an orange-red oil (5.43 g, 16.0 mmol, 24%). ^{1}H NMR (400 MHz, $(CD_3)_2CO$) δ_H/ppm: 7.28-7.44 (5H, m, H10,11,12), 5.16 (2H, s, H8), 3.68 (2H, t, J = 6.8 Hz, H5), 2.88 (2H, t, J = 6.8 Hz, H6), 1.90 (6H, s, H1); ^{13}C NMR (100 MHz, $(CD_3)_2CO$) δ_C/ppm: 219.8 (C4), 171.7 (C7), 137.3

(C9), 129.5 (C11), 129.1 (C10), 129.0 (C12), 121.0 (C3), 67.2 (C8), 44.0 (C2), 33.3 (C5), 32.4 (C6), 27.2 (C1).

*Synthesis of 3-((((2-cyanopropan-2-yl)thio)carbonothioyl)thio)propanoic acid (**2xiv**).*

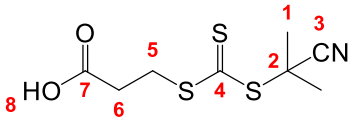

Benzyl deprotection was carried out using a modified experimental protocol from the literature.[54] To a solution of benzyl 3-((((2-cyanopropan-2-yl)thio)carbonothioyl)thio) propanoate (**2xiii**) (2.94 g, 8.67 mmol) and *N*,*N*-dimethylaniline (1.05 mL, 8.67 mmol) in DCM (50 mL) was added $AlCl_3$ (3.46 g, 26.0 mmol) at ambient temperature. After stirring for 2 h, the reaction mixture was quenched by careful addition of ice-cold water (50 mL). The aqueous layer was extracted with diethyl ether (3 × 50 mL) and the combined organic layers were washed with 1 M HCl (3 × 50 mL) and extracted with 1 M NaOH (3 × 50 mL). The combined aqueous layers were then acidified to pH 2 by the addition of 1 M HCl and extracted with diethyl ether (3 × 100 mL). The combined organic layers were washed with brine (100 mL), dried over $MgSO_4$, filtered and evaporated to dryness. Purification was carried out using column chromatography (silica gel, 1:3 pet. ether/ethyl acetate) to yield 3-((((2-cyanopropan-2-yl)thio)carbonothioyl) thio)propanoic acid as an orange red oil (0.71 g, 2.85 mmol, 33%). ^{1}H NMR (400 MHz, $CDCl_3$) δ_H/ppm: 8.00 (1H, br s, H8), 3.59 (2H, t, J = 6.8 Hz, H5), 2.83 (2H, t, J = 6.8 Hz, H6), 1.88 (6H, s, H1); ^{13}C NMR (100 MHz, $CDCl_3$) δ_C/ppm: 217.1 (C4), 176.5 (C7), 120.2 (C3), 42.6 (C2), 32.6 (C5), 30.7 (C6), 27.0 (C1).

*Synthesis of 2-cyanopropan-2-yl (3-hydroxypropyl) carbonotrithioate (**2xv**).*

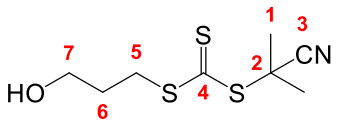

To a flame-dried round bottom flask, 3-((((2-cyanopropan-2-yl)thio)carbonothioyl)thio) propanoic acid (**2xiv**) (0.71 g, 2.85 mmol) was added followed by the addition of dry THF (25 mL) with the resulting solution cooled to -78 °C. 1 M Borane THF complex solution (3.00 mL, 3.00 mmol) was subsequently added dropwise over 30 min. The reaction mixture was left to stir for 1 h, after which the cooling bath was removed and the reaction stirred overnight at ambient temperature under a nitrogen atmosphere. After 24 h of stirring, methanol (25 mL) was added in five portions and stirred for 10 min after each addition or until no further bubbling was observed. After removal of THF and methanol *in vacuo*, the organic residue was dissolved in diethyl ether (25 mL) and washed with saturated $NaHCO_3$ solution (3 × 25 mL) and then with brine (25 mL). Further extraction using diethyl ether from the collected aqueous layers was carried out. The combined organic layers were dried over $MgSO_4$, filtered and evaporated to dryness. Purification was carried out using column chromatography (silica gel, 1:1 ethyl acetate/pet. ether) to yield 2-cyanopropan-2-yl (3-hydroxypropyl) carbonotrithioate as an orange-red oil (180 mg, 0.765 mmol, 27%). ^{1}H NMR (300 MHz, $CDCl_3$) δ_H/ppm: 3.70 (2H, t, J = 6.0 Hz, H7), 3.46 (2H, t, J = 7.2 Hz, H5), 1.94 (2H, d of t, J = 6.0 Hz and 7.2 Hz, H6), 1.86 (6H, s, H1); ^{13}C NMR (100 MHz, $CDCl_3$) δ_C/ppm: 217.8 (C4), 120.3 (C3), 60.8 (C7), 42.4 (C2), 33.2 (C5), 30.6 (C6), 26.9 (C1); HRMS (ESI-TOF) m/z: $[M + H]^+$ calculated for $C_8H_{14}NOS_3$: 236.0238; found: 236.0240.

*Synthesis of 2-cyanopropan-2-yl (3-(3,4-dibromo-2,5-dioxo-2,5-dihydro-1H-pyrrol-1-yl) propyl) carbonotrithioate (**2xvi**).*

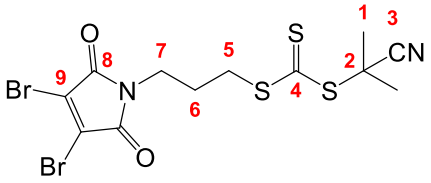

To a flame-dried round bottom flask, triphenylphosphine (201 mg, 0.765 mmol) was added followed by the addition of dry THF (20 mL) and the resulting solution cooled to -78 °C. DIAD (151 µL, 0.765 mmol) was added dropwise over 2-3 min. The reaction mixture was stirred for 5 min after which a solution of 2-cyanopropan-2-yl (3-hydroxypropyl) carbonotrithioate (**2xvi**) (180 mg, 0.765 mmol) dissolved in dry THF (5 mL) was added using air sensitive techniques and the resultant mixture stirred for 5 min. Neopentyl alcohol (34.0 mg, 0.382 mmol) was added and the reaction mixture was left to stir for 10 min. 2,3-Dibromomaleimide (195 mg, 0.765 mmol) was then added to the reaction mixture. The resulting suspension was allowed to remain at -78 °C for 10 min before the cooling bath was removed and the reaction was stirred overnight at ambient temperature under a nitrogen atmosphere. After the removal of THF *in vacuo*, purification of the crude mixture was carried out using column chromatography (silica gel, 1:2 pet. ether/DCM) to yield 2-cyanopropan-2-yl (3-(3,4-dibromo-2,5-dioxo-2,5-dihydro-1*H*-pyrrol-1-yl) propyl) carbonotrithioate as an orange-red oil (242 mg, 0.512 mmol, 67%). ^{1}H NMR (300 MHz, $CDCl_3$) δ_H/ppm: 3.71 (2H, t, J = 6.6 Hz, H7), 3.33 (2H, t, J = 7.2 Hz, H5), 2.03 (2H, d of t, J = 6.6 Hz and 7.2 Hz, H6), 1.87 (6H, s, H1); ^{13}C NMR (75 MHz, $CDCl_3$) δ_C/ppm: 217.0 (C4), 163.8 (C8), 129.5 (C9), 120.2 (C3), 42.6 (C2), 38.5 (C7), 33.2 (C5), 27.1 (C6), 27.0 (C1); HRMS (ESI-TOF) *m*/*z*: $[M + Na]^+$ calculated for $C_{12}H_{12}Br_2N_2NaO_2S_3$: 492.8325; found: 492.8324.

*Synthesis of 3-(3-bromo-4-(isopropylamino)-2,5-dioxo-2,5-dihydro-1H-pyrrol-1-yl) propyl (2-cyanopropan-2-yl) carbonotrithioate (**2xvii**).*

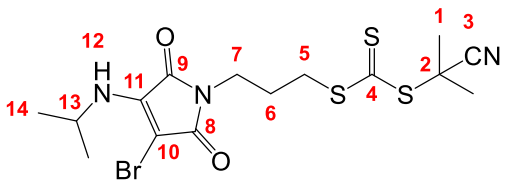

To a suspension of 2-cyanopropan-2-yl (3-(3,4-dibromo-2,5-dioxo-2,5-dihydro-1*H*-pyrrol-1-yl) propyl) carbonotrithioate (**2xvi**) (242 mg, 0.512 mmol) and Na_2CO_3 (54 mg, 0.512 mmol) in THF (HPLC-grade, 10 mL), isopropylamine (44.0 µL, 0.512 mmol) was added. The reaction mixture was stirred at ambient temperature with the conversion of **2xvi** monitored by TLC. After 1 h, THF was removed *in vacuo* and the organic residue was dissolved in DCM (10 mL) and washed with deionized water (3 × 10 mL). The organic layer was dried over $MgSO_4$, filtered and evaporated to dryness. Purification was carried out using column chromatography (silica gel, 1:3 pet. ether/DCM) to yield 3-(3-bromo-4-(isopropylamino)-2,5-dioxo-2,5-dihydro-1*H*-pyrrol-1-yl) propyl (2-cyanopropan-2-yl) carbonotrithioate as an orange-red oil (150 mg, 0.333 mmol, 65%). ^{1}H NMR (400 MHz, $CDCl_3$) δ_H/ppm: 5.30 (1H, br d, J = 8.4 Hz, H12), 4.40 (1H, d of sept., J = 6.8 Hz and 8.4 Hz, H13), 3.61 (2H, t, J = 6.8 Hz, H7), 3.32 (2H, t, J = 7.2 Hz, H5), 2.00 (2H, d of t, J = 6.8 Hz and 7.2 Hz, H6), 1.87 (6H, s, H1), 1.30 (6H, d, J = 6.8 Hz, H14); ^{13}C NMR (100 MHz, $CDCl_3$) δ_C/ppm: 217.2 (C4), 167.8 (C8), 166.1 (C9), 145.0 (C11), 120.3 (C3), 44.8 (C13), 42.5 (C2), 37.3 (C7), 33.5 (C5), 27.3 (C6), 27.0 (C1), 23.7 (C14).

2.6. References

1 A. B. Mabire, M. P. Robin, W.-D. Quan, H. Willcock, V. G. Stavros and R. K. O'Reilly, *Chem. Commun.*, 2015, **51**, 9733–9736.
2 M. P. Robin, P. Wilson, A. B. Mabire, J. K. Kiviaho, J. E. Raymond, D. M. Haddleton and R. K. O'Reilly, *J. Am. Chem. Soc.*, 2013, **135**, 2875–2878.
3 M. P. Robin and R. K. O'Reilly, *Chem. Sci.*, 2014, **5**, 2717–2723.
4 M. P. Robin, J. E. Raymond and R. K. O'Reilly, *Mater. Horizons*, 2015, **2**, 54–59.
5 F. F. Schumacher, M. Nobles, C. P. Ryan, M. E. B. Smith, A. Tinker, S. Caddick and J. R. Baker, *Bioconjug. Chem.*, 2011, **22**, 132–136.
6 M. W. Jones, R. A. Strickland, F. F. Schumacher, S. Caddick, J. R. Baker, M. I. Gibson and D. M. Haddleton, *J. Am. Chem. Soc.*, 2012, **134**, 1847–1852.
7 M. E. B. Smith, F. F. Schumacher, C. P. Ryan, L. M. Tedaldi, D. Papaioannou, G. Waksman, S. Caddick and J. R. Baker, *J. Am. Chem. Soc.*, 2010, **132**, 1960–1965.
8 F. F. Schumacher, V. A. Sanchania, B. Tolner, Z. V. F. Wright, C. P. Ryan, M. E. B. Smith, J. M. Ward, S. Caddick, C. W. M. Kay, G. Aeppli, K. A. Chester and J. R. Baker, *Sci. Rep.*, 2013, **3**, 1525.
9 C. P. Ryan, M. E. B. Smith, F. F. Schumacher, D. Grohmann, D. Papaioannou, G. Waksman, F. Werner, J. R. Baker and S. Caddick, *Chem. Commun.*, 2011, **47**, 5452–5454.
10 C. M. Grison, G. M. Burslem, J. A. Miles, L. K. A. Pilsl, D. J. Yeo, Z. Imani, S. L. Warriner, M. E. Webb and A. J. Wilson, *Chem. Sci.*, 2017, **8**, 5166–5171.
11 L. M. Tedaldi, M. E. B. Smith, R. I. Nathani and J. R. Baker, *Chem. Commun.*, 2009, **43**, 6583–6585.
12 C. Marculescu, H. Kossen, R. E. Morgan, P. Mayer, S. A. Fletcher, B. Tolner, K. A. Chester, L. H. Jones and J. R. Baker, *Chem. Commun.*, 2014, **50**, 7139–7142.
13 S. A. Fletcher, P. K. B. Sin, M. Nobles, E. Årstad, A. Tinker and J. R. Baker, *Org. Biomol. Chem.*, 2015, **13**, 9559–9563.
14 M. P. Robin, M. W. Jones, D. M. Haddleton and R. K. O'Reilly, *ACS Macro Lett.*, 2012, **1**, 222–226.
15 M. P. Robin, S. A. M. Osborne, Z. Pikramenou, J. E. Raymond and R. K. O'Reilly, *Macromolecules*, 2016, **49**, 653–662.
16 A. B. Mabire, M. P. Robin, H. Willcock, A. Pitto-Barry, N. Kirby and R. K. O'Reilly, *Chem. Commun.*, 2014, **50**, 11492–11495.
17 J. Yan, R. Wang, D. Pan, R. Yang, Y. Xu, L. Wang and M. Yang, *Polym. Chem.*, 2016, **7**, 6241–6249.
18 Y. Cui, Y. Yan, Y. Chen and Z. Wang, *Macromol. Chem. Phys.*, 2012, **214**, 470–477.
19 S. Long, Q. Tang, Y. Wu, L. Wang, K. Zhang and Y. Chen, *React. Funct. Polym.*, 2013, **80**, 15–20.
20 J.-J. Yan, D. Wang, D.-C. Wu and Y.-Z. You, *Chem. Commun.*, 2013, **49**, 6057–6059.
21 J. Gaitzsch, V. Chudasama, E. Morecroft, L. Messager and G. Battaglia, *ACS Macro Lett.*, 2016, **5**, 351–354.
22 M. P. Robin, A. B. Mabire, J. C. Damborsky, E. S. Thom, U. H. Winzer-Serhan, J. E. Raymond and R. K. O'Reilly, *J. Am. Chem. Soc.*, 2013, **135**, 9518–9524.
23 S. A. Papadimitriou, M. P. Robin, D. Ceric, R. K. O'Reilly, S. Marino and M. Resmini, *Nanoscale*, 2016, **8**, 17340–17349.
24 M. P. Robin and R. K. O'Reilly, *Polym. Int.*, 2014, **64**, 174–182.
25 H. Wang, M. Xu, M. Xiong and J. Cheng, *Chem. Commun.*, 2015, **51**, 4807–4810.
26 M. Staniforth, W.-D. Quan, T. N. V Karsili, L. A. Baker, R. K. O'Reilly and V. G. Stavros, *J. Phys. Chem. A*, 2017, **121**, 6357–6365.

27 A. B. Mabire, Q. Brouard, A. Pitto-Barry, R. J. Williams, H. Willcock, N. Kirby, E. Chapman and R. K. O'Reilly, *Polym. Chem.*, 2016, **7**, 5943–5948.
28 S. Perrier, *Macromolecules*, 2017, **50**, 7433–7447.
29 G. Gody, T. Maschmeyer, P. B. Zetterlund and S. Perrier, *Nat. Commun.*, 2013, **4**, 2505.
30 G. Gody, P. B. Zetterlund, S. Perrier and S. Harrisson, *Nat. Commun.*, 2016, **7**, 8.
31 G. Gody, T. Maschmeyer, P. B. Zetterlund and S. Perrier, *Macromolecules*, 2014, **47**, 639–649.
32 D. J. Keddie, *Chem. Soc. Rev.*, 2014, **43**, 496–505.
33 M. Benaglia, J. Chiefari, Y. K. Chong, G. Moad, E. Rizzardo and S. H. Thang, *J. Am. Chem. Soc.*, 2009, **131**, 6914–6915.
34 D. J. Keddie, G. Moad, E. Rizzardo and S. H. Thang, *Macromolecules*, 2012, **45**, 5321–5342.
35 N. Petzetakis, A. P. Dove and R. K. O'Reilly, *Chem. Sci.*, 2011, **2**, 955–960.
36 G. Moad, E. Rizzardo and S. H. Thang, *Aust. J. Chem.*, 2012, **65**, 985–1076.
37 M. A. Walker, *J. Org. Chem.*, 1995, **60**, 5352–5355.
38 K. H. Uk, Y. Y. Chang, S. S. Jin and Y. J. Ho, *J. Polym. Sci. Part A: Polym. Chem.*, 2012, **51**, 774–779.
39 Y. C. Yu, H. S. Cho, W.-R. Yu and J. H. Youk, *Polymer*, 2014, **55**, 5986–5990.
40 M. Kang, S. Y. Lee, H. H. Shin, Y. C. Yu and J. H. Youk, *Polymer*, 2016, **87**, 108–113.
41 Y. Youngchang, K. M. Sang, J. Jaehun, Z. Yingying, K. Mounggon, C. Kyeongwoon, G. Johannes, Y. J. Ho, B. S. M. and K. Jinsang, *Angew. Chemie*, 2017, **129**, 16425–16429.
42 M. C. Arno, M. Inam, Z. Coe, G. Cambridge, L. J. Macdougall, R. Keogh, A. P. Dove and R. K. O'Reilly, *J. Am. Chem. Soc.*, 2017, **139**, 16980–16985.
43 A. J. Convertine, D. S. W. Benoit, C. L. Duvall, A. S. Hoffman and P. S. Stayton, *J. Control. Release*, 2009, **133**, 221–229.
44 M. P. Robin, in *PhD Thesis - Chapter 6*, Univeristy of Warwick, 2014.
45 J. Skey and R. K. O'Reilly, *Chem. Commun.*, 2008, **35**, 4183–4185.
46 J. W. John Bosco, B. Rama Raju and A. K. Saikia, *Synth. Commun.*, 2004, **34**, 2849–2855.
47 J. Bokhove, T. J. Visser, B. Schuur and A. B. de Haan, *React. Funct. Polym.*, 2015, **86**, 67–79.
48 T. W. Green and P. G. M. Wuts, *Protective Groups in Organic Synthesis*, Wiley-Interscience, 1999.
49 B. ElAmin, G. M. Anantharamaiah, G. P. Royer and G. E. Means, *J. Org. Chem.*, 1979, **44**, 3442–3444.
50 A. M. Felix, E. P. Heimer, T. J. Lambros, C. Tzougraki and J. Meienhofer, *J. Org. Chem.*, 1978, **43**, 4194–4196.
51 F.-X. Felpin and E. Fouquet, *Chem. Eur. J.*, 2010, **16**, 12440–12445.
52 J. M. Khurana and R. Arora, *Synthesis*, 2009, **7**, 1127–1130.
53 T. Tsuji, T. Kataoka, M. Yoshioka, Y. Sendo, Y. Nishitani, S. Hirai, T. Maeda and W. Nagata, *Tetrahedron Lett.*, 1979, **20**, 2793–2796.
54 T. Akiyama, H. Hirofuji, A. Hirose and S. Ozaki, *Synth. Commun.*, 1994, **24**, 2179–2185.
55 A. E. G. Baker, E. Marchal, K. A. R. Lund and A. Thompson, *Can. J. Chem.*, 2014, **92**, 1175–1185.

3. Investigating the self-assembly behavior of pH-responsive micelles *via* copolymer blending and fluorescence labelling

3.1. Abstract

Understanding, predicting and controlling the self-assembly behavior of stimuli-responsive block copolymers remains a pertinent challenge. With regards to this, the copolymer blending protocol provides an efficient and accessible methodology for obtaining a range of intermediate polymeric nanostructures simply by blending two diblock copolymers with identical block lengths in the desired molar mixing ratio to target specific stimuli-response. Herein, the limitations and requirements of the copolymer blending protocol was investigated with a focus upon the effect of blending relatively hydrophobic amphiphilic diblock copolymers comprised of both short core-forming blocks and low T_g comonomers. To this end, the self-assembly behavior of pure *versus* blended micelles in aqueous solution was studied for a series of amphiphilic pH-responsive p(DMAEMA)-*b*-p(*n*-BuMA-*co*-DMAEMA) diblock copolymers, for which *n*-BuMA incorporation in the core-forming block was varied from 50% to 89%. Further investigation into the properties and internal structures of pH-responsive diblock copolymer micelles was conducted through fluorescence analysis *via* core-functionalization using a novel ABM-functionalized RAFT agent. Finally, the critical micelle concentration, stimuli-responsiveness, and the degree of core hydration for fluorescent pH-responsive polymer nanostructures was explored *via* steady-state fluorescence spectroscopy.

3.2. Introduction

As outlined in Chapter 1, amphiphilic block copolymers are similar in nature to small molecule surfactants and spontaneously self-assemble when dispersed in a selective solvent for the associative block.[1] A key characteristic of small molecule surfactants is that upon self-assembly they generate dynamic nanostructures in solution due to the rapid and constant exchange of single surfactant molecules between self-assembled structures, thereby driving the system to thermodynamic equilibrium.[2,3] Conversely, the self-assembly behavior of amphiphilic block copolymers in aqueous solution can be difficult to predict with out-of-equilibrium or 'frozen' nanostructures often produced.[4,5] This phenomenon has been attributed to the absence or immeasurably slow exchange of free polymer chains (unimers) between polymer nanostructures,[1,4–16] and thus amphiphilic block copolymer self-assembly has been found to be dependent upon both thermodynamic and kinetic constraints.[4,5,8,9,13,16–21] The principal reason for the unfavorable exchange dynamics often observed for amphiphilic block copolymers is attributed to a significantly high energy barrier for unimer exchange in aqueous solution.[22,23] Importantly, the latter has been found to be proportional to the length of the solvophobic block and to the interfacial tension (γ) between the solvophobic block and the solvent.[5,7,10,19,24–26] Therefore, the development of successful strategies for moderating the hydrophobic nature of the solvophobic block, as well as controlling the onset of self-assembly through external parameters, such as pH and temperature, have been extensively explored within the literature.[27–33]

3.2.1. Tuning aggregation behavior, stimuli-response and exchange dynamics *via* a copolymerization approach

pH-responsive monomers, such as acrylic acid (AA), 2-(dimethylamino)ethyl methacrylate (DMAEMA) and 2-(diethylamino)ethyl methacrylate (DEAEMA) can be incorporated into the polymer backbone to control the onset of aggregation (Figure 3.1).

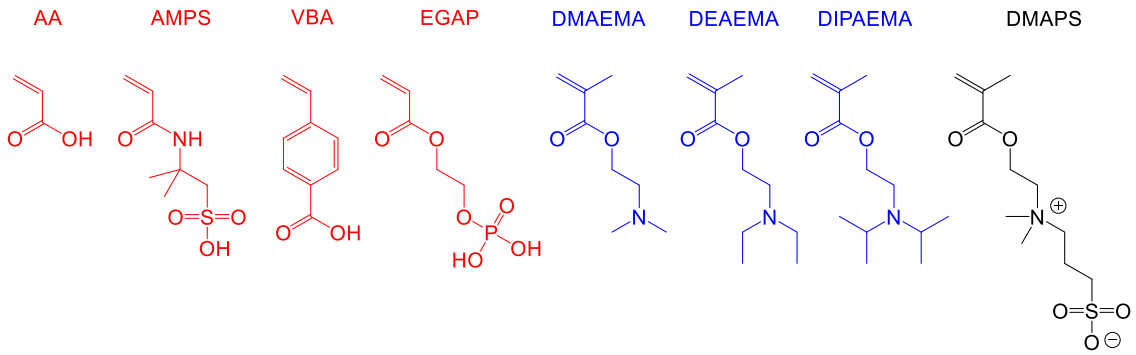

Figure 3.1: Chemical structures of anionic (red), cationic (blue) and zwitterionic (black) pH-responsive monomers. Note: AA = acrylic acid; AMPS = 2-acrylamido-2-methylpropane sulfonic acid; VBA = 4-vinylbenzoic acid; EGAP = ethylene glycol acrylate phosphate; DMAEMA = 2-(dimethylamino)ethyl methacrylate; DEAEMA = 2-(diethylamino)ethyl methacrylate; DIPAEMA = 2-(diisopropylamino)ethyl methacrylate; and DMAPS = 3-dimethyl(methacryloyloxyethyl) ammonium propane sulfonate.

Self-assembly behavior of the resultant block copolymers is governed by pH, as protonation or deprotonation of the ionizable groups causes the degree of hydrophobicity to increase, ultimately initiating aggregation.[13,34–36] Tuning the stimuli-responsiveness of such systems is key when considering their applications which include antimicrobial coatings, oil recovery, detergency, drug and gene delivery, sensors and bio-imaging.[37–43] Block copolymers synthesized *via* the copolymerization of stimuli-responsive monomers with either differently responsive or non-responsive monomers to yield statistical blocks have a distinct advantage over systems composed of homopolymeric blocks.[27] For instance, homopolymeric blocks are restricted to the intrinsic responsiveness of the

monomers used, whereas the use of block-random block copolymers allows one to select the range and extent of stimuli-responsiveness by tuning the copolymer composition. Several authors have explored this concept and evidenced its versatility and effectiveness.[44–64] For example, an ultra pH-sensitive fluorescent statistical block copolymer was successfully synthesized by Gao and co-workers with the onset of aggregation and fluorescence emission controllable over an extremely small pH range.[48,49]

More recently, Appelhans and co-workers have shown that the critical pH-response value for the membrane swelling of UV-crosslinked polymersomes can be manipulated in a controlled manner by changing the random copolymer composition of the associative block.[50] Non-responsive hydrophobic *n*-butyl methacrylate (*n*-BuMA) units or more basic pH-responsive DMAEMA units were incorporated into the core-forming block of a parent poly(ethylene glycol)-*b*-poly(DEAEMA-*co*-4-(3,4-dimethylmaleimidio)butyl methacrylate), (PEG-*b*-p(DEAEMA-*co*-DMIBMA)), amphiphilic diblock copolymer. Consequently, the size transition for the resultant vesicles could be manipulated over a pH range of 5.1 to 6.8 (Figure 3.2).[50] Furthermore, the authors discovered that the hydrodynamic diameter of pH-responsive polymersomes increased with respect to increasing hydrophobicity of the respective core-forming blocks, with aggregation and agglomeration of individual vesicles observed for the higher percentage incorporations of *n*-BuMA.[50]

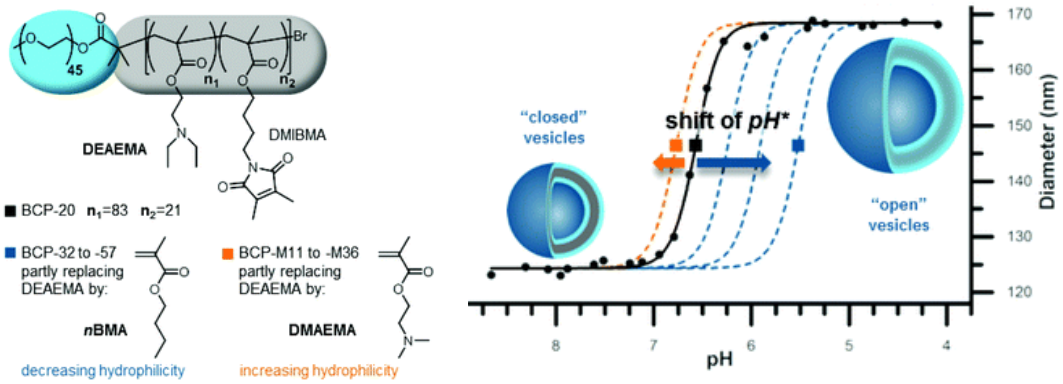

Figure 3.2: Schematic overview of the study conducted by Appelhans and co-workers. Left: chemical structure of the parent PEG_{45}-*b*-p($DEAEMA_{83}$-co-$DMIBMA_{21}$)$_{104}$ amphiphilic block copolymer (BCP-20) and of the additional monomers DMAEMA and *n*-BuMA. Right: DLS titration curves of the self-assembled vesicles with the determination of the critical pH value (pH*). PEG = poly(ethylene glycol), DMIBMA = 4-(3,4-dimethylmaleimidio)butyl methacrylate. Figure and caption adapted from ref 50.

Importantly, it has been demonstrated that the incorporation of hydrophilic units within the core-forming block of amphiphilic block copolymers can facilitate the transformation of 'frozen' kinetically trapped aggregates into dynamic self-assemblies through precise modulation of the core-forming block composition.[35,44–47,53,55–64]

This strategy was first proposed by Bendejacq and co-workers in which pH-responsive acrylic acid units were copolymerized into the associative block of poly(styrene)-*b*-poly(acrylic acid) diblock copolymers.[58,59] Moreover, Colombani and co-workers successfully applied this copolymerization approach to produce poly(*n*-butyl acrylate-*co*-acrylic acid)-*b*-poly(acrylic acid), (p(*n*BA-*co*-AA)-*b*-p(AA)), pH-responsive micelles for which the apparent aggregation number ($N_{agg,\ app}$) was found to depend reversibly upon the pH of the solution.[56,64] Critically, these seemingly dynamic self-assemblies were in stark contrast to the 'frozen' aggregates obtained previously in the literature for analogous diblock copolymers, for which the associative block consisted of a p(*n*BA) homopolymeric block.[7,18]

In another set of studies conducted by Nicolai and co-workers, it was discovered that the random incorporation of hydrophilic pH-sensitive acrylic acid units within hydrophobic p(*n*BA) blocks resulted in the formation of dynamic rather than 'frozen' networks for a series of p(*n*BA-*co*-AA)-*b*-p(AA)-*b*-p(*n*BA-*co*-AA) triblock copolymer analogues.[44,45,53] Furthermore, it was determined that the exchange time of associative blocks between flower-like micelles for these triblock copolyelectrolytes could be varied over more than 10 orders of magnitude depending on the ionization degree (α), or the respective percentage incorporation of acrylic acid units within the hydrophobic blocks.[44,45]

Colombani and co-workers highlighted the universal nature of this methodology for facilitating unimer exchange in amphiphilic block copolymer systems in a subsequent study, whereby the hydrophilic stimuli-responsive monomer was switched from acrylic acid to DMAEMA.[46] Self-assembly of the resultant p(*n*-BuMA$_{0.5}$-*co*-DMAEMA$_{0.5}$)$_{100}$-*b*-p(DMAEMA)$_{235}$ amphiphilic diblock copolymer in water *via* various preparation pathways revealed that aggregation was reversible, pathway-independent and directly corresponded to the ionization degree.[46]

A similar investigation regarding the self-assembly behavior of a dual pH-responsive amphiphilic block copolymer system was recently carried out within the O'Reilly group.[62] A series of p(DEAEMA-*co*-DMAEMA)-*b*-p(DMAEMA) diblock copolymers with varying copolymer compositions in the core-forming block were synthesized *via* reversible addition-fragmentation chain transfer (RAFT) polymerization with their micellization analyzed by light scattering measurements.[62] It was discovered that the pH range at which aggregation occurred could be shifted upon simple adjustment of the copolymer composition of the hydrophobic block (Figure 3.3).[62] Moreover, the authors observed that the aggregation number for the polymer nanostructures increased four-fold when the percentage incorporation of DEAEMA in the core-forming block was increased from 65% to 91%.[62] In a similar manner to the pH-sensitive diblock copolymer systems

highlighted above,[46,56,64] aggregation of the dual pH-responsive micelles formed in this study was shown to be reversible as well as independent of the preparation pathway used.[62]

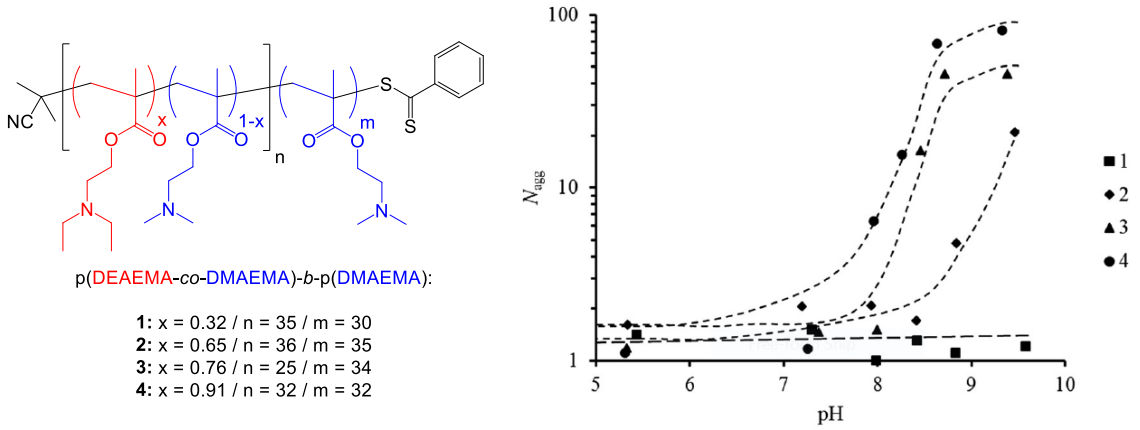

Figure 3.3: Left: chemical structure of the pH-responsive p(DEAEMA-*co*-DMAEMA)-*b*-p(DMAEMA) diblock copolymers (**1-4**) and their respective compositions used in the study by O'Reilly and co-workers.[62] Right: evolution of aggregation number (N_{agg}) with respect to pH for diblock copolymers **1-4**, for which DEAEMA incorporation increases across the series from 32% to 91%. Figure adapted from ref 62.

3.2.2. Tuning polymer properties and self-assembly behavior *via* the copolymer blending protocol

Whilst such literature results highlight the clear advantages of employing a copolymerization approach to tune stimuli-responsiveness, this technique is somewhat limited for controlling and predicting self-assembly behavior. For instance, targeting specific polymer nanostructures for a desired application requires laborious polymer synthesis to identify the correct copolymer composition that will yield the desired characteristics. Another drawback of this approach is that the random copolymerization of any two monomers to produce a statistical copolymer is not universal, and thus the resultant microstructure could adversely alter self-assembly behavior and polymer

properties. For example, the groups of Borisov and Charleux have discovered that the synthesis of amphiphilic diblock copolymers with core-forming blocks that are gradient rather than statistical in nature can significantly affect the reversibility of such systems.[57,60,65]

In light of this, an alternative strategy exists which simply involves blending two block copolymers together, that vary in functionality or stimuli-response, to obtain a range of compositions that are intermediate of the two constituent polymers.[11,26,66–74] The inherent advantages of this copolymer blending methodology are that it precludes exhaustive synthesis as well as offers a scalable and facile route for targeting a wide array of polymer nanostructures.[75] For instance, the blending of diblock copolymers has been successfully utilized in the literature to produce nanoparticle morphologies that are typically not accessed through conventional self-assembly of a single diblock copolymer system.[22,76,77] However, the formation of well-defined blended nanostructures *via* the mixing of two diblock copolymers together is non-trivial and has been found to be dependent upon a multitude of variables, including the difference in length and chemistry of the individual blocks for both diblock copolymers, the propensity for each diblock copolymer to self-assemble under the experimental conditions, the chosen molar mixing ratio, and the concentration.[55,78–92]

Despite the numerous reports concerning diblock copolymer blending, there is limited literature focused upon comparing the self-assembly behavior of blended diblock copolymer samples to pure diblock copolymer samples of the same composition.[50,67,75,93] With regards to comparing self-assemblies produced *via* copolymer blending, it is pertinent to differentiate between the two different types of polymer nanostructures. Pure nanostructures are those self-assembled from a single block copolymer with a specific composition, whilst blended nanostructures are those self-assembled from a block copolymer mixture of two block copolymers comprised of different compositions.

Importantly, theoretical studies have indicated that blended micelles with the same structure to those generated by pure micelles of the same target composition are possible as long as both thermodynamic equilibrium is reached and the incompatibility between the two self-assembling block copolymers is relatively weak.[69,71] For example, Benyahia and co-workers discovered that blended micelles composed of poly(ethylene oxide) with different alkyl end group lengths exhibited identical viscoelastic properties to those obtained from pure micelles of the same composition.[67] However, it was observed that blended micelles often differed structurally to pure micelles which the authors attributed to the formation of 'frozen' aggregates.[5,67,69,71]

Interestingly, a thermodynamic equilibrium with the dynamic exchange of unimers between micelle cores appeared to be present for the series of p(DEAEMA-*co*-DMAEMA)-*b*-p(DMAEMA) amphiphilic diblock copolymers discussed in the previous section (Figure 3.3).[62] In the resultant study carried out by O'Reilly and co-workers,[75] blended micelles were prepared *via* two different copolymer blending protocols which are depicted in Figure 3.4. Unimer blending (UB) involved mixing dry diblock copolymer powders together to match the percentage incorporation of DEAEMA in the analogous pure diblock copolymer, followed by self-assembly (Figure 3.4, Method A).[75] Micelle blending (MB) entailed solubilizing the constituent diblock copolymers (P-32 and P-91) separately before mixing to match the desired DEAEMA composition (Figure 3.4, Method B).[75]

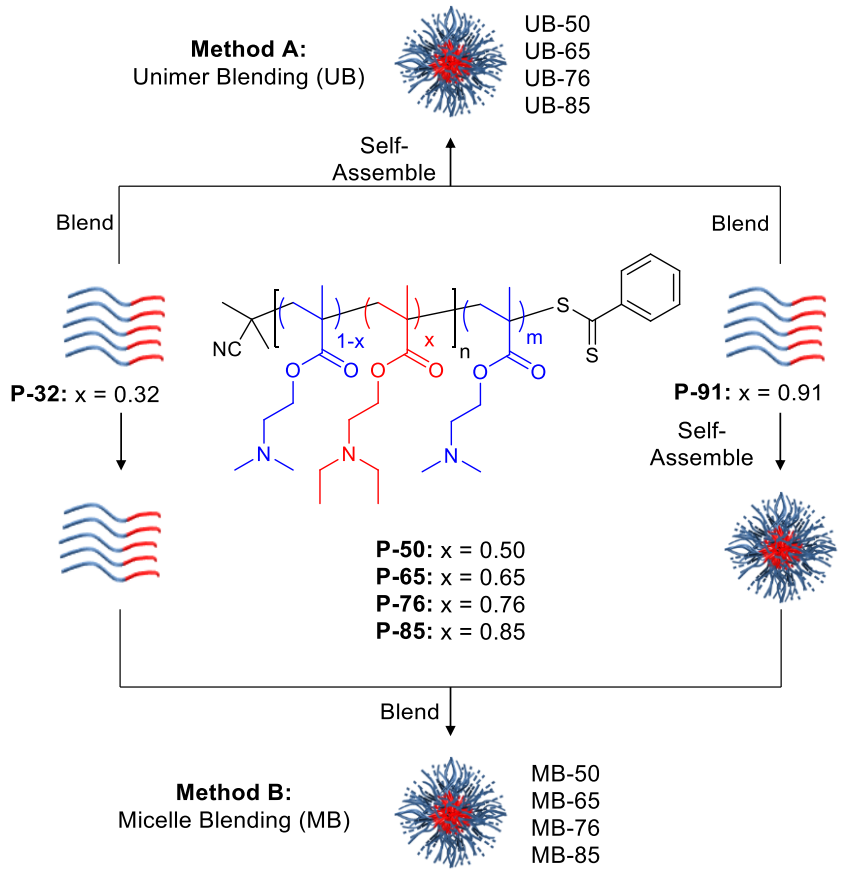

Figure 3.4: Schematic demonstrating the copolymer blending protocols employed by O'Reilly and co-workers: Method A (unimer blending) and Method B (micelle blending). Centre: chemical structure of p(DEAEMA-*co*-DMAEMA)-*b*-p(DMAEMA) diblock copolymers. Figure and caption adapted from ref 75.

Significantly, O'Reilly and co-workers discovered that blended micelles that are structurally identical to pure micelles with the same DEAEMA composition formed irrespective of the copolymer blending protocol used (Figure 3.5).[75] The authors therefore concluded that thermodynamic equilibrium must have been reached for this diblock copolymer system which allowed reorganization and comicellization to occur.[75]

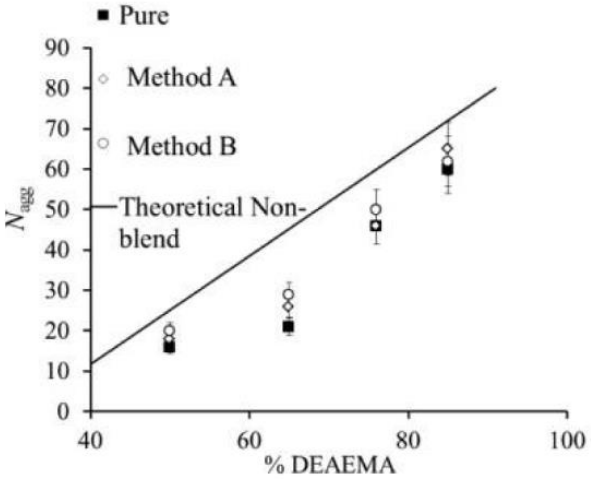

Figure 3.5: Aggregation number (N_{agg}) with respect to percentage incorporation of DEAEMA in the micelle core for both copolymer blending protocols: Method A (unimer blending) and Method B (micelle blending). Theoretical aggregation number for a non-blended mixture (straight line) and N_{agg} of the pure diblock copolymer micelles are shown for comparison. Figure and caption adapted from ref 75.

Further experimental studies by O'Reilly and co-workers revealed that the success of the copolymer blending protocol was found to be largely governed by two key factors.[93] Firstly, diblock copolymers required a core glass transition temperature (T_g) lower than the experimental temperatures used to ensure sufficient core mobility.[93] Secondly, a low enough energy barrier to allow dynamic exchange of unimers to occur was essential, which was shown to be dependent upon both the hydrophobicity and length of the associative block.[93]

However, to explore the effect of a high energy barrier upon resultant unimer exchange dynamics, O'Reilly and co-workers simultaneously increased both the length and degree of hydrophobicity of the associative block for the chosen diblock copolymers.[93] In this particular experiment, a series of low T_g poly(2-ethylhexyl acrylate-*co*-*N*-*N*-dimethylacrylamide)-*b*-poly(*N*-*N*-dimethylacrylamide) diblock copolymers were synthesized, for which the core-forming block length was increased from 70 to 250 whilst the percentage incorporation of the hydrophobic 2-ethylhexyl acrylate monomer was also increased from 40-60% to 70-90%.[93] Consequently, whilst the authors confirmed that the

resultant diblock copolymer micelles were unable to reach thermodynamic equilibrium,[93] it is unclear whether this result was due to increasing the core-forming block length, increasing the degree of hydrophobicity or a combination of the two. Moreover, the range of block copolymer compositions investigated in this study to probe the limitations of the copolymer blending protocol was relatively narrow.[93] Solely non-responsive amphiphilic diblock copolymers were analyzed and the hydrophobic monomers selected were composed of bulky alkyl groups and thus possessed high surface tension values.[93]

Recently, Chassenieux and co-workers investigated the comicellization and corresponding effect upon the rheological properties for blended mixtures of pH-responsive BAB triblock copolymers, whereby the hydrophobic B block was a random copolymer composed of hydrophilic and hydrophobic units.[55] Interestingly, it was discovered that a 'frozen' network could be transformed into a dynamic system by the co-assembly of very dynamic chains with less dynamic chains, provided that both triblock copolymers self-assembled at the experimental ionization degree.[55] On the other hand, O'Reilly and co-workers have previously demonstrated that for a similar pH-responsive system, self-assembly of the two constituent p(DMAEMA-*co*-DEAEMA)-*b*-p(DMAEMA) diblock copolymers at the experimental ionization degree was not required for successful copolymer blending (Figure 3.4).[62,75]

Ultimately, further investigation into the limitations and requirements of the copolymer blending protocol is necessary. In this Chapter, the self-assembly behavior of pure *versus* blended micelles for a series of p(DMAEMA)$_{100}$-*b*-p(*n*-BuMA-*co*-DMAEMA)$_{50}$ pH-responsive amphiphilic diblock copolymers, with varying amounts of permanently hydrophobic *n*-BuMA in the core-forming block, will be studied. Furthermore, the properties, internal structures and exchange dynamics of these aggregates will be explored through fluorescence analysis by core-functionalization using an aminobromomaleimide (ABM) fluorophore.

3.3. Results and Discussion

3.3.1. Synthesis of pH-responsive amphiphilic diblock copolymers

To explore the effects of changing the degree of hydrophobicity upon unimer exchange dynamics, a series of pH-responsive p(DMAEMA)$_{100}$-*b*-p(*n*-BuMA-*co*-DMAEMA)$_{50}$ amphiphilic diblock copolymers were prepared *via* RAFT polymerization. In contrast to the bulky hydrophobic comonomers used by O'Reilly and co-workers to investigate the limitations of the copolymer blending protocol,[93] *n*-butyl methacrylate was selected owing to its low T_g (20 °C),[94] relatively short alkyl side group and intermediate surface tension value (28.8 mN m^{-1}).[95] Similar block lengths were targeted for all diblock copolymers with a target degree of polymerization (DP) for the corona-forming block of 100 and for the core-forming block, a DP of 50. In relation to the p(*n*-BuMA$_{0.5}$-*co*-DMAEMA$_{0.5}$)$_{100}$-*b*-p(DMAEMA)$_{235}$ amphiphilic diblock copolymer previously reported by Colombani and co-workers,[46] block lengths were decreased in an attempt to lower the kinetic energy barrier related to the extraction of the hydrophobic block from the micelle core.[24,93] Moreover, the percentage incorporation of hydrophobic *n*-BuMA within the statistical p(*n*-BuMA-*co*-DMAEMA) core-forming block was increased incrementally from 50% to 90% across the diblock copolymer series. It was envisaged that the use of low T_g pH-responsive amphiphilic diblock copolymers comprised of relatively short core-forming blocks with high hydrophobic monomer incorporations will provide further understanding regarding the limitations of the copolymer blending protocol.

Initially, a p(DMAEMA) macro chain transfer agent (macroCTA) was synthesized *via* RAFT polymerization in 1,4-dioxane at 70 °C using 2-cyanopropan-2-yl dodecyl carbonotrithioate (CPDDT), as outlined in Scheme 3.1. Note that the order in which the blocks were synthesized was chosen to ensure that all diblock copolymers had identical

corona-forming p(DMAEMA) blocks. Consequently, comparison of the self-assembly behavior exhibited by the resultant amphiphilic diblock copolymers will be solely as a result of differences in the chemical nature of the core-forming block.

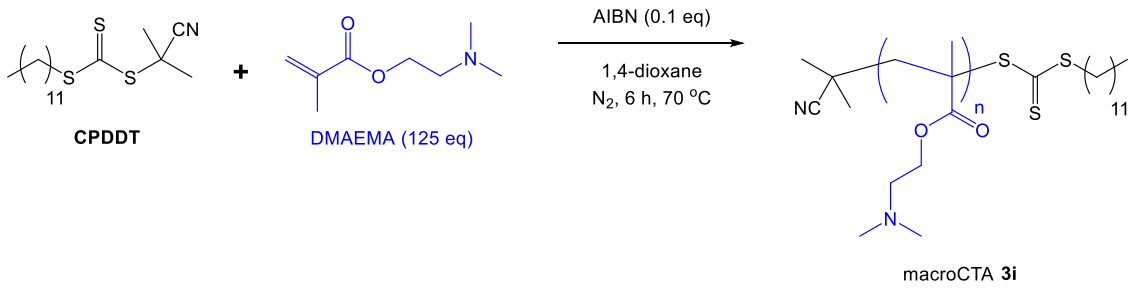

Scheme 3.1: RAFT polymerization of DMAEMA with 2-cyanopropan-2-yl dodecyl carbonotrithioate (CPDDT) to produce a p(DMAEMA)$_n$ homopolymer (macroCTA **3i**). AIBN = 2,2'-azobisisobutyronitrile.

It was key that the overall conversion for the RAFT polymerization remained below 90% to limit the number of termination reactions and ensure retention of the trithiocarbonate end group. Therefore, DMAEMA conversion was monitored throughout *via* ^{1}H NMR spectroscopy, with the RAFT polymerization quenched after 6 h upon reaching the desired block length (DP = 100). Upon purification, a p(DMAEMA)$_{100}$ macroCTA (**3i**) was isolated; characterization data for which is summarized in Table 3.1.

macroCTA	ρ^a **(%)**	DP^b	$M_{n,\,theo}{}^a$ **(kDa)**	$M_{n,\,NMR}{}^b$ **(kDa)**	$M_{n,\,SEC}{}^c$ **(kDa)**	$Đ_M{}^c$
3i	80	100	16.1	16.1	22.7	1.19

Table 3.1: Characterization data for a p(DMAEMA)$_n$ homopolymer (macroCTA **3i**). Key: [a] monomer conversion was calculated by ^{1}H NMR spectroscopy of the crude polymerization mixture (300 MHz, $CDCl_3$); [b] determined by end group analysis using ^{1}H NMR spectroscopy (400 MHz, $CDCl_3$); [c] obtained by SEC analysis based on poly(methyl methacrylate) [p(MMA)] standards with DMF as the eluent.

From the ^{1}H NMR spectrum of macroCTA **3i** (Figure 3.6), the degree of polymerization was calculated through end group analysis by comparing the peak integrals corresponding to the trithiocarbonate end group C*H*$_2$S resonance at 3.25 ppm (H$_7$) to that of the polymer's OC*H*$_2$CH$_2$N, OCH$_2$C*H*$_2$N and OCH$_2$CH$_2$N(C*H*$_3$)$_2$ resonances at 4.05, 2.56 and 2.21 ppm (H$_4$, H$_5$ and H$_6$ respectively).

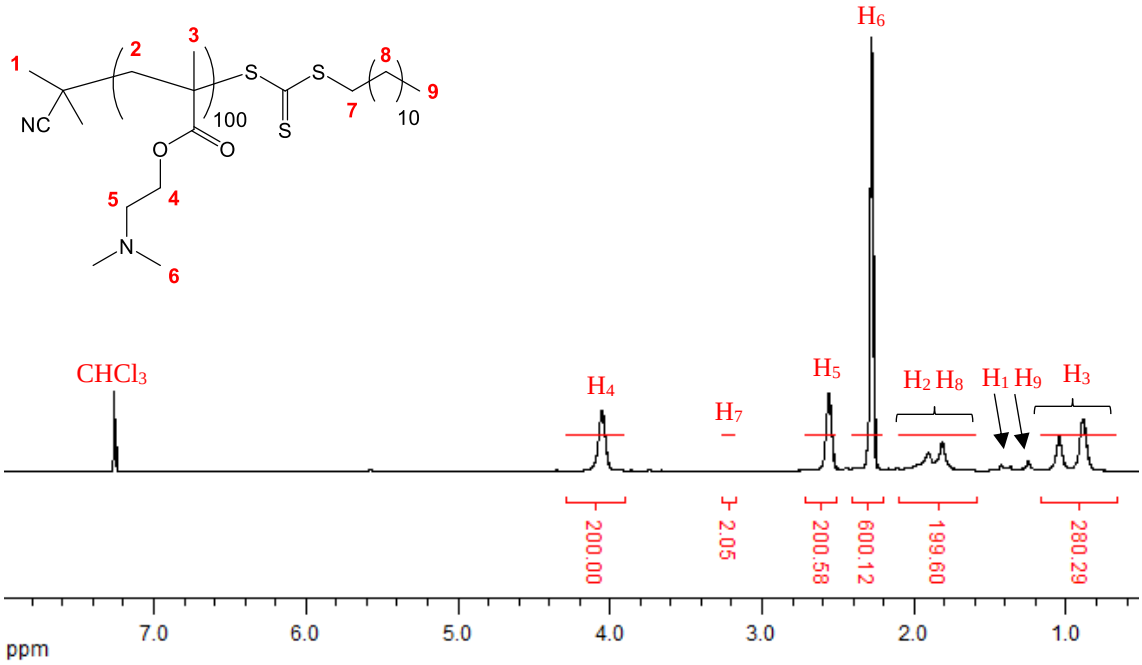

Figure 3.6: ^{1}H NMR spectrum (400 MHz, $CDCl_3$) of the p(DMAEMA)$_{100}$ macroCTA **3i**.

Upon SEC analysis, the p(DMAEMA) homopolymer (**3i**) displayed a symmetrical, unimodal molecular weight distribution with a low dispersity ($Đ_M$ = 1.19), indicating good control over the RAFT polymerization using CPDDT (Figure 3.7). Importantly, the molecular weight distributions determined by SEC using an RI and UV detector (recorded at 309 nm) overlap appreciably, thereby confirming that the trithiocarbonate end group was retained for the majority of the polymer chains which is essential for efficient chain extension.

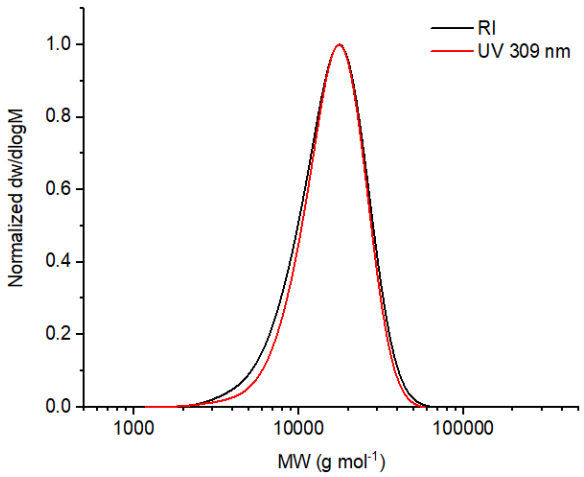

Figure 3.7: Molecular weight distributions determined by SEC ($CHCl_3$ as the eluent and calibrated against poly(styrene) [p(St)] standards) using both an RI and UV (recorded at 309 nm) detector for the $p(DMAEMA)_{100}$ homopolymer (macroCTA **3i**).

$p(DMAEMA)_{100}$ macroCTA **3i** was then chain extended *via* RAFT copolymerization of *n*-BuMA and DMAEMA at 70 °C in 1,4-dioxane, to form the desired series of amphiphilic pH-responsive diblock copolymers (Scheme 3.2). Core-forming blocks of total DP = 50 were targeted and monomer feeds were selected such that the percentage composition of hydrophobic *n*-BuMA in the core-forming block ranged from 50% to 90%.

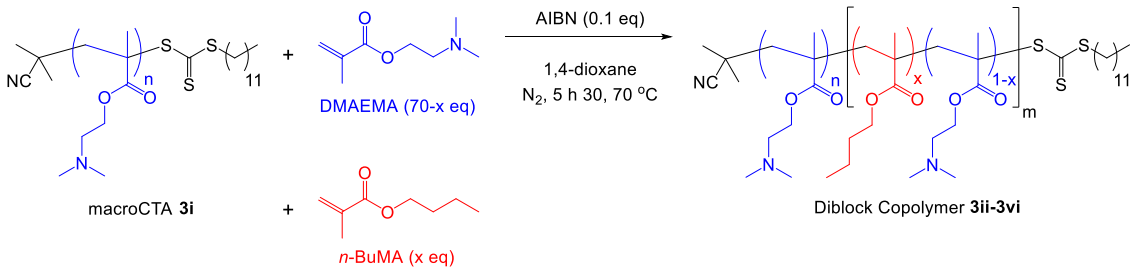

Scheme 3.2: Chain extension of macroCTA **3i** *via* RAFT copolymerization of *n*-BuMA and DMAEMA to produce a series of amphiphilic pH-responsive $p(DMAEMA)_n$-*b*-$p(n\text{-}BuMA_x\text{-}co\text{-}DMAEMA_{1-x})_m$ diblock copolymers (**3ii-3vi**).

Monomer conversion was monitored *via* ^{1}H NMR spectroscopy with chain extensions quenched upon reaching the desired block length. Upon purification, a series of five amphiphilic pH-responsive p(DMAEMA)$_n$-*b*-p(*n*-BuMA$_x$-*co*-DMAEMA$_{1-x}$)$_m$ diblock copolymers (**3ii-3vi**) were isolated; characterization data for which is summarized in Table 3.2.

With regards to the microstructure of the core-forming block, the reactivity ratios of *n*-BuMA with DMAEMA have been previously calculated in the literature and shown to yield a statistical copolymer.[46,96] As such, both monomers should be randomly incorporated into the core-forming block for all five amphiphilic diblock copolymers **3ii-3vi** and thus no phase separation of incompatible hydrophobic *n*-BuMA and hydrophilic DMAEMA units in the micellar core is expected to occur upon self-assembly.

Diblock Copolymer	***n*[a]**	***n*-BuMA:DMAEMA Feed Ratio[b]**	***x*[c]**	***m*[c]**	$M_{n,\,NMR}$[c] **(kDa)**	$M_{n,\,SEC}$[d] **(kDa)**	$Đ_M$[d]
3ii	100	1:1	0.50	54	24.2	28.2	1.20
3iii	100	3:2	0.60	52	23.8	27.7	1.19
3iv	100	7:3	0.70	50	23.4	26.4	1.20
3v	100	4:1	0.80	49	23.2	26.0	1.18
3vi	100	9:1	0.89	47	22.8	26.2	1.16

Table 3.2: Characterization data for amphiphilic pH-responsive p(DMAEMA)$_n$-*b*-p(*n*-BuMA$_x$-*co*-DMAEMA$_{1-x}$)$_m$ diblock copolymers **3ii-3vi**. Key: [a] determined by end group analysis of macroCTA **3i** using ^{1}H NMR spectroscopy (400 MHz, $CDCl_3$); [b] initial monomer feed ratio was calculated by ^{1}H NMR spectroscopic analysis of the crude polymerization mixture prior to the onset of polymerization (300 MHz, $CDCl_3$); [c] determined by end group analysis using ^{1}H NMR spectroscopy (400 MHz, $CDCl_3$); [d] obtained by SEC analysis based on p(MMA) standards with DMF as the eluent.

Final diblock copolymer compositions were calculated *via* ^{1}H NMR spectroscopy by comparing: the peak integrals corresponding to the polymer's OCH_2CH_2N resonance at

2.56 ppm (H5); the overlapping peak integrals corresponding to the polymer's OC*H*$_2$CH$_2$N and OC*H*$_2$CH$_2$CH$_2$CH$_3$ resonances at 4.05 and 3.93 ppm (H4 and H9 respectively); and the peak integral corresponding to the polymer's OCH$_2$C*H*$_2$CH$_2$CH$_3$ at 1.61 ppm (H10) to that of the ω-end group C*H*$_2$S resonance at 3.25 ppm (H13) (Figure 3.8). Percentage incorporations of *n*-BuMA and DMAEMA in the statistical p(*n*-BuMA-*co*-DMAEMA) core-forming blocks for each amphiphilic diblock copolymer (**3ii-3vi**) were in excellent agreement with the expected compositions from the initial monomer feed ratios (Table 3.2).

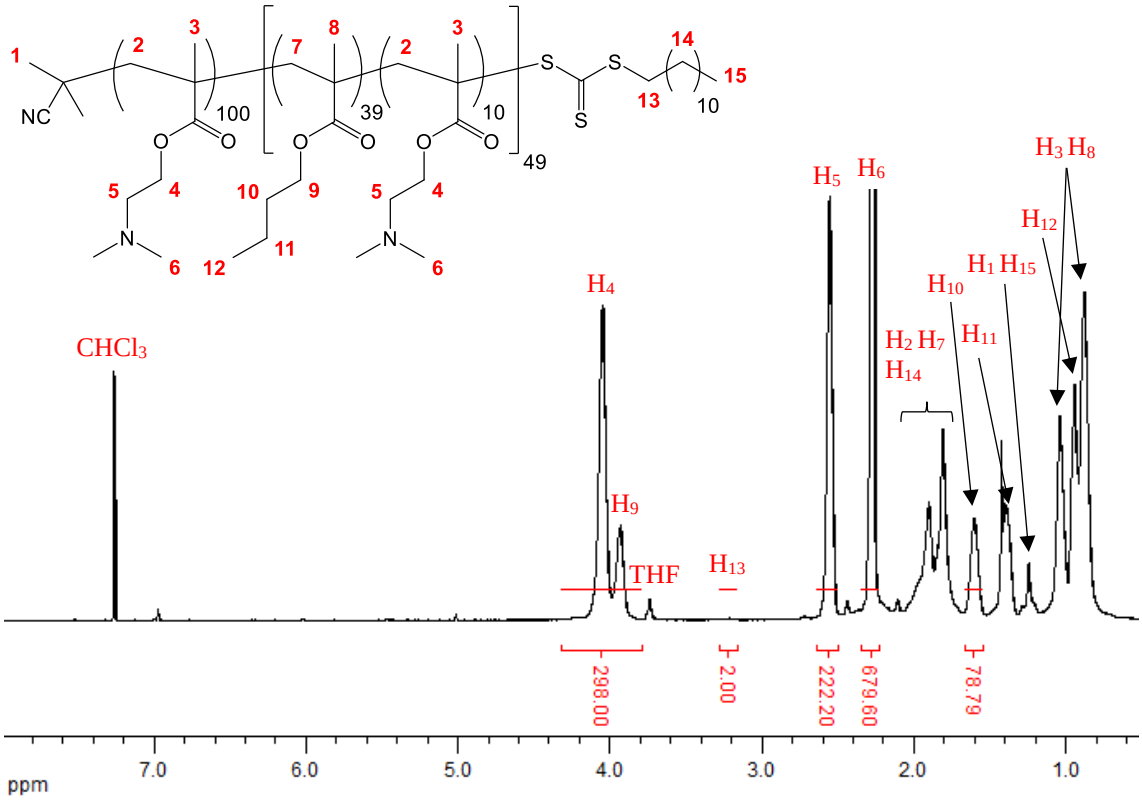

Figure 3.8: ^{1}H NMR spectrum (400 MHz, $CDCl_3$) of the amphiphilic pH-responsive p(DMAEMA)$_{100}$-*b*-p(*n*-BuMA$_{39}$-*co*-DMAEMA$_{10}$)$_{49}$ diblock copolymer **3v**.

Overall, chain extensions were highly efficient with narrow dispersity values achieved for all five amphiphilic pH-responsive diblock copolymers (**3ii-3vi**); ranging from $Đ_M$ = 1.16 – 1.20 in comparison to $Đ_M$ = 1.19 for macroCTA **3i**. Moreover, a distinct increase

in number average molecular weight ($M_{n,\,SEC}$) relative to macroCTA **3i**, was observed for each amphiphilic diblock copolymer (**3ii-3vi**) (Figure 3.9). The absence of low or high molecular weight shoulders in the RI traces obtained for all five p(DMAEMA)$_n$-*b*-p(*n*-BuMA$_x$-*co*-DMAEMA$_{1-x}$)$_m$ diblock copolymers suggested that the extent of initiator-derived copolymer formation or bimolecular polymer-polymer coupling was negligible.

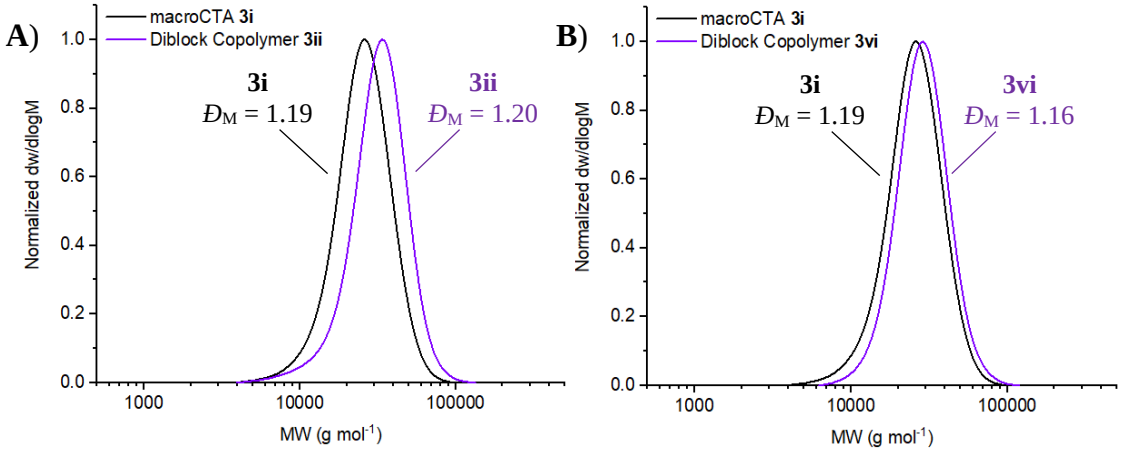

Figure 3.9: Molecular weight distributions determined by SEC (DMF as the eluent and calibrated against p(MMA) standards) using an RI detector for the following p(DMAEMA)$_n$-*b*-p(*n*-BuMA$_x$-*co*-DMAEMA$_{1-x}$)$_m$ diblock copolymers: a) **3ii**, and b) **3vi**. RI trace for p(DMAEMA)$_{100}$ macroCTA **3i** is shown for comparison.

3.3.2. Ionization behavior of pH-responsive amphiphilic diblock copolymers

Next, the ionization behavior for each amphiphilic pH-responsive p(DMAEMA)-*b*-p(*n*-BuMA-*co*-DMAEMA) diblock copolymer **3ii-3vi** was investigated *via* potentiometric titration. Initially, diblock copolymers **3ii-3vi** were dispersed in an aqueous solution with a 1.1 stoichiometric excess of 1 M HCl, with respect to the number of ionizable DMAEMA units, added to ensure complete protonation. Subsequently, the

diblock copolymer solutions were back titrated with 0.1 M NaOH to allow for accurate determination of the evolution of the ionization degree (α) with respect to pH.[54] α is defined as the ionization degree following equation (**3.1**); whereby complete protonation of the amine units corresponds to α = 1 and complete deprotonation of amine units corresponds to a = 0.

$$\alpha = \frac{[NR_2H^+Cl^-]}{[NR_2]_{total}} \qquad \textbf{3.1}$$

Importantly, potentiometric titration with NaOH revealed that all DMAEMA units, including those in the core-forming block, could be ionized and deionized for all five amphiphilic pH-responsive p(DMAEMA)-*b*-p(*n*-BuMA-*co*-DMAEMA) diblock copolymers (**3ii-3vi**) (Figure 3.10). Moreover, the percentage incorporations of pH-responsive DMAEMA units for each diblock copolymer (**3ii-3vi**) determined by potentiometric titration were within a 5% error with respect to the values obtained *via* ^{1}H NMR spectroscopy.

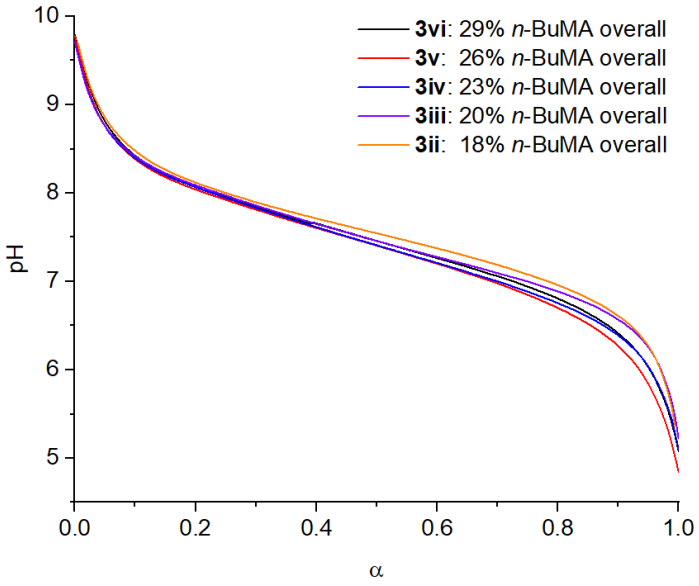

Figure 3.10: Evolution of ionization degree (α) with pH for pH-responsive diblock copolymers **3ii-3vi**.

Unsurprisingly, the random incorporation of *n*-BuMA units within the core-forming block of amphiphilic diblock copolymers did not prevent ionization of the adjacent DMAEMA units, with similar ionization behavior observed previously in the literature for diblock copolyelectrolytes.[46,54,56,58,62,64] Following this, the pKa for all five amphiphilic pH-responsive p(DMAEMA)-*b*-p(*n*-BuMA-*co*-DMAEMA) diblock copolymers was determined by measuring the pH of the solutions at $\alpha = 0.5$. Interestingly, pKa values decreased incrementally from 7.55 to 7.40 with respect to increasing *n*-BuMA content across the series. In contrast, O'Reilly and co-workers measured pKa values of approximately 8.0 for their series of p(DEAEMA-*co*-DMAEMA)-*b*-p(DMAEMA) diblock copolymers.[62] Thus, it appeared that the incorporation of highly hydrophobic *n*-BuMA units into the core-forming block resulted in a significant decrease for the pKa of the pH-responsive DMAEMA units for each diblock copolymer. Overall, the ionization behavior did not differ significantly across the series of pH-responsive diblock copolymers (**3ii**-**3vi**) analyzed herein, despite the differences in core-forming block composition (Table 3.2).

3.3.3. Self-assembly behavior of pH-responsive amphiphilic diblock copolymers

3.3.3.1. Influence of sample preparation upon self-assembly behavior

pH-responsive amphiphilic p(DMAEMA)-*b*-p(*n*-BuMA-*co*-DMAEMA) diblock copolymers **3ii-3vi** were self-assembled *via* the preparation pathway previously utilized by O'Reilly and co-workers.[62] As depicted in Scheme 3.3, self-assembly Method C entailed dispersing pH-responsive diblock copolymers **3ii-3vi** in aqueous solution followed by the addition of the corresponding amount of 1 M HCl to reach $\alpha = 1$. The

ionization degree for each diblock copolymer solution was subsequently lowered to $\alpha = 0$ *via* the addition of 1 M NaOH in small increments over time (see Section 3.5.2 for full details of sample preparation). Note, that final diblock copolymer solutions were prepared at 1 mg mL^{-1} and at a 0.1 M NaCl concentration to prevent the polyelectrolyte effect, which can lead to the apparition of slow modes by light scattering.[23,97]

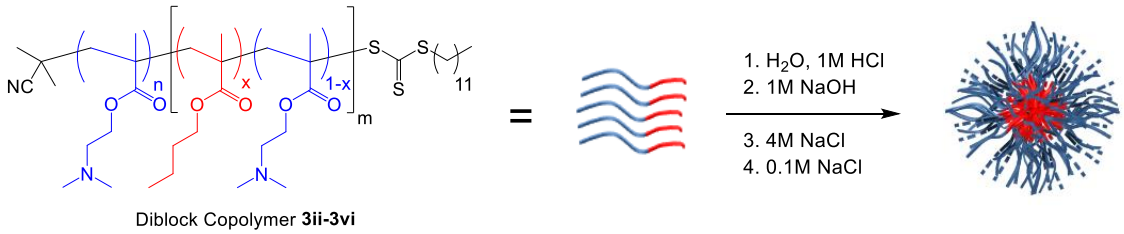

Diblock Copolymer **3ii-3vi**

Scheme 3.3: Self-assembly of pH-responsive amphiphilic p(DMAEMA)$_n$-*b*-p(*n*-BuMA$_x$-*co*-DMAEMA$_{1-x}$)$_n$ diblock copolymers **3ii-3vi** in aqueous solution *via* self-assembly Method C.

Self-assembled nanostructures were characterized by dynamic and static light scattering techniques (DLS and SLS respectively) to determine the hydrodynamic radius (R_h) and aggregation number (N_{agg}). Since all polymer nanostructures investigated provided R_h values which were much smaller than the calculated maximum chain length (L_{max}) of 37.5 nm, coupled with N_{agg} values < 500, it can be assumed that their morphology most likely matched that of a spherical micelle.[23] Considering only one concentration was used in the following analysis, R_h and N_{agg} values measured are apparent rather than absolute but still provide a good indication of micelle size and aggregation.

Initially, the aggregation number and hydrodynamic radius was measured for diblock copolymer micelles self-assembled *via* Method C, see Table 3.3. It was anticipated that an increase in the hydrophobic nature of the core-forming block would lead to a marked increase in the aggregation number, as observed for similar diblock copolymer systems within the literature.[62,98,99] Upon increasing *n*-BuMA incorporation in the core-forming block from 50% (**3ii**) to 89% (**3vi**), N_{agg} and R_h for the corresponding diblock copolymer

micelles increased from 45 to 200 and from 14.8 nm to 21.7 nm, respectively. However, spherical micelles formed from diblock copolymers with intermediate *n*-BuMA loadings (**3iii-3v**) displayed similar aggregation behavior, with N_{agg} values falling within a 5% error of one another. Therefore, it was proposed that spherical micelles self-assembled from diblock copolymers **3iv-3vi** exhibited very slow unimer exchange kinetics and thus thermodynamic equilibrium was not reached within the experimental timescale of 1 day. Consequently, the same light scattering samples were analyzed 15 days and 29 days after initial self-assembly to ascertain whether and at which point thermodynamic equilibrium was reached (Table 3.3). However, there was little change in the light scattering results obtained to suggest that thermodynamic equilibrium had been reached within the timescale of analysis for all five diblock copolymer samples. For instance, spherical micelles formed from diblock copolymers **3iv** (70% *n*-BuMA) and **3v** (80% *n*-BuMA) continued to share similar N_{agg} values (70 *c.f.* 73). Surprisingly, the aggregation number for diblock copolymer micelles formed from **3vi** (89% *n*-BuMA) varied significantly from 200 to 131 to 176 over the three time points, which suggested that some degree of equilibration had occurred. Despite this, closer inspection of the light scattering data obtained for this sample revealed that the observed discrepancies in N_{agg} was due to poor separation of fast and slow modes using the REPES routine.[100] Consequently, measured Kc/R_θ values varied significantly over the range of scattering angles used, with the error calculated from standard deviation much greater than the expected error associated with a SLS experiment of 5%.[23]

Diblock Copolymer	% *n*-BuMA in the core	$N_{agg,\ app}$[a]	$N_{agg,\ app}$[b]	$N_{agg,\ app}$[c]	$R_{h,\ app}$[a] (nm)	$R_{h,\ app}$[b] (nm)	$R_{h,\ app}$[c] (nm)
3ii	50	45 ± 2	42 ± 2	43 ± 2	14.8 ± 0.7	16.8 ± 0.8	16.1 ± 0.8
3iii	60	60 ± 3	66 ± 3	58 ± 3	14.6 ± 0.7	16.0 ± 0.8	16.2 ± 0.8
3iv	70	59 ± 3	73 ± 3	70 ± 4	15.4 ± 0.8	16.6 ± 0.8	17.4 ± 0.9
3v	80	67 ± 3	82 ± 4	73 ± 4	15.9 ± 0.8	18.5 ± 0.9	18.1 ± 0.9
3vi	89	200 ± 10	131 ± 7	176 ± 9	21.7 ± 1.1	26.6 ± 1.3	26.1 ± 1.3

Table 3.3: Summary of light scattering data obtained for spherical micelles formed from p(DMAEMA)-*b*-p(*n*-BuMA-*co*-DMAEMA) diblock copolymers **3ii-3vi** *via* self-assembly method C. N_{agg} values were calculated from SLS. R_h values were calculated from DLS. Key: [a] samples measured one day after self-assembly; [b] samples measured 15 days after self-assembly; [c] samples measured 29 days after self-assembly.

Interestingly, during the preparation of a new series of light scattering samples, a small amount of precipitation was observed upon each incremental addition of 1 M NaOH for micelle solutions formed from diblock copolymers **3v** (80% *n*-BuMA) and **3vi** (89% *n*-BuMA). Considering the precipitate re-dispersed over time, precipitation may have been missed during the preparation of the initial light scattering samples analyzed above. Moreover, light scattering samples prepared for diblock copolymers **3v** and **3vi** appeared cloudy upon reaching the desired ionization degree (α = 0), which was attributed to the formation of aggregates with hydrodynamic radii that were much larger than the calculated L_{max} value. Consequently, it was proposed that the self-assembly method used to prepare diblock copolymer micelles needed to be revised such that the base was added at a lower concentration, combined with a slower rate of addition, to avoid the formation of kinetically trapped out-of-equilibrium nanostructures.[5] Therefore, a new self-assembly protocol was outlined for which 0.01 M NaOH was slowly added to lower the ionization degree of the diblock copolymer solutions. It was envisaged that by allowing the self-assembly of pH-responsive diblock copolymers to occur more slowly, and under milder conditions, the formation of thermodynamically favored nanostructures may be

facilitated.[93] Subsequently, p(DMAEMA)-*b*-p(*n*-BuMA-*co*-DMAEMA) diblock copolymers **3ii-3vi** were self-assembled using the revised protocol (Method D, Scheme 3.4). Note, that no precipitation or formation of cloudy solutions was observed during sample preparation *via* this self-assembly method.

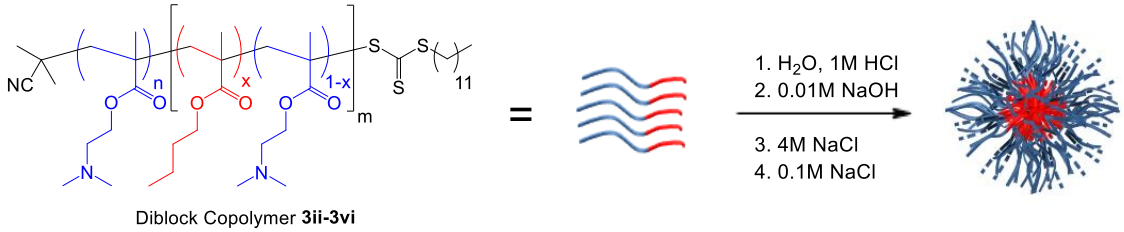

Scheme 3.4: Self-assembly of p(DMAEMA)$_n$-*b*-p(*n*-BuMA$_x$-*co*-DMAEMA$_{1-x}$)$_n$ diblock copolymers **3ii-3vi** in aqueous solution *via* self-assembly Method D.

Resultant self-assembled nanostructures were analyzed by SLS and DLS and compared to diblock copolymer samples prepared *via* self-assembly Method C (Table 3.4). Significantly, N_{agg} increased with respect to *n*-BuMA incorporation across the series of diblock copolymer micelles prepared *via* Method D, with no two diblock copolymer samples falling within a 5-10% error of one another. Moreover, N_{agg} increased fourfold when the percentage of *n*-BuMA incorporation in the core-forming block was increased from 50% (**3ii**) to 90% (**3vi**), coupled with an increase in R_h of 5.4 nm. Therefore, there was a marked improvement in terms of the observed aggregation behavior for diblock copolymer micelles **3ii-3vi** prepared *via* self-assembly Method D.

Diblock Copolymer	% *n*-BuMA in the core	Method C – 1 M NaOH		Method D – 0.01 M NaOH	
		$N_{agg,\ app}$[a]	$R_{h,\ app}$[b] (nm)	$N_{agg,\ app}$[a]	$R_{h,\ app}$[b] (nm)
3ii	50	45 ± 2	14.8 ± 0.7	28 ± 1	14.3 ± 0.7
3iii	60	60 ± 3	14.6 ± 0.7	43 ± 2	15.6 ± 0.8
3iv	70	59 ± 3	15.4 ± 0.8	56 ± 3	15.7 ± 0.8
3v	80	67 ± 3	15.9 ± 0.8	72 ± 4	17.6 ± 0.9
3vi	89	200 ± 10	21.7 ± 1.1	115 ± 6	19.7 ± 1.0

Table 3.4: Summary of light scattering data obtained for spherical micelles formed from p(DMAEMA)-*b*-p(*n*-BuMA-*co*-DMAEMA) diblock copolymers **3ii-3vi** *via* self-assembly method C and self-assembly method D. All samples were measured one day after self-assembly. Key: [a] N_{agg} values were calculated from SLS; [b] R_h values were calculated from DLS.

Overall, the light scattering results obtained for self-assembly Method D were in good agreement with the aggregation behavior previously observed by O'Reilly and co-workers for a similar series of pH-responsive diblock copolyelectrolytes.[62] Nevertheless, a single measurement of diblock copolymer samples at one ionization degree and at one concentration was insufficient for determining whether thermodynamically favored nanostructures had formed for diblock copolymers **3ii-3vi**. As outlined in Section 3.2.1, the reversible association of pH-responsive block copolymers *via* manipulation of the ionization degree has previously been demonstrated within the literature.[46,56,62,64] The authors attributed this seemingly dynamic aggregation behavior to the potential presence of a thermodynamic equilibrium, whereby unimer exchange was facilitated.[46,62,75] However, it is important to note that reversible association does not imply that a dynamic equilibrium exists at any given ionization degree.[5] Instead, the block copolymer system could still be 'frozen' before or after a change in ionization

degree but significantly, at certain intermediate ionization degrees dynamic exchange of unimers between polymer nanostructures must have occurred.

To investigate whether self-assembly Method D resulted in the formation of thermodynamically favored nanostructures, the reversible association of pH-responsive diblock copolymers **3ii-3vi** was explored. First, the ionization degree for the series of diblock copolymer micelles previously self-assembled *via* Method D (Scheme 3.4) was increased from α = 0 to α = 1 using 1M HCl. In addition, a second series of diblock copolymer solutions was prepared for which pH-responsive diblock copolymers **3ii-3vi** were dispersed in aqueous solution and 1 M HCl added to reach α = 1 (Scheme 3.5). Overall, two series of diblock copolymer samples at α = 1 were obtained, for which the target ionization degree was reached before self-assembly or post self-assembly. Note, that at α = 1 it was anticipated that diblock copolymers **3ii-3vi** would form unimers.

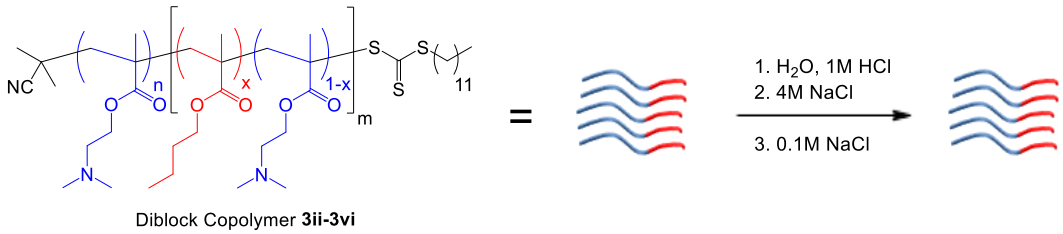

Scheme 3.5: Preparation of p(DMAEMA)$_n$-*b*-p(*n*-BuMA$_x$-*co*-DMAEMA$_{1-x}$)$_n$ diblock copolymers **3ii-3vi** at α = 1 in aqueous solution before self-assembly.

Resultant diblock copolymer solutions were then analyzed by SLS and DLS and compared with their corresponding diblock copolymer samples at α = 0 (Table 3.5).

Diblock Copolymer	% *n*-BuMA in the core	$\alpha = 1$[a]		$\alpha = 0$[b]		$\alpha = 1$[c]	
		$N_{agg,\ app}$[d]	$R_{h,\ app}$[e] (nm)	$N_{agg,\ app}$[d]	$R_{h,\ app}$[e] (nm)	$N_{agg,\ app}$[d]	$R_{h,\ app}$[e] (nm)
3ii	50	3 ± 1	5.5 ± 0.3	28 ± 1	14.3 ± 0.7	4 ± 1	6.2 ± 0.3
3iii	60	7 ± 1	8.0 ± 0.4	43 ± 2	15.6 ± 0.8	8 ± 1	8.6 ± 0.4
3iv	70	8 ± 1	8.7 ± 0.4	56 ± 3	15.7 ± 0.8	59 ± 3	21.7 ± 1.1
3v	80	78 ± 4	18.7 ± 0.9	72 ± 4	17.6 ± 0.9	114 ± 6	25.2 ± 1.3
3vi	89	98 ± 5	22.2 ± 1.1	115 ± 6	19.7 ± 1.0	147 ± 7	28.2 ± 1.4

Table 3.5: Summary of light scattering data obtained for aqueous solutions of p(DMAEMA)-*b*-p(*n*-BuMA-*co*-DMAEMA) diblock copolymers **3ii-3vi** prepared at two different ionization degrees and *via* different preparation pathways. All samples were measured one day after preparation. Key: [a] prepared at $\alpha = 1$ *via* the addition of 1 M HCl to dispersed diblock copolymers in aqueous solution; [b] prepared at $\alpha = 0$ *via* self-assembly method D; [c] prepared at $\alpha = 1$ *via* the addition of 1 M HCl to spherical micelles previously formed *via* self-assembly method D; [d] N_{agg} values were calculated from SLS; [e] R_h values were calculated from DLS.

With respect to increasing the ionization degree post self-assembly from $\alpha = 0$ to $\alpha = 1$, N_{agg} and R_h significantly decreased for spherical micelles formed from diblock copolymers **3ii** (50% *n*-BuMA) and **3iii** (60% *n*-BuMA), which was indicative of a micelle to unimer transition. Conversely, N_{agg} and R_h increased upon the addition of 1 M HCl to spherical micelles formed from diblock copolymers with higher *n*-BuMA incorporations in the core-forming block (**3iv-3vi**); which was attributed to the formation of metastable aggregates that intrinsically have a higher aggregation number.[18]

Interestingly, the light scattering data obtained for diblock copolymer solutions prepared at $\alpha = 1$ before self-assembly, revealed that diblock copolymers **3v** (80% *n*-BuMA) and **3vi** (89% *n*-BuMA) self-assembled upon initial dispersion in aqueous solution and did not undergo a transition to unimers upon complete protonation of the hydrophilic DMAEMA units. Consequently, it was postulated that 'frozen' nanostructures formed for **3v** and **3vi** since the respective aggregates showed little response to an external stimulus,

in this case change in ionization degree. Therefore, aggregation behavior for diblock copolymers **3v** and **3vi** was primarily dictated by the chosen self-assembly methodology which was akin to a direct dissolution instead of a desired solvent switch, as the latter has been found to drive the formation of thermodynamically favored nanostructures.[93]

In contrast, diblock copolymers **3ii-3iv** (50-70% *n*-BuMA) formed unimers upon reaching α = 1 after initial dispersion in aqueous solution, as confirmed by the significantly smaller N_{agg} and R_h values obtained by light scattering analysis. Whilst the measured N_{agg} values were larger than the anticipated value for unimers (N_{agg} = 1), the observed discrepancies could be attributed to the use of potentially inaccurate refractive index increment (d*n*/d*C*) values, as the latter has been previously shown in the literature to be highly dependent upon the ionization degree.[101] Unfortunately, at the time of measurement the in-house refractometer had to be replaced and thus accurate determination of the d*n*/d*C* with respect to changing ionization degree for diblock copolymers **3ii-3vi** could not be conducted. Alternatively, the N_{agg} values obtained for diblock copolymers **3iii** and **3iv** (7 and 8 respectively) prepared at α = 1 before self-assembly could be ascribed to the weak association of unimers in solution due to diblock copolymer chains attempting to minimize polymer-solvent interactions.

Regardless, reversible association of pH-responsive diblock copolymers upon changing the ionization degree was observed for **3ii** (50% *n*-BuMA) and **3iii** (60% *n*-BuMA). N_{agg} and R_h for the respective diblock copolymer samples significantly increased when the ionization degree was lowered from α = 1 to α = 0, with a corresponding decrease in N_{agg} and R_h observed upon increasing the ionization degree back to α = 1. Whilst diblock copolymer **3iv** (70% *n*-BuMA) appeared to form a population of weakly associated unimers before self-assembly (N_{agg} = 8), similar N_{agg} values were obtained at α = 0 and α = 1 post self-assembly (56 *c.f.* 59). Therefore, aggregation for **3iv** was not reversible

which was attributed to the slow or non-existent reionization of DMAEMA units within the micelle core.

In summary, increasing *n*-BuMA incorporation in the core-forming block for a series of p(DMAEMA)-*b*-p(*n*-BuMA-*co*-DMAEMA) diblock copolymers (**3ii-3vi**) has been shown to have a significant effect upon resultant diblock copolymer self-assembly. For intermediate *n*-BuMA incorporations (50-60%), dynamic micelles formed which were capable of undergoing reversible association with respect to ionization degree and thus unimer exchange appeared to be facilitated. In contrast, at a critical *n*-BuMA incorporation (>70%) out-of-equilibrium kinetically trapped 'frozen' micelles formed for which reversible association did not occur and thus dynamic exchange of unimers was precluded.

3.3.3.2. Blended micelles *versus* pure micelles – influence of hydrophobicity upon the copolymer blending protocol

As discussed in Section 3.2.2, Chassenieux and co-workers have recently demonstrated that increasing the percentage incorporation of *n*BA from 40% to 60% in the core-forming block of a p(*n*BA-*co*-AA)$_{100}$-*b*-p(AA)$_{200}$-*b*-p(*n*BA-*co*-AA)$_{100}$ statistical triblock copolymer resulted in a transition from a dynamic to a 'frozen' network.[55] Importantly, the authors discovered that blending the two constituent triblock copolymers together *via* the copolymer blending protocol led to the formation of a hybrid network with a single broad relaxation process.[55] Critically, it was found that a 'frozen' network (60% *n*BA incorporation) could be rendered dynamic by the addition of rapidly exchanging triblock copolymer chains (40% *n*BA incorporation).[55]

In light of this, a similar investigation was conducted for the series of amphiphilic pH-responsive p(DMAEMA)-*b*-p(*n*-BuMA-*co*-DMAEMA) diblock copolymers **3ii-3vi**

synthesized herein to ascertain whether the introduction of dynamic diblock copolymer chains could drive 'frozen' micelles to thermodynamic equilibrium. To this end, a series of diblock copolymer mixtures were prepared by blending diblock copolymers **3ii** (50% *n*-BuMA) and **3vi** (89% *n*-BuMA) together at various molar mixing ratios to target intermediate *n*-BuMA micelle core loadings (Table 3.6). To mirror the previous copolymer blending study conducted by O'Reilly and co-workers for a similar series of pH-responsive diblock copolymers,[75] two copolymer blending protocols were employed herein (Figure 3.11). Unimer blending (UB) entailed blending the constituent diblock copolymers (**3ii** and **3vi**) together in dry powder form to target the desired *n*-BuMA percentage incorporation, followed by self-assembly (Figure 3.11, Method E). Micelle blending (MB) involved self-assembly of the constituent diblock copolymers (**3ii** and **3vi**) separately, before blending the resultant solutions together to target the desired *n*-BuMA composition (Figure 3.11, Method F).

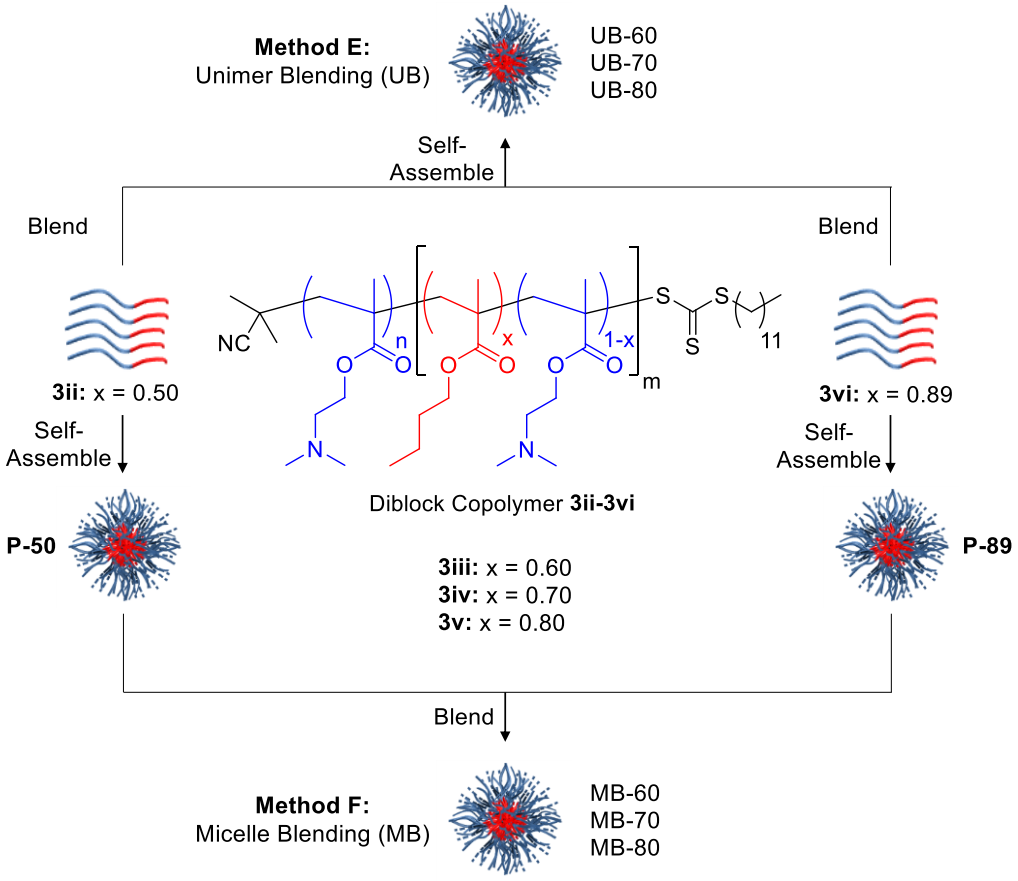

Figure 3.11: Schematic demonstrating the copolymer blending protocols employed herein. Centre: chemical structure of pH-responsive p(DMAEMA)$_n$-*b*-p(*n*-BuMA$_x$-*co*-DMAEMA$_{1-x}$)$_m$ diblock copolymers **3ii-3vi**. Method E: unimer blending (UB); diblock copolymers **3ii** and **3vi** were first blended in the powder state to target the desired *n*-BuMA *n* % and then subsequently self-assembled. Method F: micelle blending (MB); diblock copolymers **3ii** and **3vi** were first self-assembled separately and then blended to target the desired *n*-BuMA *n* %. P-50 and P-89 represent pure diblock copolymer self-assemblies with *n* % *n*-BuMA.

To distinguish between the blended and pure diblock copolymer systems, the following notation was employed: blended diblock copolymer samples prepared *via* micelle blending with *n* % *n*-BuMA in the micelle core are presented as MB-*n*; blended diblock copolymer samples prepared *via* unimer blending with *n* % *n*-BuMA in the micelle core are presented as UB-*n*; and pure diblock copolymer samples with *n* % *n*-BuMA in the micelle core are presented as P-*n*.

Blended Diblock Copolymer Sample	Mole fraction 3ii	Mole fraction 3vi	Theoretical % *n*-BuMA in the core
UB/MB-60	0.74	0.26	60
UB/MB-70	0.49	0.51	70
UB/MB-80	0.23	0.77	80

Table 3.6: Molar mixing ratios for blended diblock copolymer samples. The following notation was employed: blended diblock copolymer samples prepared *via* micelle blending with *n* % *n*-BuMA in the micelle core are presented as MB-*n*; blended diblock copolymer samples prepared *via* unimer blending with *n* % *n*-BuMA in the micelle core are presented as UB-*n*.

Following the light scattering results obtained previously for pure diblock copolymer micelles (Table 3.4), blended diblock copolymer samples were self-assembled *via* Method D (Scheme 3.4) for both copolymer blending protocols – unimer blending and micelle blending. It was hypothesized that if blended micelles formed that were structurally identical to pure micelles of the same composition, irrespective of their preparation pathway, then thermodynamic equilibrium must have been reached allowing comicellization to occur.

Initially, blended micelles prepared *via* unimer blending were analyzed *via* SLS and DLS, with their size and aggregation behavior compared to their respective pure diblock copolymer micelles (Table 3.7).

Target *n*-BuMA in the core (%)	Pure Micelles		Blended Micelles (UB)		Theoretical
	$N_{agg,\ app}$[a]	$R_{h,\ app}$[b] (nm)	$N_{agg,\ app}$[a]	$R_{h,\ app}$[b] (nm)	$N_{agg,\ avg}$[c]
50	28 ± 1	14.3 ± 0.7	-	-	28 ± 1
60	43 ± 2	15.6 ± 0.8	52 ± 3	17.5 ± 0.9	51 ± 3
70	56 ± 3	15.7 ± 0.8	71 ± 4	17.9 ± 0.9	72 ± 4
80	72 ± 4	17.6 ± 0.9	87 ± 4	18.3 ± 0.9	95 ± 5
89	115 ± 6	19.7 ± 1.0	-	-	115 ± 6

Table 3.7: Summary of light scattering data obtained for pure diblock copolymer micelles and blended diblock copolymer micelles prepared *via* unimer blending. Samples were measured one day after self-assembly. Key: [a] N_{agg} values were calculated from SLS; [b] R_h values were calculated from DLS; [c] Theoretical weight average aggregation numbers were calculated using equation (**3.2**).

Overall, there was a clear difference in the size and aggregation behavior between blended and pure diblock copolymer micelles with the same targeted *n*-BuMA incorporation. Furthermore, given that in SLS the molecular weight is related to the intensity of scattered light, a theoretical weight average aggregation number of a blended solution for which comicellization does not occur can be calculated according to equation (**3.2**);

$$N_{agg,\,avg} = \frac{\left(C_{P-89}N_{agg\,P-89}\right) + \left(C_{P-50}N_{agg\,P-50}\right)}{\left(C_{P-89} + C_{P-50}\right)} \qquad \textbf{3.2}$$

Where $C_{P\text{-}50}$ and $C_{P\text{-}89}$ are the weight concentrations of diblock copolymers **3ii** and **3vi** in the blended diblock copolymer sample respectively (Table 3.6), and $N_{agg\ P\text{-}50}$ and $N_{agg\ P\text{-}89}$ correspond respectively to the aggregation numbers obtained previously for pure diblock copolymer samples (Table 3.4).

Interestingly, experimental N_{agg} values obtained for the blended diblock copolymer samples closely matched the predicted N_{agg} values for blended solutions for which comicellization does not occur (Table 3.7). Additionally, for blended diblock copolymer

micelles prepared *via* micelle blending three overlapping modes were present in the DLS traces and thus light scattering samples could not be analyzed accurately using the REPES routine.[100] Considering the 'frozen' nature of spherical micelles formed from diblock copolymer **3vi**, the presence of three overlapping modes could be indicative of two fast modes corresponding to two populations of micelles and one slow mode corresponding to spurious aggregates with a negligible weight fraction. Ultimately, comicellization *via* either copolymer blending protocol did not occur for the pH-responsive diblock copolymer system studied herein.

3.3.4. Synthesis of ABM-functionalized fluorescent pH-responsive diblock copolymers

Further investigation into the self-assembly behavior of p(DMAEMA)-*b*-p(*n*-BuMA-*co*-DMAEMA) diblock copolymer micelles was carried out *via* fluorescence analysis using an aminobromomaleimide (ABM) fluorophore. As outlined in Chapter 2, ABMs are similar in nature to dithiomaleimides (DTMs) and are highly emissive fluorophores that offer numerous advantages for polymer nanoparticle labelling, including high sensitivity, a self-reporting nature, lack of self-quenching in the micellar state and most importantly small size.[102,103] O'Reilly and co-workers have previously exploited the solvent dependent emissive behavior of ABM fluorophores as an effective sensor within the core of crosslinked CO_2-responsive nanoparticles *via* a copolymerization approach.[103] Measured fluorescence emission of the ABM fluorophore was found to directly correspond to changes regarding the nanoparticles' size and core hydrophilicity in response to different external stimuli.[103] Therefore, it was envisaged that the functionalization of p(DMAEMA)-*b*-p(*n*-BuMA-*co*-DMAEMA) diblock copolymers with an ABM fluorophore would enable the properties and internal structures of the fluorescent diblock copolymer micelles, formed upon self-assembly, to be investigated in a similar manner. For this study, the optimum location of an ABM fluorophore within the final block copolymer structure would be within or directly adjacent to the core-forming block to ensure better protection from fluorescence quenching by electron driven proton transfer in water.[104] Upon successful core-functionalization, it was anticipated that the ABM fluorophore may allow accurate determination of the critical micelle concentration (CMC) as well as probe the stimuli-responsiveness and degree of core hydration of fluorescent polymer nanostructures – with the potential to measure unimer exchange dynamics by fluorescence spectroscopy.

It was imperative that ABM incorporation did not significantly alter the properties of p(DMAEMA)-*b*-p(*n*-BuMA-*co*-DMAEMA) diblock copolymers and thus a non-invasive method was preferred. In Chapter 2, the successful synthesis of a range of fluorescent RAFT agents, whereby the R or Z group was functionalized with an ABM fluorophore was described. Moreover, kinetic analysis of subsequent RAFT polymerizations confirmed the formation of well-defined polymers with relatively low dispersities for which no polymerization retardation or loss of control was detected. In light of this, the R group ABM-functionalized RAFT agent **2ii** was selected for the synthesis of two target fluorescent diblock copolymer analogues. In relation to the five pH-responsive p(DMAEMA)-*b*-p(*n*-BuMA-*co*-DMAEMA) diblock copolymers analyzed in Sections 3.3.1-3.3.3, the lowest and highest *n*-BuMA incorporations with regards to the core-forming block, 50% and 90%, were chosen. It was hypothesized that such a large difference in core hydrophobicity should allow for clear differences in critical micelle concentration, degree of core hydration and stimuli-responsiveness to be observed.

Initially, two ABM-functionalized p(*n*-BuMA$_x$-*co*-DMAEMA$_{1-x}$)$_n$ copolymers were synthesized *via* RAFT polymerization in 1,4-dioxane at 70 °C using **2ii**, as outlined in Scheme 3.6. In contrast to the diblock copolymers produced in Section 3.3.1, the order in which the blocks were synthesized in was switched to ensure that the ABM fluorophore would be located directly adjacent to the core-forming block. Retention of both α-end and ω-end group functionality is pivotal to the success of this study and thus 0.1 equivalents of AIBN was selected to provide a balance between a high polymerization rate and the number of initiator-derived polymer chains produced. Once again, target conversion for both RAFT copolymerizations was lower than 90% to minimize bimolecular termination events and potential loss of the trithiocarbonate end group.

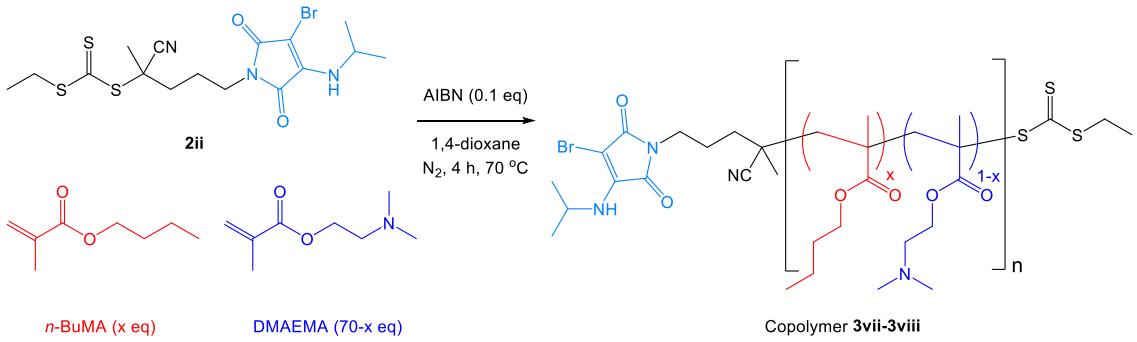

Scheme 3.6: RAFT copolymerization of *n*-BuMA and DMAEMA using the R group ABM-functionalized agent **2ii** in 1,4-dioxane at 70 °C to produce two p(*n*-BuMA$_x$-*co*-DMAEMA$_{1-x}$)$_n$ copolymers (**3vii-3viii**).

Monomer conversion was monitored using ^{1}H NMR spectroscopy with RAFT copolymerizations quenched by immersion in liquid nitrogen after 4 h upon reaching the desired block length (DP = 50). Upon purification, two fluorescent ABM-functionalized p(*n*-BuMA$_x$-*co*-DMAEMA$_{1-x}$)$_n$ copolymers (**3vii-3viii**) were isolated; characterization data for which is summarized in Table 3.8.

Copolymer	***n*-BuMA:DMAEMA Feed Ratio[a]**	***ρ*[a] (%)**	***x*[b]**	***n*[b]**	***M*$_{n,\ NMR}$[b] (kDa)**	***M*$_{n,\ SEC}$[c] (kDa)**	***Đ*$_M$[c]**
3vii	1:1	75	0.5	52	8.2	7.7	1.20
3viii	9:1	70	0.9	49	7.0	7.0	1.20

Table 3.8: Characterization data for ABM-functionalized p(*n*-BuMA$_x$-*co*-DMAEMA$_{1-x}$)$_n$ copolymers **3vii-3viii**. Key: [a] initial monomer feed ratio and monomer conversion was calculated by ^{1}H NMR spectroscopy of the crude polymerization mixture prior to the onset of polymerization and upon quenching, respectively (300 MHz, $CDCl_3$); [b] determined by end group analysis using ^{1}H NMR spectroscopy (400 MHz, $CDCl_3$); [c] obtained by SEC analysis based on p(St) standards with $CHCl_3$ as the eluent.

^{1}H NMR spectroscopy was utilized to confirm the degree of polymerization through end group analysis by comparison of the overlapping peak integrals corresponding to the polymer's OC*H*$_2$CH$_2$N and OC*H*$_2$CH$_2$CH$_2$CH$_3$ resonances at 4.05 and 3.93 ppm (H16 and H10 respectively) to that of the trithiocarbonate end group C*H*$_2$S resonance at

3.25 ppm (H19) and R group $CH_2CH_2CH_2N$ resonance at 3.52 ppm (H4) (Figure 3.12). Final percentage incorporation of *n*-BuMA for purified copolymers **3vii** and **3viii** was determined by ^{1}H NMR spectroscopy with both monomers incorporated at the respective initial monomer feed ratios: 50% *n*-BuMA for **3vii** and 90% *n*-BuMA for **3viii**.

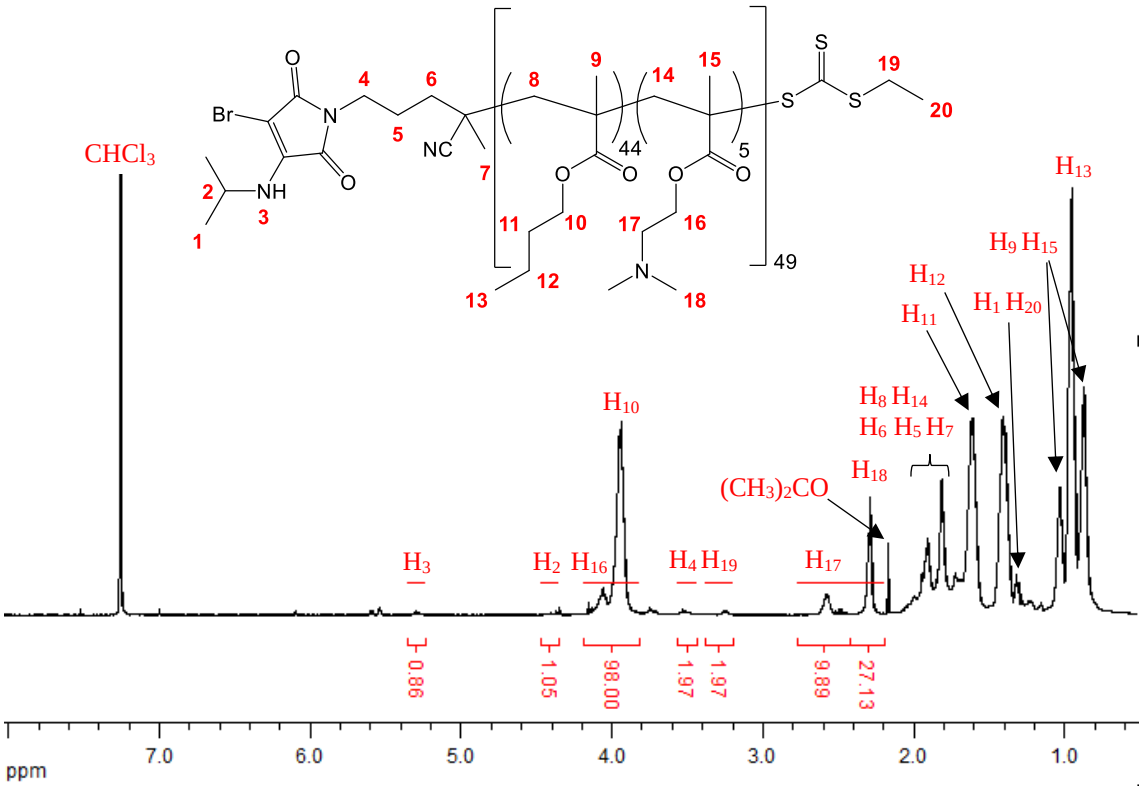

Figure 3.12: ^{1}H NMR spectrum (400 MHz, $CDCl_3$) of the ABM-functionalized p(*n*-$BuMA_{44}$-*co*-$DMAEMA_5)_{49}$ copolymer **3viii**.

Upon SEC analysis, ABM-functionalized p(*n*-$BuMA_x$-*co*-$DMAEMA_{1-x})_n$ copolymers **3vii-3viii** displayed symmetrical, unimodal molecular weight distributions with relatively low dispersities measured for both copolymers ($Đ_M$ = 1.20), indicating good control over the RAFT copolymerization using **2ii**. Importantly, excellent agreement between the molecular weight distributions obtained using an RI and UV detector (recorded at 309 nm and 400 nm) for **3vii** and **3viii** confirmed that the trithiocarbonate and ABM functionalities were appreciably retained for both copolymers (Figure 3.13).

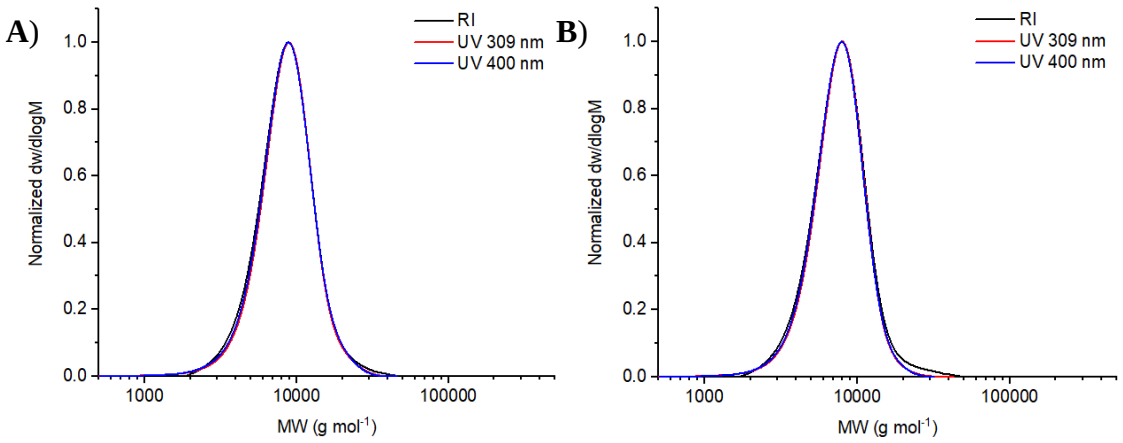

Figure 3.13: Molecular weight distributions determined by SEC ($CHCl_3$ as the eluent and calibrated against p(St) standards) using both an RI and UV (recorded at 309 and 400 nm) detector for the following p(*n*-BuMA$_x$-*co*-DMAEMA$_{1-x}$)$_n$ copolymers: a) **3vii**; b) **3viii**.

Chain extension of p(*n*-BuMA$_x$-*co*-DMAEMA$_{1-x}$)$_n$ copolymers **3vii** and **3viii** was conducted *via* RAFT polymerization of DMAEMA at 70 °C in 1,4-dioxane (Scheme 3.7). Corona-forming blocks of total DP = 100 were targeted to match the respective non-fluorescent p(DMAEMA)-*b*-p(*n*-BuMA-*co*-DMAEMA) diblock copolymer analogues (**3ii** and **3vi**) synthesized in Section 3.3.1.

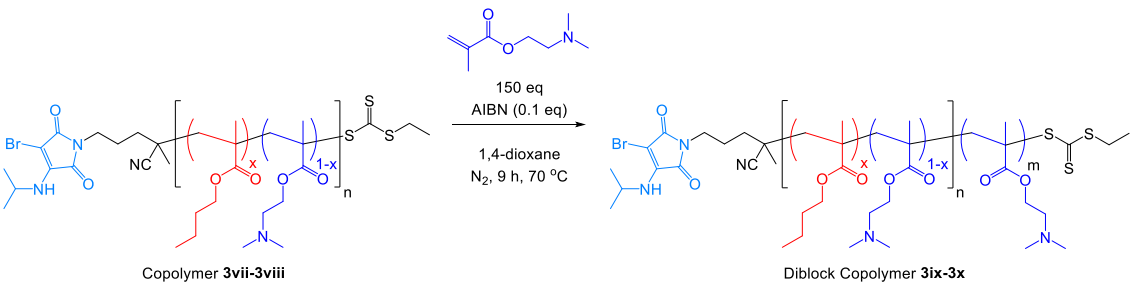

Scheme 3.7: Chain extension of ABM-functionalized p(*n*-BuMA$_x$-*co*-DMAEMA$_{1-x}$)$_n$ copolymers **3vii-3viii** *via* RAFT polymerization of DMAEMA to produce amphiphilic ABM-functionalized pH-responsive p(*n*-BuMA$_x$-*co*-DMAEMA$_{1-x}$)$_n$-*b*-p(DMAEMA)$_m$ diblock copolymers **3ix-3x**.

Upon purification, two fluorescent pH-responsive p(*n*-BuMA$_x$-*co*-DMAEMA$_{1-x}$)$_n$-*b*-p(DMAEMA)$_m$ diblock copolymers (**3ix-3x**) were isolated; characterization data for which is summarized in Table 3.9.

Diblock Copolymer	x^a	n^a	m^b	$M_{n,\,NMR}{}^b$ (kDa)	$M_{n,\,SEC}{}^c$ (kDa)	$Đ_M{}^c$
3ix	0.5	52	77	20.4	30.4	1.22
3x	0.9	49	88	21.3	29.3	1.17

Table 3.9: Characterization data for ABM-functionalized amphiphilic p(*n*-BuMA$_x$-*co*-DMAEMA$_{1-x}$)$_n$-*b*-p(DMAEMA)$_m$ diblock copolymers **3ix-3x**. Key: [a] determined by end group analysis of the respective copolymer (**3vii-3viii**) using ^{1}H NMR spectroscopy (400 MHz, $CDCl_3$); [b] determined by end group analysis using ^{1}H NMR spectroscopy (400 MHz, $CDCl_3$); [c] obtained by SEC analysis based on p(MMA) standards with DMF as the eluent.

Final diblock copolymer compositions were determined by ^{1}H NMR spectroscopy (Figure 3.14) by comparing the same peak integrals that were used to calculate the respective monomer incorporations for the non-fluorescent p(DMAEMA)-*b*-p(*n*-BuMA-*co*-DMAEMA) diblock copolymer analogues (**3ii-3vi**), analyzed in Section 3.3.1. Good agreement between the peak integrals for polymeric proton resonances with respect to the diagnostic proton resonances corresponding to the *N*-alkyl ABM α-end group at 5.31, 4.40 and 3.52 ppm (H3, H2 and H4 respectively) indicated that the relative population of undesired initiator-derived p(DMAEMA) homopolymer chains was relatively low.

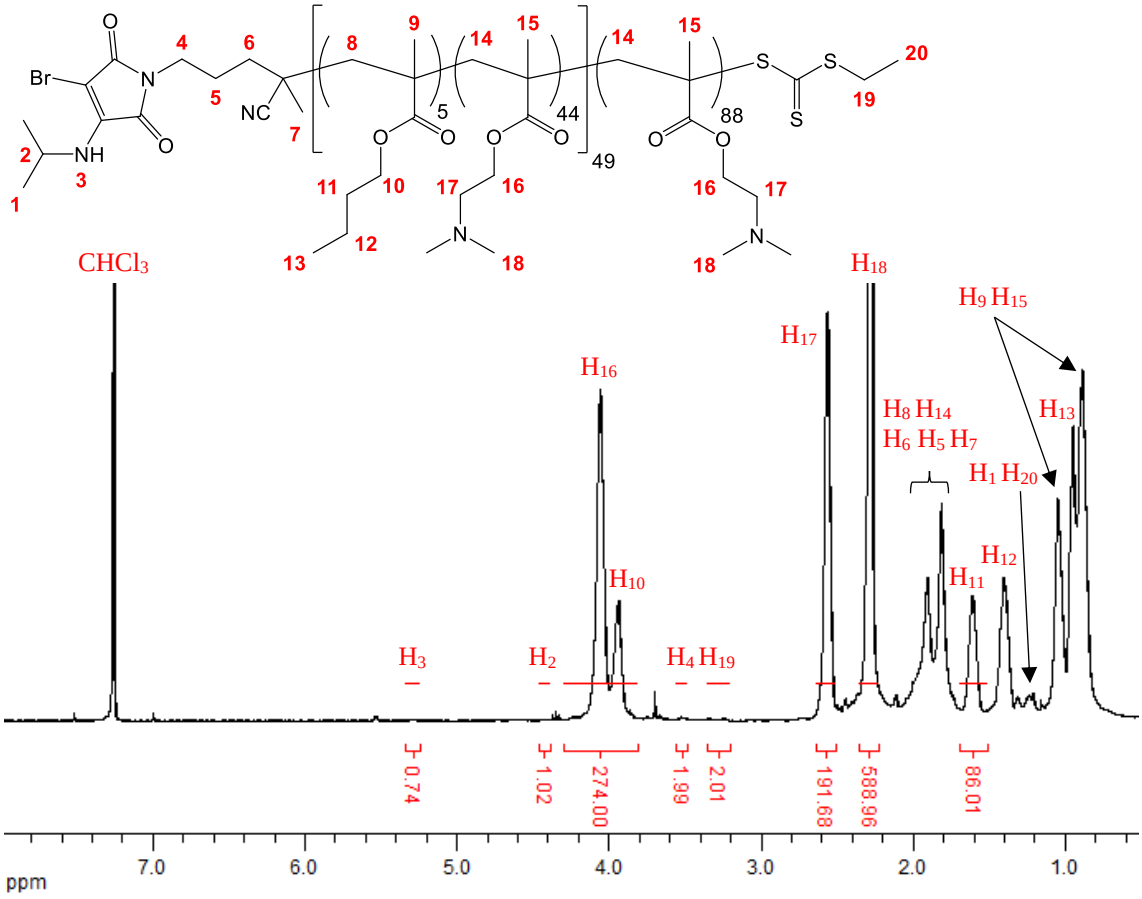

Figure 3.14: ^{1}H NMR spectrum (400 MHz, $CDCl_3$) of the ABM-functionalized p(*n*-BuMA$_{44}$-*co*-DMAEMA$_5$)$_{49}$-*b*-p(DMAEMA)$_{88}$ diblock copolymer **3x**.

Fluorescent diblock copolymers **3ix** and **3x** displayed symmetrical, narrow molecular weight distributions with a clear shift towards higher molecular weight indicating excellent control over the chain extensions using the R group ABM-functionalized RAFT agent **2ii** (Figure 3.15). The absence of any high molecular weight shoulders in the obtained RI traces for either diblock copolymer suggested that the extent of termination by disproportionation was negligible. Significantly, the molecular weight distributions obtained using an RI and UV detector (recorded at 309 nm and 400 nm) overlay appreciably for both diblock copolymers (**3ix-3x**), thereby confirming that a relatively high degree of end group fidelity was attained. Note, at the time of measurement the UV lamp of the dimethylformamide (DMF) GPC system had to be replaced and thus the

molecular weight distributions and corresponding dispersity values depicted in Figure 3.15 were obtained *via* SEC analysis using $CHCl_3$ as the eluent.

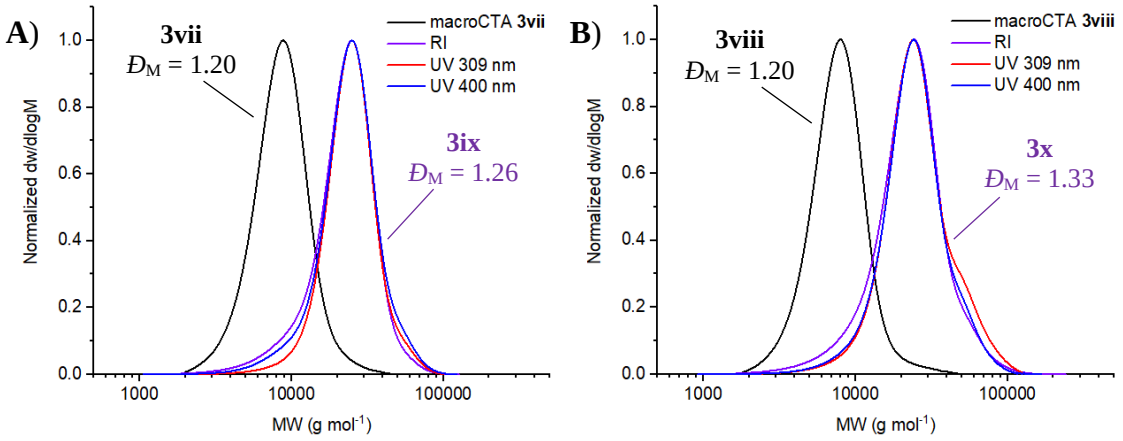

Figure 3.15: Molecular weight distributions determined by SEC ($CHCl_3$ as the eluent and calibrated against p(St) standards) using both an RI and UV (recorded at 309 and 400 nm) detector for the following ABM-functionalized p(*n*-BuMA$_x$-*co*-DMAEMA$_{1-x}$)$_n$-*b*-p(DMAEMA)$_m$ diblock copolymers: a) **3ix**; b) **3x**. Respective RI traces for p(*n*-BuMA$_x$-*co*-DMAEMA$_{1-x}$)$_n$ macroCTAs (**3vii-3viii**) are shown for comparison.

Importantly, ABM-functionalized p(*n*-BuMA-*co*-DMAEMA)-*b*-p(DMAEMA) diblock copolymers **3ix** and **3x** were achieved with low dispersities ($Đ_M$ = 1.17 and 1.22 respectively, Table 3.9) confirming that the change in RAFT agent from CPDDT to **2ii** had no adverse effects upon polymerization control. Comparison of fluorescent diblock copolymers **3ix** and **3x** with their analogous non-fluorescent counterparts (**3ii** and **3vi** respectively) revealed that core-forming block lengths and percentage incorporation of hydrophobic *n*-BuMA were near identical. Whilst corona-forming block lengths for **3ix** and **3x** (DP = 77 and 88, respectively) were lower than desired (DP = 100), the difference was relatively small and thus the potential impact upon the self-assembly behavior of fluorescent diblock copolymer micelles should be negligible.

3.3.5. Self-assembly behavior of ABM-functionalized fluorescent pH-responsive diblock copolymers

Next, the self-assembly behavior of the two fluorescent p(*n*-BuMA-*co*-DMAEMA)-*b*-p(DMAEMA) diblock copolymers **3ix** and **3x** in aqueous solution was investigated to ascertain whether the presence of the ABM fluorophore impacted self-assembly. To allow for direct comparison with their respective non-fluorescent p(DMAEMA)-*b*-p(*n*-BuMA-*co*-DMAEMA) diblock copolymer counterparts (**3ii** and **3vi**), self-assembly Method D was selected for the formation of fluorescent diblock copolymer micelles (Scheme 3.8).

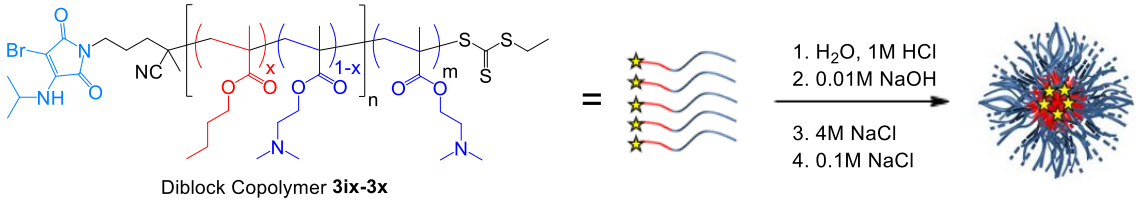

Scheme 3.8: Self-assembly of ABM-functionalized p(*n*-BuMA$_x$-*co*-DMAEMA$_{1-x}$)$_n$-*b*-p(DMAEMA)$_m$ diblock copolymers **3ix-3x** in aqueous solution *via* self-assembly Method D.

Resultant self-assembled nanostructures were characterized by DLS and SLS with N_{agg} and R_h measured for fluorescent diblock copolymer micelles and compared to their respective non-fluorescent diblock copolymer micelles of a similar copolymer composition (Table 3.10). Importantly, N_{agg} and R_h did not deviate significantly for fluorescent micelles formed from ABM-functionalized diblock copolymers **3ix** and **3x**. Therefore, the introduction of an ABM fluorophore at the α-end of the diblock copolymer structure appeared to not adversely affect subsequent self-assembly behavior; at least at $\alpha = 0$.

Diblock Copolymer	% *n*-BuMA in the core-forming block	$N_{agg,\ app}$ [a]	$R_{h,\ app}$ [b] (nm)
3ii	50	28 ± 1	14.3 ± 0.7
3ix	50	23 ± 1	12.9 ± 0.6
3vi	89	115 ± 6	19.7 ± 1.0
3x	90	114 ± 6	21.1 ± 1.1

Table 3.10: Summary of light scattering data obtained for fluorescent spherical micelles formed from ABM-functionalized p(*n*-BuMA-*co*-DMAEMA)-*b*-p(DMAEMA) diblock copolymers **3ix** and **3x** and non-fluorescent spherical micelles formed from p(DMAEMA)-*b*-p(*n*-BuMA-*co*-DMAEMA) diblock copolymers **3ii** and **3vi**. Samples were measured one day after self-assembly *via* Method D. Key: [a] N_{agg} values were calculated from SLS; [b] R_h values were calculated from DLS.

3.3.6. Probing stimuli-response and degree of core hydration *via* core-functionalization

As outlined in Chapter 2, a key characteristic of ABM fluorophores is that they are highly sensitive to their environment with a red-shift in emission and corresponding decrease in fluorescence intensity observed in protic polar solvents such as water.[102] Upon self-assembly of p(*n*-BuMA-*co*-DMAEMA)-*b*-p(DMAEMA) diblock copolymers **3ix** and **3x**, the ABM fluorophore is expected to be sequestered into the core of the subsequent spherical micelles. As a result, it was anticipated that fluorescence emission will be promoted due to better protection from fluorescence quenching by electron driven proton transfer in water.[104] In light of this, it was envisaged that the solvent dependent emissive behavior of ABM fluorophores could be utilized to probe the stimuli-responsiveness and degree of core hydration of pH-responsive diblock copolymers **3ix** and **3x**.

To this end, a series of diblock copolymer solutions were prepared at various ionization degrees ranging from $\alpha = 0$ to $\alpha = 1$ for both fluorescent diblock copolymers, **3ix** and **3x**.

Steady-state fluorescence emission profiles were recorded between 400 and 650 nm for each diblock copolymer solution with λ_{ex} = 350 nm (Figure 3.16).

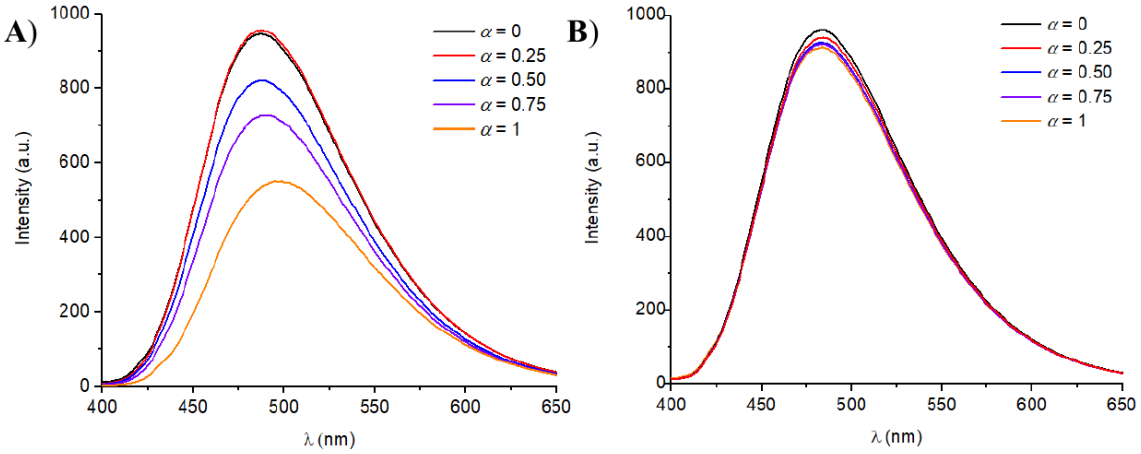

Figure 3.16: Overlaid fluorescence emission spectra of diblock copolymer solutions prepared at various ionization degrees for the following ABM-functionalized p(*n*-BuMA-*co*-DMAEMA)-*b*-p(DMAEMA) diblock copolymers: a) **3ix**; b) **3x**. Fluorescence spectra for both diblock copolymers were obtained in deionized water at 1 mg mL^{-1} and λ_{ex} = 350 nm.

For the ABM-functionalized diblock copolymer **3ix** with 50% *n*-BuMA incorporation in the core-forming block, fluorescence emission decreased with respect to increasing ionization degree (Figure 3.16 a). Interestingly, the emission maximum red-shifted from 487 nm to 498 nm upon increasing the ionization degree from 0.75 to 1 which suggested that the self-assembly of diblock copolymer **3ix** from unimers to spherical micelles occurred at $\alpha > 0.75$. Light scattering analysis confirmed this to be the case with spherical micelles observed when $\alpha < 0.75$ ($N_{agg} > 1$) and unimers observed when $\alpha > 0.75$ ($N_{agg} \sim 1$). N_{agg} and R_h were found to increase with respect to decreasing ionization degree until both values plateaued at $\alpha < 0.25$. Significantly, fluorescence emission profiles obtained for diblock copolymer **3ix** reflected this trend with the measured fluorescence emission of aqueous solutions increasing until $\alpha = 0.25$. Moreover, changes in steady-state fluorescence intensity with respect to ionization degree provided an indication of the

hydrated state of the micelle core as well as alluded to the dynamic nature of pH-responsive micelles formed form diblock copolymer **3ix**.

Conversely, fluorescence emission did not signficantly change over the range of ionization degrees studied for the ABM-functionalized diblock copolymer **3x** (Figure 3.16 b) which supported the light scattering data obtained for **3x**, whereby spherical micelles formed at all ionization degrees. As discussed in Section 3.3.3.1, out-of-equilibrium kinetically trapped micelles were previously observed to form for the analogous non-fluorescent diblock copolymer **3vi**, which has a similar *n*-BuMA composition in the core-forming block. Therefore, the absence of any change in fluorescence emission for the corresponding fluorescent diblock copolymer **3x** provided further evidence of the 'frozen' nature of the self-assembled spherical micelles, with the degree of core hydration remaining the same acrosss all ionization degrees.

Fluorescence emission intensity for micelle solutions at $\alpha = 0$ for both fluorescent diblock copolymers **3ix** and **3x** were also compared. As anticipated, diblock copolymer **3x** displayed significantly higher fluorescence emission intensity in comparison to diblock copolymer **3ix** due to the large difference in hydrophobicity between their respective core-forming blocks. Overall, steady-state fluorescence experiments highlighted the high sensitivity of the ABM fluorophore to its relative environment and was shown to provide a useful tool in probing the degree of core hydration and stimuli-responsiveness of pH-responsive polymeric micelles.

3.3.7. Critical micelle concentration determination

Critical micelle concentration (CMC) studies were carried out for both fluorescent diblock copolymers **3ix** and **3x**. It was anticipated that upon the transition from micelles to solvated unimers a significant reduction in steady-state fluorescence emission would

be observed. Fluorescence emission spectra was measured over a range of concentrations for aqueous solutions of fluorescent diblock copolymers **3ix** and **3x,** with fluorescence emission intensity integrated between 400 and 650 nm and subsequently normalized by the polymer concentration (Figure 3.17).

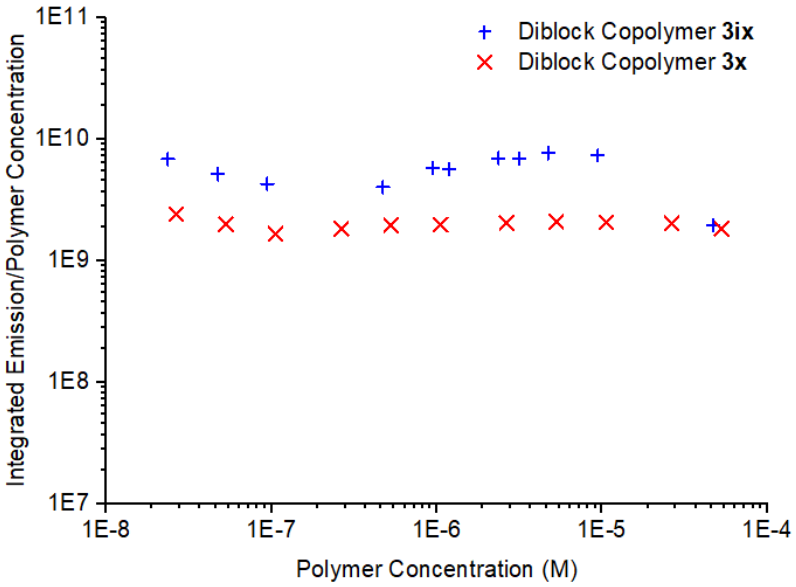

Figure 3.17: Integrated fluorescence emission intensity normalized by polymer concentration with respect to polymer concentration for ABM-functionalized p(*n*-BuMA-*co*-DMAEMA)-*b*-p(DMAEMA) diblock copolymers **3ix** and **3x**.

For both diblock copolymers **3ix** and **3x**, a relatively flat emission intensity over 3 orders of magnitude in concentration was observed corresponding to the micellar state. Therefore, the critical micelle concentration for either diblock copolymer was not reached due to the absence of a clear deviation from the flat emission intensity profiles. Unfortunately, at this point the limit of the fluorometer detector was reached for both diblock copolymers at an approximate concentration of 0.02 μM, thereby preventing any further dilutions to be measured accurately *via* steady-state fluorescence spectroscopy.

3.4. Conclusions

In this Chapter, the importance of the chosen self-assembly methodology upon the resultant aggregation behavior of highly hydrophobic pH-responsive amphiphilic diblock copolymers was highlighted by light scattering analysis of pure diblock copolymer micelles assembled *via* two different protocols. Moreover, comicellization did not occur, *via* micelle blending or unimer blending, for the range of pH-responsive p(DMAEMA)-*b*-p(*n*-BuMA-*co*-DMAEMA) diblock copolymers studied herein, as confirmed by light scattering techniques. Therefore, thermodynamic equilibrium was not reached in this study as dynamic exchange of unimers was disfavored, which was attributed to a significantly large energy barrier due to the high *n*-BuMA incorporation in the core-forming blocks.

Through the use of a novel ABM-functionalized RAFT agent, two fluorescent pH-responsive diblock copolymer analogues were successfully synthesized with low dispersities and well-defined molecular weights. Importantly, the introduction of the ABM fluorophore appeared to not significantly impact self-assembly, with similar aggregation behavior observed for fluorescent diblock copolymers with respect to their non-fluorescent counterparts. Furthermore, steady-state fluorescence measurements demonstrated that the ABM fluorophore could prove to be a useful tool for probing the degree of core hydration of micellar solutions as well as for investigating the stimuli-response, self-assembly state and solution behavior of polymer nanostructures**.** Unfortunately, determination of the critical micelle concentration for fluorescent pH-responsive diblock copolymers *via* steady-state fluorescence spectroscopy was found to be principally limited by the detection capability of the fluorometer. As a result, the viability of using an ABM fluorophore to functionalize block copolymers as a method for accurately measuring critical aggregation concentrations remained inconclusive.

3.5. Experimental Section

3.5.1. Methods and materials

Materials. The following reagents were used as received: carbon disulfide (Sigma-Aldrich, 99%); iodine (Fisher Scientific, 99%); 1-dodecanethiol (Merck, 98%); sodium hydride (60% in mineral oil, Acros Organics); 2-(dimethylamino)ethyl methacrylate (DMAEMA, Sigma-Aldrich, 98%); *n*-butyl methacrylate (*n*-BuMA, Sigma-Aldrich, 99%). 2,2'-azobisisobutyronitrile (AIBN) was received from Sigma-Aldrich (98%), recrystallized from methanol and stored in the dark at 4 °C. All solvents, including high-performance liquid chromatography (HPLC) grade solvents, were purchased from Fisher Scientific and used as received. Monomers and 1,4-dioxane were filtered through a plug of basic alumina prior to use and stored at 4 °C. Diethyl ether was purchased from Fisher Scientific and dried using an Innovative Technology Inc. Pure Solv MD-4-EN solvent purification system. Deuterated solvents and silica gel (40-63 μm) were used as received from Apollo Scientific.

^{1}H and ^{13}C NMR spectroscopy. ^{1}H NMR spectroscopy was performed at 300 MHz on a Bruker Avance AV-300 spectrometer or a Bruker Avance III HD-300 spectrometer, or at 400 MHz on a Bruker Avance III HD-400 spectrometer. ^{13}C NMR spectroscopy was performed at 100 MHz on a Bruker Avance III HD-400 spectrometer. ^{1}H and ^{13}C NMR spectra were measured in deuterated chloroform. Chemical shifts are reported as δ in parts per million (ppm) and are stated relative to the residual solvent peaks at 7.26 ppm or 77.0 ppm for chloroform. Coupling constants (J) correspond to $^{3}J_{\text{H-H}}$ unless otherwise stated. All spectra were obtained at 25 °C.

Size Exclusion Chromatography. SEC analysis was primarily performed on a Varian PL-GPC 50 system with a set of two PLgel Mixed-C columns plus one guard column and

fitted with a viscometer, an RI light scattering detector and a UV detector measuring at 309 nm or 400 nm. SEC measurements were performed with HPLC-grade dimethylformamide (DMF) with 5 mM NH_4BF_4 at 50 °C at a flow rate of 1 mL min^{-1}. The molecular weights of the synthesized polymers were calculated relative to poly(methyl methacrylate) (p(MMA)) standards and analyzed using Cirrus v3.3 software. Additional SEC analysis was performed on a Varian PL-GPC 50 system with a set of two PLgel Mixed-C columns plus one guard column and fitted with an RI and UV detector measuring at 309 nm or 400 nm. SEC measurements were performed with HPLC-grade chloroform with 0.5% triethylamine at 40 °C at a flow rate of 1 mL min^{-1}. The molecular weights of the synthesized polymers were calculated relative to p(MMA) standards and analyzed using Cirrus v3.3 software.

Mass Spectrometry. High resolution electrospray ionization time of flight mass spectrometry (HRMS (ESI-ToF)) was performed on a Bruker UHR-Q-TOF MaXis spectrometer by Dr. Lijang Song, University of Warwick.

Fluorescence Spectroscopy. Steady-state fluorescence spectra were recorded using an Agilent Cary Eclipse Fluorescence spectrophotometer. Quartz cells with screw caps and four polished sides (Starna) were used for fluorescence measurements.

Laser Light Scattering. Measurements were performed at angles of observation ranging from 30° up to 130° using an ALV/CGS-3 Compact Goniometer system operating at λ_0 = 633 nm and at 20 °C ± 1 °C. Data was collected in duplicate with 240 s run times. Calibration was achieved with filtered toluene and the background was measured with filtered solvent (NaCl 0.1 M). Light scattering samples were filtered through 0.22 µm nylon filters under a laminar flow hood prior to analysis.

Dynamic Light Scattering (DLS). The intensity autocorrelation functions $g_2(q, t)$ obtained from dynamic light scattering analysis were related to $g_1(q, t)$ (the normalized electric field autocorrelation functions) *via* the so-called Siegert relation.[23] Then $g_1(q, t)$ was

analyzed in terms of a continuous distribution of relaxation times (equation (**3.3**)) using the REPES algorithm,[100] without assuming a specific mathematical shape for the distribution of the relaxation times ($A(\tau)$).

$$g_1(t) = \int_0^\infty A(\tau) exp(-t/\tau) d\tau \qquad \textbf{3.3}$$

The apparent diffusion coefficient, D_{app}, was calculated from equation (**3.4**) given that the average relaxation rates Γ of the scattering species were q^2 dependent, where q is the scattering vector given by $q = (4\pi n_0/\lambda_0)\sin(\theta/2)$ with θ the angle of observation and n_0 = 1.333, which is the refractive index of the solvent (water).

$$D_{app} = \Gamma/q^2 \qquad \textbf{3.4}$$

The apparent diffusion coefficient was used for computing the apparent hydrodynamic radius ($R_{h,app}$) of the scattering species according to the Stokes-Einstein equation (equation (**3.5**)):

$$R_{h,app} = \frac{k_B T}{6\pi\eta D_{app}} \qquad \textbf{3.5}$$

Where η is the solvent viscosity, k_B is the Boltzmann's constant, and T is the absolute temperature.

Static Light Scattering (SLS). The Rayleigh ratio of the solutions were measured using toluene as a reference according to equation (**3.6**):

$$R_\theta = \frac{\left(I_{sample} - I_{solvent}\right)}{I_{standard}} R_{\theta,standard} \qquad \textbf{3.6}$$

Where I_i represents the intensity scattered by species i, and $R_{\theta,\,standard}$ is the Rayleigh ratio of the reference toluene. In dilute solutions if $R_g q < 1$ where R_g is the radius of gyration, the q and concentration dependence of R_θ is given by equation (**3.7**):

$$\frac{Kc}{R_\theta} = \left(\frac{1}{M_w} + 2A_{2C}\right)\left(1 + \frac{q^2 {R_g}^2}{3}\right) \qquad \textbf{3.7}$$

Where A_2 is the second virial coefficient and M_w the weight average molecular weight. K is an optical constant given by equation (**3.8**):

$$K = \frac{4\pi^2 n_0^2}{\lambda^4 N_A}\left(\frac{dn}{dc}\right)^2 \qquad \textbf{3.8}$$

Where n_0 = 1.496 which is the refractive index of the reference toluene, dn/dc is the refractive index increment determined by differential refractometry and N_A is Avogadro's number. Values of M_w are then obtained after extrapolation to zero angle and used to derive the aggregation number (N_{agg}) of the micellar aggregates (equation (**3.9**)):

$$N_{agg} = \frac{M_{w,particle}}{M_{w,polymer}} \qquad \textbf{3.9}$$

In all case where two modes of relaxation were observed by DLS measurements, R_θ was described as the sum of two contributions according to equations (**3.10**) and (**3.11**):

$$R_\theta = R_{\theta f} + R_{\theta s} \qquad \textbf{3.10}$$

Where f and s stand respectively for fast and slow;

$$R_{\theta f}(q) = \frac{A_f(q)}{\left(A_f(q) + A_s(q)\right)} R_\theta \qquad \textbf{3.11}$$

Where A_f and A_s are the relative amplitudes of the fast and slow modes obtained by DLS. The slow mode of relaxation when observed can be attributed to spurious aggregates with a negligible weight fraction but larger scattering intensity.[23] In the event of a data point from one observation angle falling outside of 10% error of Kc/R_θ, the point was excluded from the average in the calculation of $M_{w,\,particle}$.

3.5.2. Synthetic protocols

Synthesis of 2-cyanopropan-2-yl dodecyl carbonotrithioate (CPDDT).

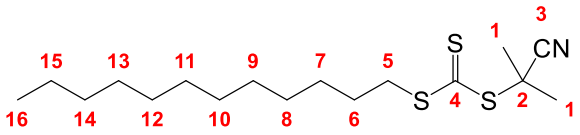

2-Cyanopropan-2-yl dodecyl carbonotrithioate was prepared according to a modified literature procedure. To an oven-dried round bottom flask, sodium hydride (60% in mineral oil) (3.12 g, 78.1 mmol) was added followed by dry diethyl ether (300 mL) with the resulting suspension cooled to 0 °C. Dodecanethiol (18.0 mL, 75.1 mmol) was subsequently added dropwise over 10 min. After stirring the resultant mixture for 10 min at 0 °C, carbon disulfide (4.72 mL, 78.1 mmol) was added dropwise over 10 min producing a thick yellow precipitate of sodium S-dodecyl trithiocarbonate. After 1 h of stirring, the yellow precipitate was collected by Büchner filtration. Sodium S-dodecyl trithiocarbonate (21.2 g, 70.5 mmol) was then re-dissolved in diethyl ether (500 mL) and iodine (8.94 g, 35.2 mmol) was added. After 1 h of stirring at ambient temperature, the reaction mixture was washed with sodium thiosulfate solution (1 M, 3 × 300 mL), deionized water (3 × 300 mL) and finally with brine (300 mL). The organic layer was dried over $MgSO_4$ and evaporated to leave a residue of bis-(dodecyl-sulfanylthiocarbonyl) disulfide (16.5 g, quantitative).

A solution of 2,2'-azobisisobutyronitrile (AIBN) (7.30 g, 44.5 mmol) and bis-(dodecyl-sulfanylthiocarbonyl) disulfide (16.5 g, 29.6 mmol) in ethyl acetate (350 mL) was refluxed overnight under a nitrogen atmosphere. After removal of ethyl acetate *in vacuo*, purification was carried out using column chromatography (silica gel, 9:1 hexane/ethyl acetate) to yield 2-cyanopropan-2-yl dodecyl carbonotrithioate (CPDDT) as an orange

red oil (14.9 g, 43.1 mmol, 73%). ^{1}H NMR (400 MHz, $CDCl_3$) δ_H/ppm: 3.34 (2H, t, J = 7.6 Hz, H5), 1.87 (6H, s, H1), 1.70 (2H, t of t, J = 7.6 Hz, H6), 1.40 (2H, t of t, J = 7.6 Hz, H7), 1.22-1.34 (16H, m, H8 to H15 inclusive), 0.88 (3H, t, J = 6.8 Hz, H16); ^{13}C NMR (100 MHz, $CDCl_3$) δ_C/ppm: 217.8 (C4), 120.4 (C3), 42.3 (C2), 36.9 (C5), 31.9 (C6), 29.7 (C7), 29.6 (C8), 29.5 (C9), 29.4 (C10), 29.3 (C11), 29.0 (C12), 28.9 (C13), 27.7 (C14), 27.0 (C1), 22.7 (C15), 14.1 (C16); HRMS (ESI-TOF) m/z: $[M + Na]^+$ calculated for $C_{17}H_{31}NNaS_3$: 368.1511; found: 368.1508.

*General procedure for the RAFT homopolymerization of DMAEMA to produce macroCTA **3i***

For a total target DP_{DMAEMA} = 100 at 80% conversion, an example synthesis is as follows: CPDDT (250 mg, 1 eq), AIBN (12.0 mg, 0.1 eq) and DMAEMA (15.2 mL, 125 eq) were dissolved in 1,4-dioxane (1:1 monomer volume/1,4-dioxane volume) and added to a dry ampoule containing a stirrer bar. The resulting solution was degassed using at least three freeze-pump-thaw cycles, back-filled with nitrogen, sealed and placed in a pre-heated oil bath at 70 °C. After 6 h, the polymerization was quenched by opening the reaction mixture to air and submerging the ampoule in liquid nitrogen. Purification was achieved *via* precipitation into petroleum ether three times before being re-dissolved in the minimum amount of HPLC grade tetrahydrofuran (THF) and dried under vacuum. The resultant residue was dissolved in the minimum amount of 18.2 MΩ cm water and subsequent lyophilization resulted in an off-white polymer powder. ^{1}H NMR (400 MHz, $CDCl_3$) δ_H/ppm: 4.05 (br s, 2H, OCH_2CH_2N), 3.22 (br s, 2H, CH_2S), 2.56 (br s, 2H, OCH_2CH_2N), 2.28 (br s, 6H, $OCH_2CH_2N(CH_3)_2$), 0.90-2.00 (m, backbone and end group).

*General procedure for the chain extension of macroCTA **3i** via RAFT copolymerization of DMAEMA and n-BuMA*

For a target DP_{core} = 50 at 71% conversion, an example synthesis is as follows: A solution of 70 equivalents of a combination of the two monomers (*n*-BuMA = *x*, DMAEMA = 70-*x*), 0.1 equivalents of AIBN and 1 equivalent of macroCTA **3i** in 1,4-dioxane (1:1 (monomer volume and macroCTA weight)/1,4-dioxane volume) was added to a dry ampoule containing a stirrer bar. The resulting solution was degassed using at least three freeze-pump-thaw cycles, back-filled with nitrogen, sealed and placed in a pre-heated oil bath at 70 °C. After 5 h 30 min, the polymerization was quenched by opening the reaction mixture to air and submerging the ampoule in liquid nitrogen. Purification was achieved *via* precipitation into petroleum ether three times before being re-dissolved in the minimum amount of HPLC grade tetrahydrofuran and dried under vacuum to yield an off-white polymer powder. ^{1}H NMR (400 MHz, $CDCl_3$) δ_H/ppm: 4.04 (br s, 2H, OCH_2CH_2N), 3.92 (br s, 2H, $OCH_2CH_2CH_2CH_3$) 3.21 (br s, 2H, CH_2S), 2.55 (br s, 2H, OCH_2CH_2N), 2.27 (br s, 6H, $OCH_2CH_2N(CH_3)_2$), 0.90-2.00 (m, backbone, end group, $OCH_2CH_2CH_2CH_3$, $OCH_2CH_2CH_2CH_3$ and $OCH_2CH_2CH_2CH_3$).

Pure diblock copolymer micelle sample preparation

Two methods for the preparation of the pure diblock copolymer solutions were used:
Method C consisted of preparing polymer stock solutions at 10 mg mL^{-1} by dispersing the polymer in 18.2 MΩ cm water containing the appropriate amount of 1 M HCl to reach α = 1. After one night of stirring α was lowered to α = 0 using the required amount of 1 M NaOH added in small increments over time and the solutions were stirred again overnight. The NaCl concentration was then adjusted to 0.1 M by the addition of 4 M NaCl and the

solutions were further stirred overnight before use. Samples at 1 mg mL^{-1} were subsequently prepared by dilution of the 10 mg mL^{-1} polymer stock solutions using 0.1 M NaCl.

Method D consisted of preparing polymer solutions at $\alpha = 1$ as described in Method C. After one night of stirring α was lowered to $\alpha = 0$ using the required amount of 0.01 M NaOH using a peristaltic pump at a flow rate of 1 mL h^{-1} and the resultant solutions were stirred again overnight. The NaCl concentration was then adjusted to 0.1 M by the addition of 4 M NaCl and the solutions were further stirred overnight before use. Polymer solutions were then diluted to reach a final concentration of 1 mg mL^{-1} using 0.1 M NaCl and then stirred overnight before use. Further dilutions were carried out using 0.1 M NaCl to maintain a NaCl concentration of 0.1 M.

Copolymer blending protocols for blended diblock copolymer samples

Two methods for the preparation of blended diblock copolymer samples were used.

Method E (Unimer blending (UB)) consisted of mixing the bulk powders of diblock copolymers **3ii** and **3vi** together in the correct molar mixing ratios to match the percentage incorporation of *n*-BuMA in the analogous pure diblock copolymer sample. Polymer solutions were then prepared in the same manner as described in Method D.

Method F (Micelle blending (MB)) involved blending together the individual P-50 and P-89 diblock copolymer solutions, prepared previously *via* Method D, in the correct stoichiometric ratios to give the targeted % *n*-BuMA.

*General procedure for the RAFT copolymerization of DMAEMA and n-BuMA using the R group ABM-functionalized RAFT agent **2ii***

For a target DP_{core} = 50 at 71% conversion, an example synthesis is as follows: A solution of 70 equivalents of a combination of the two monomers (*n*-BuMA = *x*, DMAEMA = 70-*x*), 0.1 equivalents of AIBN and 1 equivalent of **2ii** (150 mg) dissolved in 1,4-dioxane (1:1 monomer volume/1,4-dioxane volume) was added to a dry ampoule containing a stirrer bar. The resulting solution was degassed using at least three freeze-pump-thaw cycles, back-filled with nitrogen, sealed and placed in a pre-heated oil bath at 70 °C. After 6 h, the polymerization was quenched by opening the reaction mixture to air and submerging the ampoule in liquid nitrogen. Purification was achieved *via* precipitation into petroleum ether three times before being re-dissolved in the minimum amount of HPLC grade tetrahydrofuran and dried under vacuum to yield a fluorescent yellow copolymer powder. ^{1}H NMR (300 MHz, $CDCl_3$) δ_H/ppm: 5.28 (br s, 1H, N*H*CH$(CH_3)_2$) 4.41 (br s, 1H, NHC*H*$(CH_3)_2$) 4.04 (br s, 2H, OC*H*$_2$CH_2N), 3.92 (br s, 2H, OC*H*$_2$CH_2CH_2CH_3), 3.56 (br s, 2H, C*H*$_2$N$(CO)_2$) 3.22 (br s, 2H, C*H*$_2$S), 2.55 (br s, 2H, OCH_2C*H*$_2$N), 2.27 (br s, 6H, OCH_2CH_2N(C*H*$_3)_2$), 0.90-2.00 (m, backbone, end group, OCH_2C*H*$_2$CH_2CH_3, OCH_2CH_2C*H*$_2$CH_3 and OCH_2CH_2CH_2C*H*$_3$).

*General procedure for the chain extension of p(n-BuMA-co-DMAEMA) copolymers **3vii** and **3viii** with DMAEMA via RAFT polymerization*

For a target DP_{corona} = 100 at 80% conversion, an example synthesis is as follows: A solution of 125 equivalents of DMAEMA, 0.1 equivalents of AIBN and 1 equivalent of macroCTA **3vii** or **3viii** in 1,4-dioxane (1:1 monomer volume/1,4-dioxane volume and macroCTA weight) was added to a dry ampoule containing a stirrer bar. The resulting solution was degassed using at least three freeze-pump-thaw cycles, back-filled with nitrogen, sealed and placed in a pre-heated oil bath at 70 °C. After 9 h, the polymerization was quenched by opening the reaction mixture to air and submerging the ampoule in

liquid nitrogen. Purification was achieved *via* precipitation into petroleum ether three times before being re-dissolved in the minimum amount of HPLC grade tetrahydrofuran and dried under vacuum to yield a fluorescent yellow polymer powder. ^{1}H NMR (400 MHz, $CDCl_3$) δ_H/ppm: 5.28 (br s, 1H, N*H*CH$(CH_3)_2$) 4.41 (br s, 1H, NHC*H*$(CH_3)_2$) 4.04 (br s, 2H, OC*H*$_2$CH$_2$N), 3.92 (br s, 2H, OC*H*$_2$CH$_2$CH$_2$CH$_3$), 3.56 (br s, 2H, C*H*$_2$N$(CO)_2$) 3.22 (br s, 2H, C*H*$_2$S), 2.55 (br s, 2H, OCH$_2$C*H*$_2$N), 2.27 (br s, 6H, OCH$_2$CH$_2$N(C*H*$_3)_2$), 0.90-2.00 (m, backbone, end group, OCH$_2$C*H*$_2$CH$_2$CH$_3$, OCH$_2$CH$_2$C*H*$_2$CH$_3$ and OCH$_2$CH$_2$CH$_2$C*H*$_3$).

3.6. References

1 G. Riess, *Prog. Polym. Sci.*, 2003, **28**, 1107–1170.
2 I. Hamley, *The Physics of Block Copolymers*, OUP Oxford, 1998.
3 K. Holmberg, B. Jönsson, B. Kronberg and B. Lindman, *Surfactants And Polymers in Aqueous Solution*, John Wiley and Sons, 2nd Edn., 2004.
4 R. C. Hayward and D. J. Pochan, *Macromolecules*, 2010, **43**, 3577–3584.
5 T. Nicolai, O. Colombani and C. Chassenieux, *Soft Matter*, 2010, **6**, 3111–3118.
6 P. Kaewsaiha, K. Matsumoto and H. Matsuoka, *Langmuir*, 2005, **21**, 9938–9945.
7 M. Jacquin, P. Muller, R. Talingting-Pabalan, H. Cottet, J. F. Berret, T. Futterer and O. Théodoly, *J. Colloid Interface Sci.*, 2007, **316**, 897–911.
8 L. Meli, J. M. Santiago and T. P. Lodge, *Macromolecules*, 2010, **43**, 2018–2027.
9 B. K. Johnson and R. K. Prud'homme, *Phys. Rev. Lett.*, 2003, **91**, 118302.
10 J. van Stam, S. Creutz, F. C. De Schryver and R. Jérôme, *Macromolecules*, 2000, **33**, 6388–6395.
11 Y.-Y. Won, H. T. Davis and F. S. Bates, *Macromolecules*, 2003, **36**, 953–955.
12 L. Willner, A. Poppe, J. Allgaier, M. Monkenbusch and D. Richter, *Europhys. Lett.*, 2001, **55**, 667.
13 D. Bendejacq, M. Joanicot and V. Ponsinet, *Eur. Phys. J. E*, 2005, **17**, 83–92.
14 H. Schuch, J. Klingler, P. Rossmanith, T. Frechen, M. Gerst, J. Feldthusen and A. H. E. Müller, *Macromolecules*, 2000, **33**, 1734–1740.
15 A. Choucair and A. Eisenberg, *Eur. Phys. J. E*, 2003, **10**, 37–44.
16 P. D. Petrov, M. Drechsler and A. H. E. Müller, *J. Phys. Chem. B*, 2009, **113**, 4218–4225.
17 S. Cerritelli, A. Fontana, D. Velluto, M. Adrian, J. Dubochet, P. De Maria and J. A. Hubbell, *Macromolecules*, 2005, **38**, 7845–7851.
18 O. Colombani, M. Ruppel, M. Burkhardt, M. Drechsler, M. Schumacher, M. Gradzielski, R. Schweins and A. H. E. Müller, *Macromolecules*, 2007, **40**, 4351–4362.
19 I. A. Nyrkova and A. N. Semenov, *Macromol. Theory Simul.*, 2005, **14**, 569–585.
20 L. Meli and T. P. Lodge, *Macromolecules*, 2009, **42**, 580–583.
21 S. Cerritelli, C. P. O'Neil, D. Velluto, A. Fontana, M. Adrian, J. Dubochet and J. A. Hubbell, *Langmuir*, 2009, **25**, 11328–11335.
22 S. Jain and F. S. Bates, *Macromolecules*, 2004, **37**, 1511–1523.
23 J. P. Patterson, M. P. Robin, C. Chassenieux, O. Colombani and R. K. O'Reilly, *Chem. Soc. Rev.*, 2014, **43**, 2412–2425.
24 A. Halperin, *Macromolecules*, 2011, **44**, 5072–5074.
25 R. Lund, L. Willner, D. Richter and E. E. Dormidontova, *Macromolecules*, 2006, **39**, 4566–4575.
26 M. Tian, A. Qin, C. Ramireddy, S. E. Webber, P. Munk, Z. Tuzar and K. Prochazka, *Langmuir*, 1993, **9**, 1741–1748.
27 C. Tsitsilianis, G. Gotzamanis and Z. Iatridi, *Eur. Polym. J.*, 2011, **47**, 497–510.
28 A. K. Bajpai, J. Bajpai, R. Saini and R. Gupta, *Polym. Rev.*, 2011, **51**, 53–97.
29 G. Moad, *Polym. Chem.*, 2017, **8**, 177–219.
30 G. Kocak, C. Tuncer and V. Bütün, *Polym. Chem.*, 2017, **8**, 144–176.
31 D. Roy, W. L. A. Brooks and B. S. Sumerlin, *Chem. Soc. Rev.*, 2013, **42**, 7214–7243.
32 A. Gandhi, A. Paul, S. O. Sen and K. K. Sen, *Asian J. Pharm. Sci.*, 2015, **10**, 99–107.
33 Y.-J. Kim and Y. T. Matsunaga, *J. Mater. Chem. B*, 2017, **5**, 4307–4321.
34 A. S. Lee, A. P. Gast, V. Bütün and S. P. Armes, *Macromolecules*, 1999, **32**, 4302–4310.

35 G. Laruelle, J. François and L. Billon, *Macromol. Rapid Commun.*, 2004, **25**, 1839–1844.
36 A. S. Lee, V. Bütün, M. Vamvakaki, S. P. Armes, J. A. Pople and A. P. Gast, *Macromolecules*, 2002, **35**, 8540–8551.
37 J. Du, L. Fan and Q. Liu, *Macromolecules*, 2012, **45**, 8275–8283.
38 S. K. Samal, M. Dash, S. Van Vlierberghe, D. L. Kaplan, E. Chiellini, C. van Blitterswijk, L. Moroni and P. Dubruel, *Chem. Soc. Rev.*, 2012, **41**, 7147–7194.
39 S. Dinçer, M. Türk and E. Pişkin, *Gene Ther.*, 2005, **12**, S139.
40 S. Dai, P. Ravi and K. C. Tam, *Soft Matter*, 2008, **4**, 435–449.
41 A. S. Hoffman, *Adv. Drug Deliv. Rev.*, 2012, **64**, 18–23.
42 Y.-J. Gao, Z.-Y. Qiao and H. Wang, *Sci. China Chem.*, 2016, **59**, 991–1002.
43 J. Hu, G. Liu, C. Wang, T. Liu, G. Zhang and S. Liu, *Biomacromolecules*, 2014, **15**, 4293–4301.
44 A. Shedge, O. Colombani, T. Nicolai and C. Chassenieux, *Macromolecules*, 2014, **47**, 2439–2444.
45 C. Charbonneau, C. Chassenieux, O. Colombani and T. Nicolai, *Macromolecules*, 2011, **44**, 4487–4495.
46 F. Dutertre, O. Boyron, B. Charleux, C. Chassenieux and O. Colombani, *Macromol. Rapid Commun.*, 2012, **33**, 753–759.
47 C. Charbonneau, M. M. De Souza Lima, C. Chassenieux, O. Colombani and T. Nicolai, *Phys. Chem. Chem. Phys.*, 2013, **15**, 3955–3964.
48 Y. Wang, K. Zhou, G. Huang, C. Hensley, X. Huang, X. Ma, T. Zhao, B. D. Sumer, R. J. DeBerardinis and J. Gao, *Nat. Mater.*, 2013, **13**, 204.
49 K. Zhou, Y. Wang, X. Huang, K. Luby-Phelps, B. D. Sumer and J. Gao, *Angew. Chemie Int. Ed.*, 2011, **50**, 6109–6114.
50 H. Gumz, T. H. Lai, B. Voit and D. Appelhans, *Polym. Chem.*, 2017, **8**, 2904–2908.
51 J. Madsen, G. Madden, E. Themistou, N. J. Warren and S. P. Armes, *Polym. Chem.*, 2018, **9**, 2964–2976.
52 P. Cotanda, D. B. Wright, M. Tyler and R. K. O'Reilly, *J. Polym. Sci. A Polym. Chem.*, 2013, **51**, 3333–3338.
53 C. Charbonneau, C. Chassenieux, O. Colombani and T. Nicolai, *Macromolecules*, 2012, **45**, 1025–1030.
54 O. Colombani, E. Lejeune, C. Charbonneau, C. Chassenieux and T. Nicolai, *J. Phys. Chem. B*, 2012, **116**, 7560–7565.
55 L. Lauber, O. Colombani, T. Nicolai and C. Chassenieux, *Macromolecules*, 2016, **49**, 7469–7477.
56 E. Lejeune, M. Drechsler, J. Jestin, A. H. E. Müller, C. Chassenieux and O. Colombani, *Macromolecules*, 2010, **43**, 2667–2671.
57 O. Borisova, L. Billon, M. Zaremski, B. Grassl, Z. Bakaeva, A. Lapp, P. Stepanek and O. Borisov, *Soft Matter*, 2012, **8**, 7649–7659.
58 D. D. Bendejacq and V. Ponsinet, *J. Phys. Chem. B*, 2008, **112**, 7996–8009.
59 D. D. Bendejacq, V. Ponsinet and M. Joanicot, *Langmuir*, 2005, **21**, 1712–1718.
60 O. Borisova, L. Billon, M. Zaremski, B. Grassl, Z. Bakaeva, A. Lapp, P. Stepanek and O. Borisov, *Soft Matter*, 2011, **7**, 10824–10833.
61 T. Ribaut, J. Oberdisse, B. Annighofer, I. Stoychev, B. Fournel, S. Sarrade and P. Lacroix-Desmazes, *Soft Matter*, 2009, **5**, 4962–4970.
62 D. B. Wright, J. P. Patterson, A. Pitto-Barry, P. Cotanda, C. Chassenieux, O. Colombani and R. K. O'Reilly, *Polym. Chem.*, 2015, **6**, 2761–2768.
63 L. Lauber, J. Santarelli, O. Boyron, C. Chassenieux, O. Colombani and T. Nicolai, *Macromolecules*, 2017, **50**, 416–423.
64 E. Lejeune, C. Chassenieux and O. Colombani, *Prog. Colloid Polym. Sci.*, 2011,

138, 7–16.
65 X. Zhang, F. Boisson, O. Colombani, C. Chassenieux and B. Charleux, *Macromolecules*, 2014, **47**, 51–60.
66 D. F. K. Shim, C. Marques and M. E. Cates, *Macromolecules*, 1991, **24**, 5309–5314.
67 F. Renou, T. Nicolai, E. Nicol and L. Benyahia, *Langmuir*, 2009, **25**, 515–521.
68 M. A. Hillmyer, *J. Polym. Sci. Part B: Polym. Phys.*, 2007, **45**, 3249–3251.
69 A. L. Borovinskii and A. R. Khokhlov, *Macromolecules*, 1998, **31**, 7636–7640.
70 V. V Palyulin and I. I. Potemkin, *Macromolecules*, 2008, **41**, 4459–4463.
71 P. Sens, C. M. Marques and J.-F. Joanny, *Macromolecules*, 1996, **29**, 4880–4890.
72 L. Cantu, M. Corti and P. Salina, *J. Phys. Chem.*, 1991, **95**, 5981–5983.
73 F. Calderara and G. Riess, *Macromol. Chem. Phys.*, 1996, **197**, 2115–2132.
74 S. Il Yoo, B.-H. Sohn, W.-C. Zin, J. C. Jung and C. Park, *Macromolecules*, 2007, **40**, 8323–8328.
75 D. B. Wright, J. P. Patterson, A. Pitto-Barry, A. Lu, N. Kirby, N. C. Gianneschi, C. Chassenieux, O. Colombani and R. K. O'Reilly, *Macromolecules*, 2015, **48**, 6516–6522.
76 N. Yan, X. Yang, Y. Zhu, J. Xu and Y. Sheng, *Macromol. Chem. Phys.*, 2012, **213**, 2261–2266.
77 P. Schuetz, M. J. Greenall, J. Bent, S. Furzeland, D. Atkins, M. F. Butler, T. C. B. McLeish and D. M. A. Buzza, *Soft Matter*, 2011, **7**, 749–759.
78 Č. Koňák and M. Helmstedt, *Macromolecules*, 2001, **34**, 6131–6133.
79 Y. Kotsuchibashi, M. Ebara, K. Yamamoto and T. Aoyagi, *Polym. Chem.*, 2011, **2**, 1362–1367.
80 T. Liu, Y. Qian, X. Hu, Z. Ge and S. Liu, *J. Mater. Chem.*, 2012, **22**, 5020–5030.
81 H. Wu, L. Zhu and V. P. Torchilin, *Biomaterials*, 2013, **34**, 1213–1222.
82 C. Honda, K. Yamamoto and T. Nose, *Polymer*, 1996, **37**, 1975–1984.
83 M. Štěpánek, K. Podhájecká, E. Tesařová, K. Procházka, Z. Tuzar and W. Brown, *Langmuir*, 2001, **17**, 4240–4244.
84 W. Zhang, L. Shi, Y. An, L. Gao and B. He, *J. Phys. Chem. B*, 2004, **108**, 200–204.
85 W. Zhang, F. D'Agosto, O. Boyron, J. Rieger and B. Charleux, *Macromolecules*, 2011, **44**, 7584–7593.
86 K. Van Butsele, P. Sibret, C. A. Fustin, J. F. Gohy, C. Passirani, J.-P. Benoit, R. Jérôme and C. Jérôme, *J. Colloid Interface Sci.*, 2009, **329**, 235–243.
87 S. Gröger, D. Geschke, J. Kärger, F. Stallmach and Č. Koňák, *Macromol. Rapid Commun.*, 2004, **25**, 1015–1018.
88 C.-L. Lo, S.-J. Lin, H.-C. Tsai, W.-H. Chan, C.-H. Tsai, C.-H. D. Cheng and G.-H. Hsiue, *Biomaterials*, 2009, **30**, 3961–3970.
89 H. Yin, E. S. Lee, D. Kim, K. H. Lee, K. T. Oh and Y. H. Bae, *J. Control. Release*, 2008, **126**, 130–138.
90 C. Chang, H. Wei, Q. Li, B. Yang, N. Chen, J.-P. Zhou, X.-Z. Zhang and R.-X. Zhuo, *Polym. Chem.*, 2011, **2**, 923–930.
91 A. Kelarakis, V. Havredaki, X.-F. Yuan, Y.-W. Yang and C. Booth, *J. Mater. Chem.*, 2003, **13**, 2779–2784.
92 L. Yu, Z. Zhang, H. Zhang and J. Ding, *Biomacromolecules*, 2009, **10**, 1547–1553.
93 D. B. Wright, J. P. Patterson, N. C. Gianneschi, C. Chassenieux, O. Colombani and R. K. O'Reilly, *Polym. Chem.*, 2016, **7**, 1577–1583.
94 J. Brandrup, E. H. Immergut and E. A. Grulke, *Polymer Handbook*, John Wiley & Sons, 4th Edn., 1999.
95 D. Y. Kwok, A. Leung, A. Li, C. N. C. Lam, R. Wu and A. W. Neumann, *Colloid Polym. Sci.*, 1998, **276**, 459–469.

96 S. B. Lee, A. J. Russell and K. Matyjaszewski, *Biomacromolecules*, 2003, **4**, 1386–1393.
97 H. Dautzenberg, W. Jaeger, J. Kotz, B. Philipp, C. Seidel and D. Stscherbina, *Polyelectrolytes: formation, characterization and application*, 1994.
98 L. D. Blackman, M. I. Gibson and R. K. O'Reilly, *Polym. Chem.*, 2017, **8**, 233–244.
99 Y. Mai and A. Eisenberg, *Chem. Soc. Rev.*, 2012, **41**, 5969–5985.
100 J. Jakes, *Collect Czech. Chem. Commun.*, 1995, **60**, 1781–1797.
101 L. Lauber, C. Chassenieux, T. Nicolai and O. Colombani, *Macromolecules*, 2015, **48**, 7613–7619.
102 A. B. Mabire, M. P. Robin, W.-D. Quan, H. Willcock, V. G. Stavros and R. K. O'Reilly, *Chem. Commun.*, 2015, **51**, 9733–9736.
103 A. B. Mabire, Q. Brouard, A. Pitto-Barry, R. J. Williams, H. Willcock, N. Kirby, E. Chapman and R. K. O'Reilly, *Polym. Chem.*, 2016, **7**, 5943–5948.
104 M. Staniforth, W.-D. Quan, T. N. V Karsili, L. A. Baker, R. K. O'Reilly and V. G. Stavros, *J. Phys. Chem. A*, 2017, **121**, 6357–6365.

4. Tuning the cloud point of thermoresponsive polymers *via* copolymer blending

4.1. Abstract

In this Chapter, a range of thermoresponsive diblock copolymers were blended together in various combinations to investigate whether the resultant cloud point transition could be modulated by simple manipulation of the molar mixing ratio. Amphiphilic thermoresponsive diblock copolymers composed of statistical poly(*n*-butyl acrylate-*co*-*N*,*N*-dimethylacrylamide) (p(*n*BA-*co*-DMAc)) core-forming blocks and four different thermoresponsive corona-forming blocks, namely poly(diethylene glycol monomethyl ether methacrylate) (p(DEGMA)), poly(*N*-isopropylacrylamide) (p(NIPAM)), poly(*N*,*N*-diethylacrylamide) (p(DEAm)) and poly(oligo(ethylene glycol) monomethyl ether methacrylate) (p(OEGMA)) were selected. Using a combination of variable temperature turbidimetry and microcalorimetry, the thermoresponsive behavior of blended diblock copolymer solutions were analyzed and compared to their constituent pure diblock copolymer solutions to determine whether comicellization was achieved and more significantly, whether the two blended corona-forming thermoresponsive blocks exhibited cooperative behavior.

4.2. Introduction

4.2.1. Thermoresponsive polymers

As outlined in the introduction to Chapter 3, stimuli-responsive polymers can undergo phase transitions in response to an external stimulus such as pH, light, CO_2, glucose, enzymes, or redox potential, and have been of great interest to polymer chemists in recent years.[1–10] In particular, thermoresponsive polymers have been extensively studied within the literature as they offer a simple means of non-invasively altering the polymers environment and thus are attractive candidates for biological applications.[3,8,11–13]

Thermoresponsive polymers exhibit a distinct change in solubility at a critical solution temperature due to the disruption of intramolecular and intermolecular electrostatic and hydrophobic interactions between the polymer chains and the solvent, which results in either chain collapse or expansion upon heating the solution.[4] The temperature at which this change in solubility occurs at is defined as an upper or lower critical solution temperature (UCST or LCST respectively).[11,13] UCST-type polymers typically exist as one phase above their respective critical solution temperature, with phase separation between the polymer and the solvent occurring below this temperature. In contrast, LCST-type polymers are often monophasic below their respective critical solution temperature and biphasic above it (Figure 4.1).[8,11] Upon heating thermoresponsive polymer solutions above their respective LCST or cooling them below their respective UCST, macroscopic precipitation is often observed as a result of this phase separation and is typically measured *via* variable temperature turbidimetry, microcalorimetry or NMR spectroscopy.[14] Note, that the true LCST or UCST of a thermoresponsive polymeric system is defined as the lowest or highest critical point on the phase diagram and is highlighted in Figure 4.1.[11]

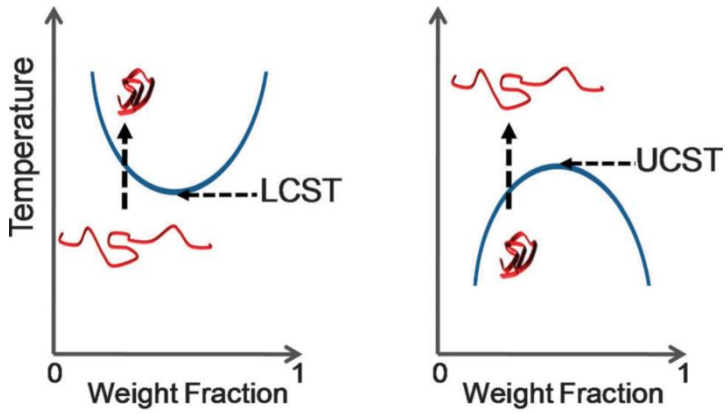

Figure 4.1: Schematic showing the phase transitions associated with LCST (lower critical solution temperature) and UCST (upper critical solution temperature) behavior. Blue line represents the phase separation boundary which produces a cloud point in solution. Figure and caption adapted from ref 11.

Considering a full phase diagram is required in order to characterize a true LCST or UCST for a thermoresponsive polymer system, the cloud point temperature (T_{cp}) is often referred to instead and is simply the temperature at which macroscopic precipitation or dissolution occurs at for any given concentration.[11]

Overall, a wide variety of thermoresponsive monomers exist and have been extensively explored within the literature, including *N*-isopropylacrylamide (NIPAM),[12,15–19] *N*,*N*-diethylacrylamide (DEAm),[20] *N*-vinylcaprolactam (NVC),[21–26] 2-(dimethylamino) ethyl methacrylate (DMAEMA),[27–34] polyethylene glycol monomethyl ether methacrylate (PEGMA),[35–41] *N*-acryloylglycinamide (NAGA),[13,42–45] and 3-dimethyl (methacryloyloxyethyl) ammonium propane sulfonate (DMAPS) (Figure 4.2).[46–48] Tuning the critical solution temperature of thermoresponsive polymers is key with regards to their applications, and has been found to be dependent upon a multitude of variables, including chemical composition, molecular weight, polymer architecture, pH, salt concentration, solution state morphology, co-solvent content, and the presence of additives.[30,32,49–56]

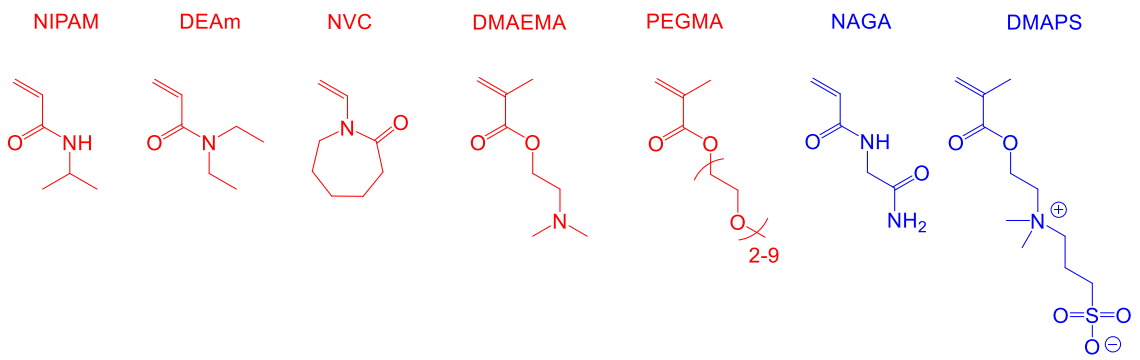

Figure 4.2: Chemical structures of select thermoresponsive monomers that exhibit either LCST (red) or UCST-type (blue) behavior. Note: NIPAM = *N*-isopropylacrylamide; DEAm = *N*,*N*-diethylacrylamide; NVC = *N*-vinylcaprolactam; DMAEMA = 2-(dimethylamino)ethyl methacrylate; PEGMA = polyethylene glycol monomethyl ether methacrylate; NAGA = *N*-acryloylglycinamide; and DMAPS = 3-dimethyl(methacryloyloxyethyl) ammonium propane sulfonate.

4.2.2. Tuning the phase transition temperature

In addition to the variables highlighted above, the LCST or UCST can be precisely tuned *via* the incorporation of hydrophilic or hydrophobic comonomers into the thermoresponsive polymer structure, or *via* end group modification.[12,57,58] For example, Stayton and co-workers copolymerized pH-responsive propylacrylic acid (PAA) with thermoresponsive NIPAM to synthesize a range of highly sensitive dual stimuli-responsive p(NIPAM-*co*-PAA) copolymers.[59] The authors discovered that increasing PAA incorporation in the copolymer resulted in an increase in the observed cloud point between pH 6-7, whilst a decrease in the cloud point was measured between pH 5.0-5.5.[59] Consequently, it was determined that the thermoresponsive behavior of the p(NIPAM-*co*-PAA) copolymers directly reflected the ionization degree of the PAA units and the corresponding pKa of the statistical copolymer. Furthermore, a complete loss in temperature response was found when PAA content in the copolymer was >39 mol %, with no macroscopic precipitation observed between 0-100 °C.[59]

Moreover, a similar investigation was conducted by Schubert and co-workers in which an extensive library of thermoresponsive copolymers were prepared *via* the copolymerization of pH-responsive methacrylic acid (MAA) with a range of oligoethylene glycol monomethyl ether methacrylate ($OEGMA_x$) monomers of various molecular weights, where x = M_n.[60] The authors discovered that the cloud point transition for p($OEGMA_{475}$-*co*-MAA) copolymers could be tuned from 20-95 °C *via* simple manipulation of the comonomer composition.[60] Interestingly, both thermoresponsive and pH-responsive behavior was observed for certain p(MAA-*co*-$OEGMA_{1100}$) copolymer compositions, despite the respective p(MAA) and p($OEGMA_{1100}$) homopolymers exhibiting no thermoresponsive behavior upon heating.[60] Moreover, in separate studies conducted by the Keenan and Mikos groups, the cloud point temperature for p(NIPAM) functionalized polymers was successfully shifted from 32 °C utilizing a copolymerization approach.[61,62] In these examples, non-responsive hydrophobic or hydrophilic monomers were incorporated into the polymer structure which resulted in a corresponding decrease or increase in the transition temperature.[61,62]

Additionally, the synthesis of thermoresponsive polymers with tunable transition temperatures can be achieved *via* the copolymerization of two or more thermoresponsive monomers with different respective cloud points. Lutz and co-workers have demonstrated the versatility of such an approach through the synthesis of thermoresponsive copolymers comprised of PEGMA monomers with two distinct ethylene glycol chain lengths.[37,39] In this case, copolymerization of diethylene glycol monomethyl ether methacrylate (DEGMA) and OEGMA (M_n = 475 g mol^{-1}) generated water soluble copolymers with cloud point temperatures that could be precisely controlled over a temperature range of 28-90 °C. In an analogous study carried out by Fu and co-workers, pH-responsive and thermoresponsive DMAEMA was copolymerized with thermoresponsive NIPAM which

resulted in the formation of random copolymers for which the thermoresponsive behavior was found to dependent upon the solution pH.[63]

More recently, O'Reilly and co-workers synthesized a series of p(NIPAM)-*b*-p(*n*BA-*co*-DMAc) diblock copolymers with varying degrees of hydrophobicity to investigate whether the cloud point transition of the resultant thermoresponsive diblock copolymers changed with respect to increasing *n*-butyl acrylate (*n*BA) incorporation (Figure 4.3).[64]

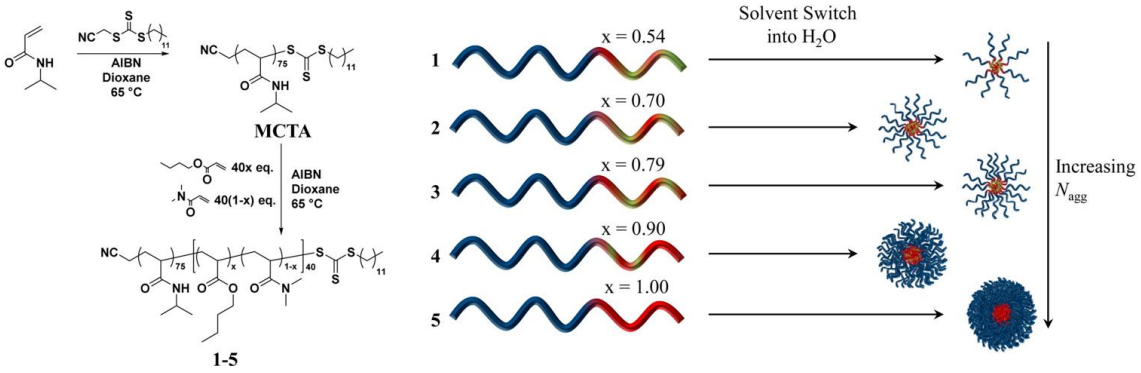

Figure 4.3: Synthesis of p(NIPAM)-*b*-p(*n*BA-*co*-DMAc) diblock copolymers and their subsequent self-assembly in water. Figure and caption adapted from ref 64.

The authors discovered that whilst the cloud point temperature of the p(NIPAM) corona-forming block was found to be independent of the core hydrophobicity, the degree of thermal hysteresis increased across the series of thermoresponsive diblock copolymer micelles with respect to *n*BA incorporation.[64] In a subsequent study by O'Reilly and co-workers, an extensive series of diblock copolymer micelles with different thermoresponsive coronas and tunable aggregation numbers were prepared in an attempt to understand the causes of thermal hysteresis.[14] Chain confinement, coronal chemistry and core hydrophobicity were all found to play a significant role with respect to the observed thermoresponsive behavior.[14]

An alternative method for tuning the phase transition temperature of thermoresponsive polymer solutions simply involves blending two polymers together, that vary in temperature response, to target a range of cloud point temperatures that are intermediate of the two constituent polymers. In particular, Gibson and co-workers discovered that a single cooperative transition was achieved upon blending thermoresponsive homopolymers, formed from the same monomer, together with varying molecular weights.[65] However, this strategy was only successful for polymer classes that exhibit a strong molecular weight dependence on their respective cloud point, in this case p(NIPAM), p(NVC) and poly(*N*-vinylpiperidone) (p(VPip)) (Figure 4.4 a).[65] In contrast, the authors found that blending $p(OEGMA)_{52}$ and $p(DEGMA)_{69}$ homopolymers together resulted in two independent thermal transitions and thus cooperative behavior was not observed for this polymer class (Figure 4.4 b).[65]

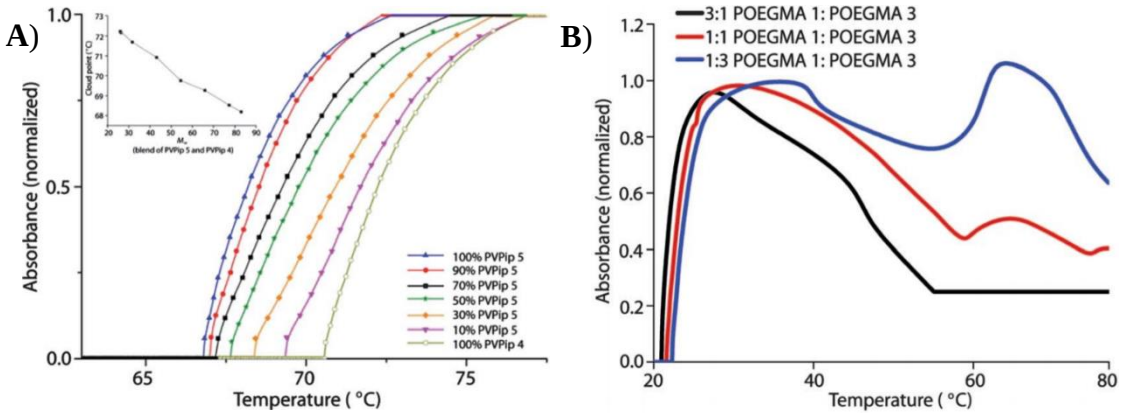

Figure 4.4: a) Turbidimetry curves of **PVPip 4** and **PVPip 5** at varying compositions at 20 mg mL^{-1} with cooperative aggregation of p(VPip) blends observed. Inset is the cloud point temperature *versus* molecular weight of the p(VPip) blends. b) Turbidimetry analysis of p(OEGMA) blends at varying compositions at 20 mg mL^{-1}, where **POEGMA 1** is a $p(DEGMA)_{69}$ homopolymer, and **POEGMA 3** is a $p(OEGMA)_{52}$ homopolymer for which the M_n of the OEGMA monomer is 300 g mol^{-1}. Figure adapted from ref 65.

Gibson and co-workers further investigated the utilization of a blending approach to modulate the transition temperature through the synthesis of a range of $p(NIPAM)_n$ coated

gold nanoparticles.[66] In this case, the authors demonstrated that blending $p(NIPAM)_{25}$ and $p(NIPAM)_{100}$ homopolymers together resulted in non-cooperative behavior with two independent cloud point transitions observed.[66] Considering p(NIPAM) has a weak molecular weight dependence with respect to its cloud point for the homopolymers analyzed in this study,[66] the absence of cooperativity was not unexpected. Significantly, the authors discovered that blending $p(NIPAM)_n$ coated gold nanoparticles of varying size, and/or molecular weight of the thermoresponsive polymer, resulted in cooperative aggregation and a single thermal transition was detected.[66] Furthermore, this cooperativity enabled the cloud point temperature to be tuned in a controlled manner *via* simple manipulation of the molar mixing ratio and more importantly, was found to be independent of the preparation pathway used by the authors (Figure 4.5).[66]

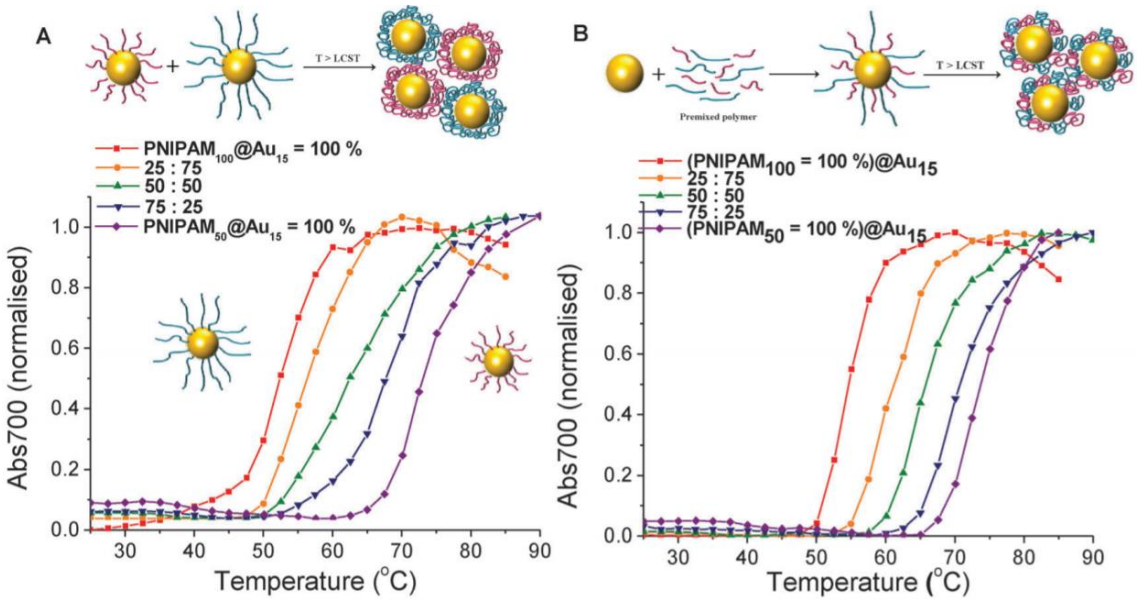

Figure 4.5: Turbidimetry curves of a) $p(NIPAM)_{50}@Au_{15}$ and $p(NIPAM)_{100}@Au_{15}$ mixture of the nanoparticles with different mass fraction, and b) pre-mixture of $p(NIPAM)_{50}$ and $p(NIPAM)_{100}$ with different mass fraction coated Au_{15} in phosphate-buffered saline (PBS) solution. In all cases the total gold core concentration of the solutions was 0.029 mg mL^{-1}. Figure and caption adapted from ref 66.

In the literature examples highlighted above, cooperativity was achieved *via* blending two thermoresponsive polymers together that varied in molecular weight but were composed of the same thermoresponsive monomer. Alternatively, Burel and co-workers have demonstrated that the cloud point transition of thermoresponsive micellar solutions can be modulated *via* blending two amphiphilic block copolymers comprised of a lipid core and two different thermoresponsive corona-forming blocks, poly(2-ethyl-2-oxazoline) (p(EtOx)) and poly(2-isopropyl-2-oxazoline) (p(*i*PrOx)).[67] Interestingly, the authors found that blending lipid-*b*-p(EtOx) and lipid-*b*-p(*i*PrOx) in various molar mixing ratios resulted in cooperative behavior with a single T_{cp} measured for micellar solutions.[67] Moreover, the obtained cloud points in this study directly matched the respective T_{cp}'s for statistical lipid-*b*-p(EtOx-*co*-*i*PrOx) diblock copolymers of the same EtOx incorporation up to 52 wt%.[67]

Despite the success of this study, there is a limited number of reports currently within the literature focusing upon blending thermoresponsive amphiphilic block copolymers together which are comprised of the same core-forming block but have different thermoresponsive corona-forming blocks. For instance, Zhang and co-workers discovered that non-cooperative behavior occurred upon the formation of mixed corona-core nanoparticles consisting of a p(NIPAM)/p(DMAEMA) mixed corona and a shared poly(styrene) (p(St)) core.[68] In this study, thermoresponsive p(NIPAM)-*b*-p(St) and p(DMAEMA)-*b*-p(St) diblock copolymers were synthesized in solution *via* co-mediated dispersion RAFT polymerization and upon self-assembly displayed two distinct cloud point transitions at 44 °C and 56 °C, which corresponded to the collapse of the p(NIPAM) chains and p(DMAEMA) chains respectively.[68] However, in this example a highly hydrophobic p(St) core-forming block with a high core glass transition temperature was selected and thus the formation of blended micelles that have reached thermodynamic equilibrium in solution is unlikely to have been favored.[69]

Ultimately, the copolymer blending protocol offers an attractive strategy for predictively modulating the cloud point temperature of thermoresponsive polymer systems. Herein, further investigation into the limitations and requirements of using this strategy to tune the resultant thermoresponsive behavior of micellar solutions in a controlled manner was carried out.

4.3. Results and Discussion

To investigate whether the cloud point of a micellar solution can be tuned simply by blending two thermoresponsive amphiphilic diblock copolymers together, careful consideration of the constituent diblock copolymer structures was required. As discussed in Chapter 3, O'Reilly and co-workers have previously demonstrated that the success of the copolymer blending protocol is largely dependent upon whether polymeric micelles can reach thermodynamic equilibrium within the experimental timeframe whilst possessing compatible core-forming blocks.[69] Therefore, it was envisaged that selecting amphiphilic diblock copolymers composed of short core-forming blocks with relatively low hydrophobic character coupled with a low core glass transition temperature (T_g) could drive the formation of thermodynamically favored blended micelles for which unimer exchange is facilitated.[69] Previously, O'Reilly and co-workers explored the main factors that influence thermal hysteresis through the synthesis of an extensive range of thermoresponsive amphiphilic diblock copolymers composed of statistical p(*n*BA-*co*-DMAc) core-forming blocks with varying degrees of hydrophobicity and four different thermoresponsive corona-forming blocks: p(DEAm), p(NIPAM), p(DEGMA) and p(OEGMA).[14]

Considering the formerly outlined prerequisites for favorable blending dynamics, amphiphilic diblock copolymers (**4i**-**4iv**) with the lowest percentage incorporation of *n*BA in the respective core-forming blocks for each of the four distinct thermoresponsive corona-forming blocks were selected herein (Scheme 4.1).[14] It was postulated that blending diblock copolymers with similar core-forming blocks but differing thermoresponsive corona-forming blocks may allow the successful formation of blended diblock copolymer micelles. Moreover, if the two corona-forming thermoresponsive blocks displayed cooperative behavior then blended diblock copolymer micelles may

potentially exhibit a cloud point transition at an intermediate temperature with respect to the two constituent pure diblock copolymer micelles.

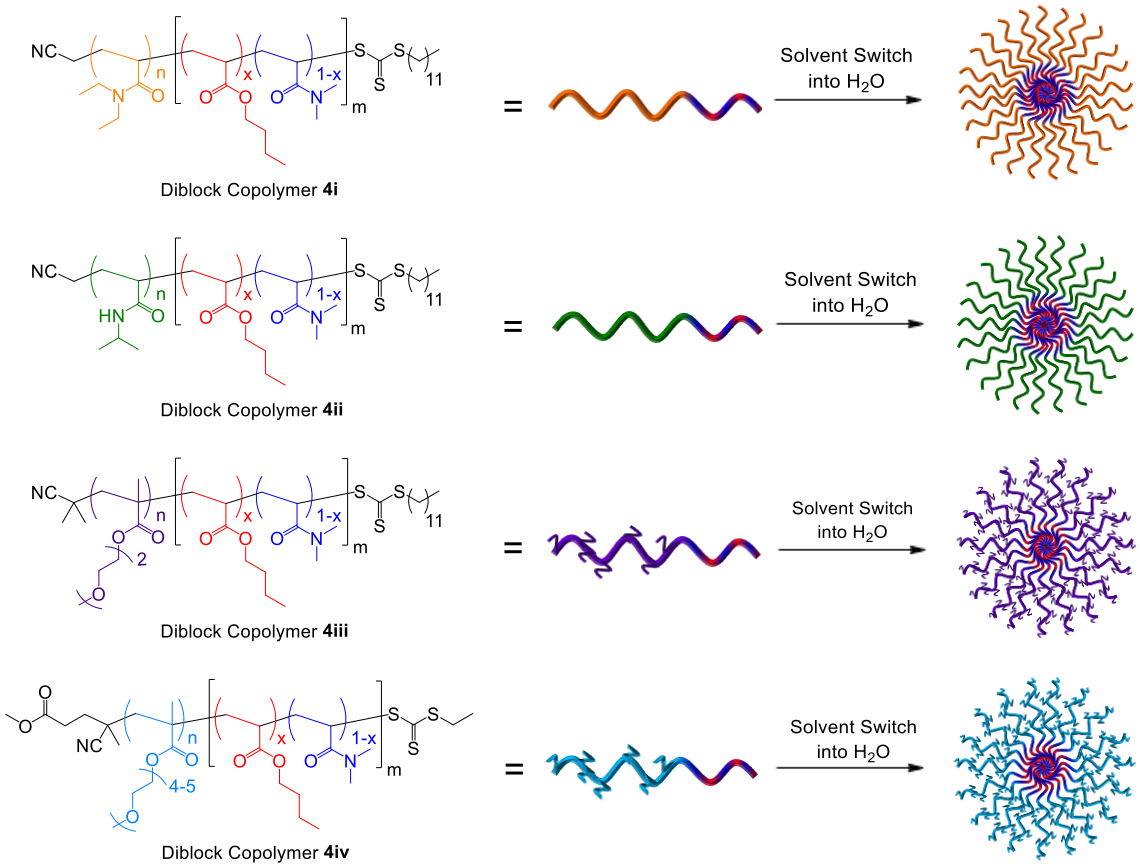

Scheme 4.1: Left: chemical structure of amphiphilic thermoresponsive diblock copolymers **4i-4iv** composed of statistical p(*n*BA$_x$-*co*-DMAc$_{1-x}$)$_m$ core-forming blocks and differing thermoresponsive corona-forming blocks; previously synthesized *via* RAFT polymerization by O'Reilly and co-workers.[14] Right: schematic representing the self-assembly of amphiphilic diblock copolymers **4i-4iv** into spherical micelles *via* a solvent switch technique into aqueous solution previously conducted by O'Reilly and co-workers.[14]

Amphiphilic thermoresponsive diblock copolymers **4i-4iv** (Scheme 4.1) were synthesized *via* RAFT polymerization by O'Reilly and co-workers prior to this study, characterization data for which is summarized in Table 4.1.[14] Turbidimetry analysis of the pure diblock copolymer micelles formed upon self-assembly allowed the authors to determine the cloud point transition (T_{cp}) for each diblock copolymer (**4i-4iv**) (Table 4.1).[14]

Diblock Copolymer	Corona	n^a	x^a	m^a	$M_{n,\,NMR}{}^a$ (kDa)	$M_{n,\,SEC}{}^b$ (kDa)	$Đ_M{}^b$	$T_{cp}{}^c$ (°C)
4i	p(DEAm)	68	0.50	38	12.9	12.0	1.16	32
4ii	p(NIPAM)	75	0.54	37	12.9	13.0	1.10	32
4iii	p(DEGMA)	66	0.46	35	16.4	15.8	1.41	20
4iv	p(OEGMA)	65	0.44	39	24.2	20.1	1.34	61

Table 4.1: Characterization data previously obtained by O'Reilly and co-workers for the following amphiphilic thermoresponsive diblock copolymers: p(DEAm)$_n$-*b*-p(*n*BA$_x$-*co*-DMAc$_{1-x}$)$_m$ (**4i**), p(NIPAM)$_n$-*b*-p(*n*BA$_x$-*co*-DMAc$_{1-x}$)$_m$ (**4ii**), p(DEGMA)$_n$-*b*-p(*n*BA$_x$-*co*-DMAc$_{1-x}$)$_m$ (**4iii**) and p(OEGMA)$_n$-*b*-p(*n*BA$_x$-*co*-DMAc$_{1-x}$)$_m$ (**4iv**).[14] Key: [a] determined by end group analysis using ^{1}H NMR spectroscopy; [b] determined by SEC analysis based on poly(methyl methacrylate) [p(MMA)] standards with either THF (**4i**) or DMF (**4ii-4iv**) as the eluent; [c] mean cloud point upon heating the micellar solutions determined using turbidimetry data across three heating and cooling cycles.[14]

As discussed in Chapter 3, when comparing self-assemblies produced *via* copolymer blending it is important to differentiate between the two different types of polymer nanostructures. Pure nanostructures are those self-assembled from a single block copolymer with a specific composition, whilst blended nanostructures are those self-assembled from a block copolymer mixture of two block copolymers comprised of different compositions.

4.3.1. Blending thermoresponsive amphiphilic diblock copolymers – an initial investigation

Initially, a series of diblock copolymer mixtures were prepared by blending thermoresponsive diblock copolymers **4i**-**4iv** together in various combinations at a 1:1 molar mixing ratio to target a range of intermediate cloud points (T_{cp}) (Scheme 4.2 and Table 4.2). In this case, blended diblock copolymer solutions were prepared *via* unimer blending (UB) which involved blending the constituent diblock copolymers together in dry powder form to match the desired molar mixing ratio, followed by self-assembly *via* a solvent switch technique from acetone into ice cold water.

As depicted in Scheme 4.2, diblock copolymer **4iii** (T_{cp} = 20 °C) composed of a p(DEGMA) corona-forming block was blended with diblock copolymers **4i** (T_{cp} = 32 °C) and **4ii** (T_{cp} = 32 °C) composed of linear p(DEAm) and p(NIPAM) corona-forming blocks respectively. Next, brush-like p(OEGMA)-*b*-p(*n*BA-*co*-DMAc) diblock copolymer **4iv** (T_{cp} = 61 °C) was blended with linear p(DEAm)-*b*-p(*n*BA-*co*-DMAc) diblock copolymer **4i** (T_{cp} = 32 °C) to explore the effect of increasing chain entanglement upon blending dynamics. Finally, p(DEGMA)-*b*-p(*n*BA-*co*-DMAc) diblock copolymer **4iii** (T_{cp} = 20 °C) was blended with p(OEGMA)-*b*-p(*n*BA-*co*-DMAc) diblock copolymer **4iv** (T_{cp} = 61 °C) with both diblock copolymers composed of corona-forming blocks with brush-like chain architectures.

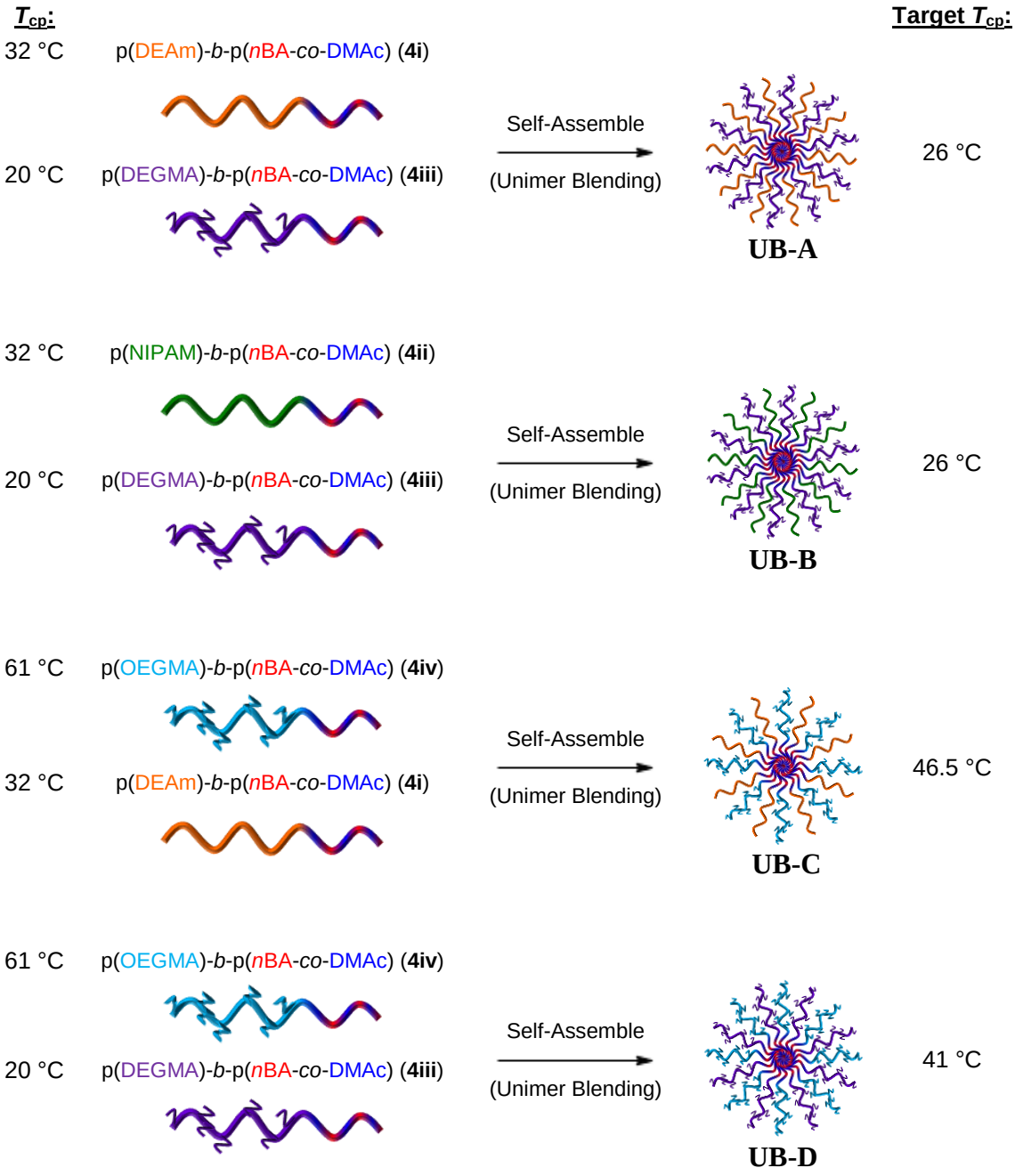

Scheme 4.2: Schematic demonstrating the different thermoresponsive diblock copolymer blending combinations investigated herein. Blended diblock copolymer solutions were prepared by unimer blending (UB): the two constituent thermoresponsive diblock copolymers (**4i-4iv**) were first blended in the powder state to match the desired molar mixing ratio of 1:1 and then subsequently self-assembled *via* a solvent switch technique into aqueous solution.

Blended Diblock Copolymer Sample	Diblock Copolymer	T_{cp} [a] (°C)	Mole fraction	Diblock Copolymer	T_{cp} [a] (°C)	Mole fraction	Target T_{cp} (°C)
UB-A	**4i**	32	0.5	**4iii**	20	0.5	26
UB-B	**4ii**	32	0.5	**4iii**	20	0.5	26
UB-C	**4iv**	61	0.5	**4i**	32	0.5	46.5
UB-D	**4iv**	61	0.5	**4iii**	20	0.5	41

Table 4.2: Molar mixing ratios for blended thermoresponsive diblock copolymer samples prepared *via* unimer blending (UB). Key: [a] mean cloud point upon heating the micellar solutions determined using turbidimetry data across three heating and cooling cycles previously obtained by O'Reilly and co-workers.[14]

With regards to blending thermoresponsive diblock copolymers with similar core-forming blocks but differing corona-forming blocks together, it was important to consider the potential outcomes and the most effective analytical method for differentiating between them. For instance, O'Reilly and co-workers have previously confirmed the formation of blended micelles that are structurally identical to pure micelles of the same composition using a combination of cryo-transmission electron microscopy, static light scattering (SLS), dynamic light scattering (DLS), and small-angle X-ray scattering (SAXS) techniques.[69,70] However, light scattering data previously obtained by O'Reilly and co-workers revealed negligible differences in the hydrodynamic radius (R_h), micellar core radius (R_{core}) and aggregation number (N_{agg}) for pure diblock copolymer micelles formed upon the self-assembly of thermoresponsive diblock copolymers **4i-4iv**.[14,64] Consequently, it was proposed that the analytical techniques listed above would not allow accurate differentiation between the successful formation of blended diblock copolymer micelles with respect to the undesired formation of two separate populations of pure diblock copolymer micelles – with regards to blending thermoresponsive diblock copolymers **4i-4iv** together in the respective combinations summarized in Table 4.2.

As outlined in the introduction to this Chapter, upon heating thermoresponsive polymers above their respective LCST, macroscopic precipitation can be observed as a result of phase separation due to the thermoresponsive polymeric block forming polymer-polymer interactions in preference to polymer-solvent interactions.[14] Note, that this optically observable macroscopic effect can be measured *via* variable temperature turbidimetry, with the cloud point transition (T_{cp}) defined as the temperature at which the amount of transmitted light is reduced to 50% with respect to the overall reduction in transmitted light over the thermal transition. Considering this, it was envisaged that variable temperature turbidimetry analysis of the blended diblock copolymer mixtures would confirm, at least qualitatively, whether blended diblock copolymer micelles had formed in solution and more importantly, whether the two corona-forming thermoresponsive blocks exhibited cooperative behavior upon comicellization.

For instance, self-assembly of thermoresponsive diblock copolymers **4iii** and **4iv** *via* unimer blending (Table 4.2) could rationally result in four different potential outcomes (Figure 4.6 a-d). Firstly, the unsuccessful formation of blended diblock copolymer micelles with the formation of two separate populations of pure diblock copolymer micelles instead. In this case, two distinct cloud point transitions would be measured upon turbidimetry analysis corresponding to the precipitation of the two constituent pure diblock copolymer micelles (Figure 4.6 a). A second potential outcome could be the formation of blended diblock copolymer micelles as well as pure diblock copolymer micelles in solution. Once again, multiple cloud point transitions would be observed corresponding to the precipitation of both pure and blended diblock copolymer micelles (Figure 4.6 b). Alternatively, copolymer blending could lead to the successful formation of blended diblock copolymer micelles for which the two thermoresponsive corona-forming blocks exhibit non-cooperative behavior upon comicellization. Consequently, one cloud point transition would be detected at the transition temperature corresponding

to the collapse of the higher thermoresponsive corona-forming block upon heating (Figure 4.6 c). Finally, self-assembly of thermoresponsive diblock copolymers *via* unimer blending may lead to the successful formation of blended diblock copolymer micelles that exhibit cooperative behavior as desired. In this case, one cloud point transition at an intermediate temperature with respect to the cloud point transitions of the constituent pure diblock copolymer micelles would be observed *via* turbidimetry (Figure 4.6 d).

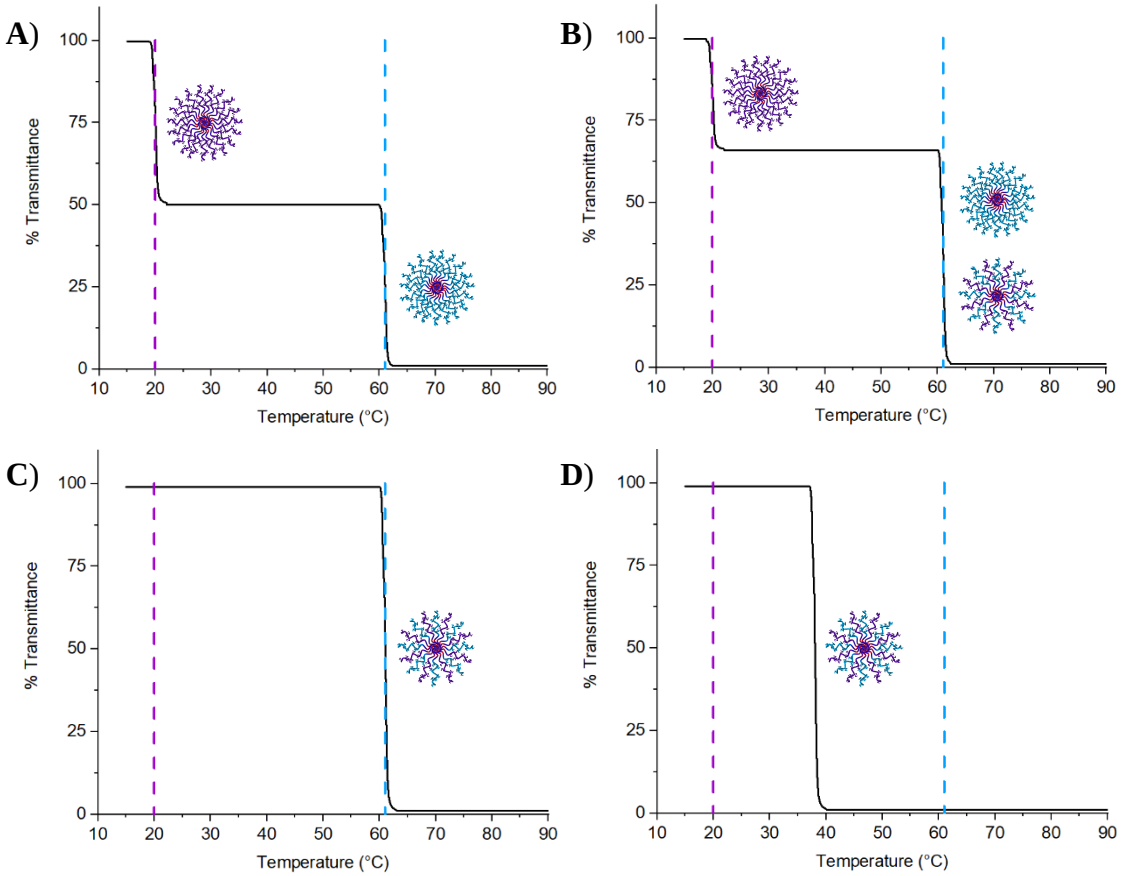

Figure 4.6: Representative variable temperature turbidimetry analyses of potential diblock copolymer mixtures that could form from the self-assembly of thermoresponsive diblock copolymers **4iii** (T_{cp} = 20 °C) and **4iv** (T_{cp} = 61 °C) *via* unimer blending: a) formation of two separate populations of pure diblock copolymer micelles; b) formation of both blended and pure diblock copolymer micelles; c) formation of blended diblock copolymer micelles that exhibit non-cooperative behavior; d) formation of blended diblock copolymer micelles that exhibit cooperative behavior. Dashed lines represent the cloud point temperature (T_{cp}) for micellar solutions of **4iii** (purple) and **4iv** (light blue).

Consequently, blended diblock copolymer mixtures **UB-A:D** were analyzed *via* variable temperature turbidimetry with their thermoresponsive behavior compared to their respective constituent pure diblock copolymer micelles (**4i-4iv**). Turbidimetry analysis was initially conducted at 1 mg mL^{-1} with a temperature ramping rate of 1 °C min^{-1} to mirror the experimental conditions previously employed by O'Reilly and co-workers to allow for comparison.[14] However, for blended diblock copolymer solutions **UB-A:D**, a relatively small decrease in the overall percentage transmittance as a result of macroscopic precipitation was observed in each case. Therefore, the concentration for blended diblock copolymer mixtures **UB-A:D** was increased to 3 mg mL^{-1} to ensure a complete reduction in percentage transmittance upon heating the micellar solutions. Note, that thermoresponsive diblock copolymers **4i-4iv** were subsequently reanalyzed at 3 mg mL^{-1} prior to this study.

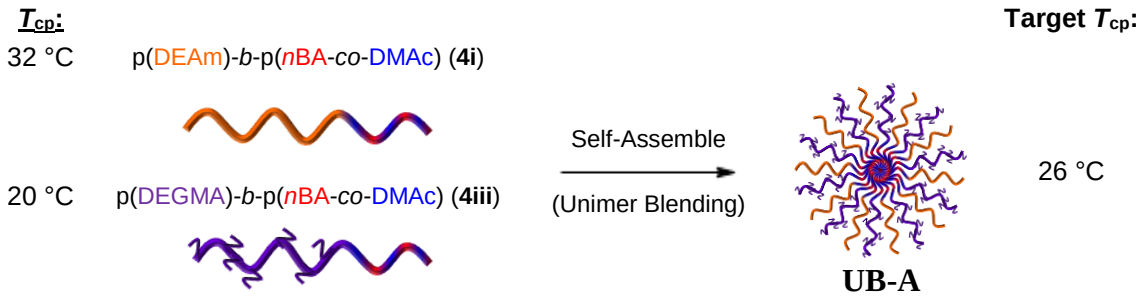

Scheme 4.3: Preparation of blended diblock copolymer solution **UB-A**: thermoresponsive diblock copolymers **4i** and **4iii** were first blended in the powder state to match the desired molar mixing ratio of 1:1 and then subsequently self-assembled *via* a solvent switch technique into aqueous solution.

Interestingly, turbidimetry analysis of blended diblock copolymer solution **UB-A**, formed from blending diblock copolymer **4iii** (T_{cp} = 20 °C) with diblock copolymer **4i** (T_{cp} = 32 °C) (Scheme 4.3), revealed a single broad cloud point transition starting at 29 °C with a T_{cp} = 33.1 °C (Figure 4.7 a).

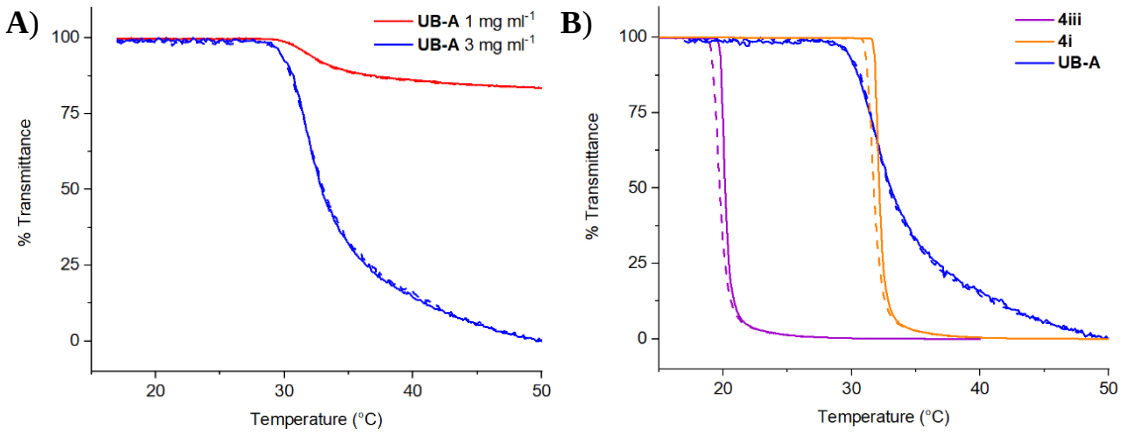

Figure 4.7: a) Variable temperature turbidimetry analysis of blended diblock copolymer solution **UB-A** at 1 mg mL^{-1} (red) and 3 mg mL^{-1} (blue); b) variable temperature turbidimetry analysis of blended diblock copolymer solution **UB-A** (blue), pure p(DEGMA) diblock copolymer micelles **4iii** (purple) and pure p(DEAm) diblock copolymer micelles **4i** (orange) at 3 mg mL^{-1}. In each case, the solid trace represents the heating cycle and the dashed trace represents the cooling cycle. Heating and cooling rate = 1 °C min^{-1}.

Comparison of the turbidimetry data obtained for **UB-A** with respect to pure p(DEGMA) diblock copolymer micelles **4iii** and pure p(DEAm) diblock copolymer micelles **4i** confirmed the successful formation of blended diblock copolymer micelles in solution (Figure 4.7 b). Critically, no significant change in percentage transmittance was observed at 20 °C for **UB-A**, which would correspond to the macroscopic precipitation of pure p(DEGMA) diblock copolymer micelles **4iii** (Figure 4.7 b). Moreover, the absence of a thermal hysteresis in the turbidimetry data obtained for **UB-A** suggested that the formation of blended diblock copolymer micelles was relatively favored given the high degree of reversibility observed for this system. However, no change in percentage transmittance was observed at 26 °C for **UB-A** as targeted (Figure 4.7) and thus the two thermoresponsive corona-forming blocks, p(DEGMA) and p(DEAm), exhibited non-cooperative behavior.

Non-cooperative behavior was also observed for blended diblock copolymer solution **UB-B**, formed from blending diblock copolymer **4iii** (T_{cp} = 20 °C) with diblock copolymer **4ii** (T_{cp} = 32 °C) (Scheme 4.4).

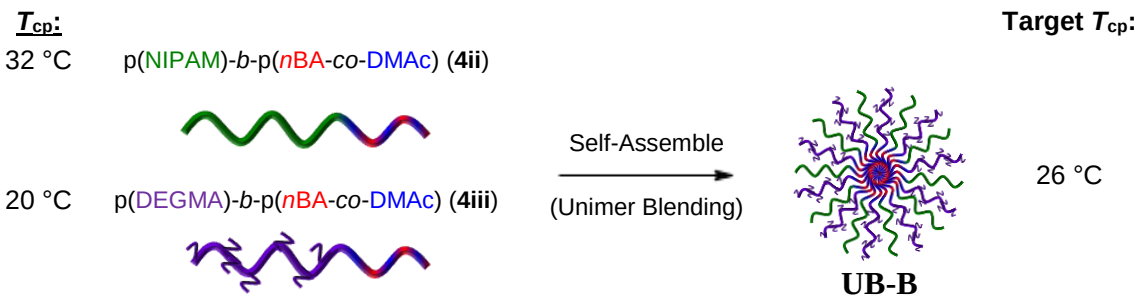

Scheme 4.4: Preparation of blended diblock copolymer solution **UB-B**: thermoresponsive diblock copolymers **4ii** and **4iii** were first blended in the powder state to match the desired molar mixing ratio of 1:1 and then subsequently self-assembled *via* a solvent switch technique into aqueous solution.

Once again, copolymer blending resulted in the successful formation of diblock copolymer micelles composed of a p(*n*BA-*co*-DMAc) core and a blend of both brush-like p(DEGMA) and linear p(NIPAM) thermoresponsive corona-forming blocks. A broad cloud point transition was detected at 31.4 °C which closely matched the respective cloud point transition of pure p(NIPAM) diblock copolymer micelles **4ii** (Figure 4.8 b). Therefore, the collapse of the brush-like p(DEGMA) chains did not directly affect the collapse of the linear p(NIPAM) chains and thus no change in percentage transmittance was observed at 26 °C as targeted (Figure 4.8). Ultimately, comicellization was achieved for **UB-A** and **UB-B**, for which macroscopic precipitation of the blended diblock copolymer micelles was measured at the transition temperature corresponding to the chain collapse of the higher thermoresponsive corona-forming block, p(DEAm) and p(NIPAM) respectively.

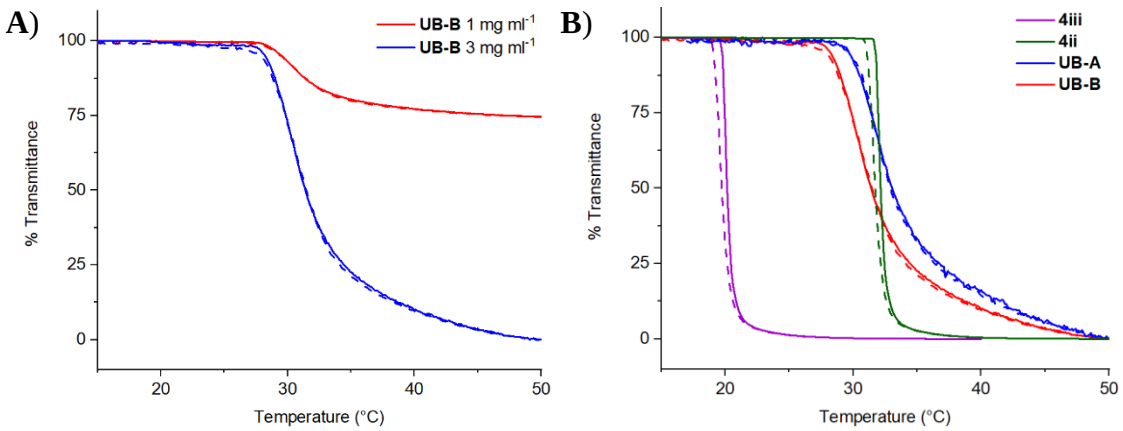

Figure 4.8: a) Variable temperature turbidimetry analysis of blended diblock copolymer solution **UB-B** at 1 mg mL^{-1} (red) and 3 mg mL^{-1} (blue); b) variable temperature turbidimetry analysis of blended diblock copolymer solution **UB-A** (blue), blended diblock copolymer solution **UB-B (**red), pure p(DEGMA) diblock copolymer micelles **4iii** (purple) and pure p(NIPAM) diblock copolymer micelles **4ii** (green) at 3 mg mL^{-1}. In each case, the solid trace represents the heating cycle and the dashed trace represents the cooling cycle. Heating and cooling rate = 1 °C min^{-1}.

In contrast to **UB-A** and **UB-B**, two distinct cloud point transitions were observed for blended diblock copolymer solution **UB-C** (Figure 4.9). As depicted in Scheme 4.5, **UB-C** was formed from blending together thermoresponsive diblock copolymers **4iv** (T_{cp} = 61 °C) and **4i** (T_{cp} = 32 °C) composed of brush-like p(OEGMA) and linear p(DEAm) corona-forming blocks respectively. In this case, turbidimetry analysis suggested the presence of three populations of micelles for **UB-C**; pure p(DEAm) diblock copolymer micelles **4i**, pure p(OEGMA) diblock copolymer micelles **4iv** and blended diblock copolymer micelles.

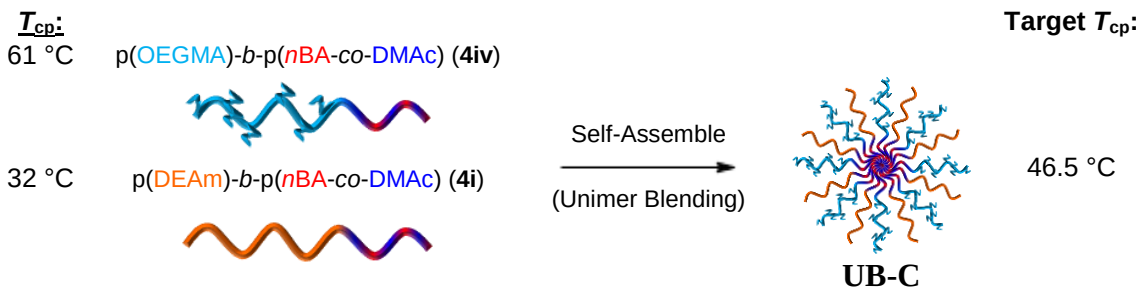

Scheme 4.5: Preparation of blended diblock copolymer solution **UB-C**: thermoresponsive diblock copolymers **4iv** and **4i** were first blended in the powder state to match the desired molar mixing ratio of 1:1 and then subsequently self-assembled *via* a solvent switch technique into aqueous solution.

As shown in Figure 4.9, upon heating **UB-C** a broad cloud point transition was initially observed at 36.6 °C which corresponded to the macroscopic precipitation of pure p(DEAm) diblock copolymer micelles **4i**. Subsequently, a second cloud point transition was detected at 60 °C which was ascribed to the chain collapse of the p(OEGMA) corona-forming block in solution. Note, that for both cloud point transitions an overall decrease of 50% transmittance was measured for **UB-C**.

As outlined previously in Figure 4.6 a, the presence of two cloud point transitions for **UB-C** suggested the formation of two separate populations of pure diblock copolymer micelles in solution as opposed to the formation of blended diblock copolymer micelles. However, in this case a significant thermal hysteresis was observed for **UB-C** which was in contrast to the turbidimetry data obtained for **UB-A** and **UB-B**. Upon cooling, an increase of only 30% transmittance as opposed to 50% transmittance for **UB-C** was detected at 60.5 °C, with a further increase of 70% transmittance recorded at 34 °C (Figure 4.9). In light of this, the initial increase in percentage transmittance upon cooling was ascribed to the resuspension of pure p(OEGMA) diblock copolymer micelles **4iv**. Moreover, the second increase in percentage transmittance corresponded to the resuspension of pure p(DEAm) diblock copolymer micelles **4i** and blended diblock copolymer micelles, with the p(DEAm) coronal chains rehydrated once the temperature

of the solution reached the respective cloud point of **4i**. Overall, the increase in chain entanglement from the introduction of the p(OEGMA) corona-forming block resulted in the formation of both pure and blended diblock copolymer micelles. Furthermore, the latter exhibited non-cooperative behavior with the cloud point transition of blended diblock copolymer micelles dependent upon the collapse state of the higher thermoresponsive corona-forming block upon heating and the lower thermoresponsive corona-forming block upon cooling.

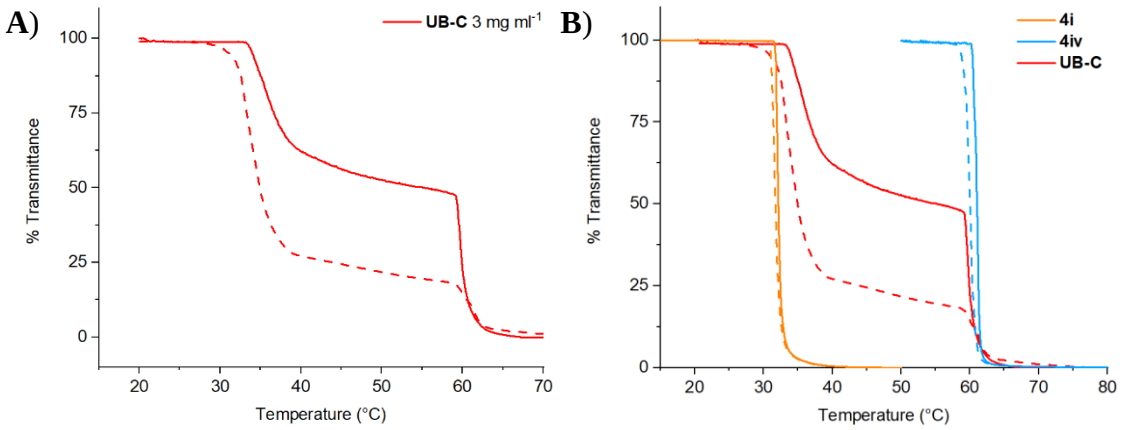

Figure 4.9: a) Variable temperature turbidimetry analysis of blended diblock copolymer solution **UB-C** at 3 mg mL^{-1} (red); b) variable temperature turbidimetry analysis of blended diblock copolymer solution **UB-C** (red), pure p(DEAm) diblock copolymer micelles **4i** (orange) and pure p(OEGMA) diblock copolymer micelles **4iv** (light blue) at 3 mg mL^{-1}. In each case, the solid trace represents the heating cycle and the dashed trace represents the cooling cycle. Heating and cooling rate = 1 °C min^{-1}.

Finally, blended diblock copolymer solution **UB-D**, formed from blending diblock copolymer **4iii** (T_{cp} = 20 °C) with diblock copolymer **4iv** (T_{cp} = 61 °C) (Scheme 4.6**Scheme 4.3**), was investigated *via* variable temperature turbidimetry. In this case, both diblock copolymers were composed of thermoresponsive corona-forming blocks with brush-like chain architectures.

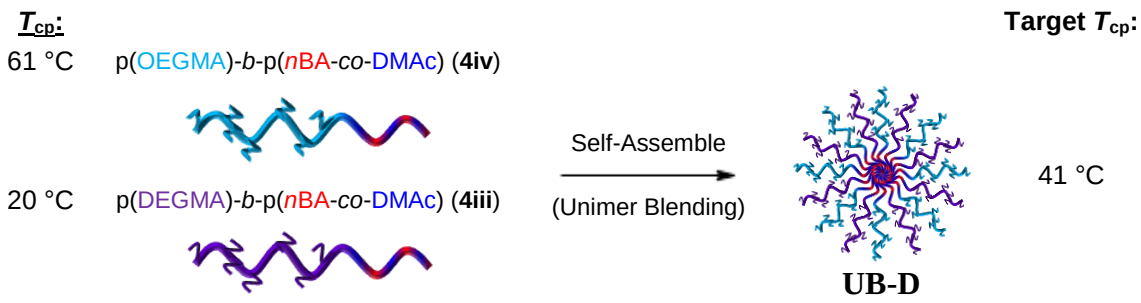

Scheme 4.6: Preparation of blended diblock copolymer solution **UB-D**: thermoresponsive diblock copolymers **4iv** and **4iii** were first blended in the powder state to match the desired molar mixing ratio of 1:1 and then subsequently self-assembled *via* a solvent switch technique into aqueous solution.

Turbidimetry analysis of **UB-D** indicated the successful formation of one population of blended diblock copolymer micelles composed of a p(*n*BA-*co*-DMAc) core and a blend of brush-like p(DEGMA) and p(OEGMA) thermoresponsive corona-forming blocks (Figure 4.10). Significantly, no change in percentage transmittance was observed for **UB-D** at 20 °C or 61 °C which correspond to the cloud point transitions for the constituent pure diblock copolymer micelles **4iii** and **4iv** respectively. Importantly, a broad cloud point transition was measured for **UB-D** at an intermediate temperature of 36.5 °C which closely matched the targeted theoretical T_{cp} of 41 °C (Table 4.2). Therefore, in this case the two thermoresponsive corona-forming blocks behaved in a cooperative manner upon comicellization, with the collapse of the thermoresponsive p(OEGMA) chains occurring at a much lower transition temperature due to the close proximity of the p(DEGMA) chains within the micelle corona.

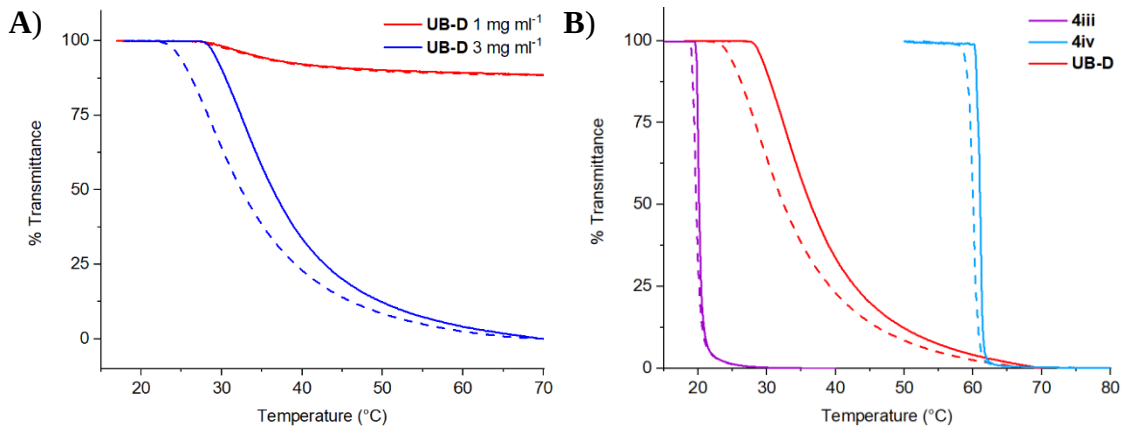

Figure 4.10: a) Variable temperature turbidimetry analysis of blended diblock copolymer solution **UB-D** at 1 mg mL^{-1} (red) and 3 mg mL^{-1} (blue); b) variable temperature turbidimetry analysis of blended diblock copolymer solution **UB-D** (red), pure p(DEGMA) diblock copolymer micelles **4iii** (purple) and pure p(OEGMA) diblock copolymer micelles **4iv** (light blue) at 3 mg mL^{-1}. In each case, the solid trace represents the heating cycle and the dashed trace represents the cooling cycle. Heating and cooling rate = 1 °C min^{-1}.

Following this initial study into blending two thermoresponsive amphiphilic diblock copolymers together to tune the cloud point, blended diblock copolymer system **UB-D** was selected for further study in order to investigate the following research aims. Namely, to determine whether the cloud point transition of **UB-D** could be modulated in a controlled manner over a temperature range *via* simple manipulation of the molar mixing ratio. Secondly, to ascertain whether the presence of a statistical p(*n*BA-*co*-DMAc) core-forming block in the constituent diblock copolymer structures and subsequent comicellization was required for cooperative behavior. Finally, to establish whether the broad nature of the cloud point transitions observed for **UB-A:D** in comparison to the sharp cloud point transitions measured for pure diblock copolymer micelles was dependent upon the sample concentration. Note, that a small amount of dispersity with regards to the cloud point transition for a blended diblock copolymer solution was expected considering blended diblock copolymer micelles will not share identical thermoresponsive coronal compositions.

4.3.2. Synthesis of thermoresponsive amphiphilic diblock copolymers with brush-like chain architectures

Unfortunately, further analysis of blended diblock copolymer system **UB-D** required the two constituent diblock copolymers, **4iii** and **4iv**, to be resynthesized. Previously, O'Reilly and co-workers synthesized amphiphilic thermoresponsive diblock copolymers **4iii** and **4iv** *via* RAFT polymerization for which either 2-cyanopropan-2-yl ethyl carbonotrithioate (CPET) or methyl 4-cyano-4-(((ethylthio)carbonothioyl)thio) pentanoate (MCETP) were selected as the RAFT agent respectively.[14] However, relatively high dispersity values for all five amphiphilic thermoresponsive diblock copolymers composed of a p(DEGMA) corona-forming block were obtained by O'Reilly and co-workers ($Đ_M$ = 1.36-1.46).[14] Therefore, it was proposed that a switch in the RAFT agent from CPET to MCETP may afford greater control for the RAFT homopolymerization of DEGMA and subsequent chain extension of the resultant macro chain transfer agent (macroCTA).

To this end, a series of RAFT homopolymerizations of OEGMA and DEGMA were conducted in 1,4-dioxane at 70 °C with either CPET or MCETP as the chosen RAFT agent (Scheme 4.7).

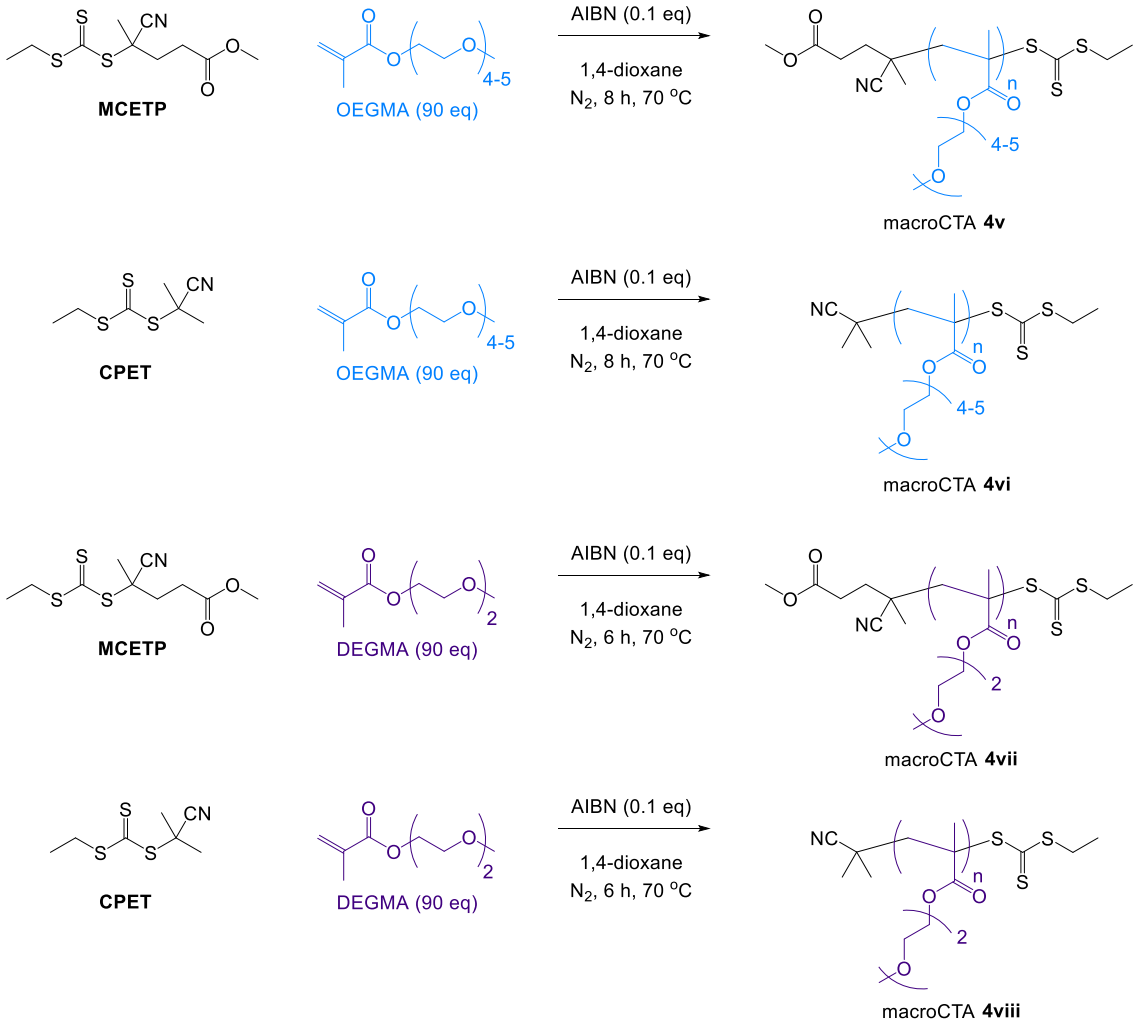

Scheme 4.7: RAFT homopolymerization of OEGMA and DEGMA with either 2-cyanopropan-2-yl ethyl carbonotrithioate (CPET) or methyl 4-cyano-4-(((ethylthio)carbonothioyl)thio)pentanoate (MCETP) to produce two p(OEGMA)$_n$ homopolymers (macroCTA **4v-4vi**) and two p(DEGMA)$_n$ homopolymers (macroCTA **4vii-4viii**). AIBN = 2,2'-azobisisobutyronitrile.

Monomer conversion was monitored throughout using ^{1}H NMR spectroscopy with RAFT homopolymerizations quenched by immersion in liquid nitrogen upon reaching the desired block length (DP = 65). Upon purification, four thermoresponsive macroCTAs (**4v-4viii**) were isolated; characterization data for which is summarized in Table 4.3.

macroCTA	RAFT agent	Corona-Forming Monomer	ρ^a (%)	DP^b	$M_{n,NMR}{}^b$ (kDa)	$M_{n,SEC}{}^c$ (kDa)	$Đ_M{}^c$
4v	MCETP	OEGMA	71	64	19.5	18.4	1.24
4vi	CPET	OEGMA	72	65	19.7	21.0	1.44
4vii	MCETP	DEGMA	74	67	12.9	12.3	1.18
4viii	CPET	DEGMA	75	68	13.0	12.8	1.26

Table 4.3: Characterization data for thermoresponsive p(OEGMA)$_n$ homopolymers (macroCTA **4v-4vi**) and p(DEGMA)$_n$ homopolymers (macroCTA **4vii-4viii**). Key: [a] monomer conversion was calculated by ^{1}H NMR spectroscopy of the crude polymerization mixture (300 MHz, $CDCl_3$); [b] determined by end group analysis using ^{1}H NMR spectroscopy (400 MHz, $CDCl_3$); [c] obtained by SEC analysis based on p(MMA) standards with $CHCl_3$ as the eluent.

Upon SEC analysis, all four thermoresponsive homopolymers (**4v-4viii)** displayed symmetrical and unimodal molecular weight distributions which indicated relatively good control over the RAFT homopolymerization for both OEGMA and DEGMA using either CPET or MCETP. However, appreciably higher dispersity values were obtained for thermoresponsive macroCTAs **4vi** ($Đ_M$ = 1.44) and **4viii** ($Đ_M$ = 1.26) synthesized using CPET in comparison to their respective thermoresponsive analogues **4v** ($Đ_M$ = 1.24) and **4vii** ($Đ_M$ = 1.18) for which MCETP was used. Importantly, the molecular weight distributions determined by SEC using an RI and UV detector (recorded at 309 nm) overlapped appreciably for both thermoresponsive macroCTAs **4v** and **4vii** which confirmed that the trithiocarbonate end group was retained for both homopolymers (Figure 4.11).

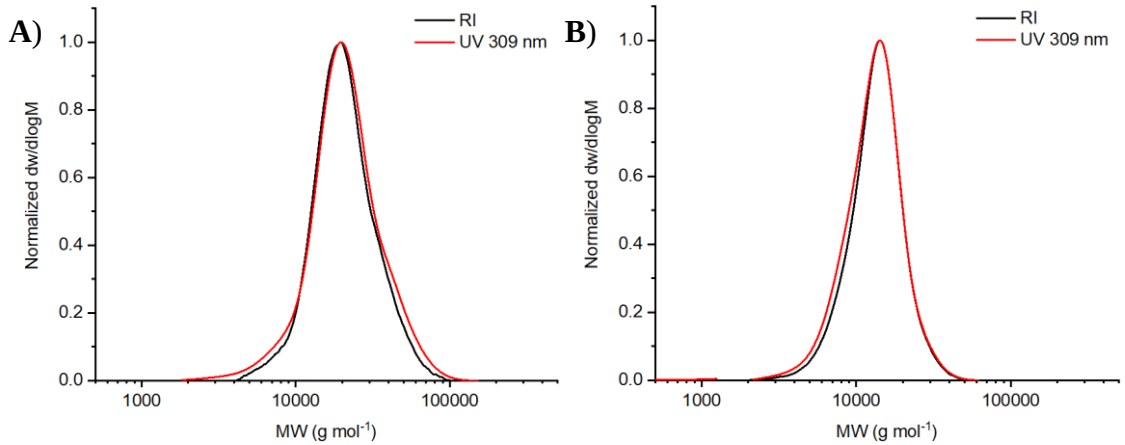

Figure 4.11: Molecular weight distributions determined by SEC ($CHCl_3$ as the eluent and calibrated against p(MMA) standards) using both an RI and UV (recorded at 309 nm) detector for the following thermoresponsive homopolymers: a) $p(OEGMA)_{64}$ (macroCTA **4v**); b) $p(DEGMA)_{67}$ (macroCTA **4vii**).

Next, $p(OEGMA)_{64}$ macroCTA **4v** and $p(DEGMA)_{67}$ macroCTA **4vii** were chain extended *via* RAFT copolymerization of *n*BA and DMAc at 70 °C in ethanol following the experimental conditions previously employed by O'Reilly and co-workers (Scheme 4.8).[14] Note, that the solvent for RAFT copolymerizations was switched from 1,4-dioxane to ethanol as the former resulted in the production of diblock copolymers that displayed bimodal RI traces upon SEC analysis as a result of inefficient chain extension of the thermoresponsive macroCTAs. Core-forming blocks of total DP = 40 were targeted and the initial monomer feed selected such that the percentage composition of hydrophobic *n*BA in the core-forming block was 50% to match the respective thermoresponsive diblock copolymer analogues **4iii** and **4iv** (Section 4.3.1, Table 4.1).

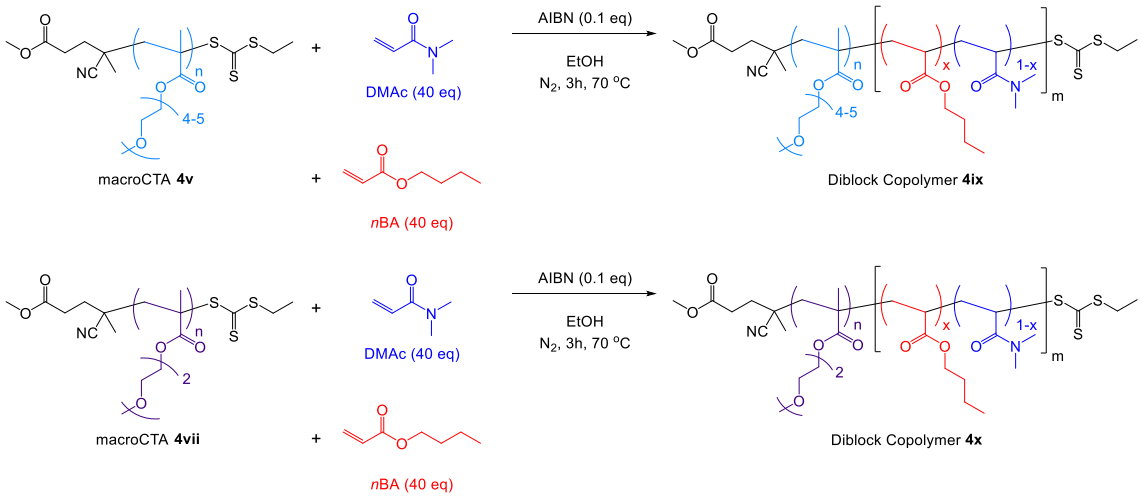

Scheme 4.8: Chain extension of p(OEGMA)$_n$ macroCTA **4v** and p(DEGMA)$_n$ macroCTA **4vii** *via* RAFT copolymerization of *n*BA and DMAc to produce amphiphilic thermoresponsive diblock copolymers p(OEGMA)$_n$-*b*-p(*n*BA$_x$-*co*-DMAc$_{1-x}$)$_m$ (**4ix**) and p(DEGMA)$_n$-*b*-p(*n*BA$_x$-*co*-DMAc$_{1-x}$)$_m$ (**4x**) respectively.

In this case, monomer conversion was monitored *via* ^{1}H NMR spectroscopy using an internal standard of trioxane with chain extensions quenched upon reaching the desired block length (DP = 40). Upon purification, two thermoresponsive diblock copolymers (**4ix-4x**) were isolated; characterization data for which is summarized in Table 4.4.

Diblock Copolymer	macroCTA	Corona	n^a	x^b	m^b	$M_{n,\,NMR}{}^b$ (kDa)	$M_{n,\,SEC}{}^c$ (kDa)	$Đ_M{}^c$
4ix	**4v**	p(OEGMA)	64	0.47	34	23.3	22.8	1.38
4x	**4vii**	p(DEGMA)	67	0.50	30	16.3	15.2	1.18

Table 4.4: Characterization data for the following amphiphilic thermoresponsive diblock copolymers: p(OEGMA)$_n$-*b*-p(*n*BA$_x$-*co*-DMAc$_{1-x}$)$_m$ (**4ix**) and p(DEGMA)$_n$-*b*-p(*n*BA$_x$-*co*-DMAc$_{1-x}$)$_m$ (**4x**). Key: [a] determined by end group analysis using ^{1}H NMR spectroscopy (300 MHz, $CDCl_3$); [b] monomer conversion was calculated by ^{1}H NMR spectroscopic analysis of the crude polymerization mixture using an internal standard (300 MHz, $CDCl_3$); [c] obtained by SEC analysis based on p(MMA) standards with $CHCl_3$ as the eluent.

Due to overlapping peak integrals corresponding to the polymer's side chain proton resonances and the trithiocarbonate end group C*H*$_2$S resonance, final diblock copolymer compositions were calculated from the conversion of DMAc and *n*BA *via* ^{1}H NMR spectroscopic analysis of the crude polymerization mixtures.

Thermoresponsive diblock copolymers **4ix** and **4x** displayed relatively symmetrical molecular weight distributions upon SEC analysis, with a distinct increase in number average molecular weight ($M_{n,\,SEC}$) relative to their respective macroCTAs, **4v** and **4vii** (Figure 4.12). The presence of a high molecular weight shoulder in the obtained RI trace for **4ix** could be attributed to a small amount of termination upon the chain extension of p(OEGMA)$_{64}$ macroCTA **4v** (Figure 4.12 a). Despite this, the product of such a recombination event would be a p(OEGMA)$_n$-*b*-p(*n*BA-*co*-DMAc)$_{2m}$-*b*-p(OEGMA)$_n$ triblock copolymer which would be expected to exhibit similar thermoresponsive and self-assembly behavior in aqueous solution with respect to the corresponding diblock copolymer analogue **4ix**. Good agreement between the molecular weight distributions obtained using an RI and UV detector (recorded at 309 nm) for both diblock copolymers (**4ix-4x**) indicated that chain extensions were relatively efficient, with a negligible population of initiator-derived copolymer chains and dead macroCTA chains present (Figure 4.12).

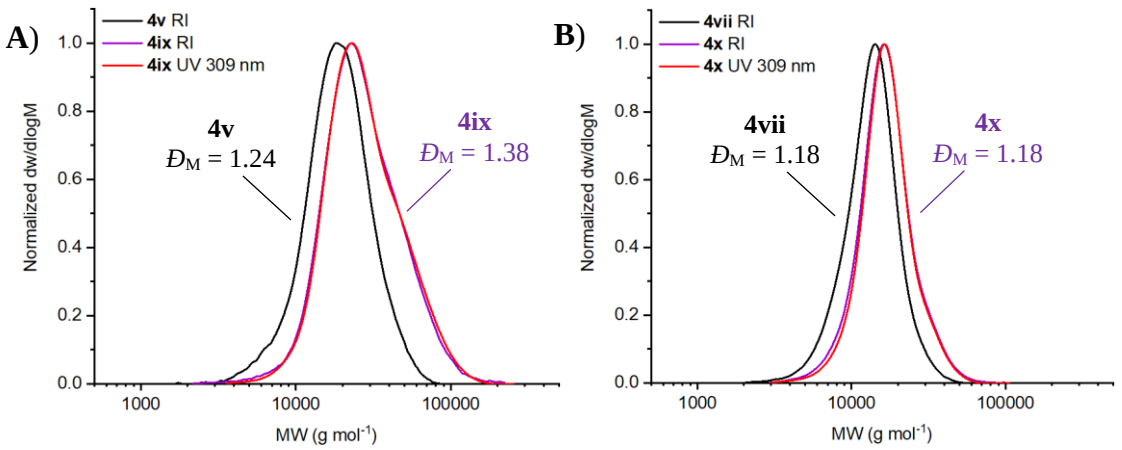

Figure 4.12: Molecular weight distributions determined by SEC ($CHCl_3$ as the eluent and calibrated against p(MMA) standards) using both an RI and UV (recorded at 309 nm) detector for the following thermoresponsive diblock copolymers: a) $p(OEGMA)_n$-*b*-$p(n BA_x$-*co*-$DMAc_{1-x})_m$ (**4ix**); b) $p(DEGMA)_n$-*b*-$p(n BA_x$-*co*-$DMAc_{1-x})_m$ (**4x**). Respective RI traces for $p(OEGMA)_{64}$ macroCTA **4v** and $p(DEGMA)_{67}$ macroCTA **4vii** are shown for comparison.

Significantly, thermoresponsive p(DEGMA)-*b*-p(*n*BA-*co*-DMAc) diblock copolymer **4x** possessed a lower dispersity ($Đ_M$ = 1.18) than the respective thermoresponsive diblock copolymer analogue **4iii** ($Đ_M$ = 1.41), thereby confirming that the change in RAFT agent from CPET to MCETP resulted in greater control over the RAFT polymerization of DEGMA. Critically, comparison of thermoresponsive diblock copolymers **4ix** and **4x** with their respective diblock copolymer analogues **4iv** and **4iii** revealed that diblock copolymer compositions were near identical as targeted (Table 4.4 and Table 4.5).

Diblock Copolymer	Corona	n^a	x^a	m^a	$M_{n,\,NMR}{}^a$ (kDa)	$M_{n,\,SEC}{}^b$ (kDa)	$Đ_M{}^b$
4iii	p(DEGMA)	66	0.46	35	16.4	15.8	1.41
4iv	p(OEGMA)	65	0.44	39	24.2	20.1	1.34

Table 4.5: Characterization data previously obtained by O'Reilly and co-workers for the following amphiphilic thermoresponsive diblock copolymers: p(DEGMA)$_n$-*b*-p(*n*BA$_x$-*co*-DMAc$_{1-x}$)$_m$ (**4iii**) and p(OEGMA)$_n$-*b*-p(*n*BA$_x$-*co*-DMAc$_{1-x}$)$_m$ (**4iv**).[14] Key: [a] determined by end group analysis using ^{1}H NMR spectroscopy; [b] determined by SEC analysis based on p(MMA) standards with DMF as the eluent.[14]

4.3.3. Blending thermoresponsive diblock copolymers with brush-like chain architectures

In Section 4.3.1, the successful formation of blended diblock copolymer micelles composed of a p(*n*BA-*co*-DMAc) core and a blend of brush-like p(DEGMA) and p(OEGMA) thermoresponsive corona-forming blocks was discovered, with comicellization resulting in cooperative behavior being observed for this system. In light of this, a similar investigation was conducted for thermoresponsive homopolymers **4v** and **4vii** to ascertain whether the introduction of statistical p(*n*BA-*co*-DMAc) core-forming blocks into the final diblock copolymer structures of **4iii** and **4iv** was required to enable the two thermoresponsive corona-forming blocks to interact in a cooperative manner.

To this end, a series of homopolymer mixtures (**UB-E-*n***) were prepared by blending brush-like thermoresponsive p(OEGMA) (**4v**) and p(DEGMA) (**4vii**) homopolymers together at various molar mixing ratios to target a range of intermediate cloud points (Scheme 4.9 and Table 4.6). Note, that a similar study has been previously conducted within the literature by Gibson and co-workers.[65]

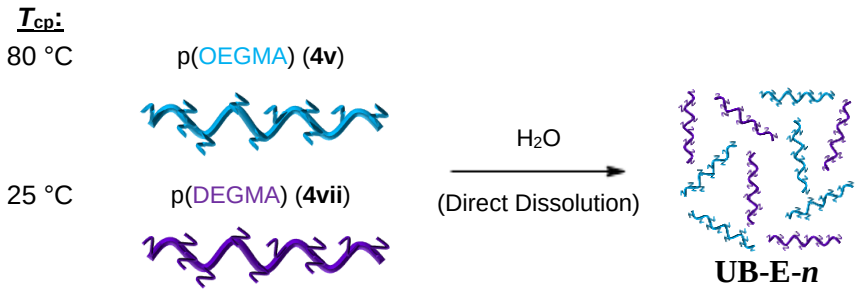

Scheme 4.9: Preparation of blended homopolymer solutions **UB-E-*n***: thermoresponsive homopolymers **4v** and **4vii** were first blended in the powder state to target the desired OEGMA *n* % and then directly dissolved in aqueous solution.

In a similar manner to blended diblock copolymer mixture **UB-D**, blended homopolymer solutions **UB-E-*n*** were formed *via* unimer blending which involved blending the constituent homopolymers **4v** and **4vii** together in dry powder form to target the desired *n* % OEGMA incorporation, followed by direct dissolution into water. Note, that a solvent switch from acetone was not required for the preparation of blended homopolymer solutions **UB-E-*n*** as the absence of an associative block in the thermoresponsive polymers ensured the production of free unimer chains in solution.

Blended Homopolymer Sample	Mole fraction 4v	Mole fraction 4vii	Theoretical % OEGMA	Target T_{cp} (°C)
UB-E-30	0.3	0.7	30	41.5
UB-E-50	0.5	0.5	50	52.5
UB-E-70	0.7	0.3	70	63.5

Table 4.6: Molar mixing ratios for a series of blended thermoresponsive homopolymer samples (**UB-E-*n***) prepared *via* unimer blending (UB) of **4v** and **4vii** with *n* % OEGMA incorporation in the unimer solution.

Blended homopolymer mixtures **UB-E-30**, **UB-E-50 and UB-E-70** were analyzed *via* variable temperature turbidimetry with their thermoresponsive behavior compared to pure homopolymer solutions of p(OEGMA) (**4v**) and p(DEGMA) (**4vii**) (Figure 4.13).

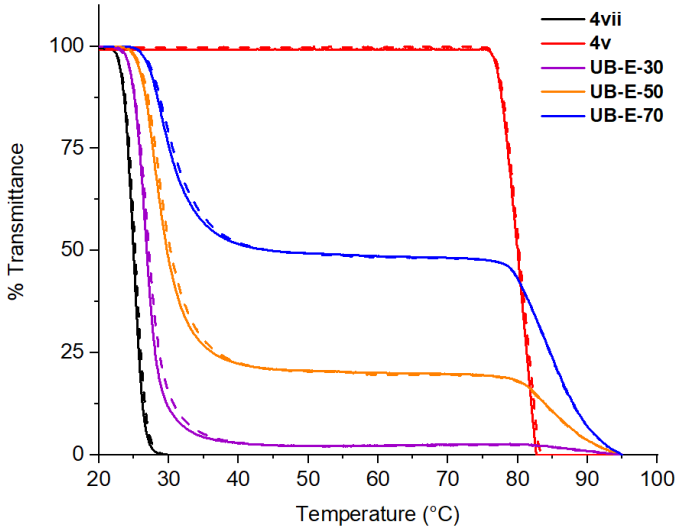

Figure 4.13: Variable temperature turbidimetry analysis of blended homopolymer solutions **UB-E-30** (purple), **UB-E-50** (orange), **UB-E-70** (blue), p(DEGMA) homopolymer solution **4vii** (black) and p(OEGMA) homopolymer solution **4v** (red) at 3 mg mL^{-1}. In each case, the solid trace represents the heating cycle and the dashed trace represents the cooling cycle. Heating and cooling rate = 1 °C min^{-1}.

For blended homopolymer solutions **UB-E-30**, **UB-E-50** and **UB-E-70**, two relatively broad cloud point transitions were observed in each case which corresponded to the macroscopic precipitation of p(DEGMA) chains (**4vii**) followed by p(OEGMA) chains (**4v**) in solution (Figure 4.13). Whilst a slight increase in the measured T_{cp} for **4vii** and **4v** with respect to increasing OEGMA percentage incorporation was discovered, no change in percentage transmittance was observed at the targeted temperatures of 41.5 °C, 52.5 °C and 63.5 °C for **UB-E-30**, **UB-E-50** and **UB-E-70** respectively. Therefore, the two thermoresponsive homopolymers **4v** and **4vii** exhibited non-cooperative behavior upon unimer blending, which matched the thermoresponsive behavior previously observed by Gibson and co-workers.[65] Overall, turbidimetry analysis of blended homopolymer

solutions **UB-E-*n*** indicated that the introduction of statistical p(*n*BA-*co*-DMAc) core-forming blocks into the final diblock copolymer structures of **4iii** and **4iv** played a key role in facilitating the cooperative behavior observed for **UB-D** (Section 4.3.1). Previously, turbidimetry analysis confirmed that comicellization was achieved for **UB-D** with the corresponding cloud point transition measured at an intermediate temperature with respect to the constituent pure diblock copolymer micelles (**4iii** and **4iv**). Furthermore, the measured T_{cp} for blended diblock copolymer micelles prepared in a 1:1 molar mixing ratio was in good agreement with the theoretical T_{cp}. Therefore, it was envisaged that the cloud point transition of blended diblock copolymer micelles could be modulated in a controlled manner over a wider temperature range *via* simple manipulation of the molar mixing ratio for **UB-D**. To this end, a series of diblock copolymer mixtures (**UB-F-*n***) were prepared by blending thermoresponsive diblock copolymers **4ix** and **4x** together at various molar mixing ratios to target a range of intermediate cloud points (Scheme 4.10 and Table 4.7).

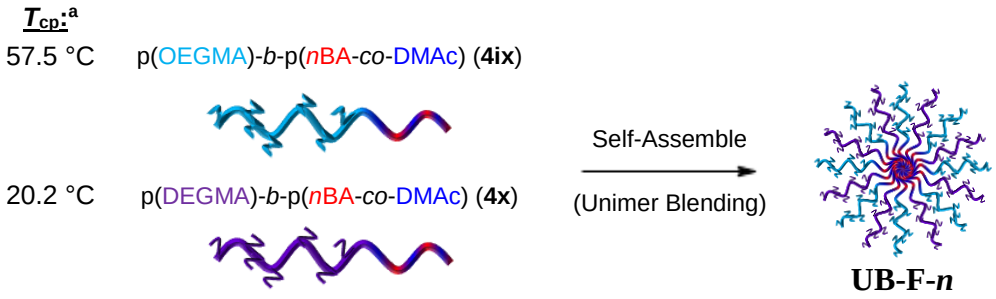

Scheme 4.10: Preparation of blended diblock copolymer solutions **UB-F-*n***: thermoresponsive diblock copolymers **4ix** and **4x** were first blended in the powder state to target the desired OEGMA *n* % in the micelle corona and then subsequently self-assembled *via* a solvent switch technique into aqueous solution. Key: [a] mean cloud point upon heating the micellar solutions determined using turbidimetry data from three heating runs.

Blended Diblock Copolymer Sample	Mole fraction 4ix	Mole fraction 4x	Theoretical % OEGMA in the micelle corona	Target T_{cp} (°C)
UB-F-10	0.1	0.9	10	23.9
UB-F-30	0.3	0.7	30	31.4
UB-F-50	0.5	0.5	50	38.9
UB-F-70	0.7	0.3	70	46.3
UB-F-90	0.9	0.1	90	53.8

Table 4.7: Molar mixing ratios for a series of blended thermoresponsive diblock copolymer samples (**UB-F-*n***) prepared *via* unimer blending (UB) of **4ix** and **4x** with *n* % OEGMA in the micelle corona.

In this case, blended diblock copolymer solutions **UB-F-*n*** were prepared in an identical manner to **UB-D**, where *n* refers to the desired OEGMA percentage incorporation in the blended diblock copolymer micelle corona. Moreover, blended diblock copolymer samples were prepared at 5 mg mL^{-1} to ascertain whether the broad nature of the cloud point transitions observed in Section 4.3.1 was due to inherent dispersity within the coronal compositions of blended diblock copolymer micelles or dependent upon the sample concentration.

Note, that variable temperature turbidimetry for the following blended diblock copolymer mixtures was conducted using an Evolution™ 350 UV-Vis spectrophotometer instead of a Perkin-Elmer Lambda 35 UV-Vis instrument which was used in the preceding experiments. Importantly, the latter instrument uses an internal reference cell of water that is subjected to identical measurement conditions as the sample. Therefore, a greater amount of control over the rate of heating and cooling is achieved as well as improved accuracy in measured sample transmittance values with respect to the recorded sample temperature. On the other hand, the former instrument uses the temperature of the heating block as the reference temperature. As such, cloud point values obtained upon heating are somewhat comparable with cloud point values determined using the latter instrument providing identical experimental parameters are used. However, upon cooling the former

instrument is considerably less accurate in measuring sample transmittance values with respect to the recorded sample temperature owing to errors in overestimating the cooling rate of the sample. Consequently, a significant degree of thermal hysteresis is often observed when using the former instrument, even for thermoresponsive samples that have previously displayed no thermal hysteresis. For example, the differences between the method by which the respective instrument measures the reference temperature was reflected in the turbidimetry data obtained for thermoresponsive diblock copolymers **4ix** and **4x** (Figure 4.14).

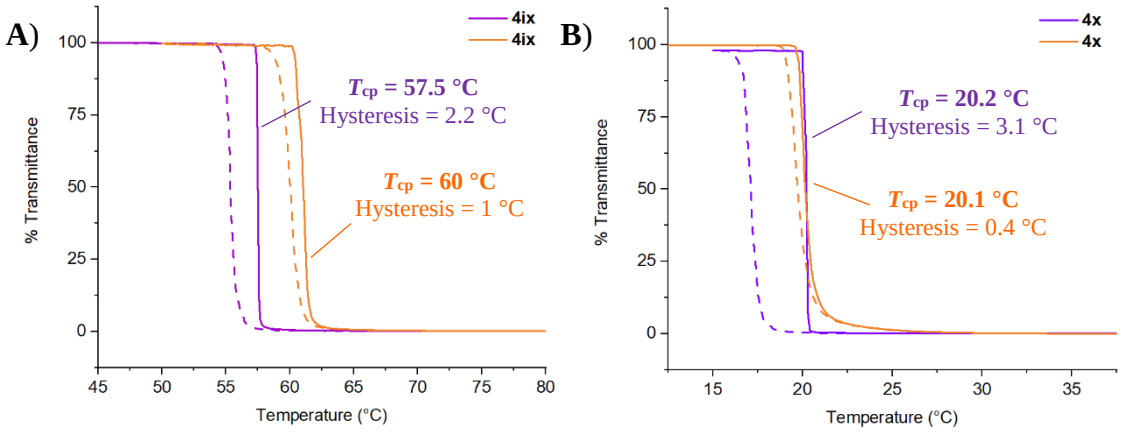

Figure 4.14: Variable temperature turbidimetry analysis conducted using either an Evolution™ 350 UV-Vis spectrophotometer (purple) or a Perkin-Elmer Lambda 35 UV-Vis instrument (orange) for micelles comprised of thermoresponsive diblock copolymers **4ix** (a) and **4x** (b) at 5 mg mL^{-1}. In each case, the solid trace represents the heating cycle and the dashed trace represents the cooling cycle. Heating and cooling rate = 1 °C min^{-1}.

In light of this, cloud point values for subsequent thermoresponsive polymer samples were solely determined using the turbidimetry curves obtained upon heating in order to minimize inconsistencies between different polymer samples.

Blended diblock copolymer mixtures **UB-F-*n*** were initially analyzed *via* variable temperature turbidimetry with their thermoresponsive behavior compared to their respective constituent pure diblock copolymer micelles **4ix** and **4x** (Figure 4.15).

Importantly, a single cloud point transition was measured for each blended diblock copolymer solution (**UB-F-*n***) which indicated the successful formation of blended diblock copolymer micelles as anticipated. Moreover, no change in percentage transmittance was detected for blended diblock copolymer solutions **UB-F-*n*** at 57.5 °C which would correspond to the macroscopic precipitation of pure p(OEGMA) diblock copolymer micelles **4ix**. However, cloud point transitions for each of the blended diblock copolymer solutions **UB-F-*n*** occurred at significantly lower temperatures than targeted (Figure 4.15 and Table 4.7). Furthermore, in comparison to the theoretical increase in T_{cp} of 29.9 °C, a relatively small increase of 10.7 °C in the measured T_{cp} for blended diblock copolymer solutions **UB-F-*n*** with respect to increasing OEGMA percentage incorporation was discovered. Ultimately, the cloud point transition for blended diblock copolymer micelles (**UB-F-*n***), composed of a p(*n*BA-*co*-DMAc) core and a blend of brush-like p(DEGMA) and p(OEGMA) thermoresponsive corona-forming blocks, could not be tuned in a controlled manner *via* simple manipulation of the molar mixing ratio.

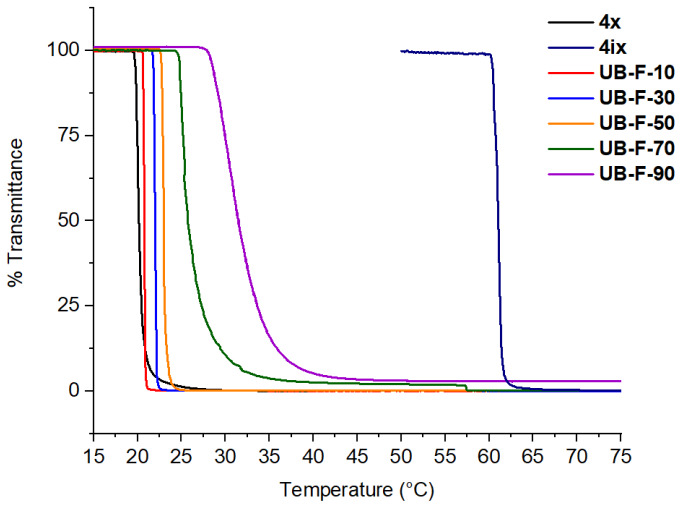

Figure 4.15: Variable temperature turbidimetry analysis of blended diblock copolymer solutions **UB-F-10** (red), **UB-F-30** (blue), **UB-F-50** (orange), **UB-F-70** (green), **UB-F-90** (purple), pure p(DEGMA) diblock copolymer micelles **4x** (black) and pure p(OEGMA) diblock copolymer micelles **4ix** (dark blue) at 5 mg mL^{-1}. Heating rate was 1 °C min^{-1}.

Following this study, thermoresponsive blended diblock copolymer solutions **UB-F-50** and **UB-F-90** were investigated further *via* microcalorimetry. Note, that the Nano DSC instrument used for microcalorimetry analysis directly uses the sample temperature as the reference and thus it was envisaged that the obtained microcalorimetry data would be much more accurate than the corresponding turbidimetry data for thermoresponsive diblock copolymer solutions. Typically, an endotherm is observed upon macroscopic precipitation due to an increase in the heat capacity of the polymer sample with the maximum of the peak defined herein as the transition temperature (T_p). Variable temperature turbidimetry and microcalorimetry data obtained for **4ix**, **4x** and blended diblock copolymer solutions **UB-F-*n*** is summarized in Table 4.8.

Diblock Copolymer Sample	**Coronal Composition**	**Target T_{cp} (°C)**	**T_{cp}[a] (°C)**	**T_{p1}[b] (°C)**	**T_{p2}[b] (°C)**
4ix	p(OEGMA)	-	57.5	59.2	-
4x	p(DEGMA)	-	20.2	21.1	28.6
UB-F-10	10% p(OEGMA)	23.9	20.8	-	-
UB-F-30	30% p(OEGMA)	31.4	22.0	-	-
UB-F-50	50% p(OEGMA)	38.9	23.0	24.1	59.2
UB-F-70	70% p(OEGMA)	46.3	25.7	-	-
UB-F-90	90% p(OEGMA)	53.8	31.5	28.7	59.2

Table 4.8: Thermal analysis data obtained for pure diblock copolymer micelles **4ix**, **4x** and blended diblock copolymer solutions **UB-F-*n***. Key: a) mean cloud point upon heating the micellar solutions determined using turbidimetry data from three heating runs; b) thermal transition temperatures determined *via* microcalorimetry upon heating the micellar solutions. Both variable temperature techniques were performed at 5 mg mL^{-1} with a temperature ramping rate of 1 °C min^{-1}.

Interestingly, microcalorimetry analysis of blended diblock copolymer mixtures **UB-F-50** and **UB-F-90** revealed the presence of two thermal transitions (T_{p1} and T_{p2}) in solution

upon heating, as shown in Figure 4.16 c and d respectively. In this case, the first thermal transition (T_{p1}) corresponded to the macroscopic precipitation of blended diblock copolymer micelles in solution. Significantly, an increase in the transition temperature from 24.1 °C to 28.7 °C was measured upon increasing OEGMA percentage incorporation in the micelle corona from 50% to 90%. For both blended diblock copolymer samples, the second thermal transition (T_{p2}) occurred at 59.2 °C which directly matched the transition temperature and thermal profile obtained for pure p(OEGMA) diblock copolymer micelles **4ix** (Figure 4.16 b).

However, two broad endotherms were dectected upon microcalorimetry analysis of pure p(DEGMA) diblock copolymer micelles **4x**, with transition temperatures of approximately 21.1 °C and 28.6 °C (Figure 4.16 a). Following this, a pure homopolymer solution of p(DEGMA) (**4vii**) was measured to determine whether the second thermal transition for **4x** corresponded to the presence of non-chain extended p(DEGMA) homopolymeric chains in solution (Figure 4.16 e). Critically, a single thermal transition with T_p = 25.4 °C was detected for **4vii** which suggested that thermoresponsive diblock copolymer **4x** consisted of p(DEGMA) homopolymer impurities upon chain extension which was not observed *via* SEC or ^{1}H NMR spectroscopic analysis. Consequently, self-assembly of thermoresponsive diblock copolymers **4ix** and **4x** *via* unimer blending would lead to the formation of blended diblock copolymer micelles coupled with a population of free p(DEGMA) homopolymer chains in solution. Upon heating the resultant solution, the collapse of free p(DEGMA) homopolymer chains in solution around 25.4 °C would likely lower the transition temperature at which the macroscopic precipitation of blended diblock copolymer micelles (**UB-F-*n***) occurred at.

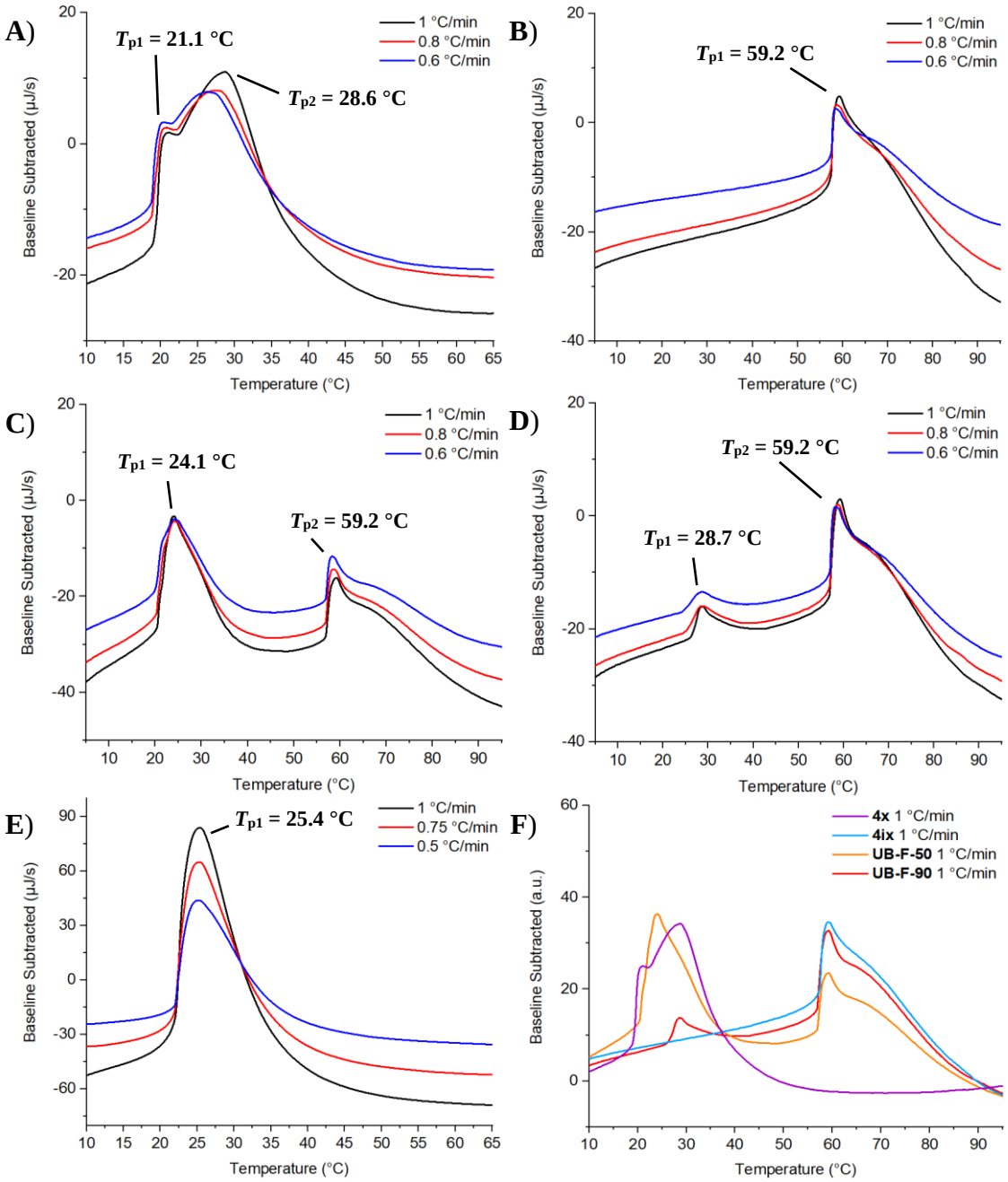

Figure 4.16: Microcalorimetry analysis of: a) pure p(DEGMA) diblock copolymer micelles **4x**; b) pure p(OEGMA) diblock copolymer micelles **4ix**; c) blended diblock copolymer solution **UB-F-50**; d) blended diblock copolymer solution **UB-F-90**; e) p(DEGMA) homopolymer solution **4vii**. In each case, polymer solutions were prepared at 5 mg mL^{-1} and heated at three different ramping rates. For comparison purposes, overlaid heating traces (f) obtained *via* microcalorimetry are shown for **4x** (purple), **4ix** (light blue), **UB-F-50** (orange) and **UB-F-90** (red) at 5 mg mL^{-1}.

In fact, the sharp cloud point transitions observed for **UB-F-10**, **UB-F-30** and **UB-F-50** (Figure 4.15) in comparison to the broad cloud point transition obtained for **UB-D** (Figure

4.10) further supported the former rationalization. Moreover, the presence of p(DEGMA) homopolymer impurities would also result in the OEGMA percentage incorporation for blended diblock copolymer solutions **UB-F-*n*** to be significantly lower than targeted owing to errors in calculating the molarity of **4x** in each solution. Therefore, the removal of p(DEGMA) homopolymer impurities from **4x** should enable the cloud point transition for blended diblock copolymer micelles (**UB-F-*n***) to be tuned in a controlled manner *via* simple manipulation of the molar mixing ratio.

4.4. Conclusions

In conclusion, this study revealed that the formation of blended diblock copolymer micelles was often favored upon copolymer blending providing that the chosen amphiphilic diblock copolymers were composed of short core-forming blocks, were relatively low in hydrophobic character and possessed a low core T_g. For blended diblock copolymer micelles with a coronal composition of brush-like p(DEGMA) with linear p(DEAm) or p(NIPAM), copolymer blending resulted in non-cooperative behavior with a broadening of the thermal transition at a T_{cp} corresponding to the chain collapse of the higher thermoresponsive corona-forming block. In contrast, blended diblock copolymer micelles composed of a p(*n*BA-*co*-DMAc) core and a blend of brush-like p(DEGMA) and p(OEGMA) thermoresponsive corona-forming blocks displayed cooperative behavior with a single thermal transition at an intermediate T_{cp} with respect to the constituent pure diblock copolymer micelles. Further investigation into the former diblock copolymer system revealed that incorporation of a statistical p(*n*BA-*co*-DMAc) core-forming block into the chemical structure of the constituent diblock copolymers was critical in facilitating this cooperativity. Significantly, the T_{cp} for brush-like blended diblock copolymer micelles could be systematically increased over a temperature range of 11 °C *via* simple manipulation of the molar mixing ratio. Overall, these findings highlight that the cloud point of a micellar solution can be modulated simply by blending two thermoresponsive amphiphilic diblock copolymers with similar coronal chemistry together.

4.5. Experimental Section

4.5.1. Methods and materials

Materials. The following reagents were used as received: 1-(3-dimethylaminopropyl)-3-ethylcarbodiimide hydrochloride (EDC·HCl, Carbosynth, 98%); 2,6-diaminopyridine (Sigma-Aldrich, 98%); *N*,*N*-dimethylacrylamide (DMAc, Sigma-Aldrich, 99%); *n*-butyl acrylate (*n*BA, Sigma-Aldrich, 99%); di(ethylene glycol) monomethyl ether methacrylate (DEGMA, Sigma-Aldrich, 95%); poly(ethylene glycol) monomethyl ether methacrylate (OEGMA, M_n = 300 g mol^{-1}, Sigma-Aldrich); 1,3,5-trioxane (Sigma-Aldrich, 99%). 2,2'-azobisisobutyronitrile (AIBN) was received from Sigma-Aldrich (98%), recrystallized from methanol and stored in the dark at 4 °C. Solvents, including high-performance liquid chromatography (HPLC) grade solvents, were purchased from Fisher Scientific and used as received. Monomers and 1,4-dioxane were filtered through a plug of basic alumina prior to use and stored at 4 °C. Deuterated solvents and silica gel (40-63 μm) were used as received from Apollo Scientific.

^{1}H and ^{13}C NMR spectroscopy. ^{1}H NMR spectroscopy was performed at 300 MHz on a Bruker Avance AV-300 spectrometer or a Bruker Avance III HD-300 spectrometer, or at 400 MHz on a Bruker Avance III HD-400 spectrometer. ^{13}C NMR spectroscopy was performed at 100 MHz on a Bruker Avance III HD-400 spectrometer. ^{1}H and ^{13}C NMR spectra were measured in deuterated chloroform. Chemical shifts are reported as δ in parts per million (ppm) and are stated relative to the residual solvent peaks at 7.26 ppm or 77.0 ppm for chloroform. Coupling constants (J) correspond to $^{3}J_{H\text{-}H}$ unless otherwise stated. All spectra were obtained at 25 °C.

Size Exclusion Chromatography. SEC analysis was performed on a Varian PL-GPC 50 system with a set of two PLgel Mixed-C columns plus one guard column and fitted with

an RI and UV detector measuring at 309 nm. SEC measurements were performed with HPLC-grade chloroform with 0.5% triethylamine at 40 °C at a flow rate of 1 mL min^{-1}. The molecular weights of the synthesized polymers were calculated relative to poly(methyl methacrylate) (p(MMA)) standards and analyzed using Cirrus v3.3 software.

Mass Spectrometry. High resolution electrospray ionization time of flight mass spectrometry (HRMS (ESI-ToF)) was performed on a Bruker UHR-Q-TOF MaXis spectrometer by Dr. Lijang Song, University of Warwick.

Turbidimetry. Turbidimetry analysis was performed on either a Perkin-Elmer Lambda 35 UV-Vis instrument or an Evolution™ 350 UV-Vis Spectrophotometer, both fitted with a Peltier heating and cooling system. Polymer samples were prepared at a suitable concentration with the transmittance of the sample measured at a wavelength of 500 nm over three heating and cooling cycles at a heating and cooling rate of 1 °C min^{-1}.

Microcalorimetry. Microcalorimetry analysis was performed at 5 mg mL^{-1} on a TA instruments Nano DSC with samples degassed for 15 minutes prior to measurement and an injection volume of 600 µL used. After 10 minutes of equilibration at the initial temperature, diblock copolymer solutions were measured at multiple heating rates (0.4 °C/min – 1.5 °C/min) and over a wide range of temperatures (0–100 °C) with alternating heating and cooling cycles. Data was baseline subtracted to remove any thermal contributions from the solvent, in this case water.

4.5.2. Synthetic protocols

Synthesis of methyl 4-cyano-4-(((ethylthio)carbonothioyl)thio)pentanoate (MCETP).

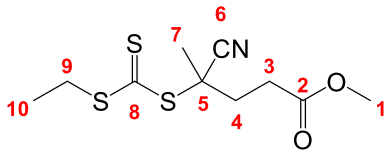

Methyl 4-cyano-4-(((ethylthio)carbonothioyl)thio)pentanoate was prepared according to a modified literature procedure.[14] To a solution of 4-cyano-4-(((ethylthio)carbonothioyl) thio)pentanoic acid (CETPA) (1.52 g, 5.76 mmol) and 2,6-diaminopyridine (352 mg, 2.88 mmol) in methanol (50 mL), EDC·HCl (2.21 g, 11.5 mmol) was added and the reaction mixture was left to stir at ambient temperature. After 16 h, methanol was removed *in vacuo* and purification was carried out using column chromatography (silica gel, 2:1 CH_2Cl_2/pet. ether) to yield methyl 4-cyano-4-(((ethylthio)carbonothioyl)thio) pentanoate (MCETP) as an orange red oil (1.28 g, 4.61 mmol, 80%). ^{1}H NMR (300 MHz, $CDCl_3$) δ_H/ppm: 3.70 (3H, s, H1), 3.34 (2H, q, J = 7.5 Hz, H9), 2.56-2.67 (2H, m, H3), 2.30-2.55 (2H, m, H4), 1.87 (3H, s, H7), 1.35 (3H, t, J = 7.5 Hz, H10); ^{13}C NMR (100 MHz, $CDCl_3$) δ_C/ppm: 216.7 (C8), 171.8 (C2), 118.9 (C6), 52.0 (C1), 46.3 (C5), 33.8 (C4), 31.3 (C9), 29.5 (C3), 24.8 (C7) 12.7 (C10); HRMS (ESI-TOF) m/z: $[M + H]^+$ calculated for $C_{10}H_{16}NO_2S_3$: 278.0343; found: 278.0342.

General procedure for the RAFT homopolymerization of DEGMA to produce macroCTA ***4vii***

For a total target DP_{DEGMA} = 65 at 72% conversion, an example synthesis is as follows: MCETP (52.0 mg, 1 eq), AIBN (3.00 mg, 0.1 eq) and DEGMA (3.17 mL, 90 eq) were dissolved in 1,4-dioxane (1:1 monomer volume/1,4-dioxane volume) and added to a dry ampoule containing a stirrer bar. The resulting solution was degassed using at least three freeze-pump-thaw cycles, back-filled with nitrogen, sealed and placed in a pre-heated oil bath at 70 °C. After 6 h, the polymerization was quenched by opening the reaction mixture to air and submerging the ampoule in liquid nitrogen. Purification was achieved *via* precipitation into a 1:9 diethyl ether/pet. ether solution three times before being re-dissolved in the minimum amount of 18.2 MΩ cm water. Subsequent lyophilization resulted in a yellow, viscous oil. ^{1}H NMR (400 MHz, $CDCl_3$) δ_H/ppm: 4.09 (br s, 2H, COOCH_2CH$_2$), 3.50-3.77 (m, 6H, OCH$_2$CH_2OCH_2CH_2), 3.38 (br s, 3H, OCH_3), 2.30-2.67 (m, 4H, CH_2CH_2COOMe of end group), 0.72-2.11 (m, backbone and end group).

General procedure for the RAFT homopolymerization of OEGMA to produce macroCTA ***4v***

For a total target DP_{OEGMA} = 65 at 72% conversion, an example synthesis is as follows: MCETP (34 mg, 1 eq), AIBN (2 mg, 0.1 eq) and DEGMA (3.34 mL, 90 eq) were dissolved in 1,4-dioxane (2:3 monomer volume/1,4-dioxane volume) and added to a dry ampoule containing a stirrer bar. The resulting solution was degassed using at least three freeze-pump-thaw cycles, back-filled with nitrogen, sealed and placed in a pre-heated oil bath at 70 °C. After 8 h, the polymerization was quenched by opening the reaction mixture

to air and submerging the ampoule in liquid nitrogen. Purification was achieved *via* precipitation into a 1:9 diethyl ether/pet. ether solution three times before being re-dissolved in the minimum amount of 18.2 MΩ•cm water. Subsequent lyophilization resulted in a yellow, viscous oil. ^{1}H NMR (400 MHz, $CDCl_3$) δ_H/ppm: 4.07 (br s, 2H, COOCH_2CH$_2$), 3.45-3.81 (m, (OCH_2CH_2)$_{4-5}$ of side chain), 3.36 (br s, 3H, OCH_3), 2.30-2.67 (m, 4H, CH_2CH_2COOMe of end group), 0.63-2.13 (m, backbone and end group).

*General procedure for the preparation of diblock copolymers **4ix** and **4x** via RAFT copolymerization of DMAc and nBA*

For a target DP_{core} = 40 at 50% conversion, an example synthesis is as follows: A solution of 80 equivalents of a combination of the two monomers (*n*BA = *x*, DMAc = 80-*x*), 0.1 equivalents of AIBN and 1 equivalent of macroCTA **4v** or **4vii** in ethanol (2:5 (monomer volume and macroCTA weight)/ethanol volume) was added to a dry ampoule containing a stirrer bar. 20 equivalents of trioxane was added to the polymerization mixture and used as an internal standard. The resulting solution was degassed using at least three freeze-pump-thaw cycles, back-filled with nitrogen, sealed and placed in a pre-heated oil bath at 70 °C. After 3 h, the polymerization was quenched by opening the reaction mixture to air and submerging the ampoule in liquid nitrogen. Purification was achieved *via* precipitation into a 1:9 diethyl ether/pet. ether solution three times before being re-dissolved in the minimum amount of HPLC grade tetrahydrofuran and dried under vacuum to yield a yellow, viscous oil. ^{1}H NMR (400 MHz, $CDCl_3$) δ_H/ppm: 3.90-4.24 (m, 4H, COOCH_2CH$_2$ and CH_2CH$_2$CH$_2$CH$_3$), 3.45-3.81 (m, (OCH_2CH_2)$_{2-5}$ of side chain), 3.40 (br s, 3H, OCH_3), 2.78-3.22 (m, 6H, CON(CH_3)$_2$), 2.30-2.77 (m, 4H, CH_2CH_2COOMe of end group), 0.75-2.06 (m, backbone and end group).

4.6. References

1 E. G. Kelley, J. N. L. Albert, M. O. Sullivan and T. H. Epps III, *Chem. Soc. Rev.*, 2013, **42**, 7057–7071.
2 F. D. Jochum and P. Theato, *Chem. Soc. Rev.*, 2013, **42**, 7468–7483.
3 D. Schmaljohann, *Adv. Drug Deliv. Rev.*, 2006, **58**, 1655–1670.
4 E. Cabane, X. Zhang, K. Langowska, C. G. Palivan and W. Meier, *Biointerphases*, 2012, **7**, 9.
5 M. A. C. Stuart, W. T. S. Huck, J. Genzer, M. Müller, C. Ober, M. Stamm, G. B. Sukhorukov, I. Szleifer, V. V Tsukruk, M. Urban, F. Winnik, S. Zauscher, I. Luzinov and S. Minko, *Nat. Mater.*, 2010, **9**, 101.
6 E. S. Gil and S. M. Hudson, *Prog. Polym. Sci.*, 2004, **29**, 1173–1222.
7 P. Theato, B. S. Sumerlin, R. K. O'Reilly and T. H. Epps III, *Chem. Soc. Rev.*, 2013, **42**, 7055–7056.
8 M. A. Ward and T. K. Georgiou, *Polymers*, 2011, **3**, 1215–1242.
9 J. Du and R. K. O'Reilly, *Soft Matter*, 2009, **5**, 3544–3561.
10 S. Dai, P. Ravi and K. C. Tam, *Soft Matter*, 2008, **4**, 435–449.
11 M. I. Gibson and R. K. O'Reilly, *Chem. Soc. Rev.*, 2013, **42**, 7204–7213.
12 D. Roy, W. L. A. Brooks and B. S. Sumerlin, *Chem. Soc. Rev.*, 2013, **42**, 7214–7243.
13 J. Seuring and S. Agarwal, *Macromol. Rapid Commun.*, 2012, **33**, 1898–1920.
14 L. D. Blackman, M. I. Gibson and R. K. O'Reilly, *Polym. Chem.*, 2017, **8**, 233–244.
15 Y. Liu, L. Meng, X. Lu, L. Zhang and Y. He, *Polym. Adv. Technol.*, 2008, **19**, 137–143.
16 S. Ohya, H. Sonoda, Y. Nakayama and T. Matsuda, *Biomaterials*, 2005, **26**, 655—659.
17 H. G. Schild, *Prog. Polym. Sci.*, 1992, **17**, 163–249.
18 Y. Zhang, J. Cai, C. Li, J. Wei, Z. Liu and W. Xue, *J. Mater. Chem. B*, 2016, **4**, 3733–3749.
19 J. S. Scarpa, D. D. Mueller and I. M. Klotz, *J. Am. Chem. Soc.*, 1967, **89**, 6024–6030.
20 Y. Lu, K. Zhou, Y. Ding, G. Zhang and C. Wu, *Phys. Chem. Chem. Phys.*, 2010, **12**, 3188–3194.
21 K. Suwa, K. Morishita, A. Kishida and M. Akashi, *J. Polym. Sci. Part A Polym. Chem.*, 1997, **35**, 3087–3094.
22 H. Vihola, A. Laukkanen, H. Tenhu and J. Hirvonen, *J. Pharm. Sci.*, 2008, **97**, 4783–4793.
23 H. Vihola, A.-K. Marttila, J. S. Pakkanen, M. Andersson, A. Laukkanen, A. M. Kaukonen, H. Tenhu and J. Hirvonen, *Int. J. Pharm.*, 2007, **343**, 238–246.
24 H. Vihola, A. Laukkanen, L. Valtola, H. Tenhu and J. Hirvonen, *Biomaterials*, 2005, **26**, 3055–3064.
25 A. C. W. Lau and C. Wu, *Macromolecules*, 1999, **32**, 581–584.
26 A. A. Tager, A. P. Safronov, E. A. Berezyuk and I. Y. Galaev, *Colloid Polym. Sci.*, 1994, **272**, 1234–1239.
27 V. San Miguel, A. J. Limer, D. M. Haddleton, F. Catalina and C. Peinado, *Eur. Polym. J.*, 2008, **44**, 3853–3863.
28 N. Takeda, E. Nakamura, M. Yokoyama and T. Okano, *J. Control. Release*, 2004, **95**, 343—355.
29 J. Moselhy, T. Vira, F.-F. Liu and X. Y. Wu, *Int. J. Nanomedicine*, 2009, **4**, 153–164.
30 M. A. Ward and T. K. Georgiou, *Soft Matter*, 2012, **8**, 2737–2745.

31 M. R. Fraylich, R. Liu, S. M. Richardson, P. Baird, J. Hoyland, A. J. Freemont, C. Alexander, K. Shakesheff, F. Cellesi and B. R. Saunders, *J. Colloid Interface Sci.*, 2010, **344**, 61–69.

32 V. Bütün, S. P. Armes and N. C. Billingham, *Polymer*, 2001, **42**, 5993–6008.

33 M. Okubo, H. Ahmad and T. Suzuki, *Colloid Polym. Sci.*, 1998, **276**, 470–475.

34 F. A. Plamper, M. Ruppel, A. Schmalz, O. Borisov, M. Ballauff and A. H. E. Müller, *Macromolecules*, 2007, **40**, 8361–8366.

35 N. H. Raduan, T. S. Horozov and T. K. Georgiou, *Soft Matter*, 2010, **6**, 2321–2329.

36 Z. Hu, T. Cai and C. Chi, *Soft Matter*, 2010, **6**, 2115–2123.

37 J.-F. Lutz, Ö. Akdemir and A. Hoth, *J. Am. Chem. Soc.*, 2006, **128**, 13046–13047.

38 S. Han, M. Hagiwara and T. Ishizone, *Macromolecules*, 2003, **36**, 8312–8319.

39 J.-F. Lutz and A. Hoth, *Macromolecules*, 2006, **39**, 893–896.

40 J.-F. Lutz, *J. Polym. Sci. Part A: Polym. Chem.*, 2008, **46**, 3459–3470.

41 S. Sun and P. Wu, *Macromolecules*, 2013, **46**, 236–246.

42 S. Glatzel, N. Badi, M. Päch, A. Laschewsky and J.-F. Lutz, *Chem. Commun.*, 2010, **46**, 4517–4519.

43 J. Seuring and S. Agarwal, *Macromolecules*, 2012, **45**, 3910–3918.

44 F. Liu, J. Seuring and S. Agarwal, *J. Polym. Sci. Part A: Polym. Chem.*, 2012, **50**, 4920–4928.

45 J. Seuring and S. Agarwal, *Macromol. Chem. Phys.*, 2010, **211**, 2109–2117.

46 K. E. B. Doncom, H. Willcock and R. K. O'Reilly, *Eur. Polym. J.*, 2017, **87**, 497–507.

47 H. Willcock, A. Lu, C. F. Hansell, E. Chapman, I. R. Collins and R. K. O'Reilly, *Polym. Chem.*, 2014, **5**, 1023–1030.

48 D. N. Schulz, D. G. Peiffer, P. K. Agarwal, J. Larabee, J. J. Kaladas, L. Soni, B. Handwerker and R. T. Garner, *Polymer*, 1986, **27**, 1734–1742.

49 N. Lucht, S. Eggers and V. Abetz, *Polym. Chem.*, 2017, **8**, 1196–1205.

50 Y. Su, M. Dan, X. Xiao, X. Wang and W. Zhang, *J. Polym. Sci. Part A: Polym. Chem.*, 2013, **51**, 4399–4412.

51 R. Hoogenboom and H. Schlaad, *Polym. Chem.*, 2017, **8**, 24–40.

52 W. Li, D. Wu, A. D. Schlüter and A. Zhang, *J. Polym. Sci. Part A: Polym. Chem.*, 2009, **47**, 6630–6640.

53 C. Kojima, K. Yoshimura, A. Harada, Y. Sakanishi and K. Kono, *J. Polym. Sci. Part A: Polym. Chem.*, 2010, **48**, 4047–4054.

54 W. Li, A. Zhang and A. D. Schlüter, *Chem. Commun.*, 2008, 5523–5525.

55 W. Li, A. Zhang, K. Feldman, P. Walde and A. D. Schlüter, *Macromolecules*, 2008, **41**, 3659–3667.

56 Z. Osváth and B. Iván, *Macromol. Chem. Phys.*, 2017, **218**, 1600470.

57 G. Chen and A. S. Hoffman, *Nature*, 1995, **373**, 49.

58 M. Shibayama and T. Tanaka, *Adv. Polym. Sci.*, 1993, **109**, 1–62.

59 X. Yin, A. S. Hoffman and P. S. Stayton, *Biomacromolecules*, 2006, **7**, 1381–1385.

60 C. R. Becer, S. Hahn, M. W. M. Fijten, H. M. L. Thijs, R. Hoogenboom and U. S. Schubert, *J. Polym. Sci. Part A Polym. Chem.*, 2008, **46**, 7138–7147.

61 K. B. Doorty, T. A. Golubeva, A. V Gorelov, Y. A. Rochev, L. T. Allen, K. A. Dawson, W. M. Gallagher and A. K. Keenan, *Cardiovasc. Pathol.*, 2003, **12**, 105–110.

62 M. C. Hacker, L. Klouda, B. B. Ma, J. D. Kretlow and A. G. Mikos, *Biomacromolecules*, 2008, **9**, 1558–1570.

63 L. Liu, C. Wu, J. Zhang, M. Zhang, Y. Liu, X. Wang and G. Fu, *J. Polym. Sci. Part A: Polym. Chem.*, 2008, **46**, 3294–3305.

64 L. D. Blackman, D. B. Wright, M. P. Robin, M. I. Gibson and R. K. O'Reilly, *ACS Macro Lett.*, 2015, **4**, 1210–1214.

65 N. S. Ieong, M. Hasan, D. J. Phillips, Y. Saaka, R. K. O'Reilly and M. I. Gibson, *Polym. Chem.*, 2012, **3**, 794–799.
66 S. Won, D. J. Phillips, M. Walker and M. I. Gibson, *J. Mater. Chem. B*, 2016, **4**, 5673–5682.
67 A. El Asmar, O. Gimello, G. Morandi, D. Le Cerf, V. Lapinte and F. Burel, *Macromolecules*, 2016, **49**, 4307–4315.
68 Q. Li, X. He, Y. Cui, P. Shi, S. Li and W. Zhang, *Polym. Chem.*, 2015, **6**, 70–78.
69 D. B. Wright, J. P. Patterson, N. C. Gianneschi, C. Chassenieux, O. Colombani and R. K. O'Reilly, *Polym. Chem.*, 2016, **7**, 1577–1583.
70 D. B. Wright, J. P. Patterson, A. Pitto-Barry, A. Lu, N. Kirby, N. C. Gianneschi, C. Chassenieux, O. Colombani and R. K. O'Reilly, *Macromolecules*, 2015, **48**, 6516–6522.

5. Fluorescent polymer nanostructures *via* polymerization-induced self-assembly using an ABM-functionalized RAFT agent

5.1. Abstract

Polymerization-induced self-assembly (PISA) is a rapidly growing and industrially relevant technology, which allows the preparation of well-defined and predictable polymer nanostructures with a diverse range of morphologies at relatively high concentrations. Moreover, there is a limited number of reports for the synthesis of fluorescently-labelled polymer nanostructures *via* a PISA approach, especially for methodologies in which no post-polymerization modification steps are required. Herein, the use of a Z-group ABM-functionalized RAFT agent to synthesize a range of fluorescent diblock copolymer nano-objects *via* RAFT-mediated PISA in aqueous milieu will be investigated. The impact that the introduction of an ABM fluorophore has upon the PISA methodology will be explored by comparing fluorescent polymer nanostructures to literature predictions using a combination of TEM imaging and DLS measurements. Finally, pure phases of three block copolymer morphologies – spherical micelles, worm-like micelles and vesicles – will be targeted with the resultant fluorescence emissive behavior measured *via* both steady-state and time-resolved fluorescence spectroscopy.

5.2. Introduction

5.2.1. Polymerization-Induced Self-Assembly (PISA)

Conventional self-assembly methodologies such as solvent switch, thin-film rehydration and direct dissolution involve the introduction of a pre-synthesized amphiphilic block copolymer to a selective solvent in a post-polymerization process. An alternative and rapidly growing field for nanoparticle fabrication is polymerization-induced self-assembly (PISA). PISA involves the chain extension of a solvophilic block, often termed the stabilizer block, with a partially or fully miscible core-forming monomer in a selective solvent (Figure 5.1).[1–3] Upon polymerization, the core-forming monomer becomes insoluble and at a critical degree of polymerization induces the self-assembly of the growing amphiphilic block copolymer chains *in situ*, which in turn continue to propagate. Moreover, the onset of micellization triggers a marked increase in polymerization kinetics due to a high localized concentration of monomer within the hydrophobic domain of the self-assembled polymer nanostructures, driving the polymerization to completion.[4]

A plethora of different morphologies are accessible *via* this technique (Figure 5.2) and as with conventional amphiphilic block copolymer self-assembly, final morphologies obtained post-PISA are primarily dictated by the packing parameter i.e. the relative volume fraction of solvophilic and solvophobic blocks.[5] A critical advantage of employing PISA to synthesize polymeric nanostructures is that it can be performed at much higher concentrations (10-50 weight percentage (wt%) of solids) in comparison to conventional block copolymer self-assembly (<1% concentration), thereby making it an economically viable and industrially relevant process.

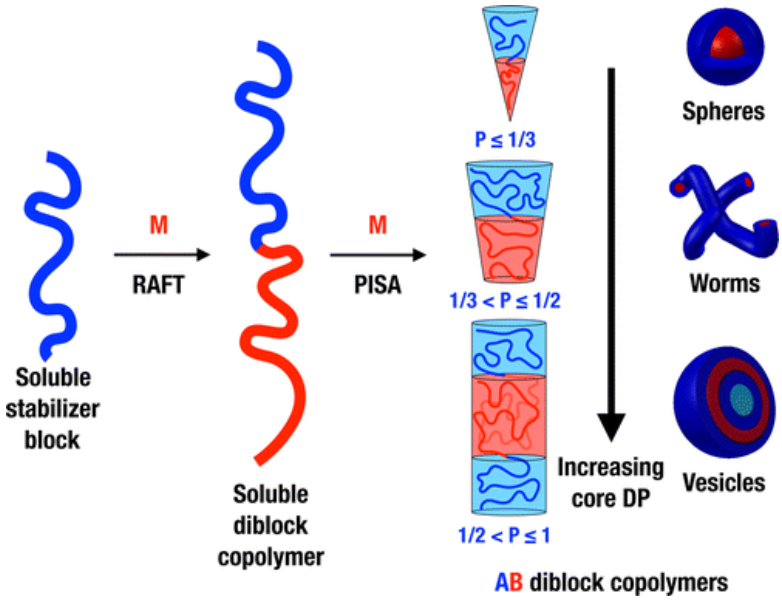

Figure 5.1: Schematic representation for the synthesis of diblock copolymer nano-objects *via* polymerization-induced self-assembly (PISA). Figure and caption adapted from ref 6.

Furthermore, the number of synthetic and purification steps required is significantly reduced due to combining both block copolymer synthesis and self-assembly together *via* a one-pot process with quantitative monomer conversions (>99%) often achieved. Overall, PISA offers an attractive route for the facile preparation of polymer nanostructure libraries with various functionalities and morphologies. Ultimately, PISA has revolutionized the field of block copolymer self-assembly with an aim towards fulfilling a wide range of applications, including nanomedicine and drug delivery.[7–10]

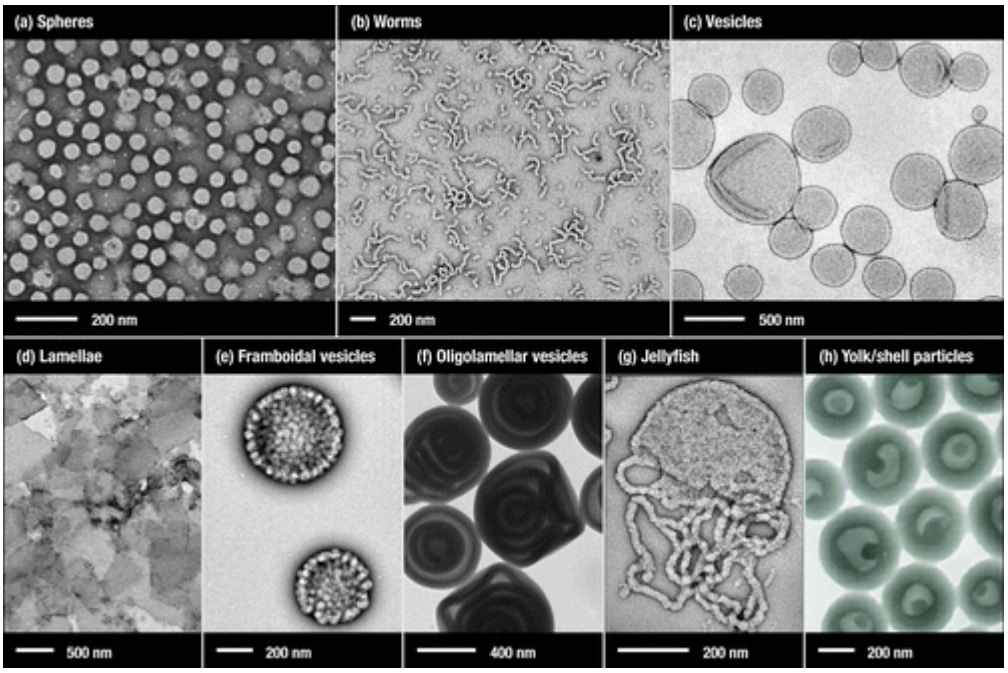

Figure 5.2: Representative transmission electron microscopy (TEM) images for various morphologies that can be synthesized using RAFT-mediated PISA including: a) spheres, b) worms, c) unilamellar vesicles, d) lamellae, e) framboidal vesicles, f) multilamellar vesicles, g) jellyfish, and h) yolk/shell nanostructures. Figure and caption adapted from ref 6.

Successful PISA necessitates a controlled polymerization technique with the vast majority of literature examples employing reversible addition-fragmentation chain transfer (RAFT) polymerization due its immense monomer scope and robust nature.[1,10-13] Alternative reversible-deactivation radical polymerization (RDRP) methodologies have also been shown to be successful for mediating PISA, including atom transfer radical polymerization (ATRP),[14] nitroxide-mediated radical polymerization (NMP),[15,16] as well as an initiators for continuous activator regeneration (ICAR) ATRP approach.[17] Moreover, ring-opening metathesis polymerization-induced self-assembly (ROMPISA) utilizing a peptide-based core-forming norbornene monomer and an oligoethylene glycol based stabilizer block was achieved to generate a range of nanostructures *in situ* in non-aqueous media.[18] Recently, O'Reilly and co-workers developed a general strategy for the synthesis of block copolymers with excellent control in aqueous media using a

commercially available ROMP catalyst. Importantly, switching the core-forming monomers to ones which became insoluble upon polymerization afforded a range of block copolymer nano-objects *via* ROMPISA.[19] In principle, PISA can be conducted in any solvent providing correct selection of the stabilizer block and respective core-forming monomer/s.[6,12] For instance, benzyl methacrylate offers an excellent choice for the core-forming block in alcoholic dispersion PISA's, as well as in non-polar solvents, but is immiscible in aqueous media and thus hinders the formation of higher order morphologies such as worm-like micelles and vesicles.[20] On the other hand, 2-hydroxypropyl methacrylate is widely utilized in RAFT aqueous dispersion PISA,[21–23] but is highly soluble in alcoholic media and thus the driving force for subsequent self-assembly upon polymerization is precluded.

Preparation of block copolymer nanostructures in aqueous media is highly appealing for various reasons, including economic and environmental concerns, but principally because resultant polymer assemblies can be directly applied to potential biomedical applications.[1] To this end, there is an abundance of literature reports concerning successful RAFT aqueous emulsion polymerizations for which the respective core-forming monomer is immiscible with water,[24–33] and RAFT aqueous dispersion polymerizations for which the core-forming monomer is partially or fully miscible in aqueous media.[4,9,34–41] However, due to monomer immiscibility in RAFT aqueous emulsion polymerizations, such systems typically result in the formation of kinetically-trapped lower order morphologies as a direct result of poor exchange dynamics.[20,24,28,32,33] Consequently, the evolution of morphologies is significantly hindered and thus few literature examples exist in which worms or vesicles are accessed for aqueous emulsion PISA formulations.[25,29–31,42,43] In contrast, RAFT aqueous dispersion polymerizations benefit from improved monomer solubility and in turn higher order morphologies can be accessed with relative ease.[1,34,35,40,44] Controlled, reproducible

and facile synthesis of higher order morphologies is paramount for biomedical applications as the resultant polymer assemblies offer distinct advantages over lower order morphologies. For instance, vesicles and cylindrical micelles enable higher loading capacities with respect to spherical micelles; with the former capable of co-encapsulating both hydrophobic and hydrophilic compounds owing to its compartmentalized structure.[45] Furthermore, more exotic morphologies (e.g. disc-shaped micelles) typically exhibit improved blood circulation lifetimes, cell targeting specificity and internalization behavior in comparison to their lower order counterparts.[46,47]

An essential prerequisite for aqueous dispersion PISA is a core-forming monomer that is partially or fully miscible in water and upon subsequent polymerization, produces a water-insoluble polymer at the experimental temperature. Until recently, the number of vinyl monomers identified for RAFT aqueous dispersion polymerizations that successfully generate block copolymer nano-objects was limited.[48] Non-ionic monomers such as 2-hydroxypropyl methacrylate (HPMA),[23,44,49] 2-hydroxybutyl methacrylate (HBMA),[50] diethylene glycol monomethyl ether methacrylate (DEGMA),[37] 2-methoxyethyl acrylate (MEA),[10,34,36] *N*-isopropylacrylamide (NIPAM),[51–53] *N*,*N*-diethylacrylamide (DEAm),[54] and diacetone acrylamide (DAAm) have been previously reported (Figure 5.3 b).[55–61] Furthermore, cationic core-forming monomer 2-aminoethylacrylamide hydrochloride (AEAm), in the presence of an anionic polyelectrolyte, induced *in situ* polyion complexation upon chain extension *via* RAFT aqueous dispersion PISA.[62]

Whilst the range of compatible core-forming monomers for aqueous dispersion polymerizations is expanding,[48] the range of suitable stabilizer blocks is already extensive and can conceivably be applied to any hydrophilic monomer (Figure 5.3 a). Select examples for successfully utilized corona-forming monomers include, glycerol methacrylate (GMA), 2-(dimethylamino)ethyl methacrylate (DMAEMA), poly(ethylene

glycol) monomethyl ether methacrylate (PEGMA), 3-dimethyl(methacryloyloxyethyl) ammonium propane sulfonate (DMAPS), 2-methacryloyloxyethyl phosphorylcholine (MPC), *N*-(2-hydroxypropyl) methacrylamide (HPMAm), 4-vinylpyridine (4VP), and *N*-*N*-dimethylacrylamide (DMAc).[1,6] Notably, surface functionalization of resultant polymer assemblies can be manipulated simply by changing the chemical nature of the initial stabilizer block. Cationic,[21,63] anionic,[64–66] zwitterionic,[35,67] and stimuli-responsive,[51] corona-forming blocks have all been successfully utilized in PISA formulations. Therefore, block copolymer nano-objects can be designed for a variety of applications for which surface chemistry plays a vital role. Whilst the functionalization of both the hydrophobic and hydrophilic domains of polymer assemblies can be easily modified through monomer selection, restrictions regarding the correct order of monomer addition still apply and must be considered to ensure successful block copolymer synthesis.[68]

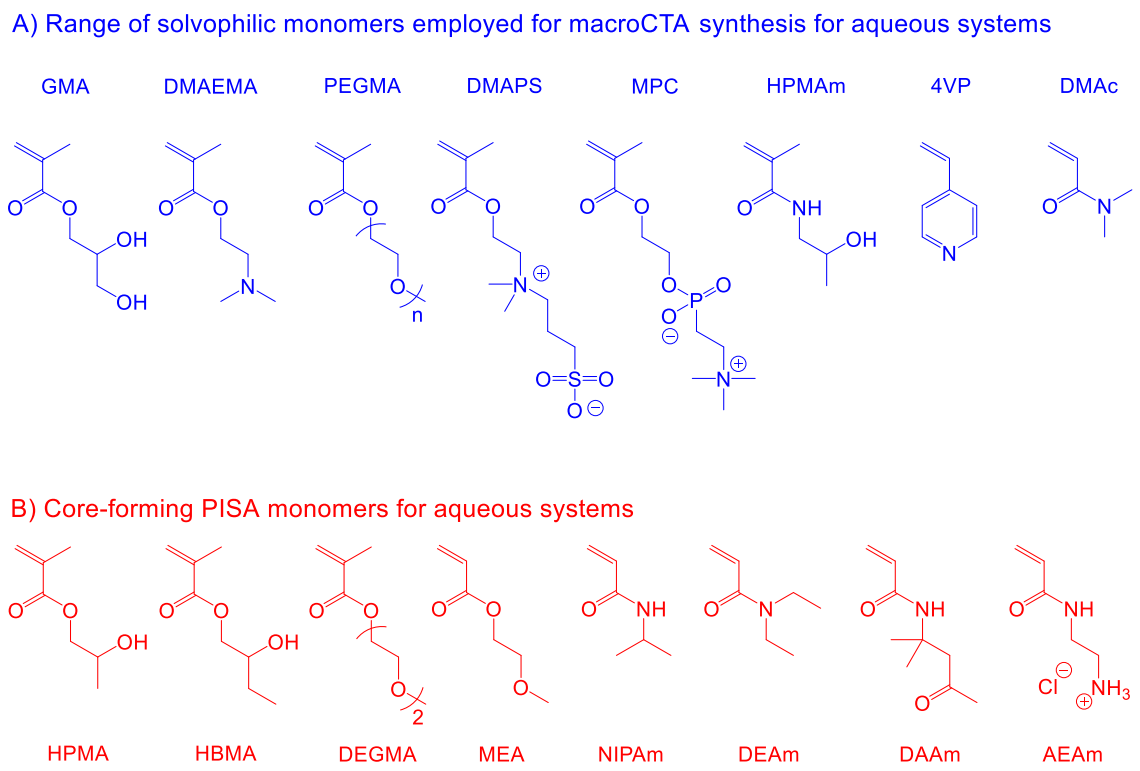

Figure 5.3: Chemical structures of a) hydrophilic corona-forming monomers compatible with PISA in aqueous systems, and b) core-forming monomers identified in the literature for use in RAFT-mediated aqueous dispersion PISA.

Construction of phase diagrams for each specific block copolymer system is essential to enable the reproducible targeting of desired pure block copolymer morphologies.[6] Three major variables principally dictate the final morphology obtained *via* PISA; monomer or total solids concentration (often referred to as the weight percentage); resultant core-forming block length upon polymerization; and molecular weight of the stabilizer block employed.[40] For instance, for the p(GMA)$_n$-*b*-p(HPMA)$_m$ system depicted in Figure 5.4, higher order morphologies were generally observed when a shorter stabilizer block (p(GMA)$_{47}$) was used (Figure 5.4 a). In comparison, lower order morphologies were often observed for respective diblock copolymer nano-objects prepared at identical copolymer concentrations and core-forming block lengths using a longer stabilizer block (p(GMA)$_{78}$) (Figure 5.4 b).

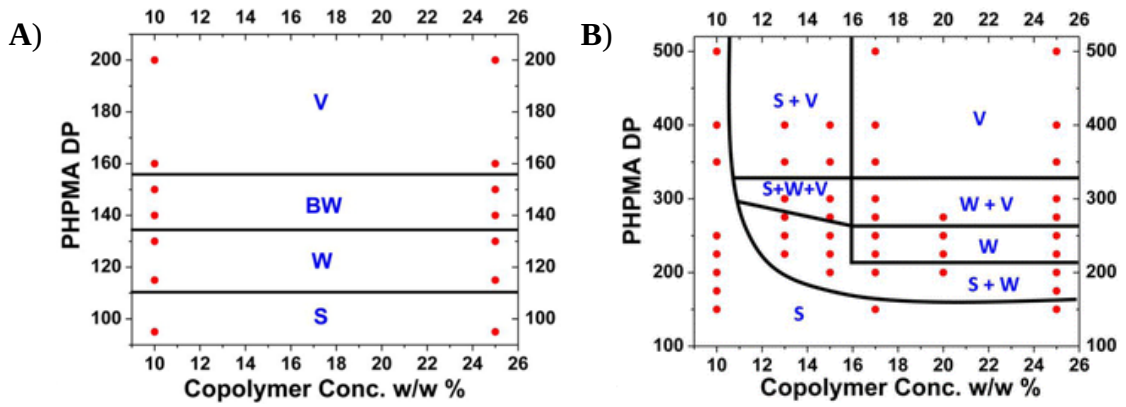

Figure 5.4: Phase diagrams for an aqueous p(GMA)$_n$-*b*-p(HPMA)$_m$ system using a short p(GMA)$_{47}$ (a) or long p(GMA)$_{78}$ (b) stabilizer block. Key: S = spheres, W = worms, BW = branched worms, and V = vesicles. Figure adapted from ref 40.

Unsurprisingly, both phase diagrams showed that higher order morphologies are generally observed with respect to increasing core-forming block length. Interestingly, increasing copolymer concentration for nano-objects prepared with a shorter stabilizer block resulted in no change in the observed morphology, whilst the opposite behavior was true when the stabilizer block was nearly double in length. This difference in block copolymer self-assembly was attributed to the relative steric stabilization of the p(GMA) corona-forming block leading to the generation of both kinetically-trapped and at equilibrium nanostructures.

As demonstrated in Figure 5.4, constructed phase diagrams for PISA-derived systems can contain a mixture of kinetically-trapped, near-equilibrium or at equilibrium nanostructures for similar block copolymer compositions. Moreover, the chosen initiation method for RAFT PISA can have a significant impact upon the observed morphologies post-PISA. The majority of reported PISA processes rely on thermally-initiated methods such as those employed in conventional RAFT polymerizations i.e. use of a thermal azo initiator.[1,6,11,12] However, photoinitiated RAFT PISA has recently garnered interest with several advantages over thermally-initiated PISA, such as increased reaction kinetics and milder experimental conditions i.e. requires lower experimental temperatures.[13,49] More

recently, O'Reilly and co-workers highlighted that obtained morphologies for identical block copolymer compositions were distinctly different for PISA formulations prepared *via* the two different initiation methods, thermally-initiated and photoinitiated.[69] In this case, the authors discovered that photoinitiated PISA formulations often generated higher order morphologies with respect to their analogous thermally-initiated formulations.[69]

5.2.2. Fluorescent nanoparticle labelling *via* PISA

Currently, there is a limited number of reports of fluorescently tagged polymer assemblies *via* a PISA approach. One such example was conducted by An and co-workers in which a fluorescein dye was used to label p(DMAc)$_{35}$-*b*-p(DAAm)$_{300}$ diblock copolymer vesicles *via* hydrazone chemistry of the pendant ketone groups of the core-forming block.[55] Subsequently, the authors found that the vesicle solution displayed a strong green fluorescence emission upon functionalization, with the degree of fluorophore incorporation calculated to be one fluorescent molecule per two diblock copolymer chains (Figure 5.5 a).[55] Furthermore, dynamic light scattering (DLS) analysis before and after functionalization revealed little change in both the hydrodynamic diameter and size distribution for fluorescently-labelled vesicles (Figure 5.5 b).[55] However, no investigation into the difference in fluorescence emission between different morphologies, in this case spherical micelles and vesicles, was made by the authors.

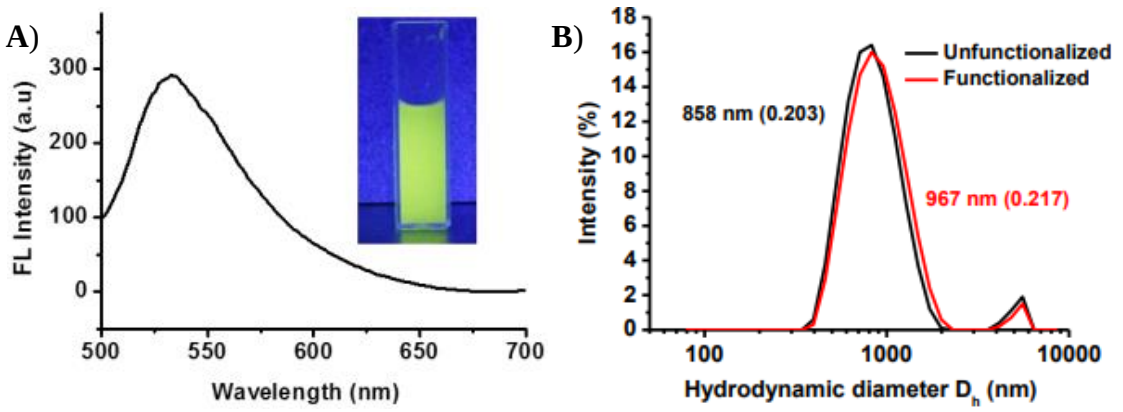

Figure 5.5: a) Fluorescence emission spectrum of fluorescently-labelled p(DMAc)$_{35}$-*b*-p(DAAm)$_{300}$ vesicles with an inset image of the vesicle solution under irradiation with 365 nm UV light. b) DLS analysis in phosphate-buffered saline solution of p(DMAc)$_{35}$-*b*-p(DAAm)$_{300}$ vesicles before and after functionalization with fluorescein-5-thiosemicarbazide. Figure adapted from ref 55.

In another study conducted by Armes and co-workers, galactose-functionalized diblock copolymer nano-objects were synthesized *via* RAFT PISA using a binary mixture of p(GMA)$_{51}$ and poly(galactose methacrylate) (p(GalSMA)$_{34}$) stabilizer blocks.[9] The internalization behavior of Rhodamine B loaded (1:9 p(GalSMA)$_{34}$/p(GMA)$_{51}$)-*b*-p(HPMA)$_{270}$ vesicles with respect to primary human dermal fibroblast (HDF) cells was subsequently investigated by the authors.[9] Confocal microscopy of live HDF cells confirmed efficient internalization of fluorescently-loaded vesicles with subsequent release of the respective dye leading to extensive staining of the HDF cell membranes (Figure 5.6 a and c).[9] Once again, a post-polymerization approach was utilized in this example to fashion fluorescently-tagged polymer assemblies after initial RAFT PISA.

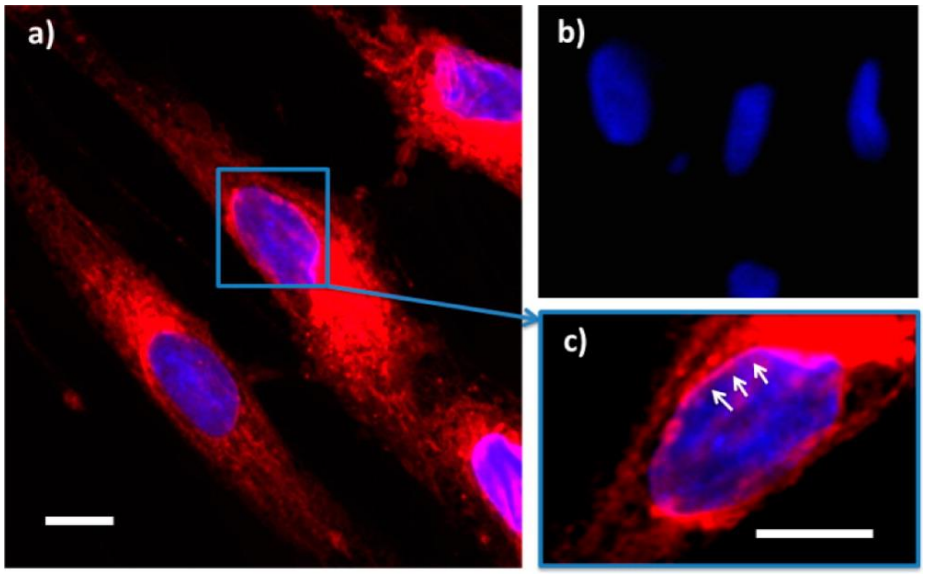

Figure 5.6: Confocal microscopy images of live HDF cells incubated for 16 h with a 1 mg mL^{-1} (1:9 $p(GalSMA)_{34}/p(GMA)_{51}$)-*b*-$p(HPMA)_{270}$ vesicle solution. a) Rhodamine B dye (red) loaded vesicles; b) non-Rhodamine B dye loaded vesicles; c) higher magnification image obtained for (a): white arrows highlight the selective staining of the nuclear membrane. Scale bar: 50 µm. Figure adapted from ref 9.

Fluorophores that exhibit aggregation-induced emission (AIE) have also been successfully utilized to probe polymer self-assemblies synthesized *via* RAFT PISA. In one report by Lu and co-workers, salicylaldehyde groups located in the nanoparticle core were reacted *via* a one-step post-polymerization modification process to produce fluorescently-labelled diblock copolymer nano-objects.[70] Upon functionalization, the authors discovered that self-assembled nanostructures displayed strong orange fluorescence emission with measured fluorescence quantum yields for spheres, worms and vesicles of 11% in both aqueous and organic media.[70]

To date, only one report has used a combinatorial approach whereby fluorescently-labelled diblock copolymer nano-objects were prepared *via* PISA with no post-polymerization modification steps. Yuan and co-workers synthesized a range of fluorescent self-assembled nanostructures with different molecular weights *via* RAFT dispersion copolymerization of benzyl methacrylate (BzMA) and AIE-active 1-ethenyl-4-(1,2,2-triphenylethenyl)benzene (TPE) in ethanol mediated by a $p(DMAc)_{39}$ stabilizer

block.[71] Importantly, the authors found that both fluorescence emission and fluorescence quantum yield demonstrated a direct dependence on the resultant diblock copolymer morphology with the following trend observed: vesicles > worms > spherical micelles (Figure 5.7).[71] Interestingly, the AIE effect was enhanced with respect to increasing the size and wall thickness for fluorescent p(DMAc)$_{39}$-*b*-p(BzMA-*co*-TPE)$_{360}$ vesicles.[71]

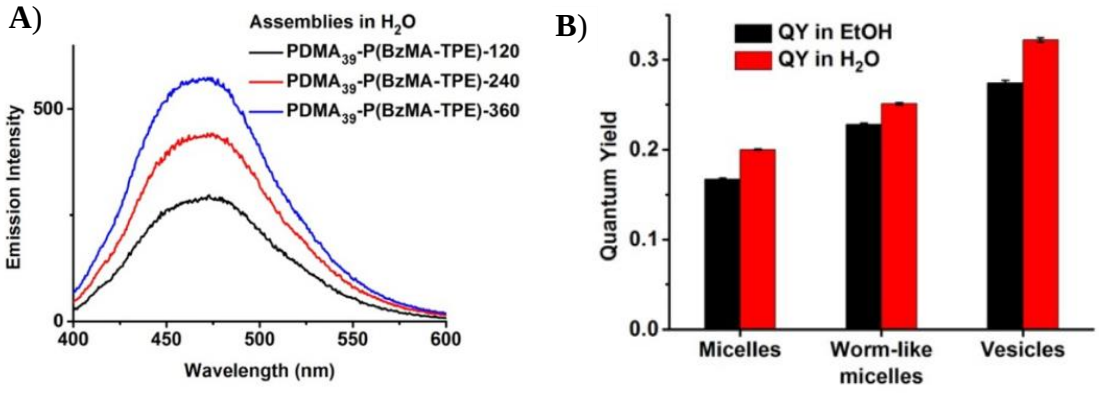

Figure 5.7: a) Fluorescence emission spectra of fluorescently-labelled p(DMAc)$_{39}$-*b*-p(BzMA-*co*-TPE)$_x$ assemblies in H_2O. b) Fluorescence quantum yields (QY) of p(DMAc)$_{39}$-*b*-p(BzMA-*co*-TPE)$_x$ assemblies in EtOH and H_2O. Note: Micelles, worms and vesicles for x = 120, 240, and 360 respectively. Figure adapted from ref 71.

Overall, this study highlights the possibility of using an environmentally-sensitive fluorophore as an effective probe for the investigation and understanding of polymer assemblies produced *via* a PISA approach. In this Chapter, the use of an aminobromomaleimide (ABM) fluorophore, as a potential alternative to bulky aromatic fluorophores, to achieve similar understanding of PISA-derived nanostructures *via* core functionalization will be explored.

5.3. Results and Discussion

As outlined in the introduction to this Chapter, RAFT dispersion PISA involves the chain extension of a solvent soluble macro chain transfer agent (macroCTA) with an initially solvent soluble monomer. Subsequently, the solvent soluble monomer becomes solvophobic upon polymerization resulting in the formation of a block copolymer with a corona- and a core-forming block respectively. At a critical degree of polymerization, spontaneous self-assembly of the growing block copolymer chains occurs which is dependent on a multitude of variables highlighted above. As discussed in previous Chapters, the optimum location for an aminobromomaleimide (ABM) fluorophore is directly adjacent to or within the hydrophobic core-forming block as this ensures minimum solvent interactions upon self-assembly thereby promoting fluorescence emission.

With regards to producing fluorescent polymer nanostructures *via* a PISA methodology in aqueous media, one research avenue would be to synthesize a water soluble ABM-functionalized monomer which demonstrates the typical characteristics of a PISA monomer. Subsequent copolymerization with a second water soluble PISA monomer would result in incorporation of the fluorophore within the core-forming block. Consequently, the ABM fluorophore would be sequestered into the hydrophobic domain of the polymeric nanostructures upon self-assembly. One critical advantage of this approach is that the degree of functionalization, in this case fluorophore incorporation, can be tuned by simple manipulation of the monomer feed ratios of the two respective core-forming monomers. However, it was envisaged that the successful synthesis of a partially or fully water miscible ABM-functionalized monomer which becomes solvophobic during RAFT aqueous polymerization would be synthetically challenging. Furthermore, extensive studies into the effect of the ABM-functionalized monomer upon

both the PISA mechanism and subsequent microstructure of the core-forming block would need to be conducted. For instance, the relative reactivity ratios for the copolymerization of the ABM-functionalized monomer with respect to the second core-forming monomer would need to be calculated to determine whether the resultant core-forming block is statistical, gradient or alternating in nature. Moreover, changing the inherent nature of the core-forming block due to the introduction of a new fluorescent comonomer could result in significant deviation between the morphology obtained and the anticipated morphology; the latter of which is determined by the respective phase diagram for the non-fluorescent block copolymer analogues. As a result, fluorophore incorporation *via* this method was considered unsuitable due to intensive synthetic requirements and limited versatility.

As alluded to in previous Chapters and in the introduction to this Chapter, an alternative method for the production of fluorescent polymer nanostructures entails introduction of the fluorophore *via* a post-polymerization modification process. It is worth noting that the principal advantages of using PISA to synthesize polymer nanostructures are that a high weight percentage of reagents can be used thereby minimizing wastage and cost, a one-pot approach is employed in which both polymerization and self-assembly are achieved, and the necessity of laborious purification steps and post-polymerization handling is precluded. Therefore, the production of fluorescent polymeric nanostructures *via* PISA which requires post-polymerization modification negates the majority of the formerly outlined advantages. Ultimately, the requirement for highly efficient reactions in which an excess of reagents is typically necessary to achieve a high degree of functionalization is in stark contrast to the inherent benefits of employing PISA to produce polymer nanostructures.

Herein, employment of a fluorescent RAFT agent to afford fluorescent polymer nanostructures *via* PISA provided the most suitable option. In Chapter 2, the successful

design and synthesis of a RAFT agent whereby the R group was functionalized with an ABM fluorophore was described, with the controlled polymerization of more activated monomers (MAMs) to fashion fluorescent diblock copolymers achieved in Chapter 3. However, for fluorescent diblock copolymers produced utilizing an R group ABM-functionalized RAFT agent, the ABM fluorophore is located adjacent to the first block synthesized i.e. α-functionalized polymers. In a PISA process, the first block synthesized is typically the corona-forming block to fashion a solvent soluble macroCTA which is subsequently chain extended *via* PISA. Consequently, if the same R group ABM-functionalized RAFT agent was used to synthesize fluorescent diblock copolymers *via* PISA, the ABM fluorophore would not be sequestered into the hydrophobic domain of the resultant self-assembled nanostructures, but instead be located in the hydrophilic domain and thus fluorescence emission would be quenched.

In light of this, one of the Z group ABM-functionalized RAFT agents that was designed and synthesized in Chapter 2 will be utilized herein. Benzyl (2-(3-bromo-4-(isopropylamino)-2,5-dioxo-2,5-dihydro-1H-pyrrol-1-yl)ethyl) carbonotrithioate (**2vi**) facilitates the controlled RAFT polymerization of acrylate, acrylamide and styrenic monomers to produce ω-functionalized fluorescent polymers. Consequently, the ABM fluorophore will be located adjacent to the core-forming block upon chain extension of a solvent soluble macroCTA synthesized *via* RAFT polymerization using **2vi**. During PISA, the ABM fluorophore will be sequestered into the hydrophobic domain of the resultant polymer nanostructures, thereby ensuring better protection from solvent quenching and thus greater fluorescence emission and longer fluorescence lifetimes should be observed.

This Chapter focuses on the synthetic efforts made towards achieving the following two research goals. Namely, to use a well-defined PISA system from the literature with a previously mapped out phase diagram and focus upon targeting a pure phase of the three

main morphologies – spherical micelles, cylindrical or worm-like micelles and vesicles. Subsequently, to confirm the obtained morphologies by transmission electron microscopy (TEM) imaging and DLS analysis and compare to literature predictions to ascertain if there is any effect of the ABM fluorophore upon the PISA mechanism. Finally, the fluorescence emission of the resultant polymer nanostructures will be measured *via* both steady-state and time-resolved fluorescence spectroscopy to confirm whether there is an anticipated difference in fluorescence emission and fluorescence lifetime of the ABM fluorophore for each morphology.[71]

The secondary research aim was to develop a PISA system whereby a low weight percentage of solids (e.g. 5 wt%) can be used to successfully synthesize fluorescent polymer nanostructures of various morphologies without an observed onset of turbidity for the polymerization mixture. Subsequently, to determine whether the polymerization kinetics and onset of micellization can be measured *via in situ* steady-state fluorescence emission for any successful system. It was anticipated that an increase in fluorescence emission will be observed with respect to both increasing degree of polymerization and self-assembly state to reflect the corresponding changes with regards to the local environment of the ABM fluorophore.

5.3.1. Fluorescent PISA – initial screening

As outlined above, the Z group ABM-functionalized RAFT agent **2vi** (Scheme 5.1) should be capable of producing ω-functionalized polymers *via* the controlled RAFT polymerization of acrylate, acrylamide and/or styrenic monomers. Furthermore, photoinitiated RAFT PISA was avoided to preclude any possible side reactions or photobleaching of the ABM fluorophore during the PISA process. Therefore, the criteria for an ideal model PISA system from the literature was as follows; conducted in aqueous

media, comprehensive phase diagram with pure phases of each main morphology, comprised of water-soluble monomers from any of the three formerly outlined monomer classes, and thermally initiated.

Armes and co-workers recently constructed a phase diagram which allowed the accurate targeting of pure block copolymer morphologies (spheres, worms and vesicles) for an extensive range of p(DMAc)$_n$-*b*-p(DAAm)$_m$ diblock copolymer compositions *via* RAFT PISA at 20 wt% in aqueous media at 70 °C.[60] Well-defined spherical micelles were formed from a p(DMAc) macroCTA with an average degree of polymerization (DP) of >68 (a); whilst pure phases of both worms (b) and vesicles (c) were identified by the authors when relatively short p(DMAc) macroCTAs (DP = 40-58) were utilized – with an extremely narrow phase space observed for worms (Figure 5.8).[60]

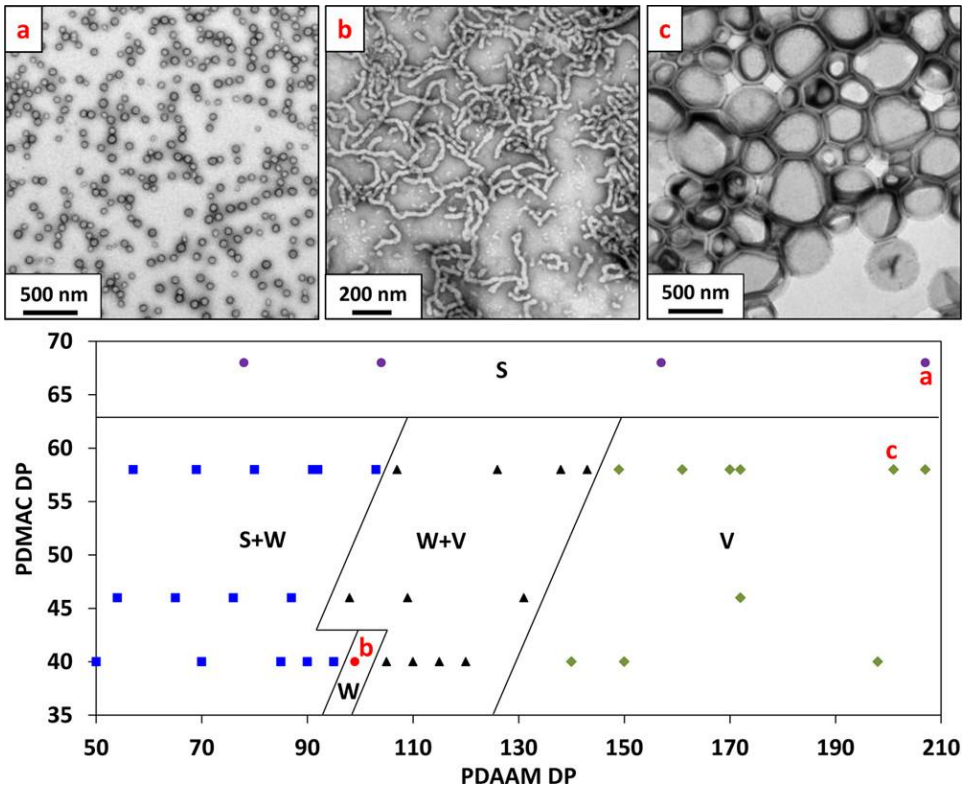

Figure 5.8: Transmission electron microscopy images (top) showing pure sphere (a), worm (b) and vesicle (c) morphologies. Phase diagram (bottom) constructed for a series of p(DMAc)$_n$-*b*-p(DAAm)$_m$ diblock copolymer compositions, where S = spheres, S + W = mixed spheres and worms, W = worms, W + V = mixed worms and vesicles, and V = vesicles. Figure and caption adapted from ref 60.

To allow for comparison with the results obtained from the literature, three fluorescent water soluble p(DMAc) homopolymers were synthesized *via* RAFT polymerization in 1,4-dioxane at 70 °C using the Z group ABM-functionalized RAFT agent **2vi** (Scheme 5.1). The following degrees of polymerization were targeted to match the respective phase spaces depicted in Figure 5.8; 68 to target spherical micelles (S), 58 to target vesicles (V), and 40 to target both vesicles (V) and worms (W).

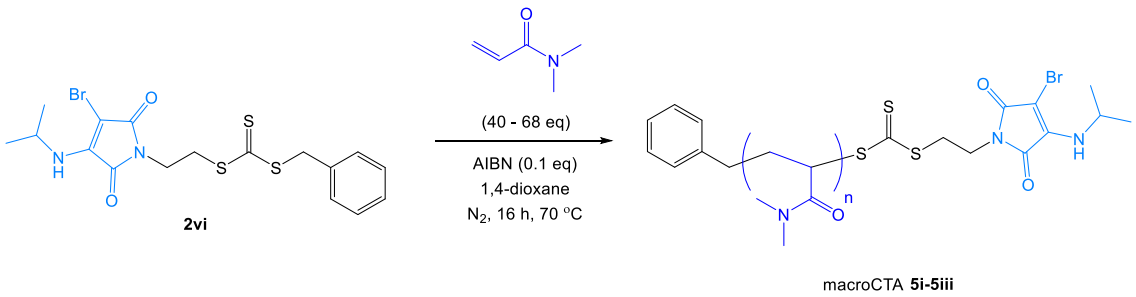

Scheme 5.1: RAFT polymerization of DMAc with the Z group ABM-functionalized RAFT agent **2vi** to produce three p(DMAc) homopolymers (macroCTA **5i-5iii**). AIBN = 2,2'-azobisisobutyronitrile.

Upon purification, three p(DMAc)$_n$ macroCTAs (**5i-5iii**) were isolated; characterization data for which is summarized in Table 5.1.

macroCTA	Target DP of DMAc	ρ[a] (%)	DP[b]	$M_{n,\,NMR}$[b] (kDa)	$M_{n,\,SEC}$[c] (kDa)	$Đ_M$[c]
5i	68	88	60	6.4	6.5	1.21
5ii	40	90	36	4.0	3.9	1.22
5iii	58	81	47	5.2	6.0	1.21

Table 5.1: Characterization data for ABM-functionalized p(DMAc)$_n$ homopolymers (macroCTA **5i-5iii**). Key: [a] monomer conversion was calculated by ^{1}H NMR spectroscopy (300 MHz, CD_3OD); [b] determined by end group analysis using ^{1}H NMR spectroscopy (300 MHz, CD_3OD); [c] obtained by SEC analysis based on poly(methyl methacrylate) (p(MMA)) standards with dimethylformamide (DMF) as the eluent.

^{1}H NMR spectroscopy was utilized to determine the degree of polymerization through end group analysis by comparing the peak integrals corresponding to the polymer methyl and methine resonances (H7 and H6 respectively) to that of the benzyl end group aromatic (H1, H2 and H3) and trithiocarbonate end group C*H*$_2$S resonances (H8) (Figure 5.9).

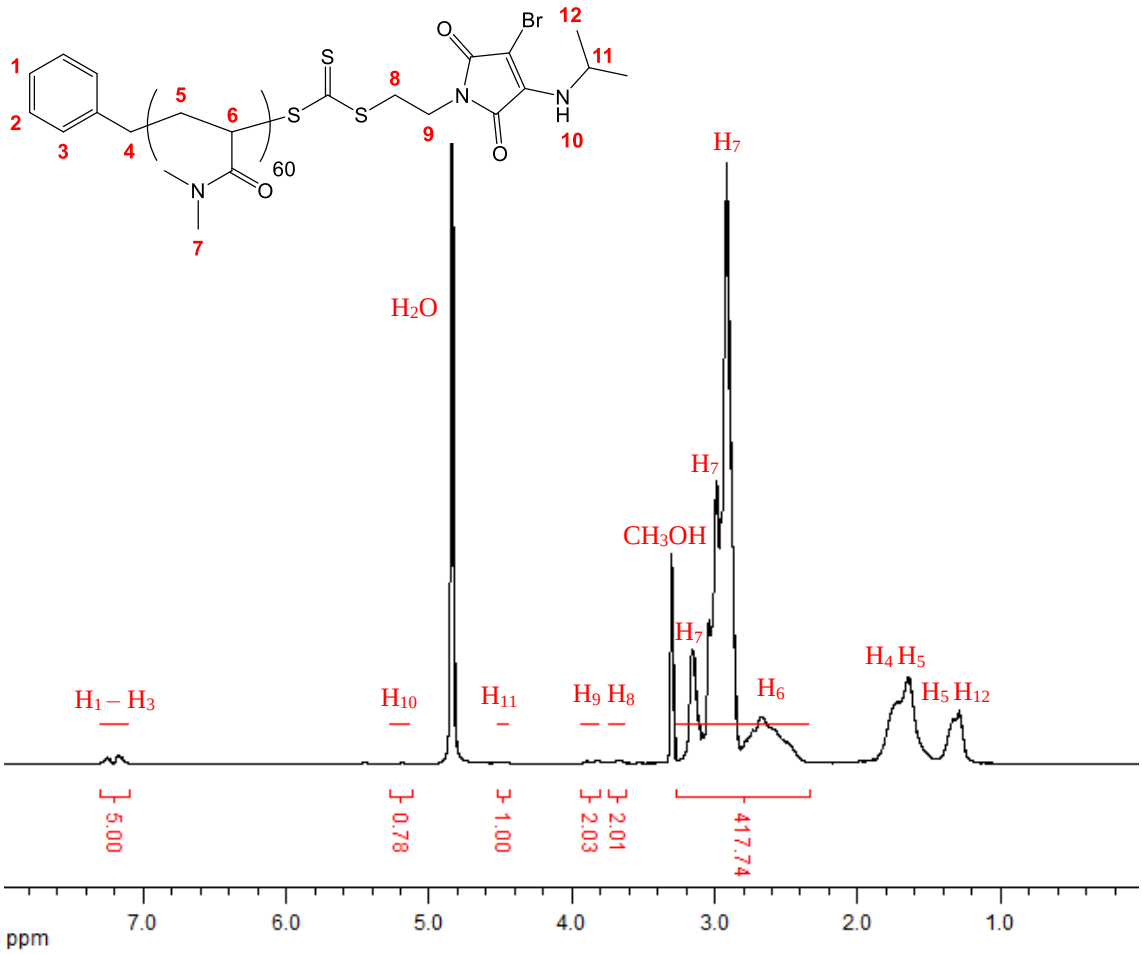

Figure 5.9: ^{1}H NMR spectrum (300 MHz, CD_3OD) of the ABM-functionalized p(DMAc)$_{60}$ macroCTA **5i**.

Upon SEC analysis, all three p(DMAc) homopolymers showed symmetrical and narrow molecular weight distributions which indicated excellent control over the RAFT polymerization using the Z group ABM-functionalized RAFT agent **2vi** (Figure 5.10). Importantly, the molecular weight distributions obtained using an RI and UV detector (recorded at 309 nm) overlap appreciably which indicated that the trithiocarbonate end

group was retained which was essential for subsequent chain extension. Unfortunately, at the time of measurement the UV lamp of the GPC system had to be replaced and thus polymer samples could not be remeasured with the UV detector recording at 400 nm to confirm retention of the ABM moiety. However, when placed under the hand-held long wave UV lamp (365 nm) all three p(DMAc) homopolymers (macroCTA **5i-5iii**) were emissive which was a good indication that the ABM functionality was retained to some degree.

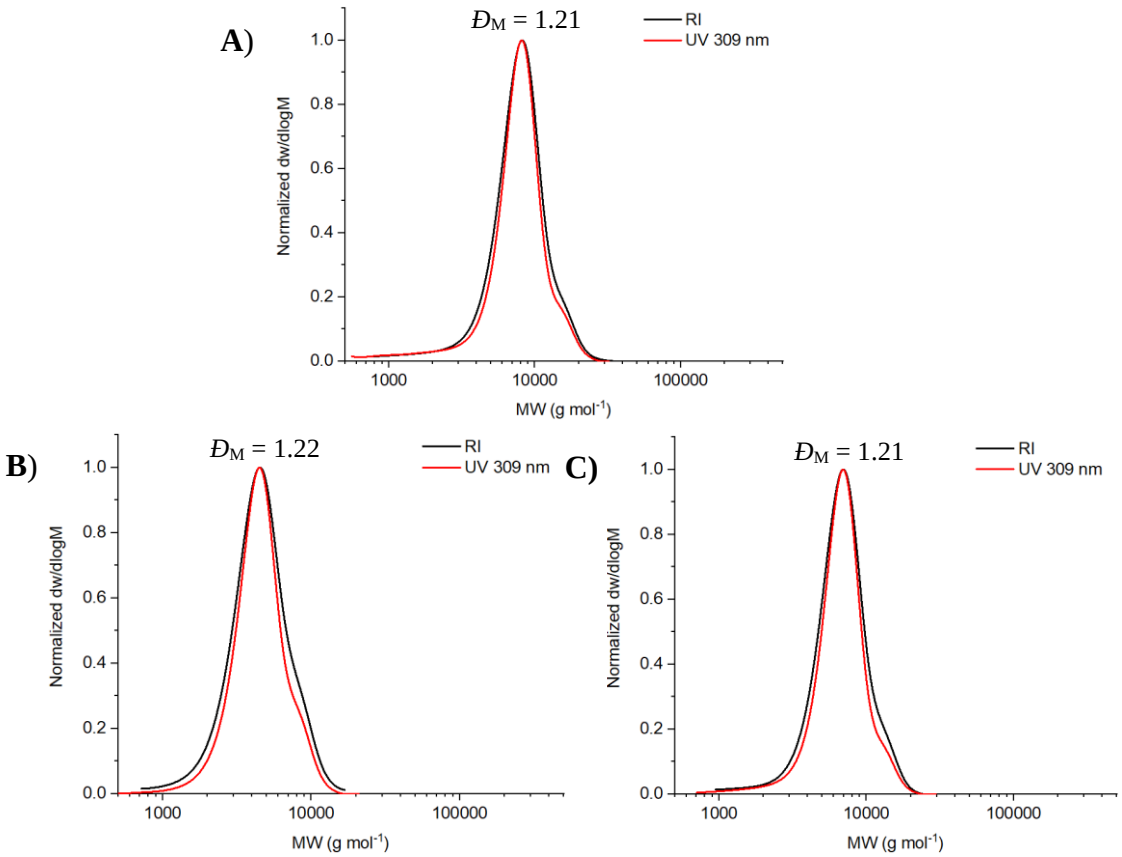

Figure 5.10: Molecular weight distributions determined by SEC (DMF as the eluent and calibrated against p(MMA) standards) using both an RI and UV (recorded at 309 nm) detector for the following ABM-functionalized p(DMAc)$_n$ homopolymers: a) **5i**, b) **5ii**, and c) **5iii**.

Note, that all three RAFT polymerizations did not reach >90% conversion after 16 hours which was unexpected. Near quantitative conversion was anticipated for a DMAc

homopolymerization due to the monomer's high propagation rate and propensity to not undergo side reactions such as backbiting which can prevent high conversions from being reached.[72] Moreover, in Chapter 2 kinetic analysis of the RAFT homopolymerization of DMAc using **2vi** revealed that whilst a relatively small induction period existed, a loss in polymerization control and/or reduction in the polymerization rate was not observed. Considering this, it was unclear as to why the RAFT homopolymerization of DMAc using the Z group ABM-functionalized RAFT agent **2vi** did not reach the target monomer conversion within the experimental timeframe.

Next, a series of chain extensions of p(DMAc) macroCTAs **5i-5iii** were conducted *via* RAFT aqueous dispersion polymerization of DAAm at 70 °C and 20 wt% solids (Scheme 5.2). A pure phase of vesicles was targeted in most cases with polymerization conditions initially reflecting those employed in the paper.[60] Note, that 0.01 M NaOH was required to solubilize the azo initiator 4,4'-azobis(4-cyanovaleric acid) (ACVA) prior to addition to the initial polymerization solution. Furthermore, HCl was not required to lower the solution pH to pH 2.5, as the p(DMAc) macroCTAs (**5i-5iii**) do not have terminal carboxylic acid groups unlike their literature analogues.[60]

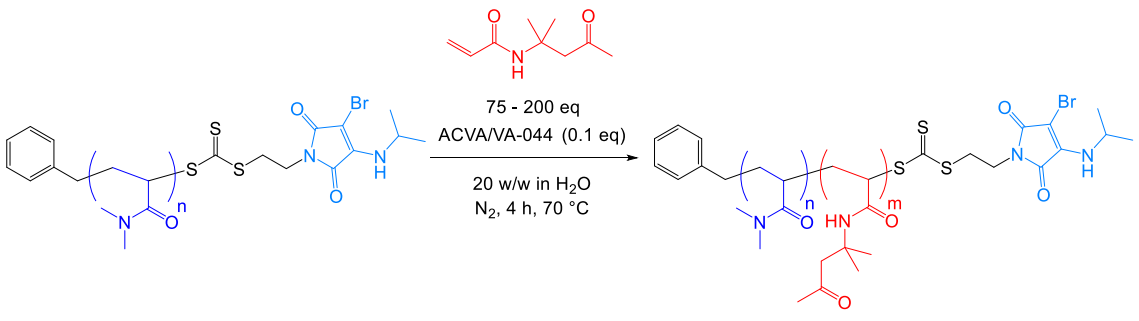

Scheme 5.2: RAFT aqueous dispersion polymerization of diacetone acrylamide (DAAm) with ABM-functionalized water soluble p(DMAc)$_n$ macroCTAs **5i-5iii** at 20 wt% solids to produce ABM-functionalized p(DMAc)$_n$-*b*-p(DAAm)$_m$ diblock copolymers **5iv-5viii**. ACVA = 4,4'-azobis(4-cyanovaleric acid). VA-044 = 2,2'-azobis(2-(2-imidazolin-2-yl)propane dihydrochloride.

DAAm conversion for all formulations was monitored *via* ^{1}H NMR spectroscopy by comparing the peak integrals corresponding to residual vinyl resonances at 6.1-6.3 ppm to that of the terminal polymeric methyl resonance at 2.18 ppm (H12, Figure 5.11).

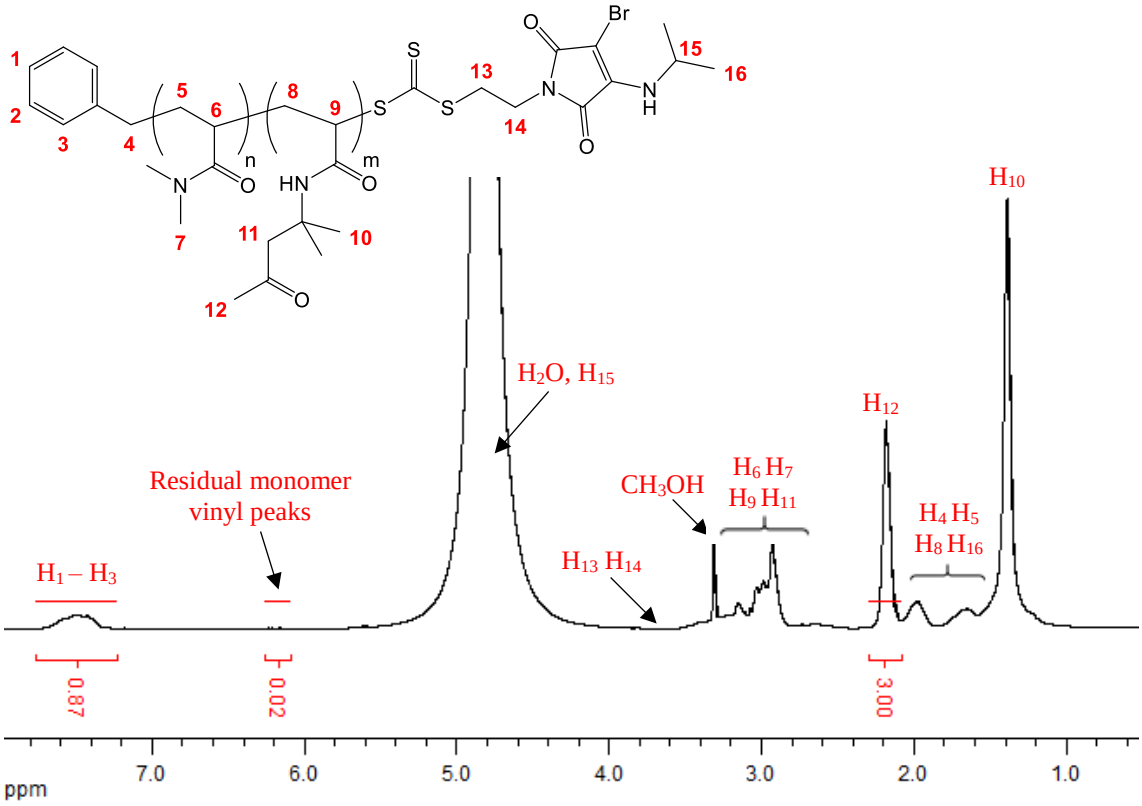

Figure 5.11: Example crude ^{1}H NMR spectrum (400 MHz, CD_3OD) taken after a RAFT aqueous dispersion polymerization had been quenched by exposure to air. DAAm conversion was calculated to be 99%.

A detailed summary of the experimental conditions and measured monomer conversions for all PISA formulations is provided in Table 5.2. For the majority of PISA formulations in which ACVA was used as the azo initiator, quantitative conversion after 4 hours was not reached as targeted and, in certain cases, low or even no conversion of DAAm was observed (Table 5.2, entries 1-7). With regards to the addition of the azo initiator to the polymerization solution, the required quantities necessitated a stock solution of ACVA with a known concentration to be used. However, ACVA is poorly water soluble and

thus required either basic pH or elevated temperatures to ensure complete dissolution. As a result, it was postulated that the presence of base in the PISA formulations was leading to competition during the RAFT aqueous dispersion polymerization between the loss of the trithiocarbonate end group *via* base hydrolysis and conversion of DAAm.

Furthermore, for PISA formulations for which the stock solution of ACVA had been prepared at elevated temperatures, negligible monomer conversions were measured which was attributed to azo initiator degradation prior to the onset of polymerization (Table 5.2, entry 4). Two alternative water-soluble azo initiators that have been utilized previously within the literature for RAFT aqueous dispersion polymerizations are 2,2'-azobis(2-(2-imidazolin-2-yl)propane dihydrochloride (VA-044) and 2,2'-azobis(2-methylpropionamidine) dihydrochloride (V-50) (Figure 5.12).[1,6,55,57,59]

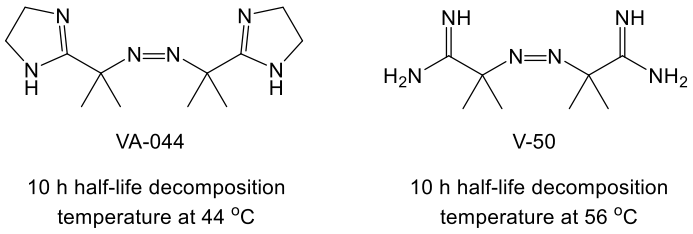

Figure 5.12: Chemical structures of water-soluble azo initiators 2,2'-azobis(2 (2 imidazolin-2-yl)propane dihydrochloride (VA-044) and 2,2'-azobis(2-methylpropionamidine) dihydrochloride (V-50).

Consequently, the azo initiator was switched from ACVA to VA-044 and the reaction temperature was lowered to 60 °C to account for the difference in the half-life decomposition temperature. Subsequent RAFT polymerization solutions became distinctly turbid within 90 minutes which was a qualitative indication of the onset of micellar nucleation. Moreover, all PISA formulations using VA-044 as the azo initiator reached near quantitative conversion after 4 hours (Table 5.2, Entries 8-12), which was in good agreement with the polymerization kinetics previously reported for this system in the literature.[55,60]

Entry	p(DMAc) macroCTA	p(DAAm) Target DP	[DAAm] (wt%)	Azo Initiator	Temperature (°C)	ρ^a (%)
1	**5i**	200	20	ACVA[b]	70	65
2	**5i**	120	20	ACVA[b]	70	64
3	**5i**	80	20	ACVA[b]	70	49
4	**5i**	200	20	ACVA[c]	70	0
5	**5iii**	170	20	ACVA[b]	70	3
6	**5iii**	100	20	ACVA[b]	70	4
7	**5iii**	75	20	ACVA[b]	70	1
8	**5i**	200	20	VA-044	60	99
9	**5i**	120	20	VA-044	60	94
10	**5i**	80	20	VA-044	60	94
11	**5ii**	150	20	VA-044	60	98
12	**5iii**	170	20	VA-044	60	98

Table 5.2: Experimental data obtained for a series of RAFT aqueous dispersion polymerizations of DAAm with an ABM-functionalized p(DMAc)$_n$ macroCTA (**5i-5iii**) to produce ABM-functionalized p(DMAc)$_n$-*b*-p(DAAm)$_m$ diblock copolymers. Key: [a] monomer conversion was calculated by ^{1}H NMR spectroscopy of the crude polymerization mixture (300 MHz, CD_3OD); [b] stock solution of ACVA was prepared using 0.01 M NaOH; [c] stock solution of ACVA was prepared at 40 °C.

To qualitatively ascertain the relative environment of the ABM fluorophore, polymerization solutions were placed under the hand-held long wave UV lamp (365 nm) prior to PISA and post-PISA. As expected, pre-PISA formulations displayed negligible fluorescence emission (Figure 5.13 a) which mirrored the behavior previously observed for ABMs in water, whereby the quantum yield is extremely low and fluorescence emission red shifted due to fluorescence quenching *via* electron drive proton transfer (EDPT).[73,74] In contrast, post-PISA formulations were visibly emissive (Figure 5.13 b) with a clear blue shift in fluorescence emission which indicated a distinct change in the

relative environment of the ABM fluorophore as a result of improved protection from fluorescence quenching.

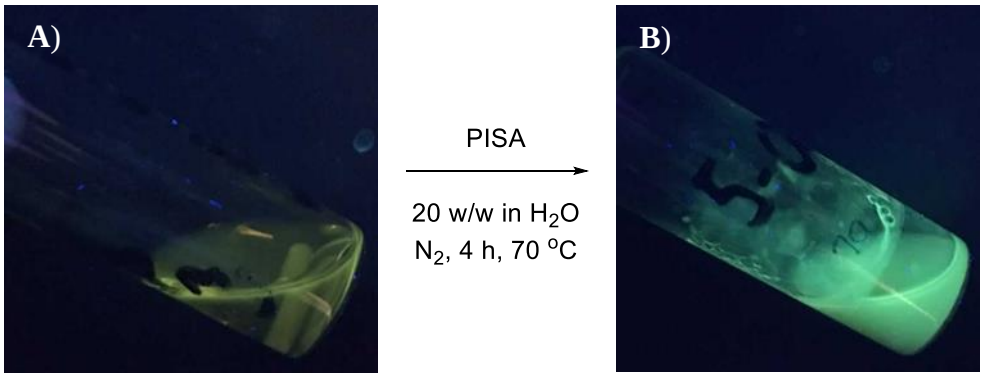

Figure 5.13: Images of a p(DMAc)$_n$-*b*-p(DAAm)$_m$ formulation under a UV lamp (λ = 365 nm): a) prior to RAFT aqueous dispersion polymerization, and b) post RAFT aqueous dispersion polymerization.

Upon purification of the successful PISA formulations (Table 5.2, entries 8-12), five ABM-functionalized p(DMAc)$_n$-*b*-p(DAAm)$_m$ diblock copolymers (**5iv-5viii**) were isolated; characterization data for which is summarized in Table 5.3.

Diblock Copolymer	***DP* DMAc**[a]	***DP* DAAm**[a]	$M_{n,\,NMR}$[a] **(kDa)**	$M_{n,\,SEC}$[b] **(kDa)**	$Đ_M$[b]
5iv	60	198	39.9	49.2	2.09
5v	60	113	25.5	29.4	1.95
5vi	60	75	19.1	21.4	1.85
5vii	36	147	28.9	38.5	5.65
5viii	47	167	33.4	50.6	1.67

Table 5.3: Characterization data for ABM-functionalized p(DMAc)$_n$-*b*-p(DAAm)$_m$ diblock copolymers **5iv-5viii**. Key: [a] determined by end group analysis using ^{1}H NMR spectroscopy (300 MHz, CD_3OD); [b] obtained by SEC analysis based on p(MMA) standards with DMF as the eluent.

High dispersity values ($Đ_M$ > 1.67) were obtained for all five p(DMAc)$_n$-*b*-p(DAAm)$_m$ diblock copolymers (**5iv**-**5viii**) with very broad molecular weight distributions and, in some cases, bimodal RI traces observed upon SEC analysis (Figure 5.14). Consequently, TEM imaging and DLS analysis was not conducted for any of the five purified PISA formulations due to poor control over the RAFT aqueous dispersion polymerization of DAAm. Following these poor results, it was postulated that the R group chosen, in this case benzyl, was not the optimal choice for polymerizing acrylamides in a controlled manner in aqueous solution. Furthermore, the number of equivalents of azo initiator used was potentially too high, resulting in an uncontrolled rate of polymerization (R_p) coupled with an increased probability of termination events hindering the overall control over the RAFT polymerization.

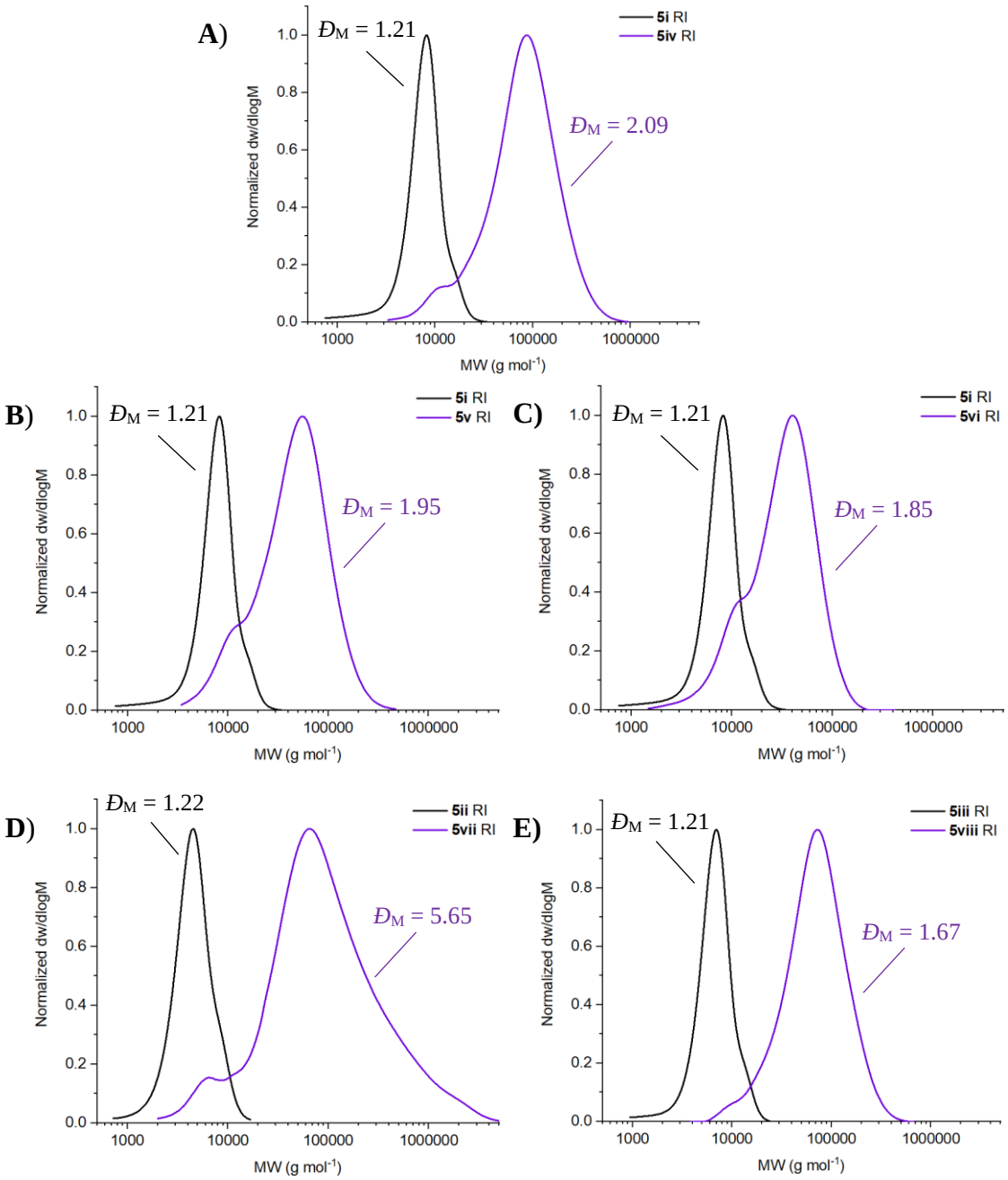

Figure 5.14: Molecular weight distributions determined by SEC (DMF as the eluent and calibrated against p(MMA) standards) using an RI detector for the following ABM-functionalized p(DMAc)$_n$-*b*-p(DAAm)$_m$ diblock copolymers: a) **5iv**, b) **5v**, c) **5vi**, d) **5vii**, and e) **5viii**. Respective RI traces for p(DMAc)$_n$ macroCTAs (**5i-5iii**) are shown for comparison.

5.3.2. Fluorescent PISA optimization

Several examples exist in the literature regarding the successful RAFT aqueous dispersion polymerization of DAAm to produce block copolymer nano-objects *via* PISA. In almost all cases, the R group of the RAFT agent used was either propionic acid, isobutyric acid, or their respective methylated ester analogues (Figure 5.15).[55,57,60,61]

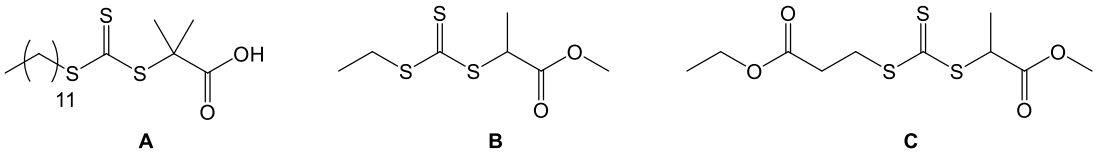

Figure 5.15: Chemical structures of RAFT agents that have been successfully used within the literature to produce well-defined p(DMAc)$_n$-*b*-p(DAAm)$_m$ diblock copolymer nano-objects *via* RAFT PISA.[55,57,60,61]

In light of this, a revised Z group ABM-functionalized RAFT agent was designed and synthesized by the three step route detailed in Scheme 5.3. Ethyl 2-((((2-hydroxyethyl) thio)carbonothioyl)thio)propanoate (**5ix**) was synthesized following the literature protocol previously used for the synthesis of benzyl (2-hydroxyethyl) carbonotrithioate (BHET) in Chapter 2,[75] with benzyl bromide switched to ethyl 2-bromopropionate. Transformation of the hydroxyl group to the pro-fluorescent dibromomaleimide (DBM) moiety was achieved *via* a modified Mitsunobu reaction to produce **5x** in an isolated yield of 38%. Subsequent reaction between the pro-fluorescent Z group DBM-functionalized precursor (**5x**) and isopropylamine afforded the desired Z group ABM-functionalized RAFT agent **5xi** in an overall yield of 13% (Scheme 5.3).

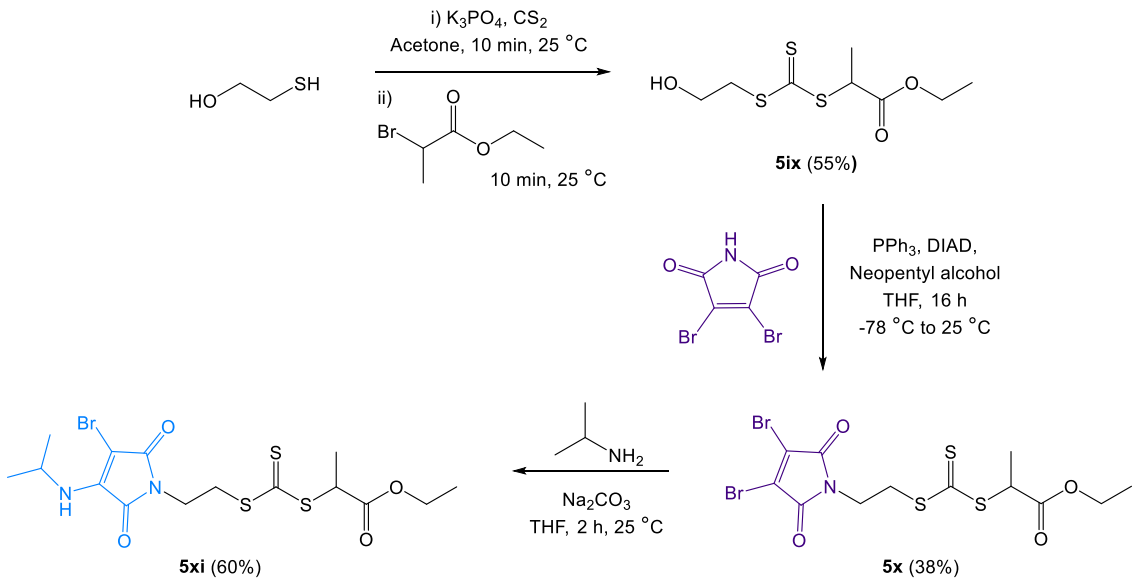

Scheme 5.3: Synthesis of a revised Z group ABM-functionalized RAFT agent **5xi**, whereby the R group is ethyl propionate and the Z group is *N*-mercaptoethyl aminobromomaleimide.

Overall, the sole difference between **5xi** and the RAFT agent used for previous PISA formulations, **2vi**, was the change in R group structure from benzyl to ethyl propionate. Furthermore, the Z group ABM-functionalized RAFT agent **5xi** was designed to closely match the chemical structure of one of the RAFT agents successfully used for the preparation of well-defined p(DMAc)-*b*-p(DAAm) diblock copolymer nano-objects from the literature (Figure 5.15, RAFT agent **B**).[55,57] As a result, it was envisaged that reproducing the experimental conditions employed in the highlighted literature examples would help to determine the effect from the introduction of the ABM fluorophore into the Z group structure of **5xi** upon the PISA methodology.

To allow for comparison with the previously obtained experimental results in Section 5.3.1, RAFT homopolymerization of DMAc using the Z group ABM-functionalized RAFT agent **5xi** was conducted in 1,4-dioxane at 70 °C, as outlined in Scheme 5.4.

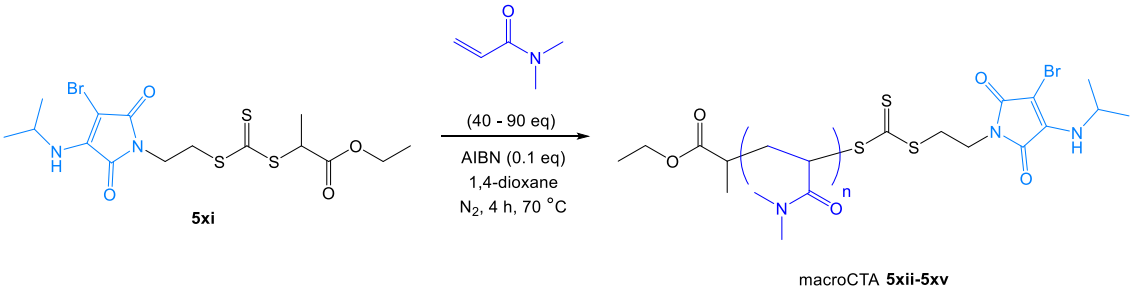

Scheme 5.4: RAFT polymerization of DMAc with the Z group ABM-functionalized RAFT agent **5xi** to produce four fluorescent ABM-functionalized p(DMAc)$_n$ homopolymers (macroCTA **5xii-5xv**).

Upon purification, a series of ABM-functionalized p(DMAc)$_n$ macroCTAs were isolated (**5xii-5xv**); characterization data for which is summarized in Table 5.4.

macroCTA	**Target DP of DMAc**	ρ^a **(%)**	DP^b	$M_{n,\,NMR}{}^b$ **(kDa)**	$M_{n,\,SEC}{}^c$ **(kDa)**	$Đ_M{}^c$
5xii	70	84	59	6.3	7.4	1.13
5xiii	55	80	44	4.8	6.4	1.11
5xiv	50	84	42	4.6	6.6	1.12
5xv	90	86	77	8.1	11.7	1.10

Table 5.4: Characterization data for ABM-functionalized p(DMAc)$_n$ homopolymers (macroCTA **5xii-5xv**). Key: [a] monomer conversion was calculated by ^{1}H NMR spectroscopy of the crude polymerization mixture (400 MHz, $CDCl_3$); [b] determined by end group analysis using ^{1}H NMR spectroscopy (400 MHz, $CDCl_3$); [c] obtained by SEC analysis based on p(MMA) standards with $CHCl_3$ as the eluent.

For the synthesis of macroCTAs **5xii** and **5xiii**, RAFT polymerizations failed to reach full conversion after 4 hours despite the change in the R group structure for the revised Z group ABM-functionalized RAFT agent **5xi**. Therefore, the number of monomer equivalents with respect to RAFT agent concentration was increased for subsequent RAFT homopolymerizations of DMAc using **5xi**. ^{1}H NMR spectroscopy was used to monitor the conversion of DMAc throughout, with the RAFT polymerizations quenched

once the target degree of polymerization was reached to prevent further propagation. As discussed in Section 5.3.1, the main aim of this Chapter was to reproduce diblock copolymer nano-objects of spherical micelles, worm-like micelles and vesicles according to the relative phase spaces depicted in Figure 5.8.[60] Consequently, macroCTAs **5xiv** and **5xv** were synthesized with p(DMAc) chain lengths that closely matched the desired DPs of 40 to target vesicles and worms, and >68 to target spherical micelles.

Retention of both the ABM and trithiocarbonate functionalities was determined by SEC analysis. Importantly, excellent agreement between the molecular weight distributions obtained using an RI and UV detector (recorded at 309 nm and 400 nm) for p(DMAc) macroCTAs **5xii** and **5xiii** confirmed that both functional groups were appreciably retained (Figure 5.16). Moreover, p(DMAc) macroCTAs **5xii-5xv** synthesized using the revised Z group ABM-functionalized RAFT agent **5xi** exhibited lower dispersities ($Đ_M$ = 1.10-1.13) than their analogous counterparts, macroCTAs **5i-5iii** analyzed in Section 5.3.2 ($Đ_M$ = 1.21-1.22).

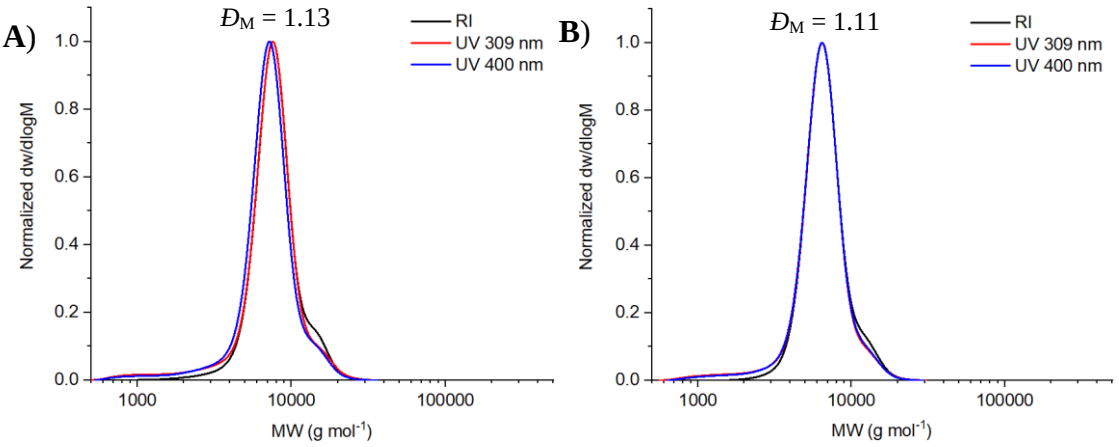

Figure 5.16: Molecular weight distributions determined by SEC ($CHCl_3$ as the eluent and calibrated against p(MMA) standards) using both an RI and UV (recorded at 309 and 400 nm) detector for the following ABM-functionalized p(DMAc)$_n$ homopolymers: a) **5xii**, and b) **5xiii**.

In Section 5.3.1, it was theorized that a relatively high azo initiator concentration coupled with an unsuitable R group choice led to poor control over the RAFT aqueous dispersion polymerization of DAAm, with the formation of highly disperse diblock copolymers during PISA. Subsequently, a revised Z group ABM-functionalized RAFT agent (**5xi**) has been designed, synthesized and utilized to produce fluorescent $p(DMAc)_n$ macroCTAs **5xii-5xv** with low dispersities, as described above. An and co-workers reported the successful formation of well-defined vesicles in a reasonable experimental timeframe using DAAm as the core-forming monomer, a $p(DMAc)_{35}$ stabilizer block, and V-50 as the water-soluble azo initiator.[55] Primarily, this study focused upon the change in both the vesicles' dimensions and size distribution with respect to the following variables; core-forming block length, number of equivalents of azo initiator used (0.02--0.05 eq), and reaction temperature (60 °C or 70 °C).[55]

As discussed previously, the Z group ABM-functionalized RAFT agent **5xi** was designed to closely match the chemical structure of the RAFT agent employed in this paper (Figure 5.15, RAFT agent **B**).[55] Therefore, subsequent chain extensions of $p(DMAc)_{44}$ macroCTA **5xiii** were conducted *via* RAFT aqueous dispersion polymerization of DAAm at 70 °C with V-50 as the water soluble azo initiator, to reflect the experimental conditions used in the paper (Scheme 5.5).[55]

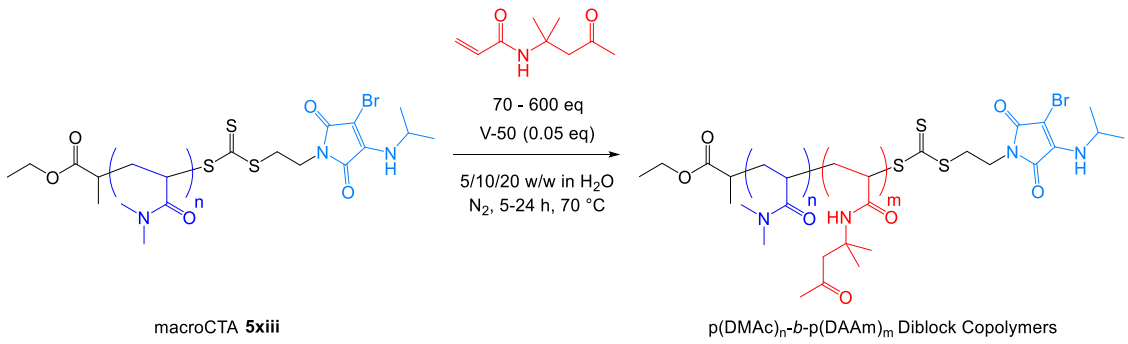

Scheme 5.5: RAFT aqueous dispersion polymerization of DAAm with ABM-functionalized water soluble p(DMAc)$_{44}$ macroCTA **5xiii** at various weight percentages to produce ABM-functionalized p(DMAc)$_{44}$-*b*-p(DAAm)$_m$ diblock copolymer nano-objects.

Initially, a series of RAFT aqueous dispersion polymerizations were conducted at various weight percentages with the target DP of the p(DAAm) core-forming block varied systematically in order to investigate the research aims discussed below. Firstly, to determine whether switching the R group of the Z group ABM-functionalized RAFT agent **2vi**, coupled with a change in azo initiator and respective concentration, facilitated the controlled RAFT aqueous dispersion polymerization of DAAm. Secondly, to ascertain whether the observed morphologies for specific diblock copolymer compositions directly matched their respective literature analogues for successful PISA formulations. Finally, to probe the limitations of this PISA system with regards to lowering the weight percentage of solids used to such a degree whereby fluorescence spectroscopy could be used to monitor the polymerization kinetics and self-assembly state of the growing block copolymer chains.

To this end, p(DMAc)$_{44}$ macroCTA **5xiii** was selected as the stabilizer block to reflect the respective p(DMAc) chain length used in the literature, p(DMAc)$_{35}$.[55] Due to the relatively short nature of the former stabilizer block, it was anticipated that higher order morphologies should be obtained for lower p(DAAm) DPs with respect to longer stabilizer blocks. Consequently, it was envisaged that resultant p(DMAc)$_{44}$-*b*-p(DAAm)$_m$ diblock copolymer nano-objects will have sufficiently small enough dimensions to

prevent an onset of turbidity for the respective polymerization solutions. However, it should be taken into consideration that the latter is also highly dependent upon the final concentration of self-assembled nanostructures. Therefore, a low weight percentage of solids combined with a short p(DMAc) stabilizer block could enable successful *in situ* steady-state fluorescence analysis without the inner filter effect or sample turbidity preventing accurate measurement.

A detailed summary of the experimental conditions, calculated monomer conversions, observed morphology, respective hydrodynamic diameters, and size distributions for all PISA formulations is provided in Table 5.5. Overall, three different weight percentages were investigated for this PISA system; 20 wt%, 10 wt% and 5 wt%.

For PISA formulations at 20 wt% (Table 5.5, entries 1-3), quantitative conversion was reached within 4 hours with the onset of turbidity observed after 60 minutes which was in good agreement with the polymerization kinetics recorded in the literature.[55] However, for PISA formulations at 5 or 10 wt% (Table 5.5, entries 4-11), extended reaction times were required to reach high conversion with no onset of turbidity observed within 6 hours. Surprisingly, for PISA formulations prepared at 5 wt%, turbid dispersions formed even though quantitative conversion was not reached within the experimental timeframe. Moreover, increasing the number of azo initiator equivalents from 0.05 to 0.10 for a 5 wt% PISA formulation did not result in a significant improvement in the measured monomer conversion (Table 5.5, entry 7). PISA formulations that reached >75% DAAm conversion (Table 5.5, entries 1-5 and 8-10) were purified by dialysis with half of the resultant dialyzate lyophilized for ^{1}H NMR spectroscopic and SEC analysis.

Entry	p(DAAm) Target DP	[DAAm] (wt%)	Time (h)	ρ[a] (%)	$M_{n,\,SEC}$[b] (kDa)	$Đ_M$[b]	D_h[c] (nm)	PD[c]	Morphology[d]
1	100	20	6	96	29.6	1.44[f]	190	0.26	Worms/Vesicles
2	200	20	5	97	78.8	1.49[f]	307	0.19	Vesicles
3	400	20	5	96	18.1	1.32	299	0.09	Vesicles
4	200	10	24	95	36.7	1.40	-	-	-
5	400	10	24	95	73.0	1.49	-	-	-
6	200	5	24	52	-	-	-	-	-
7[e]	200	5	24	60	-	-	-	-	-
8	400	5	24	87	18.0	1.62	120	0.05	Spheres
9	500	5	24	95	94.4	1.83	147	0.01	Spheres
10	600	5	24	77	94.7	1.71	133	0.02	Spheres

Table 5.5: Summary of RAFT aqueous dispersion polymerizations of DAAm with a $p(DMAc)_{44}$ macroCTA (**5xiii**) to produce ABM-functionalized $p(DMAc)_{44}$-*b*-$p(DAAm)_m$ diblock copolymer nano-objects at various weight percentages. Key: [a] monomer conversion was calculated by ^{1}H NMR spectroscopy of the crude polymerization mixture (300 MHz, $CDCl_3$); [b] obtained by SEC analysis based on p(MMA) standards with $CHCl_3$ as the eluent; [c] determined by DLS analysis; [d] determined by TEM imaging; [e] 0.1 equivalents of azo initiator V-50 was used instead of 0.05 equivalents; [f] obtained by SEC analysis based on p(MMA) standards with DMF as the eluent.

Importantly, improved control over the RAFT aqueous dispersion polymerization of DAAm to produce well-defined $p(DMAc)_{44}$-*b*-$p(DAAm)_m$ diblock copolymer nano-objects *via* PISA was confirmed upon SEC analysis. Previously, $p(DMAc)_n$-*b*-$p(DAAm)_m$ diblock copolymers **5iv-5viii** displayed high dispersity values ($Đ_M$ = 1.65-2.10) and asymmetrical molecular weight distributions with significant low molecular weight shoulders (Figure 5.14). In contrast, for $p(DMAc)_{44}$-*b*-$p(DAAm)_m$ diblock copolymers prepared at 10 wt% and 20 wt% using the revised Z group ABM-functionalized RAFT agent **5xi**, monomodal RI traces with relatively low dispersity values ($Đ_M$ = 1.32-1.49) were obtained (Figure 5.17 a, b and c). Whilst an

increase in dispersity was observed for diblock copolymer nano-objects prepared at 5 wt% ($Đ_M$ = 1.62-1.83), a clear increase in molecular weight for all analyzed diblock copolymers indicated that relatively efficient chain extension of the p(DMAc)$_{44}$ stabilizer block was achieved (Figure 5.17).

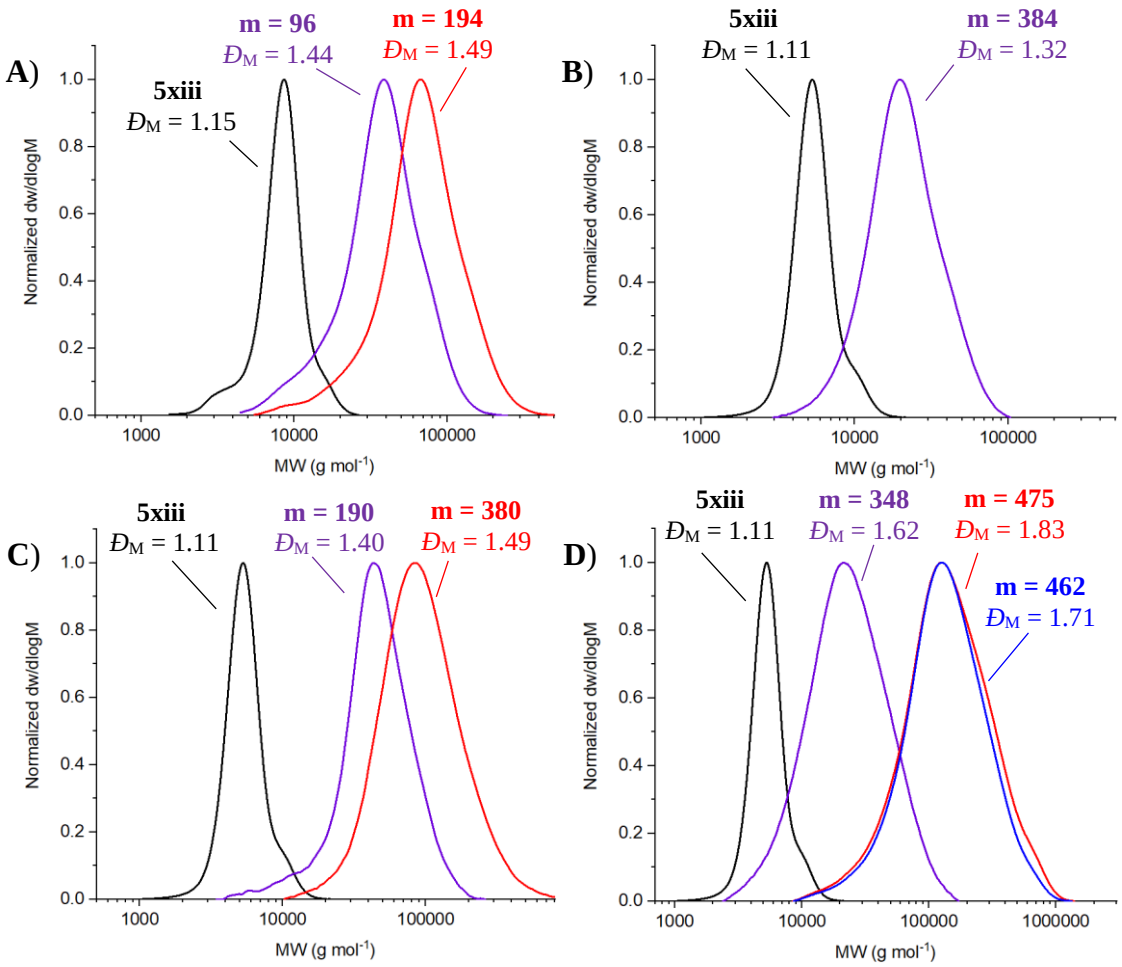

Figure 5.17: Molecular weight distributions determined by SEC using an RI detector for ABM-functionalized p(DMAc)$_{44}$-*b*-p(DAAm)$_m$ diblock copolymers (where m is denoted in each chromatogram) prepared at the following weight percentages: a) 20 wt%, b) 20 wt%, c) 10 wt%, and d) 5 wt%. DMF was the eluent for (a) whilst $CHCl_3$ was the eluent for (b), (c) and (d). SEC data was calibrated against p(MMA) standards in all cases. RI trace for p(DMAc)$_{44}$ macroCTA **5xiii** is shown for comparison.

Critically, the obtained SEC results compared favorably to the literature.[55,60] For instance, for a series of p(DMAc)$_{77}$-*b*-p(DAAm)$_m$ diblock copolymers prepared at 20 wt% by

Armes and co-workers using RAFT agent **A** (Figure 5.15), the measured dispersity values ($Đ_M$ = 1.35-1.57) were in good agreement with those obtained herein.[60] Ultimately, the marked improvement in polymerization control could be principally attributed to the change in the R group for the Z group ABM-functionalized RAFT agent **5xi** from benzyl to ethyl propionate.

Following SEC analysis, dialyzed PISA formulations prepared at 5 wt% and 20 wt% were diluted to a suitable concentration to be further analyzed *via* TEM imaging and DLS measurements. Observed morphologies from TEM micrographs were compared to literature predictions for various p(DMAc)$_n$-*b*-p(DAAm)$_m$ diblock copolymer compositions to determine the effect of the ABM fluorophore upon the PISA process. Representative TEM images for each fluorescent p(DMAc)$_{44}$-*b*-p(DAAm)$_m$ diblock copolymer composition (Table 5.5, entries 1-3 and 8-10) are shown in Figure 5.18, with corresponding intensity-weighted DLS size distributions displayed in Figure 5.19.

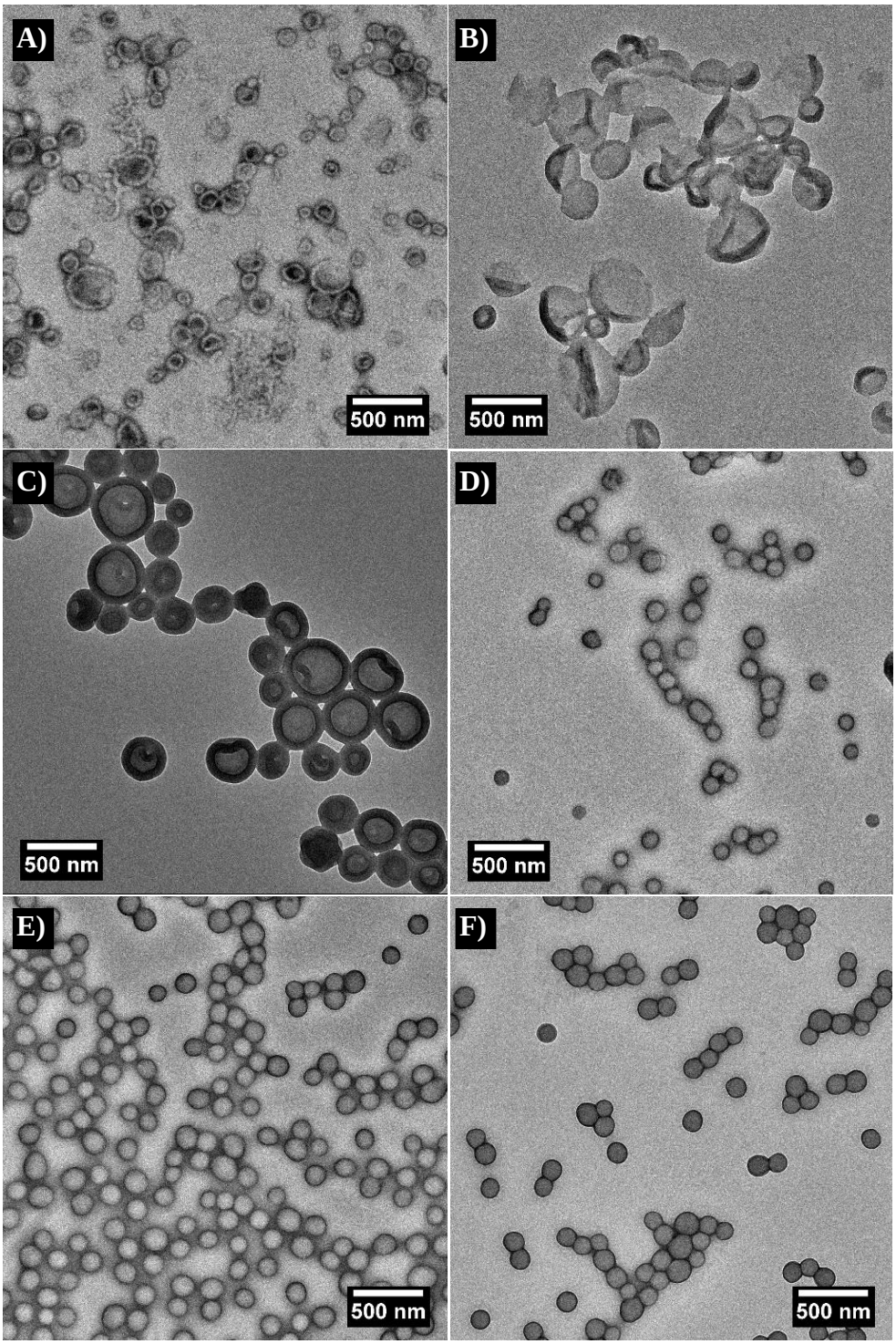

Figure 5.18: Dry-state stained TEM images and observed morphologies for the following $p(DMAc)_{44}$-*b*-$p(DAAm)_m$ compositions: a) worms/vesicles (20 wt%, m = 96); b) vesicles (20 wt%, m = 194); c) vesicles (20 wt%, m = 384); d) spheres (5 wt%, m = 348); e) spheres (5 wt%, m = 475); f) spheres (5 wt%, m = 462). Formvar-coated copper grids were stained using a 1 wt% uranyl acetate (UA) solution.

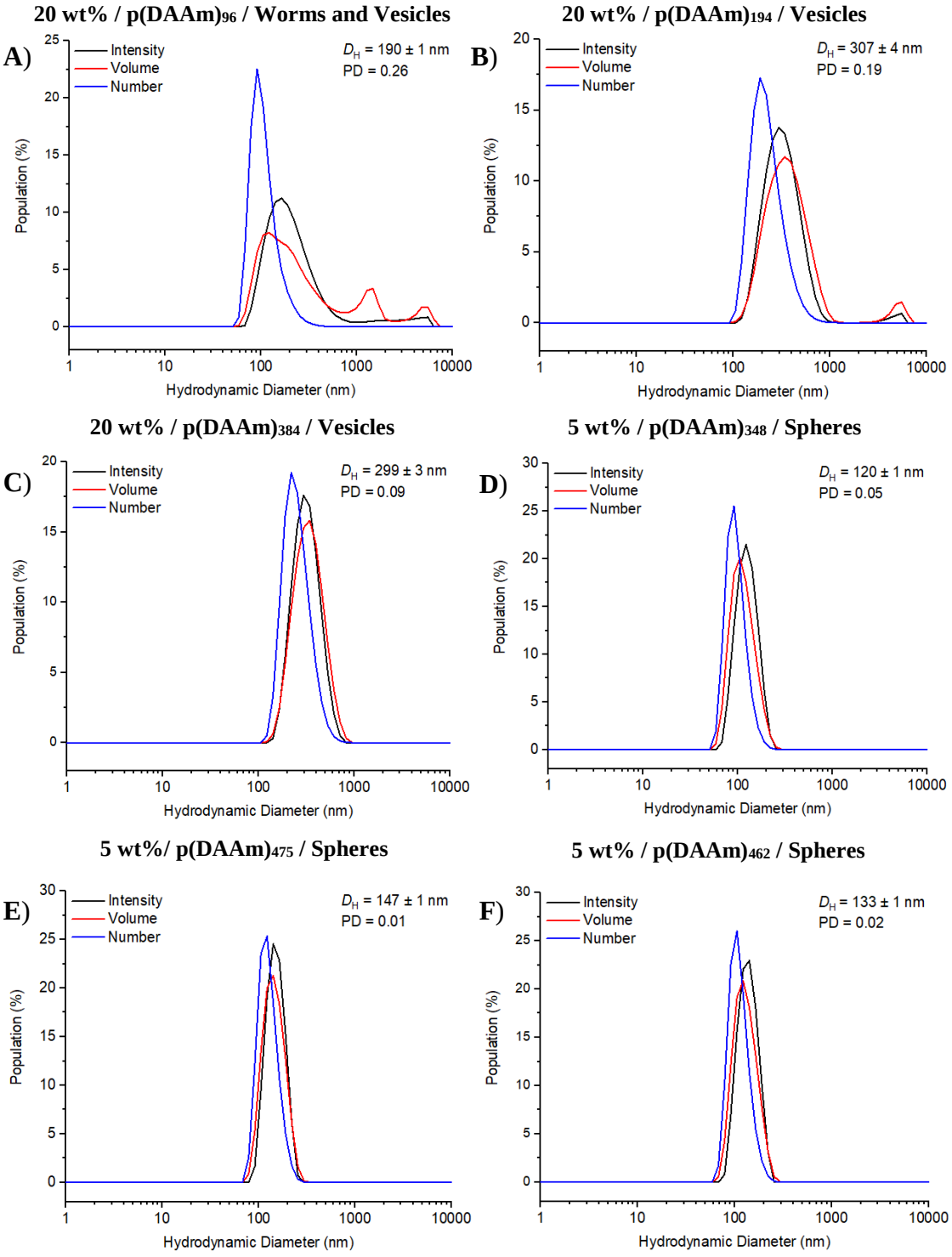

Figure 5.19: Intensity-weighted size distributions by DLS for the following p(DMAc)$_{44}$-*b*-p(DAAm)$_m$ compositions: a) 20 wt%, m = 96; b) 20 wt%, m = 194; c) 20 wt%, m = 384; d) 5 wt%, m = 348; e) 5 wt%, m = 475; f) 5 wt%, m = 462. Morphology obtained from TEM imaging is stated above for reference.

Crucially, the introduction of an ABM fluorophore using the Z group ABM-functionalized RAFT agent **5xi** did not affect the final morphology obtained post-PISA, as confirmed *via* TEM imaging and DLS analysis. For instance, p(DMAc)$_{44}$-*b*-p(DAAm)$_{96}$ and p(DMAc)$_{44}$-*b*-p(DAAm)$_{194}$ diblock copolymer compositions directly matched their respective predicted morphologies based upon the constructed phase diagram at 20 wt% for the same PISA system (Figure 5.8).[60] Furthermore, increasing p(DAAm) DP from 194 to 384 for 20 wt% PISA formulations resulted in no significant change in hydrodynamic diameter (307 nm and 299 nm respectively), with an increase in membrane thickness for unilamellar vesicles observed instead (Figure 5.18 b and c respectively). This phenomenon has been previously observed for PISA-derived vesicles whereby membrane thickness has been shown to be directly dependent upon core-forming block length above a critical DP.[71] For 5 wt% formulations, highly monodisperse spherical micelles (PD = 0.01-0.05) were formed for all three p(DMAc)$_{44}$-*b*-p(DAAm)$_{m}$ diblock copolymer compositions (Figure 5.18 d, e and f), with a linear increase in hydrodynamic size with respect to increasing core-forming block length observed.

Finally, the limitations of this thermally-initiated PISA system was explored. Further experimental studies revealed that below 5 wt%, PISA formulations did not reach quantitative conversion within the experimental timeframe, regardless of the target core-forming block length. Moreover, PISA formulations prepared at 5 wt% with a target p(DAAm) DP lower than 200 failed to reach high conversion, with no evidence of any self-assembled polymer nanostructures upon DLS analysis. Without an onset of micellization, the corresponding marked increase in polymerization kinetics did not occur which ultimately prevented RAFT aqueous dispersion polymerizations from reaching completion. Therefore, no combination of experimental conditions was found whereby the onset of turbidity for the resultant polymerization mixture was precluded to allow for

in situ steady-state fluorescence analysis. Consequently, it was proposed that a significantly shorter stabilizer block (DP = 10–25) would be required to overcome the difficulties encountered herein.

5.3.3. Pure block copolymer morphologies *via* fluorescent PISA

As outlined in Section 5.3.1, the principle aim for this Chapter was to target pure phases of the following block copolymer morphologies – spherical micelles, cylindrical or worm-like micelles, and vesicles. To this end, p(DMAc)$_{42}$ and p(DMAc)$_{77}$ stabilizer blocks (macroCTA **5xiv** and **5xv** respectively) were successfully synthesized using the Z group ABM-functionalized RAFT agent **5xi**, with retention of the ABM moiety confirmed *via* SEC analysis (see Section 5.3.2). It was envisaged that the longer p(DMAc)$_{77}$ stabilizer block would allow a pure phase of spherical micelles to be successfully targeted, whilst the shorter p(DMAc)$_{42}$ stabilizer block would enable access to pure phases of both vesicles and worms. Consequently, it was anticipated that a difference in fluorescence lifetime with respect to block copolymer morphology would be observed upon time-resolved fluorescence spectroscopy. Moreover, by measuring the steady-state fluorescence emission and the corresponding fluorescence quantum yield for each block copolymer morphology, it was proposed that any change regarding the hydrated state of the ABM fluorophore would be observed.

According to the phase diagram constructed at 20 wt% for this all acrylamide PISA system (Figure 5.8), the phase boundary for a pure phase of worms was extremely narrow with only one successful block copolymer composition found; p(DMAc)$_{40}$-*b*-p(DAAm)$_{99}$. Note, that in this paper end group analysis for all five p(DMAc) macroCTAs produced *via* RAFT polymerization was conducted using UV spectroscopy instead of ^{1}H NMR spectroscopy.[60] Whilst end group analysis using a calibration curve for the UV

absorption of the trithiocarbonate end group is a viable technique, evaluation of the experimental protocol utilized by Armes and co-workers for the RAFT homopolymerization of DMAc revealed potentially significant inaccuracies between the calculated and theoretical molecular weights.[60] For instance, the ratio of monomer concentration with respect to RAFT agent concentration was [60]:[1] for the synthesis of a $p(DMAc)_{68}$ stabilizer block, with 89% monomer conversion achieved as determined by ^{1}H NMR spectroscopic analysis.[60] Therefore, upon purification the expected average degree of polymerization for this respective p(DMAc) macroCTA would be 53, which is significantly different to the calculated value of 68, this in turn is greater than the number of DMAc equivalents originally used.[60] Considering that the isolated p(DMAc) macroCTA possessed a low dispersity ($Đ_M$ = 1.12) and efficient chain extension was achieved by the authors,[60] it was unlikely that the initial RAFT homopolymerization was uncontrolled. In light of this, possible discrepancies regarding the DP of the p(DMAc) stabilizer block for the phase diagram constructed in this paper (Figure 5.8) should be considered with respect to directly reproducing specific diblock copolymer compositions and corresponding morphologies.[60]

Using the experimental conditions employed in the previous section, a series of RAFT aqueous dispersion polymerizations of DAAm were conducted at 20 wt% in an attempt to target pure block copolymer morphologies (Scheme 5.6). Fluorescent ABM-functionalized water soluble $p(DMAc)_n$ macroCTAs **5xiv** and **5xv** were utilized, with a complete summary of the experimental and analytical data obtained for PISA formulations provided in Table 5.6.

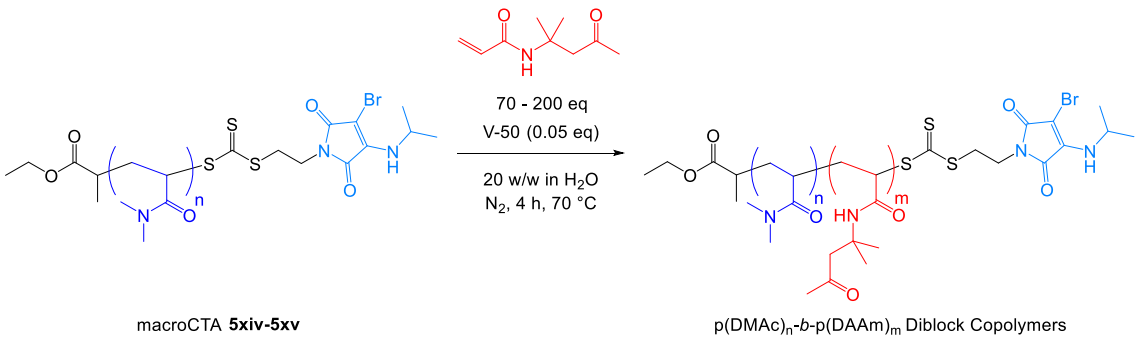

Scheme 5.6: RAFT aqueous dispersion polymerization of DAAm with ABM-functionalized water soluble p(DMAc) macroCTAs **5xiv-5xv** at 20 wt% to produce ABM-functionalized $p(DMAc)_n$-*b*-$p(DAAm)_m$ diblock copolymer nano-objects.

Initially, five different block copolymer compositions were selected using the shorter $p(DMAc)_{42}$ stabilizer block in an attempt to obtain a pure phase of worms. Target p(DAAm) DP was varied systematically between 90 and 110 (Table 5.6, entries 1-5) with the formation of a viscous gel observed after 4 hours, thereby providing a qualitative indication of worm formation. Upon purification *via* dialysis, dry state stained TEM imaging of the diluted samples confirmed that a mixed phase of worms and vesicles was obtained in all cases. Interestingly, it appeared that the relative population of vesicles with respect to worms for each mixed phase lowered with respect to decreasing core-forming block length. Consequently, by methodically reducing the target p(DAAm) DP for subsequent PISA formulations (Table 5.6, entries 6-9), a critical $p(DMAc)_{42}$-*b*-$p(DAAm)_m$ diblock copolymer composition was discovered for which a pure phase of worms was obtained which had a respective p(DAAm) core-forming block length of 73 (Table 5.6, entry 7).

Entry	p(DMAc) DP	p(DAAm) Target DP	ρ^{a} (%)	p(DAAm) DP^{b}	D_h^{d} (nm)	Morphology[e]
1	42	90	91	82	-	Worms/Vesicles
2	42	95	91	87	-	Worms/Vesicles
3	42	100	92	92	-	Worms/Vesicles
4	42	105	92	97	-	Worms/Vesicles
5	42	110	92	101	-	Worms/Vesicles
6	42	85	91	77	178	Worms/Vesicles
7	42	80	91	73	191	Worms
8	42	75	91	68	130	Worms/Vesicles
9	42	70	91	64	94	Worms/Vesicles
10	42	150	92	138	217	Vesicles
11	42	200	85	170	226	Vesicles
12	77	160	91	146	50	Spheres

Table 5.6: Summary of RAFT aqueous dispersion polymerizations of DAAm with an ABM-functionalized p(DMAc)$_n$ macroCTA (**5xiv-5xv**) to produce ABM-functionalized p(DMAc)$_n$-*b*-p(DAAm)$_m$ diblock copolymer nano-objects at 20 wt%. Key: [a] monomer conversion was calculated by ^{1}H NMR spectroscopy (300 MHz, $CDCl_3$); [b] determined by end group analysis using ^{1}H NMR spectroscopy (400 MHz, $CDCl_3$); [d] determined by DLS analysis; [e] determined by TEM imaging.

Moreover, upon increasing the number of DAAm equivalents whilst keeping the same stabilizer block length, a pure phase of vesicles was achieved (Table 5.6, entries 10-11). Finally, a pure phase of spherical micelles was produced when a longer p(DMAc)$_{77}$ stabilizer block was used (Table 5.6, entry 12). Interestingly, the latter two morphologies directly matched the respective phase spaces predicted from the literature (Figure 5.8). Representative TEM images for pure block copolymer phases of fluorescent p(DMAc)$_n$-*b*-p(DAAm)$_m$ diblock copolymers are shown in Figure 5.20 with corresponding intensity-weighted DLS size distributions displayed in Figure 5.21. Note, that a mixed

phase of worms and vesicles is shown for comparison purposes (Figure 5.20**Figure 5.19** a and Figure 5.21 a, Table 5.6, entry 6).

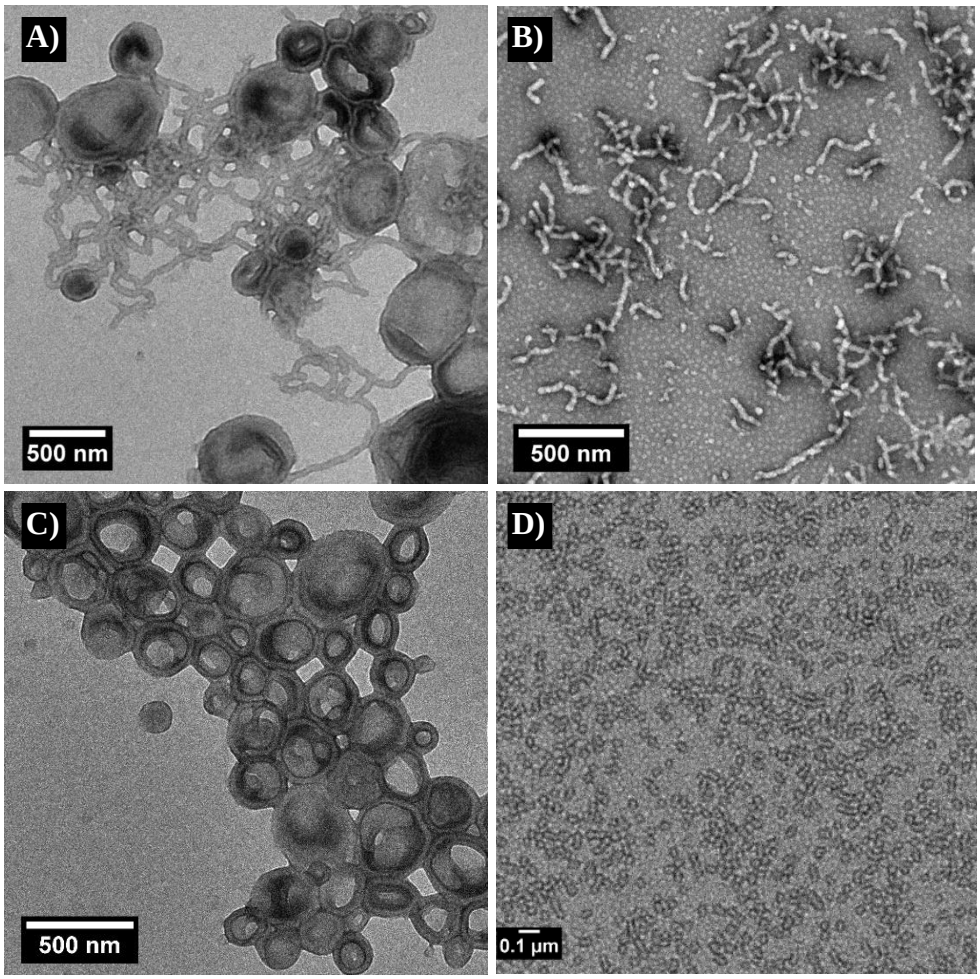

Figure 5.20: Dry-state stained TEM images and observed morphologies for the following p(DMAc)$_n$-*b*-p(DAAm)$_m$ diblock copolymer compositions: a) worms/vesicles (n = 42, m = 77); b) worms (n = 42, m = 73); c) vesicles (n = 42, m = 138); d) spheres (n= 77, m = 146). Formvar-coated copper grids were stained using a 1 wt% uranyl acetate (UA) solution.

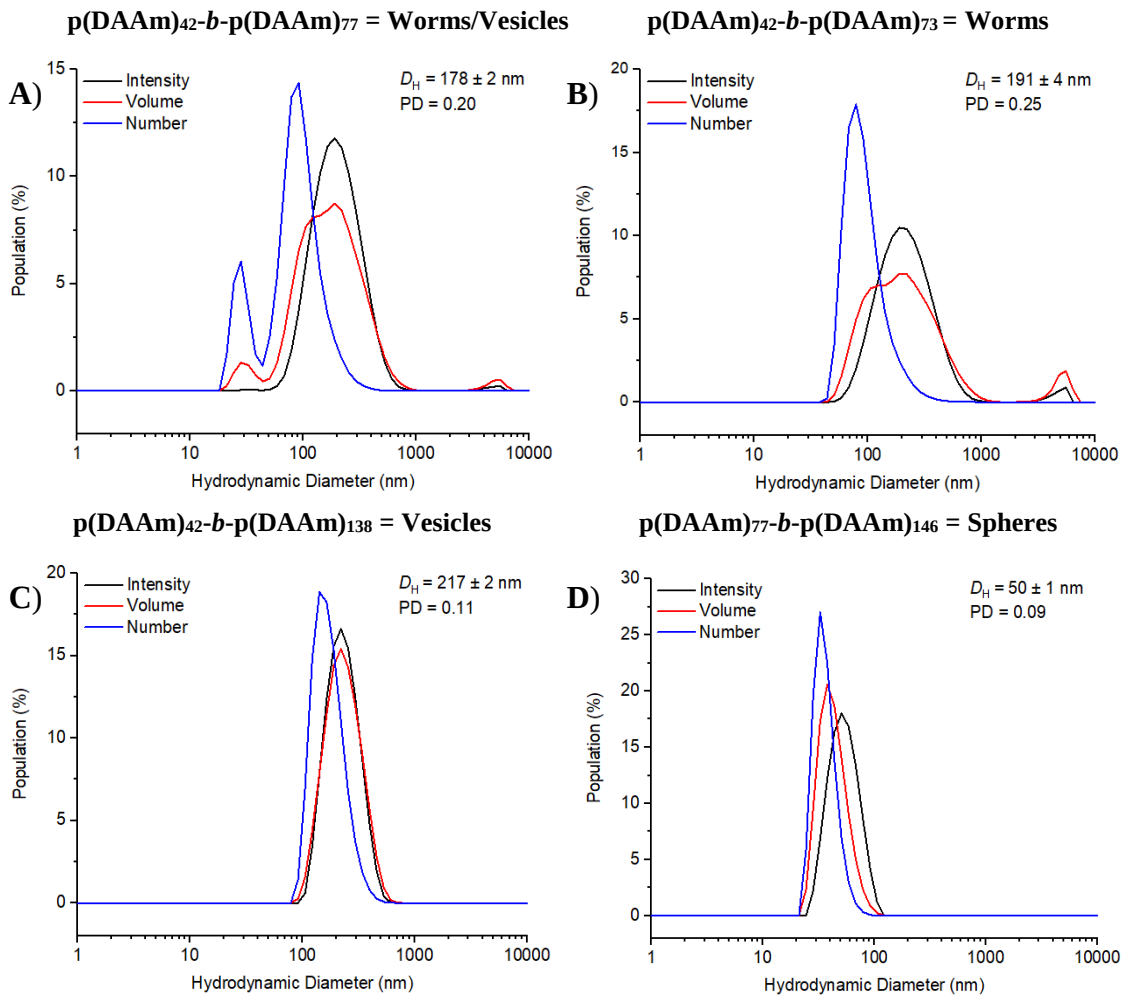

Figure 5.21: Intensity-weighted size distributions by DLS for the following $p(DMAc)_n$-*b*-$p(DAAm)_m$ diblock copolymer compositions prepared at 20 wt%: a) n = 42, m = 77; b) n = 42, m = 73; c) n = 42, m = 138; d) n= 77, m = 146. Morphology obtained from TEM imaging is stated above for reference.

Unfortunately, at the time of measurement both the $CHCl_3$ and DMF GPC systems were down for maintenance and thus SEC analysis of the lyophilized $p(DMAc)_n$-*b*-$p(DAAm)_m$ diblock copolymers (Table 5.6) could not be carried out. Furthermore, due to unforeseen circumstances purified PISA formulations could not be analyzed for 6 months, at which point hydrolysis of the trithiocarbonate end group and/or amide bonds of the polymer backbone resulted in significant changes in the observed morphology upon reimaging. Consequently, the fluorescence lifetime, steady-state fluorescence emission, and fluorescence quantum yield of the ABM fluorophore with respect to each block

copolymer morphology – spherical micelles, worm-like micelles and vesicles – could not be measured for the PISA formulations synthesized herein.

5.4. Conclusions

In this Chapter, the successful synthesis of fluorescent p(DMAc)$_n$-*b*-p(DAAm)$_m$ diblock copolymer nano-objects with well-defined molecular weights and relatively low dispersities utilizing a Z group ABM-functionalized RAFT agent was demonstrated. The importance of the chosen R group of the Z group ABM-functionalized RAFT agent was highlighted, with improved control over the RAFT-mediated PISA achieved with **5xi** with respect to **2vi**. Furthermore, the observed morphologies for fluorescent diblock copolymers formed *via* RAFT-mediated PISA closely matched literature predictions as confirmed *via* a combination of TEM imaging and DLS analysis. Importantly, the introduction of an ABM fluorophore appeared to not significantly impact the PISA methodology with pure phases of spherical micelles, worm-like micelles, and vesicles obtained upon systematic manipulation of the p(DAAm) core-forming block length. Unfortunately, the anticipated differences in the fluorescence lifetime and quantum yield of the ABM fluorophore with respect to each block copolymer morphology could not be determined thus far *via* time-resolved fluorescence spectroscopy. Overall, these findings highlight that the production of fluorescently-labeled polymeric nanostructures *via* RAFT-mediated PISA could be achieved without post-polymerization modification through the simple use of an ABM-functionalized RAFT agent.

5.5. Experimental Section

5.5.1. Methods and materials

Materials. The following reagents were used as received: triphenylphosphine (Sigma-Aldrich, 99%); diisopropyl azodicarboxylate (DIAD, Alfa Aesar, 94%); neopentyl alcohol (Acros Organics, 99%); 2,3-dibromomaleimide (Sigma-Aldrich, 97%); isopropylamine (Sigma-Aldrich, 99.5%); 2-mercaptoethanol (Sigma-Aldrich, 99%), carbon disulfide (Sigma-Aldrich, 99%); ethyl 2-bromopropionate (Sigma-Aldrich, 99%); potassium phosphate tribasic (Sigma-Aldrich, 98%); *N*,*N*-dimethylacrylamide (DMAc, Sigma-Aldrich, 99%); diacetone diacrylamide (DAAm, Sigma-Aldrich, 99%); 2,2'-azobis(2-methylpropionamidine) dihydrochloride (V-50, Acros Organics, 98%); 2,2'-azobis(2-(2-imidazolin-2-yl)propane dihydrochloride (VA-044, Wako, 98%); 4,4′-azobis(4-cyanovaleric acid) (ACVA, Sigma-Aldrich, 98%). 2,2'-azobisisobutyronitrile (AIBN) was received from Sigma-Aldrich (98%), recrystallized from methanol and stored in the dark at 4 °C. Solvents, including high-performance liquid chromatography (HPLC) grade solvents, were purchased from Fisher Scientific and used as received. *N*,*N*-dimethylacrylamide and 1,4-dioxane were filtered through a plug of basic alumina prior to use and stored at 4 °C. Tetrahydrofuran (THF) was purchased from Fisher Scientific and dried using an Innovative Technology Inc. Pure Solv MD-4-EN solvent purification system. Deuterated solvents and silica gel (40-63 μm) were used as received from Apollo Scientific.

^{1}H and ^{13}C NMR spectroscopy. ^{1}H NMR spectroscopy was performed at 300 MHz on a Bruker Avance AV-300 spectrometer or a Bruker Avance III HD-300 spectrometer, or at 400 MHz on a Bruker Avance III HD-400 spectrometer. ^{13}C NMR spectroscopy was performed at 100 MHz on a Bruker Avance III HD-400 spectrometer. ^{1}H and ^{13}C NMR

spectra were measured in deuterated chloroform or methanol. Chemical shifts are reported as δ in parts per million (ppm) and are stated relative to the residual solvent peaks at 7.26 ppm or 77.0 ppm for chloroform, and 3.31 ppm and 49.05 ppm for acetone Coupling constants (J) correspond to $^{3}J_{\text{H-H}}$ unless otherwise stated. All spectra were obtained at 25 °C.

Size Exclusion Chromatography. SEC analysis was primarily performed on a Varian PL-GPC 50 system with a set of two PLgel Mixed-C columns plus one guard column and fitted with a viscometer, an RI light scattering detector and a UV detector measuring at 309 nm or 400 nm. SEC measurements were performed with HPLC-grade dimethylformamide (DMF) with 5 mM NH_4BF_4 at 50 °C at a flow rate of 1 mL min^{-1}. The molecular weights of the synthesized polymers were calculated relative to poly(methyl methacrylate) (p(MMA)) standards and analyzed using Cirrus v3.3 software. Additional SEC analysis was performed on a Varian PL-GPC 50 system with a set of two PLgel Mixed-C columns plus one guard column and fitted with a RI and UV detector measuring at 309 nm or 400 nm. SEC measurements were performed with HPLC-grade chloroform with 0.5% triethylamine at 40 °C at a flow rate of 1 mL min^{-1}. The molecular weights of the synthesized polymers were calculated relative to poly(styrene) (p(St)) or p(MMA) standards and analyzed using Cirrus v3.3 software.

Mass Spectrometry. High resolution electrospray ionization time of flight mass spectrometry (HRMS (ESI-ToF)) was performed on a Bruker UHR-Q-TOF MaXis spectrometer by Dr. Lijang Song, University of Warwick.

Dynamic Light Scattering (DLS). DLS analysis of the PISA samples was conducted using a Malvern Zetasizer Nano S instrument equipped with a 4 mW He-Ne 633 nm laser module at 25 °C and at a detection angle of 173°. Purified samples were diluted with 18.2 MΩ cm water, with the diluted samples not filtered prior to analysis to ensure larger

nanostructures remained in solution. Average z-average hydrodynamic diameters (D_H) were calculated from 5 repeat measurements using Malvern DTS 6.20 software.

Transmission Electron Microscopy (TEM). Dry state stained TEM analysis was performed on a JEOL 2200 FX microscope operating at 200 kV. Purified samples were diluted with 18.2 MΩ cm water then deposited onto formvar-coated copper grids. After roughly 1 min, excess sample was blotted from the grid and the grid stained with an aqueous 1 wt% uranyl acetate (UA) solution for 1 min prior to blotting, drying and microscopic analysis. TEM images were collected alongside Mr. Spyridon Varlas (O'Reilly Group, University of Birmingham).

5.5.2. Synthetic protocols

*Synthesis of ethyl 2-((((2-hydroxyethyl)thio)carbonothioyl)thio)propanoate (**5ix**).*

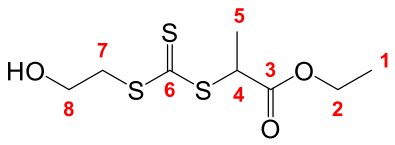

2-mercaptoethanol (5.00 mL, 71.4 mmol) was added to a stirred suspension of K_3PO_4 (15.1 g, 71.4 mmol) in acetone (125 mL) and stirred for 10 min. Carbon disulfide (6.34 mL, 107 mmol) was added and the solution turned bright yellow. After stirring for 10 min, ethyl 2-bromopropionate (10.5 mL, 71.4 mmol) was added and an instant precipitation of KBr was noted. After stirring for 10 min, the suspension was filtered and the precipitate washed with acetone. After removal of acetone *in vacuo*, purification of the crude mixture was carried out using column chromatography (silica gel, 1:1 pet. ether/ethyl acetate) affording ethyl 2-((((2-hydroxyethyl)thio)carbonothioyl)thio) propanoate (**5ix**) as an orange red oil (9.93 g, 39.0 mmol, 55%). ^{1}H NMR (400 MHz, $CDCl_3$) δ_H/ppm: 4.78 (1H, q, J = 7.2 Hz, H4), 4.19 (2H, q, J = 7.2 Hz, H2), 3.87 (2H, t, J = 6.4 Hz, H8), 3.59 (2H, t, J = 6.4 Hz, H7), 1.59 (3H, d, J = 7.2 Hz, H5), 1.27 (3H, t, J = 7.2 Hz, H1); ^{13}C NMR (100 MHz, $CDCl_3$) δ_C/ppm: 221.9 (C6), 170.9 (C3), 61.9 (C2), 60.3 (C8), 48.4 (C4), 39.3 (C7), 16.8 (C5), 14.0 (C1).

*Synthesis of ethyl 2-((((2-(3,4-dibromo-2,5-dioxo-2,5-dihydro-1H-pyrrol-1-yl)ethyl)thio) carbonothioyl)thio)propanoate (**5x**).*

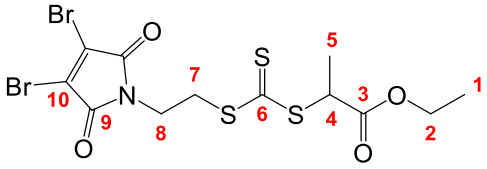

To a flame-dried round bottom flask, triphenylphosphine (10.2 g, 39.0 mmol) was added followed by the addition of dry THF (200 mL) and the resulting solution cooled to -78 °C. Diisopropyl azodicarboxylate (DIAD) (7.69 mL, 39.0 mmol) was added dropwise over 2-3 min. The reaction mixture was stirred for 5 min after which ethyl 2-((((2-hydroxyethyl)thio)carbonothioyl)thio) propanoate (**5ix**) (9.93 g, 39.0 mmol) dissolved in dry THF (50 mL) was added using air sensitive techniques and the resultant mixture stirred for 5 min. Neopentyl alcohol (1.72 g, 19.5 mmol) was added and the reaction mixture was left to stir for 10 min. 2,3-Dibromomaleimide (9.95 g, 39.0 mmol) was then added to the reaction mixture. The resulting suspension was allowed to remain at -78 °C for 10 min before the cooling bath was removed and the reaction was stirred overnight at ambient temperature under a nitrogen atmosphere. After removal of THF *in vacuo*, purification of the crude mixture was carried out using column chromatography (silica gel, 2:1 CH_2Cl_2/pet. ether followed by 1:1 CH_2Cl_2/ethyl acetate) affording ethyl 2-((((2-(3,4-dibromo-2,5-dioxo-2,5-dihydro-1H-pyrrol-1-yl)ethyl)thio)carbonothioyl)thio) propanoate (**5x**) as an orange red oil (7.19 g, 14.6 mmol, 38%). ^{1}H NMR (400 MHz, $CDCl_3$) δ_H/ppm: 4.76 (1H, q, J = 7.2 Hz, H4), 4.18 (2H, q, J = 7.2 Hz, H2), 3.93 (2H, t, J = 6.8 Hz, H8), 3.61 (2H, t, J = 6.8 Hz, H7), 1.59 (3H, d, J = 7.2 Hz, H5), 1.26 (3H, t, J = 7.2 Hz, H1); ^{13}C NMR (100 MHz, $CDCl_3$) δ_C/ppm: 220.4 (C6), 170.7 (C3), 163.4 (C9), 129.5 (C10), 61.9 (C2), 48.5 (C4), 37.6 (C7), 34.1 (C8), 16.8 (C5), 14.0 (C1); HRMS

(ESI-TOF) *m/z*: $[M + Na]^+$ calculated for $C_{12}H_{13}Br_2NNaO_4S_3$: 511.8271; found: 511.8268.

*Synthesis of ethyl 2-((((2-(3-bromo-4-(isopropylamino)-2,5-dioxo-2,5-dihydro-1H-pyrrol-1-yl)ethyl)thio)carbonothioyl)thio)propanoate (**5xi**).*

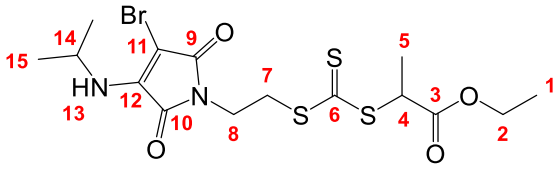

To a suspension of ethyl 2-((((2-(3,4-dibromo-2,5-dioxo-2,5-dihydro-1H-pyrrol-1-yl)ethyl)thio)carbonothioyl)thio)propanoate (**5x**) (7.19 g, 14.6 mmol) and Na_2CO_3 (1.71 g, 16.1 mmol) in THF (HPLC-grade, 125 mL), isopropylamine (1.38 mL, 16.1 mmol) was added. The reaction mixture was stirred at ambient temperature with the conversion of **5x** monitored by TLC. After 1 h, THF was removed *in vacuo* and the organic residue dissolved in dichloromethane (DCM) (50 mL) and washed with deionized water (3 × 50 mL). The organic layer was dried over $MgSO_4$, filtered and evaporated to dryness. Purification was carried out using column chromatography (silica gel, 3:1 DCM/pet. ether followed by 1:1 DCM/ethyl acetate) affording ethyl 2-((((2-(3-bromo-4-(isopropylamino)-2,5-dioxo-2,5-dihydro-1H-pyrrol-1-yl)ethyl)thio)carbonothioyl)thio) propanoate (**5xi**) as an orange red oil (3.98 g, 8.47 mmol, 60%). ^{1}H NMR (400 MHz, $CDCl_3$) δ_H/ppm: 5.29 (1H, br d, *J* = 8.4 Hz, H13), 4.78 (1H, q, *J* = 7.2 Hz, H4), 4.40 (1H, d of sept., *J* = 6.4 Hz and 8.4 Hz, H14), 4.19 (2H, q, *J* = 7.2 Hz, H2), 3.83 (2H, t, *J* = 6.8 Hz, H8), 3.59 (2H, t, *J* = 6.8 Hz, H7), 1.60 (3H, d, *J* = 7.2 Hz, H5), 1.29 (6H, d, *J* = 6.4 Hz, H15), 1.27 (3H, t, *J* = 7.2 Hz, H1); ^{13}C NMR (100 MHz, $CDCl_3$) δ_C/ppm: 220.6 (C6), 170.8 (C3), 167.3 (C9), 165.7 (C10), 146.9 (C12), 61.9 (C2), 48.4 (C4), 44.8 (C14),

36.5 (C7), 34.7 (C8), 23.7 (C15), 16.9 (C5), 14.1 (C1); HRMS (ESI-TOF) *m*/*z*: $[M + Na]^+$ calculated for $C_{15}H_{21}BrN_2NaO_4S_3$: 490.9745; found: 490.9749.

*General procedure for the RAFT homopolymerization of N,N-dimethylacrylamide (DMAc) with **2vi** and **5xi***

2vi or **5xi** (1 eq), AIBN (0.1 eq) and *N*,*N*-dimethylacrylamide (DMAc) (35 - 90 eq) were dissolved in 1,4-dioxane (1:1 monomer volume/1,4-dioxane volume) and added to a dry ampoule containing a stirrer bar. The resulting solution was degassed using at least three freeze-pump-thaw cycles, back-filled with nitrogen, sealed and placed in a pre-heated oil bath at 70 °C. After 6 h, the polymerization was quenched by opening the reaction mixture to air and submerging the ampoule in liquid nitrogen. Purification was achieved *via* precipitation into diethyl ether three times before being redissolved in the minimum amount of 18.2 MΩ cm water. Subsequent lyophilization yielded a fluorescent orange yellow polymer powder. The degree of polymerization was determined by ^{1}H NMR spectroscopy by assessing the conversion of the monomer vinyl peaks at 6.59 ppm, 6.31 ppm and 5.68 ppm to the polymeric peaks between 2.20-3.20 ppm.

General procedure for thermally initiated aqueous PISA of p(DMAc)$_n$-b-p(DAAm)$_m$ diblock copolymers

A typical experiment, to achieve p(DMAc)$_{42}$-*b*-p(DAAm)$_{100}$ at 20 wt% DAAm, was as follows. p(DMAC)$_{42}$ macroCTA (30 mg, 6.43 μmol), DAAm (109 mg, 64.3 μmol) and V-50 (87 μg, 0.322 μmol) were dissolved in 18.2 MΩ cm water (555 μL) in a sealed 7 mL scintillation vial with a magnetic stirrer bar. The mixture was degassed by sparging with N_2 for 30 min. The sealed vial was heated to 70 °C with magnetic stirring for 4 h to ensure

high monomer conversion. After this time, the vial was opened to air and allowed to cool to room temperature before conversion ^{1}H NMR spectroscopic analysis. ^{1}H NMR spectroscopic and SEC analyses of the purified diblock copolymer were obtained after lyophilization of an aliquot of the post-polymerization solution. TEM and DLS analysis were performed on samples after dilution to an appropriate analysis concentration.

5.6. References

1 N. J. Warren and S. P. Armes, *J. Am. Chem. Soc.*, 2014, **136**, 10174–10185.
2 B. Charleux, G. Delaittre, J. Rieger and F. D'Agosto, *Macromolecules*, 2012, **45**, 6753–6765.
3 J.-T. Sun, C.-Y. Hong and C.-Y. Pan, *Polym. Chem.*, 2013, **4**, 873–881.
4 A. Blanazs, J. Madsen, G. Battaglia, A. J. Ryan and S. P. Armes, *J. Am. Chem. Soc.*, 2011, **133**, 16581–16587.
5 Y. Mai and A. Eisenberg, *Chem. Soc. Rev.*, 2012, **41**, 5969–5985.
6 S. L. Canning, G. N. Smith and S. P. Armes, *Macromolecules*, 2016, **49**, 1985–2001.
7 I. Canton, N. J. Warren, A. Chahal, K. Amps, A. Wood, R. Weightman, E. Wang, H. Moore and S. P. Armes, *ACS Cent. Sci.*, 2016, **2**, 65–74.
8 D. E. Mitchell, J. R. Lovett, S. P. Armes and M. I. Gibson, *Angew. Chem. Int. Ed. Engl.*, 2016, **55**, 2801–2804.
9 V. Ladmiral, M. Semsarilar, I. Canton and S. P. Armes, *J. Am. Chem. Soc.*, 2013, **135**, 13574–13581.
10 G. Liu, Q. Qiu, W. Shen and Z. An, *Macromolecules*, 2011, **44**, 5237–5245.
11 Y. Pei, A. B. Lowe and P. J. Roth, *Macromol. Rapid Commun.*, 2016, **38**, 1600528.
12 M. J. Derry, L. A. Fielding and S. P. Armes, *Prog. Polym. Sci.*, 2016, **52**, 1–18.
13 J. Yeow and C. Boyer, *Adv. Sci.*, 2017, **4**, 1700137.
14 M. Obeng, A. H. Milani, M. S. Musa, Z. Cui, L. A. Fielding, L. Farrand, M. Goulding and B. R. Saunders, *Soft Matter*, 2017, **13**, 2228–2238.
15 X. G. Qiao, P.-Y. Dugas, B. Charleux, M. Lansalot and E. Bourgeat-Lami, *Polym. Chem.*, 2017, **8**, 4014–4029.
16 X. G. Qiao, M. Lansalot, E. Bourgeat-Lami and B. Charleux, *Macromolecules*, 2013, **46**, 4285–4295.
17 G. Wang, M. Schmitt, Z. Wang, B. Lee, X. Pan, L. Fu, J. Yan, S. Li, G. Xie, M. R. Bockstaller and K. Matyjaszewski, *Macromolecules*, 2016, **49**, 8605–8615.
18 D. B. Wright, M. A. Touve, L. Adamiak and N. C. Gianneschi, *ACS Macro Lett.*, 2017, **6**, 925–929.
19 J. C. Foster, S. Varlas, L. D. Blackman, L. A. Arkinstall and R. K. O'Reilly, *Angew. Chemie Int. Ed.*, 2018, **57**, 10672–10676.
20 E. R. Jones, M. Semsarilar, P. Wyman, M. Boerakker and S. P. Armes, *Polym. Chem.*, 2016, **7**, 851–859.
21 M. Williams, N. J. W. Penfold, J. R. Lovett, N. J. Warren, C. W. I. Douglas, N. Doroshenko, P. Verstraete, J. Smets and S. P. Armes, *Polym. Chem.*, 2016, **7**, 3864–3873.
22 K. E. B. Doncom, L. D. Blackman, D. B. Wright, M. I. Gibson and R. K. O'Reilly, *Chem. Soc. Rev.*, 2017, **46**, 4119–4134.
23 N. J. Warren, O. O. Mykhaylyk, D. Mahmood, A. J. Ryan and S. P. Armes, *J. Am. Chem. Soc.*, 2014, **136**, 1023–1033.
24 V. J. Cunningham, A. M. Alswieleh, K. L. Thompson, M. Williams, G. J. Leggett, S. P. Armes and O. M. Musa, *Macromolecules*, 2014, **47**, 5613–5623.
25 S. Boissé, J. Rieger, K. Belal, A. Di-Cicco, P. Beaunier, M.-H. Li and B. Charleux, *Chem. Commun.*, 2010, **46**, 1950–1952.
26 C. J. Ferguson, R. J. Hughes, D. Nguyen, B. T. T. Pham, R. G. Gilbert, A. K. Serelis, C. H. Such and B. S. Hawkett, *Macromolecules*, 2005, **38**, 2191–2204.
27 S. Binauld, L. Delafresnaye, B. Charleux, F. D'Agosto and M. Lansalot, *Macromolecules*, 2014, **47**, 3461–3472.
28 I. Chaduc, A. Crepet, O. Boyron, B. Charleux, F. D'Agosto and M. Lansalot, *Macromolecules*, 2013, **46**, 6013–6023.

29 X. Zhang, S. Boissé, W. Zhang, P. Beaunier, F. D'Agosto, J. Rieger and B. Charleux, *Macromolecules*, 2011, **44**, 4149–4158.
30 W. Zhang, F. D'Agosto, P.-Y. Dugas, J. Rieger and B. Charleux, *Polymer*, 2013, **54**, 2011–2019.
31 W. Zhang, F. D'Agosto, O. Boyron, J. Rieger and B. Charleux, *Macromolecules*, 2012, **45**, 4075–4084.
32 N. P. Truong, M. V Dussert, M. R. Whittaker, J. F. Quinn and T. P. Davis, *Polym. Chem.*, 2015, **6**, 3865–3874.
33 J. Rieger, W. Zhang, F. Stoffelbach and B. Charleux, *Macromolecules*, 2010, **43**, 6302–6310.
34 S. Sugihara, A. H. Ma'Radzi, S. Ida, S. Irie, T. Kikukawa and Y. Maeda, *Polymer*, 2015, **76**, 17–24.
35 S. Sugihara, A. Blanazs, S. P. Armes, A. J. Ryan and A. L. Lewis, *J. Am. Chem. Soc.*, 2011, **133**, 15707–15713.
36 G. Liu, Q. Qiu and Z. An, *Polym. Chem.*, 2012, **3**, 504–513.
37 W. Shen, Y. Chang, G. Liu, H. Wang, A. Cao and Z. An, *Macromolecules*, 2011, **44**, 2524–2530.
38 R. Jutta, G. Chloé, C. Bernadette, A. David and J. Christine, *J. Polym. Sci. Part A: Polym. Chem.*, 2009, **47**, 2373–2390.
39 C. Grazon, J. Rieger, N. Sanson and B. Charleux, *Soft Matter*, 2011, **7**, 3482–3490.
40 A. Blanazs, A. J. Ryan and S. P. Armes, *Macromolecules*, 2012, **45**, 5099–5107.
41 M. Semsarilar, V. Ladmiral, A. Blanazs and S. P. Armes, *Langmuir*, 2012, **28**, 914–922.
42 Y. Ning, L. A. Fielding, L. P. D. Ratcliffe, Y.-W. Wang, F. C. Meldrum and S. P. Armes, *J. Am. Chem. Soc.*, 2016, **138**, 11734–11742.
43 J. Lesage de la Haye, Z. Xuewei, C. Isabelle, F. Brunel, M. Lansalot and F. D'Agosto, *Angew. Chemie Int. Ed.*, 2016, **55**, 3739–3743.
44 Y. Li and S. P. Armes, *Angew. Chemie Int. Ed.*, 2010, **49**, 4042–4046.
45 P. Tanner, P. Baumann, R. Enea, O. Onaca, C. Palivan and W. Meier, *Acc. Chem. Res.*, 2011, **44**, 1039–1049.
46 L. Tao, W. Hu, Y. Liu, G. Huang, B. D. Sumer and J. Gao, *Exp. Biol. Med.*, 2011, **236**, 20–29.
47 S. E. A. Gratton, P. A. Ropp, P. D. Pohlhaus, J. C. Luft, V. J. Madden, M. E. Napier and J. M. DeSimone, *Proc. Natl. Acad. Sci.*, 2008, **105**, 11613–11618.
48 J. C. Foster, S. Varlas, B. Couturaud, J. R. Jones, R. Keogh, R. T. Mathers and R. K. O'Reilly, *Angew. Chemie Int. Ed.*, 2018, **57**, 15733–15737.
49 J. Tan, H. Sun, M. Yu, B. S. Sumerlin and L. Zhang, *ACS Macro Lett.*, 2015, **4**, 1249–1253.
50 L. P. D. Ratcliffe, A. Blanazs, C. N. Williams, S. L. Brown and S. P. Armes, *Polym. Chem.*, 2014, **5**, 3643–3655.
51 C. A. Figg, A. Simula, K. A. Gebre, B. S. Tucker, D. M. Haddleton and B. S. Sumerlin, *Chem. Sci.*, 2015, **6**, 1230–1236.
52 Z. An, Q. Shi, W. Tang, C.-K. Tsung, C. J. Hawker and G. D. Stucky, *J. Am. Chem. Soc.*, 2007, **129**, 14493–14499.
53 L. Hou, K. Ma, Z. An and P. Wu, *Macromolecules*, 2014, **47**, 1144–1154.
54 G. Delaittre, M. Save and B. Charleux, *Macromol. Rapid Commun.*, 2007, **28**, 1528–1533.
55 W. Zhou, Q. Qu, Y. Xu and Z. An, *ACS Macro Lett.*, 2015, **4**, 495–499.
56 Y. Jiang, N. Xu, J. Han, Q. Yu, L. Guo, P. Gao, X. Lu and Y. Cai, *Polym. Chem.*, 2015, **6**, 4955–4965.
57 Q. Qu, G. Liu, X. Lv, B. Zhang and Z. An, *ACS Macro Lett.*, 2016, **5**, 316–320.
58 P. Gao, H. Cao, Y. Ding, M. Cai, Z. Cui, X. Lu and Y. Cai, *ACS Macro Lett.*, 2016,

5, 1327–1331.
59 X. Wang, J. Zhou, X. Lv, B. Zhang and Z. An, *Macromolecules*, 2017, **50**, 7222–7232.
60 S. J. Byard, M. Williams, B. E. McKenzie, A. Blanazs and S. P. Armes, *Macromolecules*, 2017, **50**, 1482–1493.
61 G. Mellot, P. Beaunier, J.-M. Guigner, L. Bouteiller, J. Rieger and F. Stoffelbach, *Macromol. Rapid Commun.*, 2018, **0**, 1800315.
62 Q. Yu, Y. Ding, H. Cao, X. Lu and Y. Cai, *ACS Macro Lett.*, 2015, **4**, 1293–1296.
63 V. Ladmiral, A. Charlot, M. Semsarilar and S. P. Armes, *Polym. Chem.*, 2015, **6**, 1805–1816.
64 A. Hanisch, P. Yang, A. N. Kulak, L. A. Fielding, F. C. Meldrum and S. P. Armes, *Macromolecules*, 2016, **49**, 192–204.
65 Y. Ning, L. A. Fielding, T. S. Andrews, D. J. Growney and S. P. Armes, *Nanoscale*, 2015, **7**, 6691–6702.
66 J. R. Lovett, L. P. D. Ratcliffe, N. J. Warren, S. P. Armes, M. J. Smallridge, R. B. Cracknell and B. R. Saunders, *Macromolecules*, 2016, **49**, 2928–2941.
67 K. E. B. Doncom, N. J. Warren and S. P. Armes, *Polym. Chem.*, 2015, **6**, 7264–7273.
68 D. J. Keddie, *Chem. Soc. Rev.*, 2014, **43**, 496–505.
69 L. D. Blackman, K. E. B. Doncom, M. I. Gibson and R. K. O'Reilly, *Polym. Chem.*, 2017, **8**, 2860–2871.
70 J. Huang, H. Zhu, H. Liang and J. Lu, *Polym. Chem.*, 2016, **7**, 4761–4770.
71 M. Huo, Q. Ye, H. Che, X. Wang, Y. Wei and J. Yuan, *Macromolecules*, 2017, **50**, 1126–1133.
72 S. Perrier, C. Barner-Kowollik, J. F. Quinn, P. Vana and T. P. Davis, *Macromolecules*, 2002, **35**, 8300–8306.
73 A. B. Mabire, M. P. Robin, W.-D. Quan, H. Willcock, V. G. Stavros and R. K. O'Reilly, *Chem. Commun.*, 2015, **51**, 9733–9736.
74 M. Staniforth, W.-D. Quan, T. N. V Karsili, L. A. Baker, R. K. O'Reilly and V. G. Stavros, *J. Phys. Chem. A*, 2017, **121**, 6357–6365.
75 J. Skey and R. K. O'Reilly, *Chem. Commun.*, 2008, **35**, 4183–4185.

Conclusions and Future Work

Overall, this thesis has explored the use of copolymer blending and fluorescence labelling with an ABM fluorophore for probing, understanding and controlling the self-assembly and/or stimuli-responsive behavior of amphiphilic block copolymers in solution.

In Chapter 2, the design and synthesis of a range of ABM-functionalized RAFT agents was successfully achieved *via* both R and Z group functionalization. However, the synthetic route developed for the Z group ABM-functionalized RAFT agent **2xvii** with a tertiary R group was extremely low yielding and thus alternative protecting group chemistries need to be explored in the future to optimize its synthesis. Furthermore, the feasibility of utilizing an ABM-functionalized RAFT agent to synthesize fluorescent α- and ω-functionalized block copolymers was demonstrated in this thesis. However, the monomer scope for the synthesized RAFT agents was principally limited to more activated monomers such as (meth)acrylamides and (meth)acrylates. Therefore, to improve the versatility of this approach a change in Z group functionality would be required to target the formation of less active RAFT agents, such as xanthates or dithiocarbamates, in order to facilitate the controlled RAFT polymerization of less activated monomers, and ultimately expand the range of block copolymer compositions.

In Chapter 3, it was discovered that thermodynamic equilibrium was not reached for the series of pH-responsive p(DMAEMA)-*b*-p(*n*-BuMA-co-DMAEMA) diblock copolymer micelles analyzed and thus comicellization did not occur *via* unimer or micelle blending. Future work in this project would center upon targeting lower *n*-BuMA incorporations in order to reduce the energy barrier for unimer exchange and thus increase the dynamic nature of the diblock copolymers. Moreover, to determine whether a diblock copolymer system is under thermodynamic equilibrium, non-fluorescent and fluorescent micelles with similar block copolymer compositions could be blended together with the

fluorescence lifetime of the ABM fluorophore measured to ascertain whether unimer exchange is facilitated.

Steady-state fluorescence measurements of fluorescent diblock copolymer analogues also showed that the ABM fluorophore could prove to be a useful tool in probing the degree of core hydration of micellar solutions self-assembled from different block copolymers. As such, further research in this area could involve the synthesis of an extensive range of pH-responsive diblock copolymers for which the hydrophobic comonomer in the core-forming block is varied (e.g. methyl, ethyl, propyl, *n*-butyl methacrylate), whilst the hydrophobic comonomer incorporation is increased across each comonomer series. Consequently, using a combination of steady-state and time-resolved fluorescence spectroscopy, the sensitivity of the ABM fluorophore could be investigated by comparing polymeric micelles with different hydrophobic comonomers but similar hydrophobic comonomer incorporations, or *vice versa*.

In Chapter 4, blended diblock copolymers micelles composed of a p(*n*BA-*co*-DMAc) core and a blend of brush-like p(DEGMA) and p(OEGMA) thermoresponsive corona-forming blocks displayed cooperative behavior with a single thermal transition measured over a range of intermediate T_{cp}'s. However, microcalorimetry analysis suggested that the thermoresponsive diblock copolymer **4x** consisted of p(DEGMA) homopolymer impurities and thus the resultant cloud point transitions occurred at significantly lower temperatures than targeted. Consequently, resynthesizing **4x** may allow the successful formation of blended diblock copolymer micelles whose respective transition temperature can be modulated in a robust manner *via* simple manipulation of the molar mixing ratio. Further investigation into this thermoresponsive diblock copolymer system could also be conducted *via* fluorescence analysis. Through the synthesis of fluorescent diblock copolymer analogues using an ABM-functionalized RAFT agent, the collapse of the p(DEGMA) or p(OEGMA) coronal chains in solution could be monitored by

fluorescence spectroscopy providing the ABM fluorophore was situated adjacent to the thermoresponsive block. In addition, copolymer blending could potentially be confirmed *via* FRET measurements if the two constituent thermoresponsive diblock copolymers were functionalized with different fluorophores.

Finally, in Chapter 5 pure phases of spherical micelles, worm-like micelles, and vesicles were obtained for a series of p(DMAc)-*b*-p(DAAm) diblock copolymers prepared *via* RAFT-mediated PISA using a Z group ABM-functionalized RAFT agent. Further work in this project would focus upon measuring the fluorescence lifetime, steady-state fluorescence emission, and fluorescence quantum yield of the ABM fluorophore with respect to each block copolymer morphology. If measured fluorescence lifetimes vary as a function of particle morphology as anticipated, then the differential uptake of these polymer nanostructures into cells could be monitored *via* FLIM in future studies.